Syafwan, Mahdhivan (2012) The existence and stability of solitons in discrete nonlinear Schrödinger equations. PhD thesis, University of Nottingham.

The existence and stability of solitons in discrete nonlinear Schrödinger equations

Mahdhivan Syafwan, S.Si.

Thesis submitted to The University of Nottingham
for the degree of Doctor of Philosophy

November 2012

"...Then which of the favours of your Lord would you deny?..."
(QS. Ar-Rahman 55)

Dedicated to:
My parents, my wife and my son.

Acknowledgements

First and above all, I praise the Almighty Allah, the Most Gracious and the Most Merciful. Indeed, it is only because of His favours and bounties that I got the ability to accomplish this thesis.

There were many people who contributed in the completion of this thesis. Thus, I take this opportunity to express my gratitude to them. However, to mention them all here is indeed not possible, but they will never be forgotten. Firstly, and certainly, I would like to offer my deepest gratitude to Dr. Hadi Susanto and Dr. Stephen M. Cox who provided me invaluable supervision throughout my PhD studies. I feel honoured while getting benefits from their knowledge and mathematical experiences. I am also grateful for their kind support, guidance and suggestions during my studies, including their useful comments and corrections on the manuscripts of this thesis. Special thanks should be addressed to *mas* Hadi who helped me lot during my stay in the UK.

Next, I must express my sincere thanks and respect to my parents, Mama and Papa, for their boundless love and unlimited support. Their continuous prayers brought me at this stage. My sincere thanks also goes to my late grandmother (may Allah bless her with *jannah*) for her amazing kindness and care, as well as to my father-in-law who always treated me as his own son.

The most heartfelt gratitude is to my beloved wife and truly friend, Maya Sari Syahrul, for her total moral support, passion and companionship. Also for my little prince and beloved son, Faithulkhaliv Mahdhivan, the most lovely 'gift' who arrived in the period of my studies. Both of you have been sources of my inspiration. Furthermore, I also thanks to my brother and sister, Havid and Ivat, for their prayers and encouragement.

It is a pleasure to single out *pak* Saeed and Irfan *bhai*, for their help and warm brotherhood. I also acknowledge Boris Malomed for his valuable suggestions while working on variational approximations as well as Hill Meijer for fruitful discussions on Matcont. Finally, I am thankful to the Ministry of National Education of the Republic of Indonesia for providing me financial support.

Contents

2 Lattice solitons in a parametrically driven discrete nonlinear Schrödinger equation 27

Abstract

In this thesis, we investigate analytically and numerically the existence and stability of discrete solitons governed by discrete nonlinear Schrödinger (DNLS) equations with two types of nonlinearity, i.e., cubic and saturable nonlinearities. In the cubic-type model we consider stationary discrete solitons under the effect of parametric driving and combined parametric driving and damping, while in the saturable-type model we examine travelling lattice solitons.

First, we study fundamental bright and dark discrete solitons in the driven cubic DNLS equation. Analytical calculations of the solitons and their stability are carried out for small coupling constant through a perturbation expansion. We observe that the driving can not only destabilise onsite bright and dark solitons, but also stabilise intersite bright and dark solitons. In addition, we also discuss a particular application of our DNLS model in describing microdevices and nanodevices with integrated electrical and mechanical functionality.

By following the idea of the work above, we then consider the cubic DNLS equation with the inclusion of parametric driving and damping. We show that this model admits a number of types of onsite and intersite bright discrete solitons of which some experience saddle-node and pitchfork bifurcations. Most interestingly, we also observe that some solutions undergo Hopf bifurcations from which periodic solitons (limit cycles) emerge. By using the numerical continuation software Matcont, we perform the continuation of the limit cycles and determine the stability of the periodic solitons.

Finally, we investigate travelling discrete solitons in the saturable DNLS equation. A numerical scheme based on the discretization of the equation in the moving coordinate frame is derived and implemented using the Newton-Raphson method to find traveling solitons with non-oscillatory tails, i.e., embedded solitons. A variational approximation (VA) is also applied to examine analytically the travelling solitons and their stability, as well as to predict the location of the embedded solitons.

Frequently used abbreviations

DNLS	discrete nonlinear Schrödinger (equation)
PDNLS	parametrically driven discrete nonlinear Schrödinger (equation)
PDDNLS	parametrically driven damped discrete nonlinear Schrödinger (equation)
AL	Ablowitz-Ladik (equation)
ILM	intrinsic localised mode
EVP	eigenvalue problem
AC	anticontinuum
PN	Peierls-Nabarro (barrier)
MEMS	microelectromechanical system
NEMS	nanoelectromechanical system
ES	embedded soliton
VA	variational approximation
NS	Neimark-Sacker (bifurcation)
LPC	limit point cycle
BPC	branch point cycle
c.c.	complex conjugate

Publications

Most of the work of this thesis has been published or is going to appear for publication.

- Parts of Chapter 2 in this thesis have been published in:

  M. Syafwan, H. Susanto and S. M. Cox, *Discrete solitons in electromechanical resonators*, Phys. Rev. E **81**, 026207 (2010).

- Parts of Chapter 3 in this thesis are going to appear in:

  M. Syafwan, H. Susanto and S. M. Cox, *Solitons in a parametrically driven damped discrete nonlinear Schrödinger equation*. In B. A. Malomed (Ed), *Spontaneous Symmetry Breaking, Self-Trapping, and Josephson Oscillations in Nonlinear Systems* (Springer, Berlin, 2012).

- Parts of Chapter 4 in this thesis have been published in:

  M. Syafwan, H. Susanto, S. M. Cox and B. A. Malomed, *Variational approximations for traveling solitons in a discrete nonlinear Schrödinger equation*, J. Phys. A: Math. Theor. **45**, 075207 (2012).

CHAPTER 1

Introduction

Solitons are the main object of study in this thesis. Particular attention is given to models described by discrete nonlinear Schrödinger equations. Therefore, it will be advantageous to firstly provide introductory information and a general review about solitons and the considered models. In addition, it is also important to outline particular topics which are relevant and useful for subsequent chapters. This outline is discussed in this chapter.

1.1 What is a soliton?

Following Scott [1] and Drazin & Johnson [2], the term *soliton* is defined as a localised nonlinear wave which:

(i) maintains its shape when it travels at constant speed, and

(ii) can interact strongly with other solitons and retain its identity unchanged (except possibly for a phase shift).

The first condition reflects a characteristic of the so-called *solitary wave* while the second describes the particle-like interaction property from which the name *soliton* was coined in 1965 by Norman Zabusky and Martin Kruskal [3]. The phenomenon of solitons appears not only in continuous media, but also in discrete systems. For the latter, they are called *discrete* or *lattice solitons*, which are the main objects of investigation in this thesis.

The word *soliton* originally refers to a solitary wave of an 'ideal' system which supports precisely the solitonic conditions as described above. In the real world, however, such an 'ideal' soliton rarely occurs. Instead, one should deal with a situation where nonsolitonic or perturbational effects such as frictional loss, damping loss, internal or external driving force, defects and so forth, are inevitable (some of these effects are considered in two chapters of this thesis, i.e., internal (or so-called parametric) driving in Chapter 2 and combined parametric driving and damping in Chapter 3). For such systems, the meaning of soliton becomes degraded, i.e., it refers to a merely localised entity whose persistence and interaction properties are not really emphasised. Throughout this thesis, we use the terminology soliton with this weaker meaning. Moreover, since we omit the interaction property in our definition of soliton, the distinction between *solitary waves* and *solitons* becomes blurred. Thus, in this thesis, as most widely adopted in the physics literature, we will use these two terms interchangeably.

Before proceeding to the next section, it should be noted here that what we mean by a localised wave in this thesis is restricted to either the solution having a peak with tails decaying exponentially to 0 as the spatial coordinate x tends to $\pm\infty$, or one which has different asymptotic values at $x = \infty$ and $x = -\infty$. The former is called a *pulse*, while the latter is a *kink* (see Fig. 1.1). In addition to a kink, there is also an *anti-kink*, which is simply a mirror-image of the kink. Unless otherwise stated, from now on we refer to the profile with a pulse-like shape as a soliton.

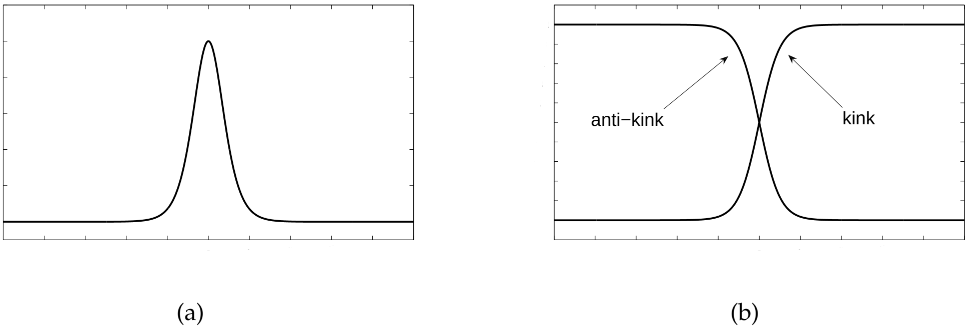

(a)

(b)

Figure 1.1: (a) A pulse soliton. (b) A kink and anti-kink soliton.

1.2 A brief history of solitons

In the following, we explain a brief historical development of solitons. What we present here is mostly extracted from [1, 2, 4–8].

The birth of the soliton (or solitary wave) was first scientifically reported by the Scottish engineer John Scott Russell in August 1834 through an accidental event. At that time, he was carrying out experiments on the Union Canal near Edinburgh to measure the relationship between the speed of the boat and its propelling force in order to find design parameters for conversion from horse power to steam. One day, the boat suddenly stopped since the tow rope connecting the horses to the boat broke. Surprisingly he observed that the mass of water in front of the boat “*...rolled forward with great velocity, assuming the form of a large solitary elevation, a rounded, smooth and well-defined heap of water, which continued its course along the channel apparently without change of form or diminution of speed*” (Russell [9]). He excitedly followed this “strange” wave on horseback and found it still rolling at a constant rate and preserving its original form for over two miles. Later, he called this serendipitous phenomenon the *Wave of Translation*.

Scott Russell reported his observations to one of the leading scientists of the day, Sir John Herschel. However, Herschel was not impressed with Scott Russell’s finding and commented that it was simply half of a common wave that had been cut off. To disprove this assertion, Scott Russell then set a number of laboratory experiments with shallow water waves in a tank to recreate his solitary waves’ phenomenon. The research brought him to demonstrate the following four facts (see, e.g., Zabusky & Porter [6]):

1. The solitary waves have a hyperbolic secant shape and travel with permanent form and velocity.
2. A sufficiently large initial mass of water produces two or more independent solitary waves.
3. Solitary waves can cross each other without change, except for a small displacement to each as a result of their interaction.
4. In a shallow water channel of height h, a solitary wave of amplitude A travels at a speed $\sqrt{g(A+h)}$ (where g is the gravitational acceleration), implying that larger-amplitude solitary waves move faster than smaller ones, i.e., confirming a nonlinear effect.

Scott Russell thought that his observations were of huge scientific impact. Unfortunately, his work had difficulty to get acceptance from the scientific community at a meeting of the British Association for the Advancement of Science in 1844, because it could not be explained by the existing waves theory at that time: waves either spread out to nothing or rise up until they break.

In 1895, after about 50 years being ignored, interest in Scott Russell’s soliton was rekindled by Diederik Korteweg together with his PhD student, Hendrik de Vries [10]. They derived a nonlinear partial differential equation (PDE) confirming the existence of Scott Russell’s (hydrodynamic) solitary waves mathematically. The equation, now called the Korteweg-de Vries (KdV) equation, modelled the evolution of waves in a shallow one-dimensional (1D) water channel, and is given by

$$\eta_t + c\eta_x + \varepsilon\eta_{xxx} + \gamma\eta\eta_x = 0. \tag{1.2.1}$$

In the above equation, $c = \sqrt{gh}$ represents the velocity of small amplitude waves, $\varepsilon = c(h^2/6 - T/(2\rho g))$ indicates the dispersive parameter, $\gamma = 3c/(2h)$ is the nonlinear parameter, T is the surface tension and ρ is the density of water. Korteweg and de Vries showed that Eq. (1.2.1) has exact travelling localised solutions which agreed with Scott Russell's observation. It should be noted that although Eq. (1.2.1) is named for Korteweg and de Vries, it was apparently first investigated (in the absence of surface tension) independently by Boussinesq [11] and Lord Rayleigh [12].

Mathematically, the formation of a soliton in the KdV equation can be explained as follows. In the absence of dispersive and nonlinear terms, i.e., when $\varepsilon = \gamma = 0$, the KdV equation becomes a dispersionless linear wave equation and thus has a travelling wave solution for any shape (including a localised form) at any velocity c. If one reinstates the dispersion term only, i.e., by setting $\varepsilon \neq 0$ and $\gamma = 0$, different Fourier components of any initial condition will propagate at different velocities, thus the wave profile will spread out (disperse). In contrast, if one reinstates only the nonlinear term, i.e., when $\varepsilon = 0$ and $\gamma \neq 0$, the wave will experience harmonic generation so that the crest of the wave moves faster than the rest; this then leads to wave breaking. However, by considering both dispersion and nonlinearity, there will be a situation such that the effect of dispersion is balanced by that of nonlinearity. In the latter case, a solitary wave can form.

Although Korteweg and de Vries had succeeded in modelling Scott Russell's solitary waves, they could not find general solutions of their equation. As a result, their work and also interest in the soliton fell (again) into obscurity.

The next development which indirectly restimulated interest in Scott Russell's solitary waves was made in the post-war era via the rapid advances in digital computers. In 1955, through the Los Alamos MANIAC computing machine, Enrico Fermi, John Pasta and Stanislaw Ulam (FPU)[1] [13] explored the dynamics of energy equipartition in a slightly nonlinear mechanical system, i.e., a chain of equal mass particles connected by slightly nonlinear springs (the equation model of such a nonlinear spring-mass system will be introduced in the following section). It was expected that if all the energy was initially introduced in a single mode, the small nonlinearity would cause energy redistribution among all the modes (thermalisation). But surprisingly, their numeri-

---

[1] Maria Tsingou also contributed significantly in the numerical part of the FPU study, therefore some also quote this study as the Fermi-Pasta-Ulam-Tsingou (FPUT) problem as first recommended by Dauxois [14].

cal results confirmed that all the energy returned almost periodically to the originally excited mode and a few nearby modes.

Motivated to find an explanation for this “FPU recurrence”, two American physicists, Norman Zabusky and Martin Kruskal [3], in 1965 approximated the FPU spring-mass system in the continuum limit using the KdV equation. They solved the equation numerically through a finite difference approach and reported that the KdV solitary waves can pass through each other without change in their shape or speed (the only change was a small phase shift after a collision). In fact, this is the same as what had been discovered by Scott Russell more than 100 years earlier. Zabusky and Kruskal then introduced for the first time the term *soliton* for such solitary waves, in order to emphasise their particle-like character (the ending “on” is Greek for “particle” (Dodd *et al.* [8])).

In 1967, another new development stimulating the mathematical study of solitons accredited to Clifford Gardner, John Greene, Martin Kruskal and Robert Miura [15], who discovered a method to find exact solutions (including soliton solutions) of the KdV equation. Their method is now known as the *inverse-scattering method* (ISM) and has become one of the most important discoveries achieved in mathematics in the past 50 years (Skuse [16]). Though it was initially used to explain solitons in the KdV equation, ISM was later found to provide a more general means for generating the exact soliton solutions in many integrable nonlinear PDEs.

Next, Vladimir Zakharov and Alexei Borisovich Shabat [17] in 1972, by constructing ISM, solved the nonlinear Schrödinger (NLS) equation. They demonstrated both the integrability and the existence of soliton solutions. The NLS equation is written as

$$\mathrm{i}\psi_t + \psi_{xx} \pm \beta|\psi|^2\psi = 0. \tag{1.2.2}$$

The ‘plus’ and ‘minus’ signs in the nonlinearity term are referred to as the so-called *focusing* and *defocusing* nonlinearities, respectively. The focusing NLS permits a pulse-like soliton, while the defocusing one has a kink-shaped soliton (see again Fig. 1.1). In nonlinear optics, they are known as *bright* and *dark* solitons, respectively (we shall use these terminologies in this thesis in a general manner). The NLS equation takes its name because its structure is formally similar to the Schrödinger equation of quantum mechanics (Dodd *et al.* [8]). The NLS equation was found as a fundamental model in many important applications. To mention but a few, it was used to describe nonlinear envelope waves in hydrodynamics, nonlinear optics, nonlinear acoustics and plasma waves (see, e.g., Scott [7]).

Next, in 1973, Mark Ablowitz, David Kaup, Alan Newell and Harvey Segur [18] also applied ISM for solving the sine-Gordon (SG) equation and presented its soliton solutions as well. The SG equation is given by

$$\theta_{tt} - \theta_{xx} = \sin(\theta), \tag{1.2.3}$$

which admits kink and anti-kink solitons. The SG equation also appears in many physical applications, including the propagation of crystal defects and the propagation of quantum units of magnetic flux (called *fluxons*) on long Josephson (superconducting) transmission lines (Scott [7]).

In addition to the discovery of the integrable nonlinear PDEs (continuous systems) mentioned above, from which the corresponding exact soliton solutions can be constructed, some integrable difference-differential equations (discrete systems) admitting exact discrete solitons have also been discovered. Among the prime examples are the Toda lattice [19, 20] and the Ablowitz-Ladik equation [21] (these two lattice equations will be explored more in the next section).

Since the mid-1970s, many other integrable nonlinear equations exhibiting soliton solutions both in continuous and discrete systems have been studied by many researchers. These studies have established the soliton concept in several areas of applied science. Nevertheless, soliton studies in non-integrable equations (either continuous or discrete) are also of great interest. Apart from their rich mathematical properties, these equations are of interest because they arise in a huge number of useful and promising applications. This motivates many researchers to perform both theoretical and experimental observations of solitons in those systems.

In this thesis, our study is devoted to the investigation of solitons in lattice systems governed by discrete nonlinear Schrödinger (DNLS) equations. Before discussing these lattice equations further, we first give a short review about the development of studies on discrete solitons. This also includes a review of some relevant applications.

1.3 Discrete solitons

1.3.1 Development of studies on discrete solitons: a review

As explained in the previous section, the rise of interest in solitons, although they were first observed in 1834, is mainly due to the attempts at explaining a nonlinear lattice problem, namely FPU recurrence (reported by Fermi *et al.* [13]). This problem was modelled by a one-dimensional lattice consisting of equal masses connected with weakly nonlinear springs, which can be written mathematically as

$$\frac{\mathrm{d}^2 r_n}{\mathrm{d}t^2} = V'(r_{n+1}) - 2V'(r_n) + V'(r_{n-1}). \tag{1.3.1}$$

Here $r_n = y_n - y_{n-1}$, where y_n is the displacement of the nth spring from its equilibrium position, and $V'(r)$ is the derivative of the spring potential given by

$$V'(r) = r + ar^m, \quad m = 2, 3. \tag{1.3.2}$$

The spring-mass lattice equation above is now known as the FPU lattice. Zabusky and Kruskal [3] showed that the FPU lattice in the continuum limit can be reduced to the KdV equation from which its soliton solutions were then confirmed numerically.

In the meantime, a Japanese mathematical physicist, Morikazu Toda [19, 20], in 1967 investigated a spring-mass system (1.3.1) but with spring potential of the form

$$V(r) = ar + \frac{a}{b}\mathrm{e}^{-br}, \quad a, b > 0. \tag{1.3.3}$$

The resulting equation of motion is thus given by

$$\frac{\mathrm{d}^2 r_n}{\mathrm{d}t^2} = -a(\mathrm{e}^{-br_{n+1}} - 2\mathrm{e}^{-br_n} + \mathrm{e}^{-br_{n-1}}), \tag{1.3.4}$$

which is now called Toda lattice. Toda found explicit solutions of Eq. (1.3.4) for two-soliton collisions. Seven years later Flaschka [22] proved the integrabililty of Toda lattice using ISM formulations.

It should be mentioned here that an early recorded study on discrete solitons was made in 1962 by Perring and Skyrme, who studied the discrete sine-Gordon equation derived originally by Frenkel and Kontorova in 1939 (see, e.g., Scott [7]). The lattice equation modelled a motion of crystal dislocations, given by

$$\frac{\mathrm{d}^2 \theta_n}{\mathrm{d}t^2} - \frac{\theta_{n+1} - 2\theta_n + \theta_{n-1}}{h^2} = \sin(\theta_n), \tag{1.3.5}$$

where θ_n is the displacement of the nth atom from its equilibrium position and h represents the lattice spacing. The discrete sine-Gordon equation (1.3.5) in the limit $h \to 0$ reduces to the sine–Gordon equation (1.2.3); this suggests the name 'discrete' in the former equation. Analogous with its continuum counterpart, the discrete sine-Gordon lattice supports discrete kink and anti-kink solitons. Perring and Skyrme examined numerically a collision of two kinks from which it was shown in the continuum limit that the solitons emerging from the collision have the same shapes and velocities with which they entered. They also found an exact analytical description of the collision phenomenon, although, in fact, had been derived a decade earlier by Seeger, Donth and Konchendörfer (see Scott *et al*. [23]).

The next lattice equation which should be discussed here is the discrete nonlinear Schrödinger (DNLS) equation. This equation is found as a ubiquitous model in discrete systems with profoundly important and wide-ranging applications. There is a number of types of DNLS equations which can be identified from their nonlinearities. We next point out some of them (we refer the reader to the book by Kevrekidis [24] for a comprehensive review of theoretical and experimental studies in the DNLS equations).

1.3.1.1 Cubic DNLS equation

The cubic DNLS equation is arguably the most studied version of the DNLS equations. Due to this fact, this equation is also referred to as a "standard DNLS" or simply a "DNLS" lattice. A cubic DNLS equation is given by

$$\mathrm{i}\dot{\psi}_n = -\varepsilon\Delta_2\psi_n + \beta\left|\psi_n\right|^2\psi_n, \tag{1.3.6}$$

where $\psi_n \equiv \psi_n(t)$ represents a complex function of time t at site n, the overdot denotes time derivative, ε is the so-called coupling constant between two adjacent sites, $\Delta_2\psi_n = \psi_{n+1} - 2\psi_n + \psi_{n-1}$ is the 1D discrete Laplacian and β is the nonlinearity parameter. The value of β can be either negative or positive, indicating the focusing or defocusing nonlinearity, respectively. In the above equation, both ε and β can be scaled out without loss of generality, i.e., $\varepsilon > 0$ and $\beta \gtrless 0$ can be scaled out to 1 and ±1, respectively, by the transformation

$$t \to t/\varepsilon, \quad \psi_n \to \psi_n/\sqrt{\varepsilon/|\beta|}. \tag{1.3.7}$$

However, we let ε and β remain in Eq. (1.3.6) for later illustrative purposes.

The cubic nonlinearity in the above equation is sometimes called the diagonal ("on-site") nonlinearity. This because the matrix representing the nonlinearity term is diagonal. Another name for the cubic nonlinearity, in the context of nonlinear optics, is the so-called *Kerr* nonlinearity, subject to a particular type of material whose nonlinear refractive index change $\Delta n(I)$ is linearly dependent upon the light intensity I (Lederer *et al.* [25]), i.e.,

$$\Delta n(I) = n_2 I, \tag{1.3.8}$$

where n_2 is the Kerr coefficient.

The DNLS (1.3.6) serves both as a model in its own right, i.e., modelling cases where the nature of the problem is discrete, or as a discretization of the continuous nonlinear Schrödinger equation (1.2.2), i.e., by considering the discrete Laplacian term as a central difference approximation for the spatial derivative term in Eq. (1.2.2). In this thesis, the DNLS equation (1.3.6) is considered in its own right (the former case), thus we will not relate its properties with the corresponding continuous equation. This also holds for the study of another type of DNLS equation, i.e., saturable lattice, which will be explained later. The cubic DNLS system is known, except for the case of only two lattice sites, to be nonintegrable (Scott [7]).

Historically (see, e.g., Scott [1, 7] and references therein), the cubic DNLS equation was first derived by Holstein in 1959 to model the motion of a self-trapped electron (polaron) in a one-dimensional crystal lattice. The equation reappeared in 1972 when Davydov studied the energy transfer in biomolecules. The same equation was also used by Christodoulides and Joseph in 1988 to model the dynamics of an optical field in a nonlinear coupled waveguide array. Furthermore, in the 1990s the DNLS equation was also studied as a model of systems of coupled anharmonic oscillators which admit the so-called *intrinsic localised modes* or *discrete breathers* (we will explain this later). Quite recently, Trombettoni and Smerzi also used this equation in 2001 to describe a Bose-Einstein (BEC) condensate trapped in a periodic potential. Two of those applications mentioned above, i.e., optical waveguide arrays and systems of coupled anharmonic oscillators (in the context of micro- and nano-electromechanical resonators) will be discussed in more detail later.

1.3.1.2 Ablowitz-Ladik (AL) DNLS equation

Another type of DNLS equations, which is integrable, is the Ablowitz-Ladik (AL) lattice. This equation was originally formulated by Ablowitz and Ladik [21] in 1976. This lattice is obtained by replacing the diagonal ("on-site") nonlinearity in Eq. (1.3.6) with an off-diagonal ("inter-site") nonlinearity, resulting

$$\mathrm{i}\dot{\psi}_n = -\varepsilon\Delta_2\psi_n + \frac{\beta}{2}\left|\psi_n\right|^2\left(\psi_{n+1}+\psi_{n-1}\right). \tag{1.3.9}$$

In the continuum limit, i.e., when $\psi_n \approx \psi$, $(\psi_{n+1}+\psi_{n-1})/2 \approx \psi$ and $\varepsilon\Delta\psi_n \approx \psi_{xx}$, the above equation reduces to the NLS equation (1.2.2). Since the AL equation is integrable, there exists an exact soliton solution, given by (after the rescalings $\varepsilon = 1$ and $\beta = 2$)

$$\psi_n(t) = \sinh(\chi)\,\mathrm{sech}[\chi(n-ct)]\mathrm{e}^{\mathrm{i}(kn+\omega t+\alpha)}, \tag{1.3.10}$$

where χ, k and α are free parameters, $c = 2\sinh(\chi)\sin(k)/\chi$ and $\omega = 2(\cosh(\chi)\cos(k) - 1)$. In spite of having no direct physical application (up to this date), the AL equation is commonly used as a starting point in perturbational studies for other models, like Eq. (1.3.6), which are more physically meaningful (Scott [7]).

1.3.1.3 Salerno DNLS equation

In 1992, Salerno [26] proposed an interesting model of the DNLS equation of the form

$$\mathrm{i}\dot{\psi}_n = -\varepsilon\Delta_2\psi_n + 2(1-\alpha)\left|\psi_n\right|^2\psi_n + \alpha\left|\psi_n\right|^2\left(\psi_{n+1}+\psi_{n-1}\right), \tag{1.3.11}$$

which interpolates between the cubic DNLS (1.3.6) at $\alpha = 0$ and the AL lattice (1.3.9) at $\alpha = 1$. Due to its property of incorporating the cubic and AL DNLS lattices, the Salerno equation becomes an ideal general model for studying, e.g., the interplay between on-site and inter-site nonlinearities, discreteness and continuum, integrability and non-integrability, etc (see Scott [1] and references therein).

1.3.1.4 Saturable DNLS equation

Another variant of DNLS equations that is very relevant to discuss in this thesis is a DNLS lattice featuring the so-called *saturable* nonlinearity. This equation is written as

$$\mathrm{i}\dot{\psi}_n = -\varepsilon\Delta_2\psi_n + \frac{\sigma\psi_n}{1+\left|\psi_n\right|^2}, \tag{1.3.12}$$

which represents a discrete version of the Vinetskii-Kukhtarev equation [27]. Most recently, the continuum version of Eq. (1.3.12) in the defocusing case also occurred in azo-dye doped nematic liquid crystal as reported by Piccardi *et al.* [28].

As in the cubic case, the nonlinearity term in the saturable DNLS lattice can be either focusing or defocusing, indicated by $\sigma > 0$ or $\sigma < 0$, respectively. In the optical context, this equation appears to model light propagation in photorefractive media which exhibit a saturation behaviour, i.e., the nonlinear refractive index change has an upper limit (Lederer *et al.* [25]), which is modelled by

$$\Delta n(I) = \frac{\Delta n_0}{1+I/I_s}, \tag{1.3.13}$$

where I_s is the saturation intensity.

Among the DNLS equations discussed above, the cubic and saturable lattices are studied in this thesis. These two equations will be elaborated further in the next section. Before that, we review two relevant applications motivating cubic and saturable DNLS equations.

1.3.2 Discrete solitons in two relevant applications

1.3.2.1 Optical waveguide arrays

In optics, arrays or lattices of coupled waveguides are considered as prime examples of physical structures in which the dynamics of a discrete optical field (light) can be observed (Christodoulides *et al.* [29]). These arrays consist of equally spaced identical waveguide elements or sites (see Fig. 1.2). From a classical perspective, light discretization is rather naturally impossible since light itself is a continuous function in time and space. However, the realisation of microfabrication technology for such arrays made this unnatural idea into reality.

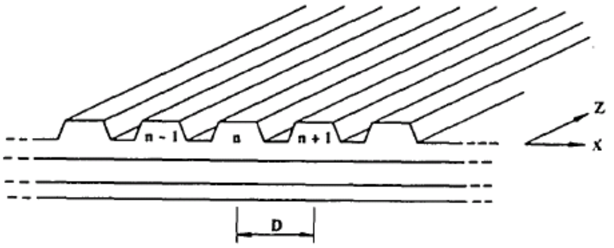

Figure 1.2: A nonlinear array of coupled waveguides. Reprinted from Christodoulides & Joseph [32].

The study of light propagation in a linear coupled waveguide array was first theoretically investigated by Jones [30] in 1965, and then experimentally observed by Somekh *et al.* [31] using a gallium arsenide (GaAs) waveguide array in 1973. Both studies showed that the coupling among adjacent waveguides causes light to spread from one waveguide to the others, i.e., confirming the effect of the so-called *discrete diffraction*.

In 1988, Christodoulides and Joseph [32] theoretically suggested that the discrete diffraction could be counteracted in a nonlinear waveguide array which allows the light to be self-localised. This state of self-localisation emerges as a result of a balance between nonlinearity and discrete diffraction effects. As a result, the light is confined within only a few waveguide lattices, i.e., propagating as a discrete soliton.

In deriving their model, Christodoulides and Joseph assumed that the waveguide array is lossless, infinite (big enough), weakly coupled (considering only nearest-neighbour interactions) and made from a *Kerr* material. Under these assumptions, they showed that the dynamics of discrete optical solitons can be described by the cubic DNLS equation (1.3.6). In the context of this model, the integer variable n in Eq. (1.3.6) indexes the waveguides, while t indicates the longitudinal spatial coordinate, i.e., the distance along the waveguides. $|\psi_n(t)|^2$ is the light intensity at a distance t along the nth waveguide.

The above theoretical prediction was tested initially by Eisenberg *et al.* [33] in 1998. Using a nonlinear aluminium gallium arsenide (AlGaAs) waveguide array (see Fig. 1.3(a)), they obtained the following experimental results (see Fig. 1.3(b)). At low powers (70 W) the input light beam injected into one waveguide becomes discretely diffracted in the array. This can be justified theoretically by neglecting the nonlinear term of Eq. (1.3.6), which basically reconfirms the earlier study of a linear coupled waveguide array. If the power is increased (320 W), the distribution of light converges to form a bell shape. Providing even more power (500 W), the optical field self-localises leading to a discrete soliton formation.

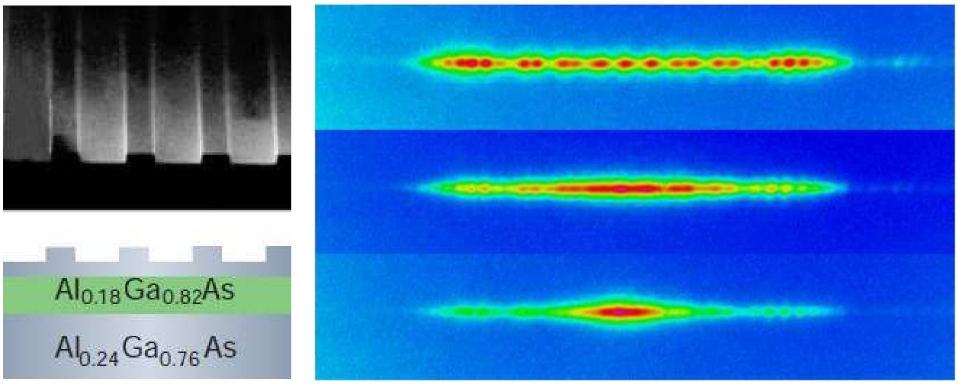

(a) (b)

Figure 1.3: First experimental observations of discrete optical solitons in a coupled waveguide array made from aluminium gallium arsenide (AlGaAs). (a) Microscopic image of the array. (b) Experimental results depicting the output facet of a waveguide array for different power levels: at 70 W (top) the beam is discretely diffracted, at 320 W (centre) the beam's distribution is narrowing, and at 500 W (bottom) a discrete soliton is formed. Reprinted from Christodoulides *et al.* [29].

The above initial experiment stimulated a large number of subsequent observations from which interesting phenomena were reported. These include the first experimental demonstration of the effect of the Peierls-Nabarro (PN) potential (Morandotti *et al.* [34]), diffraction management (Eisenberg *et al.* [35]), the interaction of discrete soliton with structural defects (Morandotti *et al.* [36]), discrete solitons in photorefractive arrays (Segev *et al.* [37], Efremidis *et al.* [38] and Fleischer *et al.* [39]), to mention a few. For a comprehensive review of recent experimental and theoretical developments in the field of optical discrete solitons, the interested reader can refer to, e.g., Lederer *et al.* [25] and Kivshar & Agrawal [40]. In what follows, we point out the last mentioned example.

Initially, optical waveguide arrays were fabricated as a lattice of separate waveguides where specialised materials with fixed geometries are required. This would limit their potential application. However, as firstly suggested by Segev *et al.* [37] and experimentally tested by Efremidis *et al.* [38] and Fleischer *et al.* [39], waveguide arrays can be optically induced in media made from photorefractive materials. The most commonly used form of nonlinearity for such materials is the saturable nonlinearity. This leads to the creation of a new type of optical discrete soliton governed by saturable DNLS (1.3.12). In the initial experiments of Efremidis *et al.* [38], the photorefractive material of choice was SBN:75 crystal.

One of the fascinating applications of discrete solitons in optical waveguide arrays is their realisation in optical routing and switching processing which, in fact, play a vital role in future communication and information systems. In such a realisation, as theoretically demonstrated by Christodoulides & Eugenieva (& Efremidis) [41–43] and experimentally tested recently by Keil *et al.* [44], a discrete soliton moves transverse to the axes of waveguide array networks and can be routed along the pre-assigned array pathways which act like "soliton wires" (see Fig.1.4(a)). In addition, and more interestingly, a discrete soliton at array intersections can also be routed towards one of the paths. The basic idea for such a scheme, as illustrated in Fig.1.4(b), is by utilising an elastic collision of two different discrete soliton families, i.e., the so-called 'signals' and 'blockers'. Blockers are immobile and strongly confined (localised effectively to a single lattice), while, in contrast, signals are highly mobile and moderately confined. The blockers are used to block, reflect or redirect a signal, and placed at the entrance of the paths which a signal is prohibited to pass through. As a consequence, a signal is routed towards the other branch. The later implementation opens the gate for the possibility of optical switching processing. Apparently, the mobility of travelling solitons plays a main role in the abovementioned schemes, and this is the subject of Chapter 4 in this thesis.

1.3.2.2 MEMS and NEMS resonators

Current advances in the fabrication and control of electromechanical systems on a micro and nanoscale bring many technological promises (Ventra *et al.* [45]). These include efficient and highly sensitive sensors to detect stresses, vibrations and forces at the atomic level; to detect chemical signals; and to perform signal processing (Cleland [46]). As a particular example, a nanoelectromechanical system (NEMS) can detect the mass of a single atom, due to its mass that is very small (Roukes (and Cleland) [47, 48]).

On a fundamental level, NEMS with high frequency will allow research on quantum mechanical effects. This is because NEMS, as a miniaturisation of microelectromechanical systems (MEMS), can contain a macroscopic number of atoms, yet still require quan-

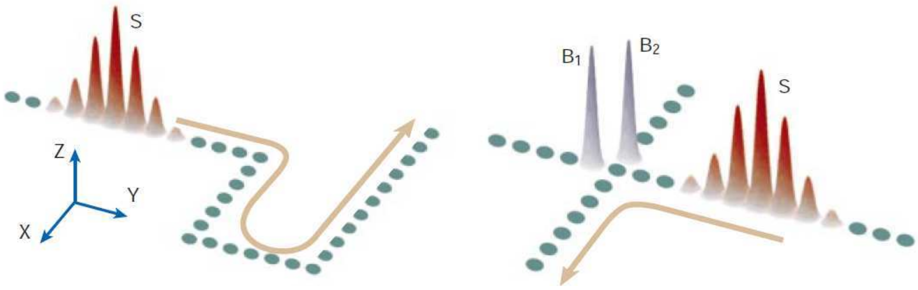

(a) (b)

Figure 1.4: (a) Intensity profile of a discrete soliton, S, travelling along the specific pathways (shown by the arrow) in a transverse $x - y$ plane perpendicular to the nonlinear waveguide array network (the cross-section of the lattice network is shown by the circles). The pulse, as shown by Christodoulides & Eugenieva [41], can successfully negotiate a sequence of bends, i.e., it can be routed on predefined tracks. (b) An X-switching junction using two different discrete soliton families, i.e., the so-called 'signals' and 'blockers' (see text). In the junction, the signal S interacts elastically with two blockers (B_1 and B_2) placed at the entries of the respective pathways. As a result, the signal is routed towards the other branch as indicated by the arrow. Reprinted from Christodoulides *et al*. [29].

tum mechanics for their proper description. Thus, NEMS can be considered as a natural playground for a study of mechanical systems at the quantum limit and quantum-to-classical transitions (see, e.g., Katz *et al*. [49] and references therein).

Typically, nanoelectromechanical devices comprise an electronic device coupled to an extremely high frequency nanoresonator (recently going beyond 10 GHz) with relatively weak dissipation parametrised by a quality factor[2] in the range of $10^2 - 10^4$ (Lifshitz *et al*. [50]). In such devices, it will be easy to obtain sufficient data to characterise the steady state motion, as transients tend to disappear rapidly. Moreover, weak dissipation and weak nonlinearity can be treated as small perturbations. These facts provide a great advantage for quantitative comparisons between theoretical and experimental studies.

A large number of arrays of MEMS and NEMS resonators have recently been fabricated experimentally (see, e.g., Buks & Roukes [51]). One direction of research in the study of such arrays has focused on intrinsic localised modes (ILMs) or discrete breathers. ILMs can be present due to parametric instabilities in an array of oscillators (Wiersig [52]). ILMs in driven arrays of MEMS have been observed experimentally by Sato *et al*. [53–

---

[2] A quality factor of the nanoresonator is defined as $Q = \omega_0/\Delta\omega$, where ω is the fundamental resonance frequency of the resonator and $\Delta\omega$ is the frequency width of the resonant response at half maximum (Cleland & Roukes [48]).

55] (to illustrate how such experiments are constructed, see Fig. 1.5 and the explanation in the figure).

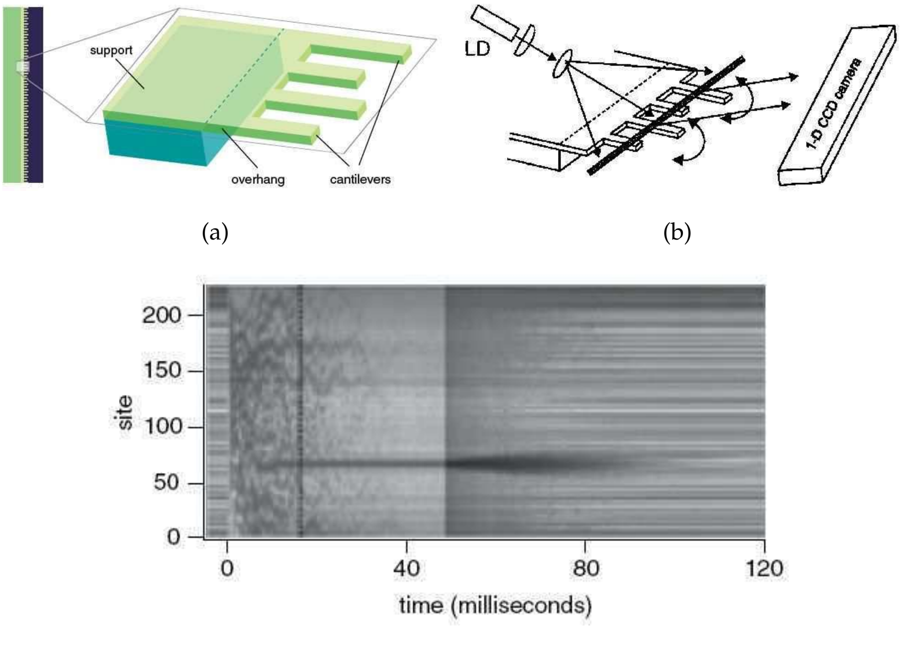

(a) (b)

(c)

Figure 1.5: An experimental setup for observing ILMs. (a) The cantilever array in which each behaves as a nonlinear oscillator coupled together via an overhang region. (b) The observational technique for recording the dynamics of the cantilever array. A line shaped laser beam is focused on and reflected from the array. The reflected beam is imaged on a 1D CCD camera. When a cantilever acquires a large vibrational amplitude, its image darkens. (c) The resulting image of vibration of the array. After a few tens of milliseconds, the vibration becomes localised as shown by dark horizontal line. Reprinted from Sato *et al.* [53] and Porter *et al.* [56].

The first realisation of a large array of MEMS and NEMS resonators was reported by Buks and Roukes (BR) [51]. The device was designed in the form of two interdigitated combs such that all even-numbered beams were connected to one comb and all odd-numbered beams to a second one (see Fig. 1.6(a)). A dc voltage V_{dc} was then applied to introduce a coupling between each beam and its nearest neighbours. Also, an ac voltage V_{ac} was used to parametrically excite the modes of vibration. To describe the dynamics of the system, BR employed a simple 1D model for an N-element array of coupled pendulums (see Fig. 1.6(b)). The first and last pendulums in the array are stationary and clamped with distance L, while all others $(n = 2, 3, ..., N-1)$ are free to oscillate about their equilibrium positions na, where a is the equilibrium spacing between neighbouring pendulums. The displacement of the system is described by a set of coordinates x_n for $n = 1, 2, ..., N$.

The experiment of BR above was modelled mathematically by Lifshitz and Cross [57] and simplified later by Kenig *et al.* [58]. In the latter reference, the creation, stability and interaction of ILMs in the simplified model with low damping have been studied in the case of strong-coupling limit or slowly varying solutions. In Chapter 2 of this thesis, we consider a similar study but in the case of small coupling or strongly localised solutions.

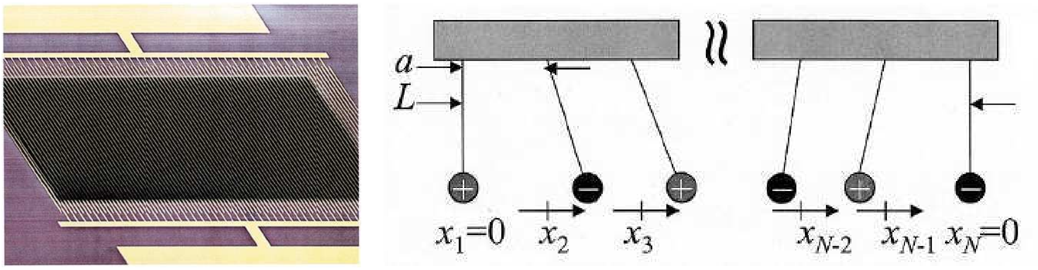

(a) (b)

Figure 1.6: (a) A side view micrograph of an array of MEMS resonators. (b) A model of N coupled pendulums employed to describe the dynamics of (a). Reprinted from Buks & Roukes [51].

1.4 The cubic and saturable DNLS equations

1.4.1 Stationary discrete solitons: preliminary analysis

Let us first consider cubic DNLS (1.3.6). To obtain stationary discrete soliton solutions, we substitute the ansatz

$$\psi_n(t) = u_n \mathrm{e}^{\mathrm{i}\Lambda t}, \tag{1.4.1}$$

where u_n is time independent and Λ is the oscillation frequency, into Eq. (1.3.6). Thus, the stationary amplitudes u_n satisfy the coupled lattice equation

$$(\Lambda + \beta |u_n|^2) u_n = \varepsilon (u_{n+1} - 2u_n + u_{n-1}). \tag{1.4.2}$$

Solutions u_n are generally complex valued. However, for localised solutions under the condition

$$u_n \to \pm a \quad \text{as} \quad n \to \pm\infty, \tag{1.4.3}$$

with either $a = 0$ (bright solitons) or $a \neq 0$ (dark solitons), the analysis can be simplified, without loss of generality, by taking real-valued solutions only. This fact can be explained as follows (our presentation here is mainly adopted from Kevrekidis [24] and Hennig & Tsironis [59]).

If one multiplies Eq. (1.4.2) by u_n^* (i.e., complex conjugate[3] of u_n) and then subtract the complex conjugate of the resulting equations, this leads to a conserved quantity

$$u_n^* u_{n+1} - u_n u_{n+1}^* = \text{const.} \tag{1.4.4}$$

Since we consider localised solutions under the condition (1.4.3), the constant in the last equation becomes 0. Thus, we have

$$\frac{u_{n+1}}{u_{n+1}^*} = \frac{u_n}{u_n^*} \quad \Rightarrow \quad \arg(u_{n+1}) = \arg(u_n) \pmod{\pi}. \tag{1.4.5}$$

Consequently, if one chooses $\arg(u_{n_0})$ such that u_{n_0} is real for at least one $n_0 \in \mathbb{Z}$, then u_n are real for all $n \in \mathbb{Z}$. One can check that this fact also holds for stationary discrete solitons in saturable DNLS (1.3.12).

Basically, there are infinitely many configurations for discrete soliton solutions. However, the two most commonly studied solutions are the one centred on a lattice site and the one centred between two subsequent lattice sites (Kevrekidis *et al.* [60]). We call the former *onsite* soliton and the latter *intersite* soliton. For bright and dark solitons, i.e., when $a = 0$ and $a \neq 0$ in Eq. (1.4.3), respectively, these two modes become onsite and intersite bright solitons, and onsite and intersite dark solitons. In the case of bright solitons, onsite and intersite modes were initially proposed by Sievers and Takeno [61] and by Page [62], respectively.

In addition to the abovementioned configurations, there also exist the so-called *staggered* solitons, i.e., those obtained by simply using staggering transformations $v_n = (-1)^n u_n$. Thus, the fundamental localised modes in staggered configurations also emerge accordingly from the unstaggered ones; they are onsite and intersite staggered bright solitons, and onsite and intersite staggered dark solitons. Note that in each of the cubic and saturable DNLS equations, the corresponding staggered bright (dark) solitons exist in the de(focusing) case. In this thesis, we will not study such solitons and thus reserve the names bright and dark soliton, unless otherwise stated, to the unstaggered case.

It is noteworthy to mention here that the intersite modes can be either *in-phase* or *out-of-phase*. The latter case is also called a *twisted* mode. In carrying out the study of stationary lattice solitons in the next chapters, the only intersite modes that we consider are those with in-phase oscillations.

---

[3] Another way to represent complex conjugation which is also used in this thesis is by writing $\overline{u}_n$.

1.4.2 Gauge invariance

One of important properties of cubic and saturable DNLS equations, that we should address here, is the existence of the so-called *gauge invariance* (Kevrekidis *et al.* [24, 60]), i.e., if we use a transformation

$$\psi_n \to \psi_n \mathrm{e}^{\mathrm{i}\theta}, \tag{1.4.6}$$

for an arbitrary $\theta \in \mathbb{R}$, then Eqs. (1.3.6) and (1.3.12) are left unchanged. The above invariance is also called *phase* or *rotational invariance*. Thus, another way to express Eqs. (1.3.6) and (1.3.12) is by writing

$$\psi_n(t) = \phi_n(t)\mathrm{e}^{\mathrm{i}\Lambda t}, \tag{1.4.7}$$

where $\phi_n(t)$ is now a solution of

$$\mathrm{i}\dot{\phi}_n = -\varepsilon\Delta_2\phi_n + \Lambda\phi_n + \beta\left|\phi_n\right|^2\phi_n, \tag{1.4.8}$$

for the cubic case, or

$$\mathrm{i}\dot{\phi}_n = -\varepsilon\Delta_2\phi_n + \Lambda\phi_n + \frac{\sigma\phi_n}{1+\left|\phi_n\right|^2}, \tag{1.4.9}$$

for the saturable case. Parameter Λ in Eq. (1.4.7) is an adjustable parameter. However, we also can treat it as a frequency parameter.

Stationary discrete solitons for the last two equations can be obtained by simply setting ϕ_n to be time-independent. Thus, the obtained stationary solitons for these equations will be exactly the same as the previous ones [Eqs. (1.3.6) and (1.3.12)]. The fundamental difference between the former and the latter forms of the DNLS equations is in its dynamical manifestation. In Eqs. (1.3.6) and (1.3.12), its dynamics is in the form of soliton oscillation while in Eqs. (1.4.8) and (1.4.9), the oscillation is absent. We call the solution in the former situation an *intrinsic localised mode* (ILM) or *discrete breather*, i.e., one which is localised in space and periodic in time. In the rest of this thesis, except for some particular purposes, we will take cubic and saturable DNLS equations in the latter forms, i.e., Eqs. (1.4.8) and (1.4.9).

1.4.3 Travelling discrete solitons: Peierls-Nabarro (PN) barrier analysis

In continuous systems, the translational invariance (also known as Galilean or Lorentz invariance) hints at the existence of a travelling soliton, provided a stationary one exists. In discrete models (in most cases), however, such a property no longer exists.

Before moving to the next discussion, we note that cubic and saturable DNLS systems are conservative under the respective Hamiltonians [for notational convenience, here we consider Eqs. (1.3.6) and (1.3.12)],

$$H_{\text{cub}} = \sum_{n=-\infty}^{\infty} \left[\varepsilon |\psi_{n+1} - \psi_n|^2 + \frac{\beta}{2} |\psi_n|^4 \right], \tag{1.4.10}$$

and

$$H_{\text{sat}} = \sum_{n=-\infty}^{\infty} \left[\varepsilon |\psi_{n+1} - \psi_n|^2 + \sigma \ln(1 + |\psi_n|^2) \right]. \tag{1.4.11}$$

In addition, the total power,

$$P = \sum_{n=-\infty}^{\infty} |\psi_n|^2, \tag{1.4.12}$$

is also conserved in both systems.

When a discrete soliton moves across the lattice, there are only two possibilities: one centred on a lattice site (onsite soliton) and the other centred between two adjacent lattice sites (intersite soliton). The difference between the Hamiltonians (for the same power) in the two configurations is termed the *Peierls-Nabarro* (PN) barrier [63, 64], which accounts for the resistance that the soliton has to overcome during transverse propagation. Therefore, to make a soliton moves freely along the lattice, the PN barrier must be surmounted.

In the cubic DNLS, it is known that, for the same power, the Hamiltonian is always minimum in the (stable) onsite soliton, and maximum in the (unstable) intersite one. Thus, as power level increases, the PN barrier also increases. This fact has also been demonstrated experimentally by Morandotti *et al.* [34]; see Fig. 1.7. This sign-definite PN barrier indeed restricts the mobility of solitons in the cubic case.

Interestingly, in the saturable DNLS model, the sign-definite PN barrier is no longer the case. The PN barrier in this equation, in fact, can exhibit sign reversal, hence may vanish at isolated points. This fact was initially investigated by Hadžievski *et al.* [65]; see Fig. 1.8. Instead of measuring the PN barrier $\Delta E = H_{\text{sat}}^{os} - H_{\text{sat}}^{is}$ as a function of power P as that used in the latter reference (here the superscripts *os* and *is* represent onsite and intersite modes), Melvin *et al.* [66, 67] measured the generalised PN barrier defined by $\Delta G = G^{os} - G^{is}$, where $G^x = H_{\text{sat}}^x - \Lambda P^x$ ($x = os$ or is) and Λ is the frequency of the solution, as a function of one of parameters (in this case ε). By performing linear stability of the solitons using linearisation around a solution profile u_n of the form $\psi_n = e^{i\Lambda t}[u_n + \delta(a_n e^{\lambda t} + b_n e^{\lambda^* t})]$, they found that stability-instability alternation in both onsite and intersite solitons occurs *not* at the points of vanishing ΔE, but at the zeros of ΔG (see Fig. 1.9). At these points, the corresponding eigenvalue λ crosses zero, i.e., may possibly restore an effective translational invariance in the model. Therefore, one might intuitively expect that genuinely travelling localised solutions, i.e., ones with vanishing oscillatory tails, might exist in the saturable lattice. The issue of undistorted travelling

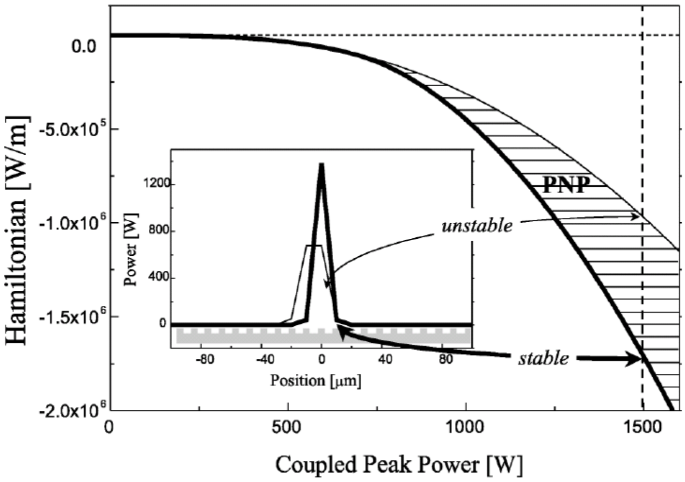

Figure 1.7: The experimental results of Morandotti *et al.* [34] showing Hamiltonian versus power for onsite and intersite solitons in cubic DNLS (1.3.6). The difference between the Hamiltonians is the Peierls-Nabarro potential (PNP) barrier. The inset exhibit the profile for two types of solitons in a peak power indicated by the vertical dashed lines. Reprinted from Morandotti *et al.* [34].

solitons in DNLS type lattices is of particular interest, since it would be desirable to transport optical (in the case of optical waveguides) or quantum (in the case of Bose-Einstein condensates (BECs) in optical lattices) bits of information without radiative losses (Melvin *et al.* [67]).

Motivated by the interesting results mentioned above, Melvin *et al.* [66, 67] then proceeded to numerically study the existence and stability of travelling discrete solitons in the saturable DNLS model, from which it was confirmed that genuinely travelling lattice solitons exist at isolated points. In Chapter 4, we revisit this study by following the ideas in the previous works but by using a different numerical scheme and corroborated with an analytical approach.

Travelling solitons with vanishing oscillatory tails have also been observed earlier in the Salerno model (1.3.11) using a different numerical method (Gómez-Gardeñes *et.al* [68]), showing that the travelling localised waves acquire non-vanishing tails as soon as parameter α deviates from the integrable AL limit $\alpha = 1$. Later, Melvin *et al.* [69] used exponential asymptotic expansions to prove the (non)existence of travelling solitons in this model.

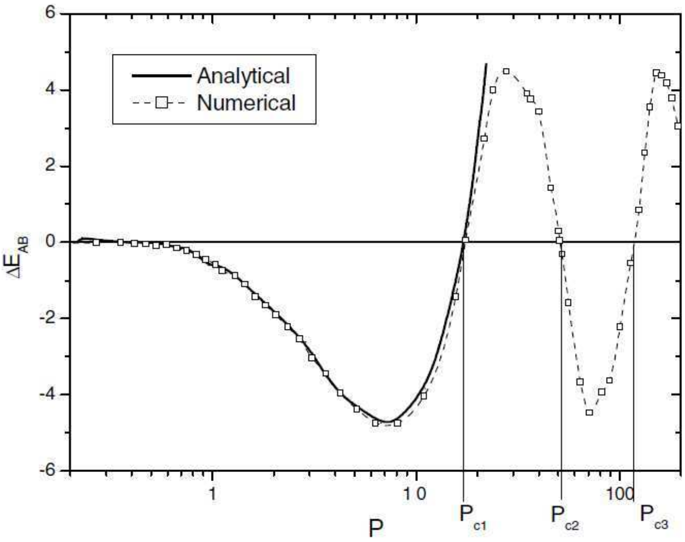

Figure 1.8: PN barrier versus power P for discrete solitons in saturable DNLS (1.3.12), calculated analytically and numerically using parameter values $\sigma = 18.2$ and $\varepsilon = 2$. Reprinted from Hadžievski *et al*. [65].

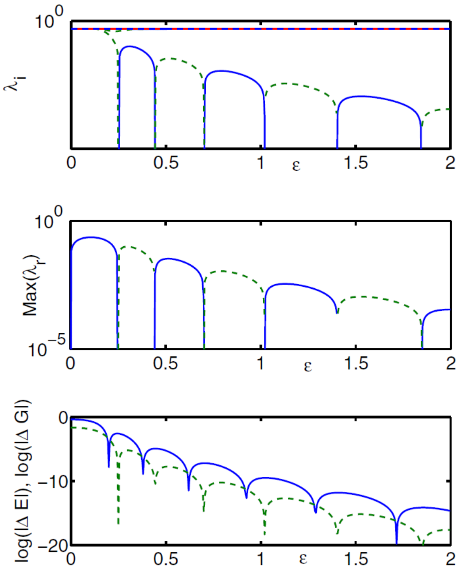

Figure 1.9: The upper panel shows the imaginary part (on an exponential scale) of the eigenvalues λ for the onsite (dashed line) and intersite (solid line) modes as functions of ε with frequency $\Lambda = 0.5$ (see text how the eigenvalues arise). The middle panel indicates the maximum of the real part of the corresponding eigenvalues λ as shown in the upper panel. The lower panel indicates the values of $\log(|\Delta E|)$ (solid lines) and $\log(|\Delta G|)$ (dashed lines) as functions of ε (see text). Reprinted from Melvin *et al*. [66].

1.4.4 Analytical methods

In this section, we review some theoretical approaches which will be employed in this thesis.

1.4.4.1 The anticontinuum limit approach

The so-called *anticontinuum (AC) limit approach* was introduced initially by MacKay and Aubry [70] when they studied the existence of localised solutions (in the form of breathers) for networks of weakly coupled oscillators. In the same paper, they also applied this approach to prove the existence of breather solutions in the DNLS equation (1.3.6).

In this approach, as the name suggests, the analysis of the lattice equation is started by considering the case of zero coupling limit ($\varepsilon = 0$). In this limit, the sites are uncoupled and one can construct exact solutions of the ensuing equation. These solutions then can be continued for nonzero ε. MacKay and Aubry [70] have shown that all solutions which exist in the limit $\varepsilon = 0$ can be continued up to some positive value ε^*. Later, a number of various bounds for the limit value of ε^* have been explored (see, e.g., Hennig & Tsironis [59] and Alfimov *et al.* [71]). In particular, for localised solutions, for example by setting all sites but one to be zero in the AC limit, they remain localised under this continuation with the tails decaying exponentially as $n \to \pm\infty$. A justification for this statement was given by Alfimov *et al.* [71].

1.4.4.2 Perturbation expansions

These methods are used to approximate solutions of a system, which is not explicitly solvable, in a small range of parameter values. As 'small' is relative, we first need to nondimensionalise the variables of the system. The next step is to find special cases that can serve as a starting point for approximating the solution in the nearby cases. Most often, these cases can be obtained by setting some of the parameters equal to zero. This applies in our case as the exact solutions of the lattice equations are available in the AC limit $\varepsilon = 0$. Once an exact solution is obtained, we then can generate the approximate solution in the form of a perturbation expansion for the first few terms, usually for the first two or three terms. A standard form of a perturbation expansion is in a power series of a small perturbation parameter. For example, we can expand a solution u_n in the stationary equation (1.4.2) as

$$u_n = u_n^{(0)} + \varepsilon u_n^{(1)} + \varepsilon^2 u_n^{(2)} + \cdots , \tag{1.4.13}$$

where $u_n^{(0)}$ is the exact solution in the AC limit. Upon substituting the above expansion into Eq. (1.4.2) and collecting the terms in successive powers of ε, we obtain a number of order equations from which the solutions $u_n^{(1)}, u_n^{(2)}$, etc can be solved iteratively.

A guarantee that the above expansion is convergent in an interval $0 \leqslant \varepsilon < \varepsilon_0$ for some ε_0, was given by Lemma 2.2 in Pelinovsky *et al.* [72]. A basis for the lemma follows from the Implicit Function Theorem, as the Jacobian matrix for the system (1.4.2) is non-singular at $u_n = u_n^{(0)}$, while the right hand-side of the system (1.4.2) is analytic in ε.

1.4.4.3 The variational approximations

The variational approximation (VA) is a semi-analytical technique which is well known and has been long used to approximate solutions (including the localised states) of a nonlinear evolution equation. It is called *semi-analytical* because in practice this method involves numerical computations in dealing with the resulting equations which are generally too complicated to be solved analytically.

The method of the VA is systematically described in the following steps (Kaup & Vogel [73]):

1. Establish the Lagrangian of the governing equation.
2. Choose a reasonable trial function (ansatz) containing a finite number of parameters (also called variational parameters).
3. Substitute the chosen ansatz into the Lagrangian and perform the resulting sums (for discrete systems) or integrations (for continuous system).
4. Determine the critical points of the variational parameters by solving the Euler-Lagrange equations.

One would expect that the 'success' of the variational method mainly depends on the choice of the trial function representing the 'actual shape' of the system. At the same time, the selection of this function should be in line with the practical consideration, i.e., they must be such that the resulting sums or integrations are expressible in a closed form. In addition, as this method basically reduces an original system with infinitely many degrees of freedom into a finite-dimensional one, we may argue that the number of the parameters capturing the 'nature' of the system would also affect to the accuracy of the VA; the more parameters used, the more accurate the approximations obtained. However, adding more parameters to the VA indeed increase the complexity of the calculations. This makes the VA sometimes an art rather than a science. For a comprehensive review of the VA in various applications, we refer the reader to Malomed [74].

In the context of DNLS model with cubic nonlinearity, the VA has been applied in a number of papers and its agreement has been confirmed with the corresponding numerical results; see, e.g., Aceves *et al.* [75], Cuevas *et al.* [76] and Kaup [77]. In those references, various trial functions have been exploited where some better than others. For example, the ansatz used by Aceves *et al.* [75] can only construct the onsite solutions, while the ansatz by Cuevas *et al.* [76] is also applicable for the (symmetric) intersite configurations. Moreover, the ansatz proposed by Kaup [77] can predict the asymmetric intersite solutions, thus the VA can also be used to explain bifurcations linking solutions. The validity of the VA for the cubic DNLS equation in the limit of small coupling has been justified rigorously by Chong *et al.* [78] from which it was shown that the trial function for stationary discrete solitons with more parameters provides more accurate approximations.

The use of VA has been also applied for other variants of DNLS equations, for example those with power-law cubic nonlinearity (Malomed & Weinstein [79] and Cuevas *et al.* [80]), combination of competing self-focusing cubic and defocusing quintic onsite nonlinearities (or so-called cubic-quintic DNLS) (Carretero-González *et al.* [81] and Chong & Pelinovsky [82]) and extended linear coupling (Rasmussen *et al.* [83] and Chong *et al.* [84]). By using different forms of the trial configuration, including those used in the cubic model, the VA in those DNLS was successful in approximating the different types of emerging solutions. In particular, the VA developed by Chong & Pelinovsky [82] was also able to predict correctly the spectrum determining the stability of a configuration.

1.5 Overview of thesis

The aim of this thesis is to examine the existence and stability of lattice solitons governed by discrete nonlinear Schrödinger (DNLS) equations with cubic and saturable nonlinearities. For the cubic-type DNLS model, we introduce a parametric driving and combined parametric driving and damping, where attention is on the study of the stationary soliton solutions. For the saturable DNLS model, we particularly focus on investigations of travelling lattice solitons.

We begin our work in Chapter 2 by considering the DNLS equation (1.3.6) in the presence of a parametric driving; we call this model a parametrically driven discrete nonlinear Schrödinger (PDNLS) equation. Analytical and numerical calculations are carried out to determine the existence and stability of stationary discrete solitons. In particular, we examine the fundamental onsite and intersite lattice solitons in both focusing and defocusing PDNLS equations, which admit bright and dark discrete solitons, respectively. Our analytical method in this study is based on the anticontinuum (AC) limit approach which has been already discussed in the previous section. This method allows us to perform existence and stability analyses for small coupling constant using a perturbation expansion. The analytical results are then corroborated with numerics. Moreover, numerical integrations of the considered model are performed to confirm the stability results of our analysis.

A further complementary work of our study in Chapter 2 is the application of a parametrically driven DNLS model in arrays of parametrically-driven nonlinear resonators of microelectromechanical and nanoelectromechanical systems (MEMS and NEMS). A brief review about the experimental and theoretical studies on MEMS and NEMS resonators has been discussed in the previous section. As we shall show, the PDNLS equation, by using a multiscale expansion method, can be derived from the governing equation of MEMS and NEMS resonators, i.e., a particular type of the so-called parametrically driven discrete Klein-Gordon equation. We then perform numerical simulations of the Klein-Gordon equation and confirm the relevance of our analysis.

Next, in Chapter 3 we extend the ideas of Chapter 2 by introducing the effect of damping in the PDNLS system; we refer to this model as a parametrically driven damped discrete nonlinear Schrödinger (PDDNLS) equation. As we identify later, there exist a number of types of onsite and intersite stationary discrete soliton in this model. Our further analysis demonstrates that saddle-node and pitchfork bifurcations occur in the lattice soliton solutions. More interestingly, some solutions admit Hopf bifurcations from which periodic solitons (limit cycles) emerge. The continuation of the limit cycles as well as the stability of the periodic solitons are computed through the numerical continuation software Matcont. To confirm our stability findings, the numerical integrations of the PDDNLS equation are performed for both stationary and periodic solitons.

In Chapter 4, we study the existence and stability of travelling solitary waves in the saturable DNLS (1.3.12). As mentioned previously, this study has been discussed earlier numerically by Melvin *et al*. [66, 67]. In their work, they used a pseudo-spectral method to solve the equation in a moving coordinate frame, which is an advance–delay-differential equation. The numerically obtained soliton solutions generally exhibit nonzero oscillatory tails, which is due to a resonance with the system's linear radiation. To obtain an isolated genuine travelling-soliton state on the discrete lattice, they proposed the use of a measure based on an appropriately crafted tail condition.

Our work in Chapter 4 basically follows the idea in the abovementioned references but by employing a different numerical scheme based on the discretization of the advance–delay-differential equation. To find a genuinely travelling discrete soliton, we propose an alternative measure to be used together with the measure modified from the previous work. Moreover, to study analytically the travelling solitary waves of the saturable DNLS lattice and their stability, as well as to predict the location of travelling solitons with non-oscillatory tails, we apply a semi-analytical approach based on the formulation of variational approximation (VA). A brief review of this analytic method has been discussed in the previous section of this chapter.

Finally, in Chapter 5 we summarise our work carried out in this thesis. In the same chapter, we also outline several interesting problems related to our models which might be proposed for future investigations.

CHAPTER 2

Lattice solitons in a parametrically driven discrete nonlinear Schrödinger equation

In the previous chapter, we have briefly discussed some properties and early works on lattice solitary waves in the discrete nonlinear Schrödinger (DNLS) equation with cubic nonlinearity. In this chapter, we examine the existence and stability of fundamental bright and dark discrete solitons in the DNLS equation in the presence of parametric driving.

2.1 Introduction

We consider a parametrically driven discrete nonlinear Schrödinger (PDNLS) equation given by

$$\mathrm{i}\dot{\phi}_n = -\varepsilon\Delta_2\phi_n \pm \Lambda\phi_n \pm \gamma\overline{\phi}_n \mp |\phi_n|^2\phi_n, \tag{2.1.1}$$

where $\phi_n \equiv \phi_n(t)$ is a complex-valued wave function at site $n \in \mathbb{Z}$, the overdot and the overline denote, respectively, the time derivative and the complex conjugation, ε represents the coupling constant between two adjacent sites, $\Delta_2\phi_n = \phi_{n+1} - 2\phi_n + \phi_{n-1}$ is the discrete Laplacian in one spatial dimension and γ is the parametric driving coefficient with frequency Λ. The "minus" and "plus" signs of the nonlinearity term (or, accordingly, the "plus" and "minus" signs in front of Λ and γ) correspond to the focusing and defocusing cases, respectively. To the best of our knowledge, Eq. (2.1.1) was studied for the first time by Hennig [85] with the inclusion of a damping term (the presence of this term will be discussed in the next chapter of this thesis).

The PDNLS (2.1.1) has a conserved quantity

$$H = \sum_{n=-\infty}^{\infty} \varepsilon(\overline{\phi}_n \phi_{n+1} + \phi_n \overline{\phi}_{n+1}) - (2\varepsilon \pm \Lambda)|\phi_n|^2 \mp \frac{\gamma}{2}(\overline{\phi_n}^2 + \phi_n^2) \pm \frac{1}{2}|\phi_n|^4. \tag{2.1.2}$$

With canonical variables $p_j = \overline{\phi}_n$ and $q_j = \phi_n$, the equations of motion (2.1.1) can be derived from (2.1.2) by the Hamilton equations $\dot{p}_j = -\mathrm{i}\frac{\partial \mathcal{H}}{\partial q_j}$ and $\dot{q}_j = \mathrm{i}\frac{\partial \mathcal{H}}{\partial p_j}$, where $\mathcal{H}$ is the Hamiltonian density, i.e., the summand of Eq. (2.1.2). Due to the parametric driving, Eq. (2.1.1) does not have a conserved norm. The change of the norm is given by

$$\frac{\mathrm{d}P}{\mathrm{d}t} = \mp\mathrm{i} \sum_{n=-\infty}^{\infty} \gamma(\overline{\phi}_n^2 - \phi_n^2), \tag{2.1.3}$$

where $P = |\phi_n|^2$. Note that when $\gamma = 0$, the norm is indeed conserved.

In the undriven case ($\gamma = 0$), Eq. (2.1.1) admits the existence of the phase or gauge invariance as we explained in Section 1.4.1 (see the transformation (1.4.6)). In the driven case ($\gamma \neq 0$), this invariance no longer exists due to the presence of the complex-conjugate term. However, transformation $\phi_n \to \phi_n \mathrm{e}^{\mathrm{i}\theta}$ is valid in the parametrically driven DNLS (2.1.1) for $\theta = \pi + 2k\pi$ and $\theta = -\pi/2 + 2k\pi$ with $k \in \mathbb{Z}$, which lead, respectively, to the reflection symmetry under transformation

$$\phi_n \to -\phi_n, \tag{2.1.4}$$

and

$$\phi_n \to -\mathrm{i}\phi_n, \quad \gamma \to -\gamma. \tag{2.1.5}$$

Consequently, transformation (2.1.5) allows us to only consider the driving constant $\gamma > 0$.

In this chapter, we are particularly interested in steady-state localised solutions of Eq. (2.1.1) having the form $\phi_n = u_n$ where u_n is complex valued and time-independent. In this case, u_n satisfies the stationary equation,

$$-\varepsilon\Delta_2 u_n \pm \Lambda u_n \pm \gamma\overline{u}_n \mp |u_n|^2 u_n = 0, \tag{2.1.6}$$

under localisation conditions

$$u_n \to 0 \text{ as } n \to \pm\infty, \tag{2.1.7}$$

which correspond to discrete bright soliton solutions in the focusing case, and

$$u_n \to \pm a \text{ for } a \neq 0, \text{ as } n \to \pm\infty, \tag{2.1.8}$$

which yield discrete dark soliton solutions in the defocusing case. Here we set $\varepsilon > 0$. The case $\varepsilon < 0$ can be obtained accordingly by the staggering transformation

$$u_n \to (-1)^n u_n, \quad \Lambda \to (\Lambda - 4\varepsilon). \tag{2.1.9}$$

By this transformation, localised solutions with boundary conditions (2.1.7) and (2.1.8) then lead to the respective staggered bright and dark discrete solitons. However, as we mentioned in the previous chapter, we will not discuss such solitons in this thesis.

2.1.1 Review of some previous works

In the absence of parametric driving, i.e., when $\gamma = 0$, it was shown, e.g., by Kevrekidis [24] and Hennig & Tsironis [59] that all localised solutions of Eq. (2.1.6) satisfying the conditions (2.1.7) and (2.1.8) are real-valued (see again the relevant explanation in Section 1.4.1). Discrete bright solitons in such a system have been discussed, e.g., by Hennig & Tsironis [59], Alfimov *et al*. [71] and Pelinovsky *et al*. [72], where it was shown that one-excited-site (onsite) solitons are stable for any coupling constant ε and two-excited-site (intersite) solitons are unstable for nonzero ε. Undriven discrete dark solitons have also been examined [86–90]; it is known that intersite dark solitons are always unstable for any ε, and onsite dark solitons are stable only in a small window of ε. For larger ε, an onsite dark soliton is unstable due to the presence of a quartet of complex eigenvalues, i.e., it suffers oscillatory instability.

The parametrically driven DNLS (2.1.1) with focusing nonlinearity and finite ε has been considered briefly by Susanto *et al*. [91], where it was shown that an onsite bright discrete soliton can be destabilised by parametric driving. The existence and stability of localised solutions of Eq. (2.1.1) in the presence of a dissipation term have been explored earlier by Hennig [85] using a nonlinear map approach which exhibited rich dynamical localisation effects.

In the continuous limit, localised excitations of the parametrically driven DNLS, i.e., Eq. (2.1.1) with $\varepsilon \to \infty$, have been considered by Barashenkov and co-workers in a different context of applications [92–100]. The same equation also applies to the study of Bose–Einstein condensates, describing the so-called long bosonic Josephson junctions (Kaurov & Kuklov [101, 102]).

2.1.2 Overview

In this chapter, we consider Eq. (2.1.1) with either focusing and defocusing nonlinearities, which admits bright and dark discrete solitons, respectively. The existence and stability of the fundamental onsite and intersite excitations of each of bright and dark solitons are examined analytically and numerically

The analytical calculations of the soliton solution and its stability are carried out for small coupling constant ε by using a perturbation expansion, i.e., we follow the idea of the *anticontinuum (AC) limit approach* which was introduced initially by MacKay and Aubry [70] (a brief review of this approach was given in the previous chapter).

In the presence of parametric driving, i.e., when $\gamma > 0$, we will show later in Chapter 3 that, there are only two possibilities for a localised solution of the stationary PDNLS (2.1.6), i.e., either real (provided $\Lambda > -\gamma$) or purely imaginary (provided $\Lambda > \gamma$), where the purely imaginary solution in the focusing case is always unstable. We should notice that the purely imaginary solution can always be obtained from the real one through transformation (2.1.5). Therefore, the study in this chapter will be only devoted for real valued solutions u_n.

The findings obtained from the analytical calculations are then compared with the corresponding numerical counterparts. By solving a corresponding eigenvalue problem numerically for a range of values of the coupling and driving constants, ε and γ, we produce stability regions in the (ε, γ)-plane for all the fundamental solitons. Approximations to the onset of instability are also derived using perturbation theory, with accompanying numerical results. The typical dynamics of solitons in the stable and unstable parameter ranges is then confirmed by direct numerical integrations of the governing equation (2.1.1). These theoretical analyses are presented in Sections 2.2 and 2.3 which are devoted, respectively, for bright and dark solitons.

In Section 2.4, we particularly discuss parametrically driven DNLS (2.1.1) in arrays of parametrically-driven nonlinear resonators with application to microelectromechanical and nanoelectromechanical systems (MEMS and NEMS). As we shall show, a particular type of parametrically driven discrete Klein-Gordon equation describing MEMS and NEMS resonators can be reduced, by using a multiscale expansion, to the PDNLS (2.1.1). The stability results obtained for the PDNLS are then confirmed by numerical simulations of the Klein-Gordon equation.

Finally, in Section 2.5 we summarise our work and give conclusions to our findings.

2.2 Bright solitons in the focusing PDNLS

In this section we first consider the existence and stability of bright solitons in the focusing stationary PDNLS equation (2.1.6). For a real valued solution u_n, it follows that

$$-\varepsilon\Delta_2 u_n + (\Lambda + \gamma)u_n - u_n^3 = 0. \tag{2.2.1}$$

Once such discrete solitary-wave solutions have been found, their linear stability is determined by solving a corresponding eigenvalue problem. To do so, we introduce the linearisation ansatz $\phi_n = u_n + \delta\epsilon_n$ where $\delta \ll 1$, and substitute this into Eq. (2.1.1) to yield the following linearised equation at $\mathcal{O}(\delta)$:

$$\mathrm{i}\dot{\epsilon}_n = -\varepsilon\Delta_2\epsilon_n + \Lambda\epsilon_n + \gamma\overline{\epsilon}_n - 2u_n^2\epsilon_n - u_n^2\overline{\epsilon}_n. \tag{2.2.2}$$

Writing $\epsilon_n = \eta_n \mathrm{e}^{\mathrm{i}\omega t} + \overline{\xi}_n \mathrm{e}^{-\mathrm{i}\overline{\omega}t}$, we then obtain from Eq. (2.2.2) the eigenvalue problem (EVP)

$$\begin{bmatrix} \varepsilon\Delta_2 - \Lambda + 2u_n^2 & u_n^2 - \gamma \\ -u_n^2 + \gamma & -\varepsilon\Delta_2 + \Lambda - 2u_n^2 \end{bmatrix} \begin{bmatrix} \eta_n \\ \xi_n \end{bmatrix} = \omega \begin{bmatrix} \eta_n \\ \xi_n \end{bmatrix}, \tag{2.2.3}$$

which can be subsequently solved numerically for the eigenvalues ω and the corresponding eigenvectors $[\eta_n, \xi_n]^T$.

In the physics literature, ω is referred to as eigenfrequency, while $\lambda = \mathrm{i}\omega$ is an eigenvalue. Moreover, as the stability matrix of the EVP (2.2.3) is real-valued, $\overline{\omega}$ is also an eigenvalue. Therefore, we can conclude that the solution u_n is (linearly) stable only when $\mathrm{Im}(\omega) \neq 0$ for all eigenvalues ω.

We note that Eq. (2.2.3) is linear. Hence, we may eliminate one component of the eigenvectors, for instance the component ξ_n, to obtain an alternative expression of the eigenvalue problem in the form

$$\mathcal{L}_+(\varepsilon)\mathcal{L}_-(\varepsilon)\eta_n = \omega^2\eta_n = \Omega\eta_n, \tag{2.2.4}$$

where the operators $\mathcal{L}_-(\varepsilon)$ and $\mathcal{L}_+(\varepsilon)$ are defined by

$$\mathcal{L}_-(\varepsilon) \equiv -\varepsilon\Delta_2 - (3u_n^2 - \Lambda - \gamma), \tag{2.2.5}$$

$$\mathcal{L}_+(\varepsilon) \equiv -\varepsilon\Delta_2 - (u_n^2 - \Lambda + \gamma). \tag{2.2.6}$$

In view of the relation $\Omega = \omega^2$, it follows that a soliton is unstable if it has an eigenvalue with either $\Omega < 0$ or $\mathrm{Im}(\Omega) \neq 0$.

2.2.1 Analytical calculations

Analytical calculations of the existence and stability of discrete solitons can be carried out for small coupling constant ε, using a perturbation analysis. This analysis exploits the exact solutions of Eq. (2.2.1) in the uncoupled limit $\varepsilon = 0$, which we denote by $u_n = u_n^{(0)}$, in which each $u_n^{(0)}$ must take one of the three values given by

$$0, \pm\sqrt{\Lambda + \gamma}, \tag{2.2.7}$$

provided

$$\Lambda > -\gamma. \tag{2.2.8}$$

Solutions of Eq. (2.2.1) for small ε can then be calculated analytically by writing

$$u_n = u_n^{(0)} + \varepsilon u_n^{(1)} + \varepsilon^2 u_n^{(2)} + \cdots . \tag{2.2.9}$$

On substituting the above expansion into Eq. (2.2.1) and collecting the terms in successive powers of ε, one obtains, at $\mathcal{O}(1)$ and $\mathcal{O}(\varepsilon)$, respectively, the equations

$$\begin{aligned} \left(u_n^{(0)}\right)^3 - (\Lambda+\gamma)u_n^{(0)} &= 0, & (2.2.10)\\ \Delta_2 u_n^{(0)} - (\Lambda+\gamma)u_n^{(1)} + 3u_n^{(1)}\left(u_n^{(0)}\right)^2 &= 0. & (2.2.11) \end{aligned}$$

Together, the above equations give the leading order correction, $u_n^{(1)}$, as

$$u_n^{(1)} = \frac{\Delta_2 u_n^{(0)}}{-3\left(u_n^{(0)}\right)^2 + \Lambda + \gamma}. \tag{2.2.12}$$

Because solutions $u_n^{(0)}$ at each site n are independent of each other, there will be infinitely many combinations for configuration of $u_n^{(0)}$. Here, however, we focus our attention on configuration of onsite and intersite bright solitons whose the mode structures in the AC limit $\varepsilon = 0$ are, respectively, of the form

$$u_n^{(0)} = \begin{cases} \sqrt{\Lambda+\gamma}, & n = 0,\\ 0, & \text{otherwise}, \end{cases} \tag{2.2.13}$$

and

$$u_n^{(0)} = \begin{cases} \sqrt{\Lambda+\gamma}, & n = 0, 1,\\ 0, & \text{otherwise}. \end{cases} \tag{2.2.14}$$

In the above configuration, due to the reflection symmetry (2.1.4), we neglect the negative quantity of the excited site(s).

Next, in studying the stability problem, it is natural to also expand the eigenvector having component η_n and the eigenvalue Ω in powers of ε, as

$$\eta_n = \eta_n^{(0)} + \varepsilon\eta_n^{(1)} + \mathcal{O}(\varepsilon^2), \quad \Omega = \Omega^{(0)} + \varepsilon\Omega^{(1)} + \mathcal{O}(\varepsilon^2). \tag{2.2.15}$$

Upon substituting this expansion into Eq. (2.2.4) and identifying coefficients of successive powers of the small parameter ε, we obtain from the equations at $\mathcal{O}(1)$ and $\mathcal{O}(\varepsilon)$

$$\begin{aligned} \left[\mathcal{L}_+(0)\mathcal{L}_-(0) - \Omega^{(0)}\right]\eta_n^{(0)} &= 0, & (2.2.16)\\ \left[\mathcal{L}_+(0)\mathcal{L}_-(0) - \Omega^{(0)}\right]\eta_n^{(1)} &= f_n, & (2.2.17) \end{aligned}$$

where

$$f_n = [(\Delta_2 + 2u_n^{(0)}u_n^{(1)})\mathcal{L}_-(0) + \mathcal{L}_+(0)(\Delta_2 + 6u_n^{(0)}u_n^{(1)}) + \Omega^{(1)}]\eta_n^{(0)}. \tag{2.2.18}$$

As $\mathcal{L}_+(0)\mathcal{L}_-(0) = (3(u_n^{(0)})^2 - \Lambda - \gamma)((u_n^{(0)})^2 - \Lambda + \gamma)$ represents only a single independent quantity for each n, we simply infer that the operator $[\mathcal{L}_+(0)\mathcal{L}_-(0) - \Omega^{(0)}]$ in the above equations is self-adjoint.

In the uncoupled limit, $\varepsilon = 0$, the eigenvalue problem is thus simplified to

$$\Omega^{(0)} = \mathcal{L}_+(0)\mathcal{L}_-(0), \tag{2.2.19}$$

from which we conclude that there are two possible eigenvalues, given by

$$\Omega_C^{(0)} = \Lambda^2 - \gamma^2, \quad \Omega_E^{(0)} = 4(\Lambda + \gamma)\gamma, \tag{2.2.20}$$

which correspond, respectively, to the solutions $u_n^{(0)} = 0$ (for all n) and $u_n^{(0)} = \pm\sqrt{\Lambda + \gamma}$ (for all n). Note that the expression of $\Omega_C^{(0)}$ in Eq. (2.2.20) shows that Λ plays an important role. When $\Lambda < \gamma$ or $\Lambda < -\gamma$, it is clear that 0 is an unstable solution.

Considering onsite and intersite bright soliton solutions then implies that (for $\varepsilon = 0$) the eigenvalues $\Omega_E^{(0)}$ and $\Omega_C^{(0)}$ have finite and infinite multiplicity, respectively. These then generate a corresponding discrete and continuous spectrum (phonon band) for finite positive ε.

To investigate the significance of the continuous spectrum, we introduce a plane-wave expansion

$$\eta_n = a\mathrm{e}^{\mathrm{i}\kappa n} + b\mathrm{e}^{-\mathrm{i}\kappa n}, \tag{2.2.21}$$

from which one obtains the dispersion relation

$$\Omega = [2\varepsilon(\cos\kappa - 1) - \Lambda]^2 - \gamma^2. \tag{2.2.22}$$

This in turn shows that the continuous band lies between

$$\Omega_L = \Lambda^2 - \gamma^2, \text{ when } \kappa = 0, \tag{2.2.23}$$

and

$$\Omega_U = \Lambda^2 - \gamma^2 + 8\varepsilon(\Lambda + 2\varepsilon), \text{ when } \kappa = \pi. \tag{2.2.24}$$

Let us now investigate all the possible cases in the continuous spectrum through the analysis of the parameter values Λ and γ and their relation (recall that ε and γ have been set to be positive in the beginning). For $\Lambda > 0$, by considering the condition (2.2.8), there are two cases, i.e., $\Lambda \geq \gamma > 0$ or $\gamma > \Lambda > 0$. The first case implies that all the eigenvalues $\Omega \in [\Omega_L, \Omega_U]$ lie along the positive real axis for all ε which means that the continuous spectrum does not cause instability. On the contrary, the second case yields $\Omega_L < 0$ which leads to the instability of soliton for all ε. Next, for $\Lambda \leq 0$, we should require $\gamma > -\Lambda \geq 0$ due to the condition (2.2.8). The latter case, as in the case of $\gamma > \Lambda > 0$, makes Ω_L always negative resulting in the instability of soliton for any value of ε.

We are not interested in the case in which the solitons are already found to be unstable for all ε. Therefore the range of parameter values Λ and γ which we consider in the next analysis for onsite and intersite bright solitons is

$$\Lambda \geq \gamma > 0. \tag{2.2.25}$$

By this consideration, we only need to examine the stability of the soliton from the dynamics of the discrete spectrum. For this reason, we also sometimes call the discrete spectrum the critical eigenvalues.

2.2.1.1 Onsite bright solitons

The existence and stability of a single excited state, i.e., an onsite bright soliton, in the presence of parametric driving have been considered by Susanto *et al.* [91]. When $\varepsilon = 0$, as previously explained, this soliton has the leading-order solution (2.2.13). Upon substituting the values of $u_n^{(0)}$ into Eq. (2.2.12), one obtains

$$u_n^{(1)} = \begin{cases} 1/\sqrt{\Lambda+\gamma}, & n = 0, 1, -1 \\ 0, & \text{otherwise.} \end{cases} \tag{2.2.26}$$

Thus, for small ε, an onsite bright soliton is given by

$$u_n = \begin{cases} \sqrt{\Lambda+\gamma} + \varepsilon/\sqrt{\Lambda+\gamma} + \mathcal{O}(\varepsilon^2), & n = 0, \\ \varepsilon/\sqrt{\Lambda+\gamma} + \mathcal{O}(\varepsilon^2), & n = -1, 1, \\ \mathcal{O}(\varepsilon^2), & \text{otherwise.} \end{cases} \tag{2.2.27}$$

Let us now evaluate the discrete eigenvalues of the above soliton. At $\varepsilon = 0$, there is only one nonzero excited site. Therefore, from Eq. (2.2.16), an onsite bright soliton has one leading-order eigenvalue $\Omega_E^{(0)} = 4(\Lambda+\gamma)\gamma$ corresponding to the normalised eigenvector with the components $\eta_n^{(0)} = 0$ for $n \neq 0$ and $\eta_0^{(0)} = 1$.

To calculate the continuation of the eigenvalue $\Omega_E^{(0)}$ for nonzero ε, we can consider Eq. (2.2.17). As the rank of the corresponding operator is not full due to $\mathcal{L}_+(0)\mathcal{L}_-(0) - \Omega_E^{(0)} = 0$ at $n = 0$, we need a solvability condition. From the Fredholm alternative theorem, we should require that $\mathbf{f} = \text{col}(..., f_{-1}, f_0, f_1, ...)$ is orthogonal to the nullspace of the adjoint of the operator $[\mathcal{L}_+(0)\mathcal{L}_-(0) - \Omega_E^{(0)}]$. Nevertheless, the operator is self-adjoint thus the eigenvector associated with the eigenvalue $\Omega_E^{(0)}$ is in the nullspace of the adjoint of the operator (see again Eq. (2.2.16)). Because all the components of the eigenvector are zero except at site $n = 0$, this in return, gives $f_0 = \Omega^{(1)} - 8\gamma = 0$ from which we deduce that $\Omega^{(1)} \equiv \Omega_E^{(1)} = 8\gamma$. Hence the discrete eigenvalue of an onsite bright soliton is given by

$$\Omega_E = 4(\Lambda + \gamma)\gamma + 8\gamma\varepsilon + \mathcal{O}(\varepsilon^2). \tag{2.2.28}$$

It was shown by Susanto *et al.* [91] that the configuration (2.2.27), which is known to be stable for any value of ε when $\gamma = 0$, can be destabilised by parametric driving. Furthermore, it was shown that there are two mechanisms of destabilisation, as sketched in Fig. 2.1. The two instability scenarios, as illustrated in the figure, are determined by the relative positions of $\Omega_E^{(0)}$ and $\Omega_C^{(0)}$, as we now summarise. First, we note that there is a threshold value[1], $\gamma_{\text{th}} = \Lambda/5$, at which the two leading-order eigenvalues coincide, so that $\Omega_E^{(0)} = \Omega_C^{(0)}$. For $\gamma > \gamma_{\text{th}}$ (see lower panel of Fig. 2.1), upon increasing ε from $\varepsilon = 0$, the instability is caused by the collision of Ω_E with Ω_U (this leading-to-instability collision is confirmed after numerical observation); taking $\Omega_E = \Omega_U$ then yields the corresponding approximate critical value

$$\gamma_{\text{cr},1} \quad = \quad -\frac{2}{5}\Lambda - \frac{4}{5}\varepsilon + \frac{1}{5}\sqrt{9\Lambda^2 + 56\varepsilon\Lambda + 96\varepsilon^2}. \tag{2.2.29}$$

For $\gamma < \gamma_{\text{th}}$ (see upper panel of Fig. 2.1), by contrast, the instability is caused by the collision of Ω_E with an eigenvalue bifurcating from Ω_L. However, we assume here that the bifurcating eigenvalue moves slowly so that it can be represented by Ω_L. In this case, the critical value of γ can be approximated by taking $\Omega_E = \Omega_L$, giving

$$\gamma_{\text{cr},2} \quad = \quad -\frac{2}{5}\Lambda - \frac{4}{5}\varepsilon + \frac{1}{5}\sqrt{9\Lambda^2 + 16\varepsilon(\Lambda + \varepsilon)}. \tag{2.2.30}$$

Together, $\gamma_{\text{cr},1}$ and $\gamma_{\text{cr},2}$ give approximate boundaries of the instability region in the (ε, γ)-plane.

2.2.1.2 Intersite bright solitons

The next natural fundamental solution to be considered is an intersite bright soliton, i.e., a two-excited-site discrete mode. In the uncoupled limit, as presented above, the mode structure $u_n^{(0)}$ is of the form (2.2.14). By substituting the values of $u_n^{(0)}$ into Eq. (2.2.12), one can show that

$$u_n^{(1)} = \begin{cases} 1/(2\sqrt{\Lambda + \gamma}), & n = 0, 1, \\ 1/\sqrt{\Lambda + \gamma}, & n = -1, 2, \\ 0, & \text{otherwise}. \end{cases} \tag{2.2.31}$$

---

[1] There is a typo for this value in Susanto *et al.* [91].

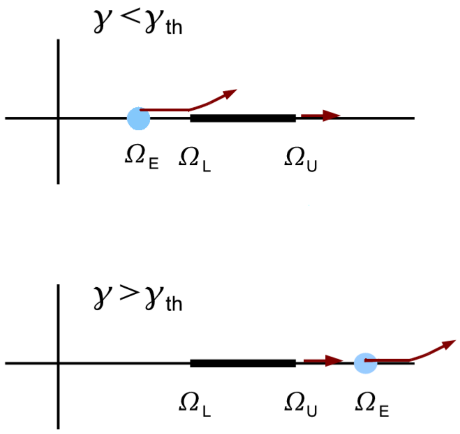

Figure 2.1: A sketch of the dynamics of the eigenvalues and the continuous spectrum of a stable onsite bright soliton in the (Re(Ω),Im(Ω))-plane. The arrows indicate the direction of movement as the coupling constant ε increases. Note that a soliton is unstable if there is some Ω with either $\Omega < 0$ or $\mathrm{Im}(\Omega) \neq 0$.

Therefore, an intersite bright soliton for small coupling ε is given by

$$u_n = \begin{cases} \sqrt{\Lambda+\gamma} + \frac{1}{2}\varepsilon/\sqrt{\Lambda+\gamma} + \mathcal{O}(\varepsilon^2), & n = 0,1, \\ \varepsilon/\sqrt{\Lambda+\gamma} + \mathcal{O}(\varepsilon^2), & n = -1,2, \\ \mathcal{O}(\varepsilon^2), & \text{otherwise.} \end{cases} \tag{2.2.32}$$

To study the stability of the intersite bright soliton above, let us first consider the $\mathcal{O}(1)$ equation (2.2.16). Due to the presence of two non-zero excited sites at $\varepsilon = 0$, the soliton (2.2.32) has at leading order the double eigenvalue $\Omega_E^{(0)} = 4(\Lambda+\gamma)\gamma$, which corresponds to the eigenvector having components $\eta_n^{(0)} = 0$ for $n \neq 0,1$, $\eta_0^{(0)} \neq 0$, and $\eta_1^{(0)} \neq 0$.

The continuation of the eigenvalue $\Omega_E^{(0)}$ for nonzero coupling ε can be obtained from Eq. (2.2.17) by applying, as before, a Fredholm solvability condition. Because the eigenvector corresponding to the eigenvalue $\Omega_E^{(0)}$ has zero components except at $n = 0,1$, we only need to require $f_0 = 0$ and $f_1 = 0$, i.e.,

$$(2\Lambda + \Omega^{(1)})\eta_0^{(0)} - 2(\Lambda+2\gamma)\eta_1^{(0)} = 0, \tag{2.2.33}$$

$$(2\Lambda + \Omega^{(1)})\eta_1^{(0)} - 2(\Lambda+2\gamma)\eta_0^{(0)} = 0. \tag{2.2.34}$$

Our simple calculation then shows $\eta_0^{(0)} = \pm\eta_1^{(0)}$ from which we immediately deduce that the double eigenvalue $\Omega_E^{(0)}$ splits into two distinct eigenvalues, which are given as functions of ε by

$$\Omega_{E,1} = 4(\Lambda+\gamma)\gamma + 4\gamma\varepsilon + \mathcal{O}(\varepsilon^2), \tag{2.2.35}$$

$$\Omega_{E,2} = 4(\Lambda+\gamma)\gamma - 4(\Lambda+\gamma)\varepsilon + \mathcal{O}(\varepsilon^2). \tag{2.2.36}$$

As is the case for onsite discrete solitons, interite bright solitons can also become unstable. The mechanism of the instability, after confirmation from numerics, is again determined by the relative positions of $\Omega_E^{(0)}$ and $\Omega_C^{(0)}$, as sketched in Fig. 2.2. Performing an analysis corresponding to that in Susanto *et al.* [91], we find that the two mechanisms of destabilisation for an onsite discrete soliton also occur here. The two scenarios have corresponding critical values of γ, which are given as functions of ε by

$$\gamma_{\text{cr},1} = -\frac{2}{5}\Lambda + \frac{2}{5}\varepsilon + \frac{1}{5}\sqrt{9\Lambda^2 + 52\Lambda\varepsilon + 84\varepsilon^2}, \tag{2.2.37}$$

$$\gamma_{\text{cr},2} = -\frac{2}{5}\Lambda - \frac{2}{5}\varepsilon + \frac{1}{5}\sqrt{9\Lambda^2 + 8\Lambda\varepsilon + 4\varepsilon^2}, \tag{2.2.38}$$

which are obtained, respectively, by taking $\Omega_{E,2} = \Omega_U$ for $\gamma > \gamma_{\text{th}}$ and $\Omega_{E,1} = \Omega_L$ for $\gamma < \gamma_{\text{th}}$.

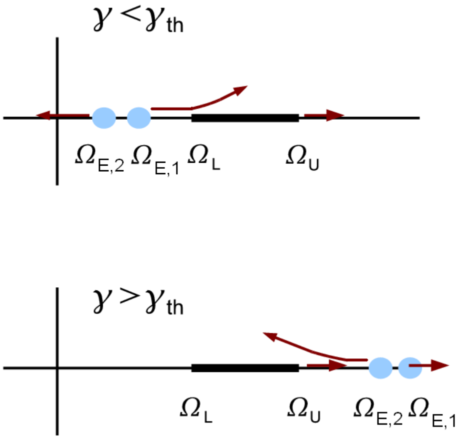

Figure 2.2: As Fig. 2.1, but for a stable intersite bright soliton.

We emphasise, as is apparent from the sketch shown in Fig. 2.2, that there is another possible mechanism of destabilisation for $\gamma < \gamma_{\text{th}}$, namely when $\Omega_{E,2}$ becomes negative. The third critical choice of parameter values is then obtained by setting $\Omega_{E,2} = 0$ which gives

$$\gamma_{\text{cr},3} = \varepsilon. \tag{2.2.39}$$

Furthermore, by solving $\gamma_{\text{cr},2} = \gamma_{\text{cr},3}$ we find that $\gamma = (\sqrt{13} - 2)\Lambda/9$, which then gives a more specific domain of γ's for the two possible scenarios of destabilisation above; $\gamma_{\text{cr},3}$ is for $\gamma < (\sqrt{13} - 2)\Lambda/9$ and $\gamma_{\text{cr},2}$ for $(\sqrt{13} - 2)\Lambda/9 < \gamma < \gamma_{\text{th}}$.

2.2.2 Comparisons with numerical calculations

We have solved the steady-state equation (2.2.1) numerically using a Newton–Raphson method and analysed the stability of the numerical solution by solving the eigenvalue problem (2.2.3). In this section, we compare these numerical results with the analytical calculations of the previous section. For the sake of simplicity, we set $\Lambda = 1$ in all the illustrative examples. This setting, however, does not lose generality as $\Lambda > 0$ can be scaled out to 1 by the transformation

$$u_n \to u_n\sqrt{\Lambda}, \quad \varepsilon \to \varepsilon\Lambda \quad \text{and} \quad \gamma \to \gamma\Lambda. \tag{2.2.40}$$

2.2.2.1 Onsite bright solitons

Comparisons between numerical calculations and analytical approximations for the case of onsite bright solitons have been fully presented and discussed by Susanto *et al.* [91]. For the sake of completeness, we reproduce the results of [91] for the (in)stability domain of onsite bright solitons in the (ε, γ)-plane in Fig. 2.3 by introducing the colour representation for the maximum value of $|\mathrm{Im}(\omega)|$. Approximations (2.2.29) and (2.2.30) are also shown there from which we can see that the former gives better prediction for the occurrence of the instability point than the latter. This is understandable as the onset of the instability approximated by Eq. (2.2.29) is indeed caused by the collision of the discrete eigenvalue with the upper band of the continuous spectrum and also typically occurs for small ε. This is not the case in approximation (2.2.30) where the actual collision is with an eigenvalue bifurcating from the inner edge of the phonon band and occurs for relatively large ε. Moreover, for $\gamma < 0$, as shown in Fig. 2.3, the onsite bright soliton is always unstable for all ε. This is still in accordance with our analytical prediction, i.e., if we set γ to be negative (provided $\Lambda > -\gamma$) in approximate eigenvalue (2.2.28), the eigenvalue Ω_E becomes negative for any value of coupling constant ε.

2.2.2.2 Intersite bright solitons

For the stability of intersite bright solitons, we start by examining the validity of our analytical prediction for the critical eigenvalues as given by Eqs. (2.2.35) and (2.2.36). In Fig. 2.4, we present a comparison between the analytical approximation and the numerics for some values of γ, specifically $\gamma = 0.1, 0.18, 0.5$, to represent the three possible cases explained in the previous section. One should notice that the appearance of the branching curves for each value of γ in the figure manifests the fact (from numerics and analytics) that the double eigenvalue of an intersite bright soliton splits into two distinct eigenvalues once the coupling is turned on. The figure reveals the relative accuracy of the small-ε approximations, and we conclude that their range of validity is wider for the lower branches of each branching curve.

Next we turn to a description of the eigenvalue structure of this intersite configuration

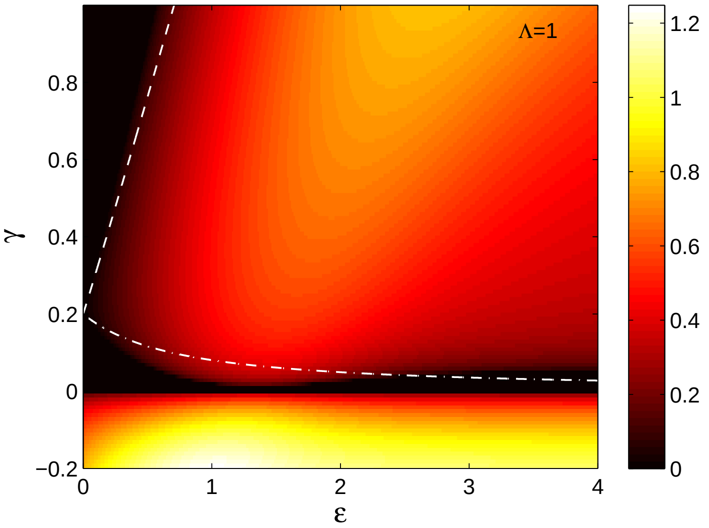

Figure 2.3: The (in)stability region of onsite bright solitons in (ε, γ)-space. For each value of ε and γ, the corresponding colour indicates the maximum value of $|\mathrm{Im}(\omega)|$ (over all eigenvalues ω) for the steady-state solution at that point. Stability is therefore indicated by the region in which $\mathrm{Im}(\omega) = 0$, namely the black region (recall that ω and $\overline{\omega}$ are eigenvalues as the stability matrix of the EVP (2.2.3) is real-valued). White dashed and dash-dotted lines give the analytical approximations (2.2.29) and (2.2.30), respectively.

for the three values of γ given above; this is shown in Fig. 2.5, where the left and right panels respectively present the structure just before and just after the first collision that results in the mode instability. We now describe the results in more detail for the three values of γ above.

For $\gamma = 0.1$, when $\varepsilon = 0$ the critical eigenvalues ω lie in the gap between the two parts of the continuous spectrum, and the instability is caused by a collision between one of the critical eigenvalues and its twin at the origin (see the top panels of Fig. 2.5). For $\gamma = 0.18$, the critical eigenvalues ω also lie in the gap between the two parts of the continuous spectrum, but the instability in this case is due to a collision between one of the critical eigenvalues and the inner edge of the continuous spectrum at $\omega = \pm\sqrt{\Omega_L}$ (see the middle panels of Fig. 2.5). In contrast to the two cases above, for $\gamma = 0.5$ the critical eigenvalues lie beyond the continuous spectrum, and the instability is caused by a collision between one of the critical eigenvalues and the outer boundary at $\omega = \pm\sqrt{\Omega_U}$ (see the bottom panels of Fig. 2.5). All the numerical results presented here are in accordance with the sketch shown in Fig. 2.2. Back to Fig. 2.4, the critical eigenvalues which are most responsible for the instability as illustrated above are shown by the upper branch for $\gamma = 0.18$ (the middle branching curve) and the lower ones for $\gamma = 0.5$ and $\gamma = 0.1$ (the other branching curves).

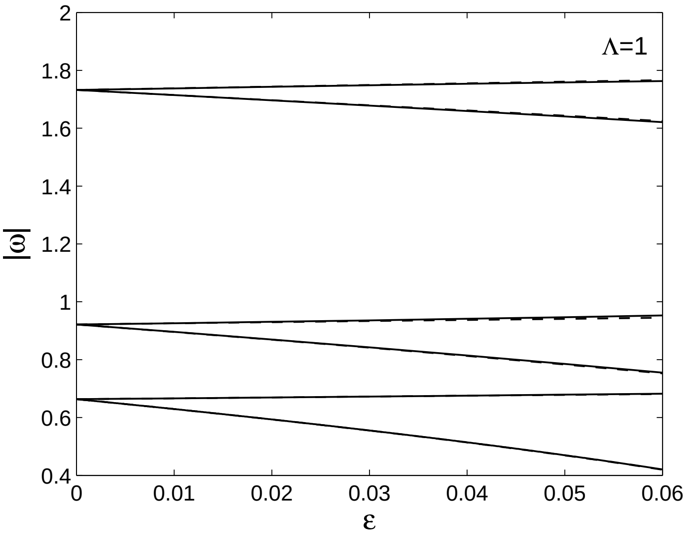

Figure 2.4: Comparison between the critical eigenvalues of intersite bright solitons obtained numerically (solid lines) and their analytical approximation (dashed lines). The appearance of the branching curves confirms the fact of the splitting of the double eigenvalues as ε increases (see text). The upper and lower branching curves correspond, respectively, to $\gamma = 0.5$ and $\gamma = 0.1$, whereas the middle one corresponds to $\gamma = 0.18$. The upper and lower branches of each branching curve is approximated, respectively, by Eq. (2.2.35) and Eq. (2.2.36); note that these approximations for $\gamma = 0.1$ (the lower branching curve) are indistinguishable from the numerical results.

Numerical solution of the EVP (2.2.3) for intersite bright solitons, for a relatively large range of ε and γ, give us the (in)stability domain of the bright solitons in the two-parameter (ε, γ)-plane, which is presented in Fig. 2.6. Again, we use colours to represent the maximum of $|\text{Im}(\omega)|$ as a function of ε and γ; thus solitons are stable in the black region. Our analytical predictions for the occurrence of instability, given by Eqs. (2.2.37)–(2.2.39), are also shown, respectively, by dash-dotted, dotted and dashed lines. Particularly for $\gamma < 0$, Fig. 2.6 reveals the unstable region of the intersite bright solitons for all ε. This fact also agrees with our analytical prediction shown by both $\Omega_{E,1}$ in Eq. (2.2.35) and $\Omega_{E,2}$ in Eq. (2.2.36) being negative at any value of ε when driving γ is negative (provided $\Lambda > -\gamma$).

We now move on the examination of the dynamics of the governing equation (2.1.1) for an intersite bright soliton. By using a Runge-Kutta time integrator with the perturbed intersite soliton solution as the initial condition, we show in Fig. 2.7 the numerical evolution of the soliton for the same parameter values as those used in Fig. 2.5, which corresponds to each of the instability scenarios. We can see from the figure that the dynamics of the unstable solitons (right panels) manifests itself into different mechanisms. In the top right panel, the soliton's centre shifts to another site forming an onsite configuration. In contrast, the typical instability of the unstable soliton in the middle right panel is in the form of soliton decay, while in the bottom right panel the soliton collapses into different sites.

2.3 Dark solitons in the defocusing PDNLS

In this section we consider the existence and stability of onsite and intersite dark solitons for the defocusing PDNLS equation. Then a stationary (real-valued and time-independent) solution u_n of Eq. (2.1.1) satisfies

$$-\varepsilon\Delta_2 u_n - (\Lambda + \gamma)u_n + u_n^3 = 0. \tag{2.3.1}$$

To examine the stability of u_n, we again introduce the linearisation ansatz $\phi_n = u_n + \delta\epsilon_n$, where $\delta \ll 1$. Substituting this ansatz into the defocusing equation (2.1.1), writing $\epsilon_n = \eta_n e^{i\omega t} + \overline{\xi}_n e^{-i\overline{\omega} t}$ and linearising in δ, we find

$$\begin{bmatrix} \varepsilon\Delta_2 + \Lambda - 2u_n^2 & -u_n^2 + \gamma \\ u_n^2 - \gamma & -\varepsilon\Delta_2 - \Lambda + 2u_n^2 \end{bmatrix} \begin{bmatrix} \eta_n \\ \xi_n \end{bmatrix} = \omega \begin{bmatrix} \eta_n \\ \xi_n \end{bmatrix}. \tag{2.3.2}$$

The eigenvalue problem above can be simplified further as for the focusing case, to the alternative form

$$\mathcal{L}_+(\varepsilon)\mathcal{L}_-(\varepsilon)\eta_n = \omega^2\eta_n = \Omega\eta_n, \tag{2.3.3}$$

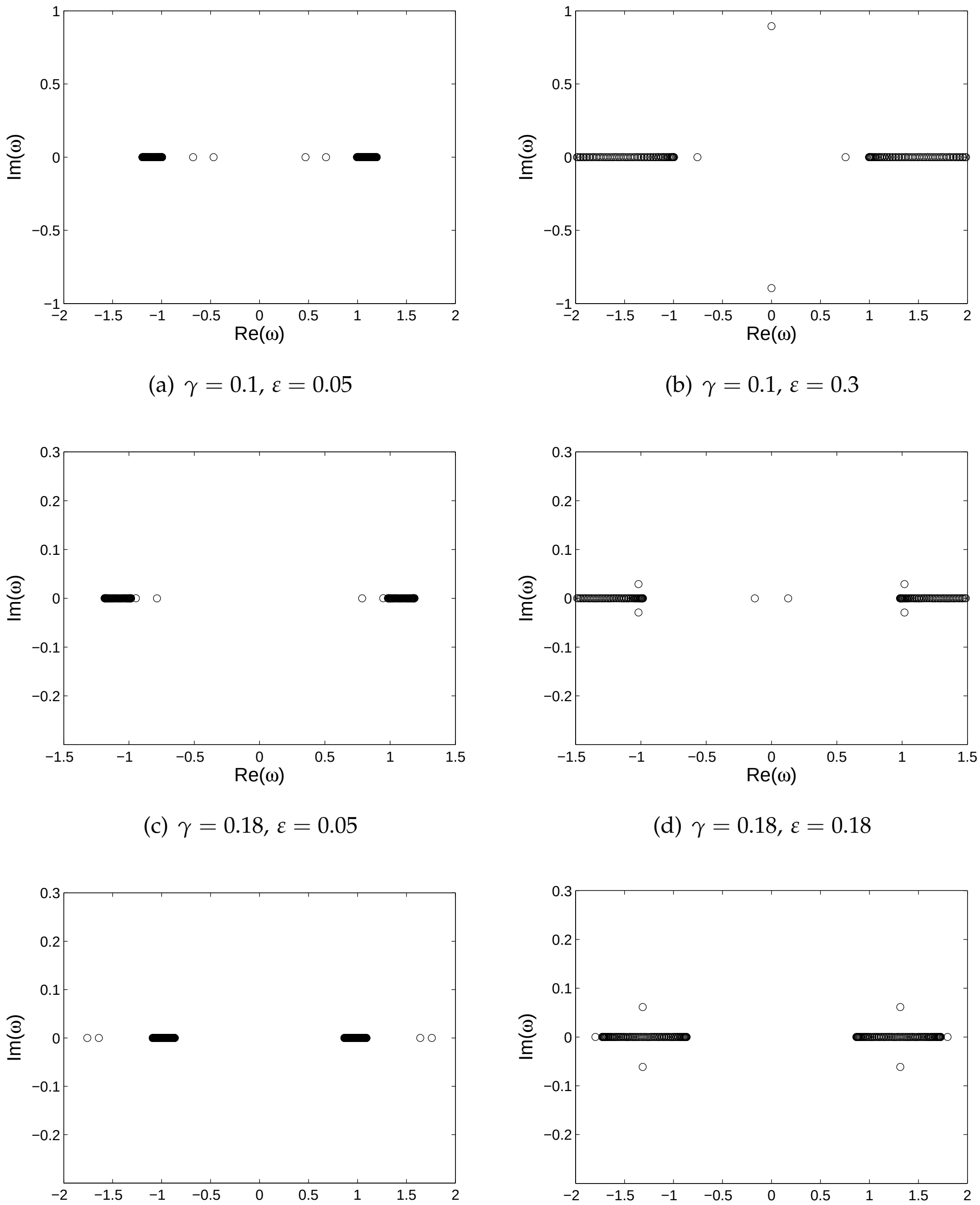

(a) $\gamma = 0.1$, $\varepsilon = 0.05$

(b) $\gamma = 0.1$, $\varepsilon = 0.3$

(c) $\gamma = 0.18$, $\varepsilon = 0.05$

(d) $\gamma = 0.18$, $\varepsilon = 0.18$

(e) $\gamma = 0.5$, $\varepsilon = 0.05$

(f) $\gamma = 0.5$, $\varepsilon = 0.2$

Figure 2.5: The structure of the eigenvalues of intersite bright solitons in the complex plane for three values of γ, as indicated in the caption of each plot. Left and right panels depict the eigenvalues of stable and unstable solitons, respectively.

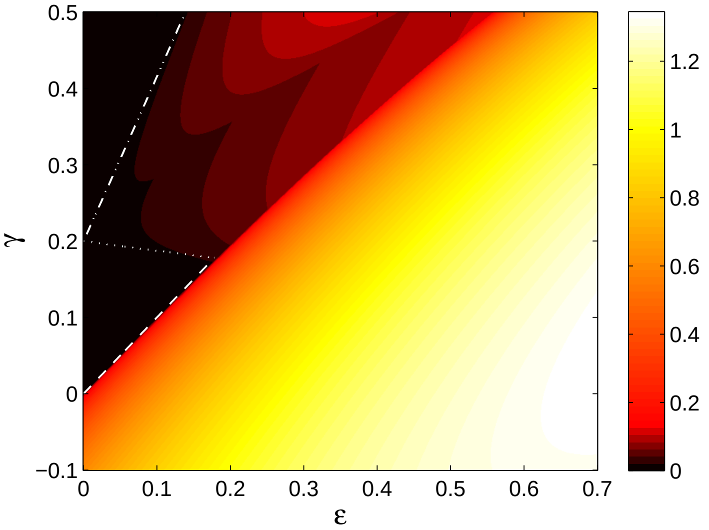

Figure 2.6: As Fig. 2.3, but for intersite bright solitons. Our analytical approximations, given by Eqs. (2.2.37), (2.2.38) and (2.2.39), are shown as white dash-dotted, dotted and dashed lines, respectively.

but the operators $\mathcal{L}_{\pm}(\varepsilon)$ are now defined as

$$\mathcal{L}_{-}(\varepsilon) \equiv -\varepsilon\Delta_2 + (3u_n^2 - \Lambda - \gamma), \tag{2.3.4}$$

$$\mathcal{L}_{+}(\varepsilon) \equiv -\varepsilon\Delta_2 + (u_n^2 - \Lambda + \gamma). \tag{2.3.5}$$

2.3.1 Analytical calculations

To perform analytical calculations of the existence and stability of the dark solitons for small coupling constant ε, we again use a perturbation analysis. As before, in the uncoupled limit $\varepsilon = 0$, the exact solutions $u_n = u_n^{(0)}$ at each site n can acquire one of the three values $0, \pm\sqrt{\Lambda+\gamma}$, provided $\Lambda > -\gamma$. By expanding u_n in powers of ε as in (2.2.9), we arrive at $\mathcal{O}(1)$ and $\mathcal{O}(\varepsilon)$ equations which, in turn, give the solutions u_n at order ε as

$$u_n^{(1)} = \frac{\Delta_2 u_n^{(0)}}{3\left(u_n^{(0)}\right)^2 - (\Lambda+\gamma)}. \tag{2.3.6}$$

In this section, we consider onsite and intersite dark solitons where the respective configurations in the AC limit $\varepsilon = 0$ are given by

$$u_n^{(0)} = \begin{cases} -\sqrt{\Lambda+\gamma}, & n = -1, -2, \ldots, \\ 0, & n = 0, \\ \sqrt{\Lambda+\gamma}, & n = 1, 2, \ldots, \end{cases} \tag{2.3.7}$$

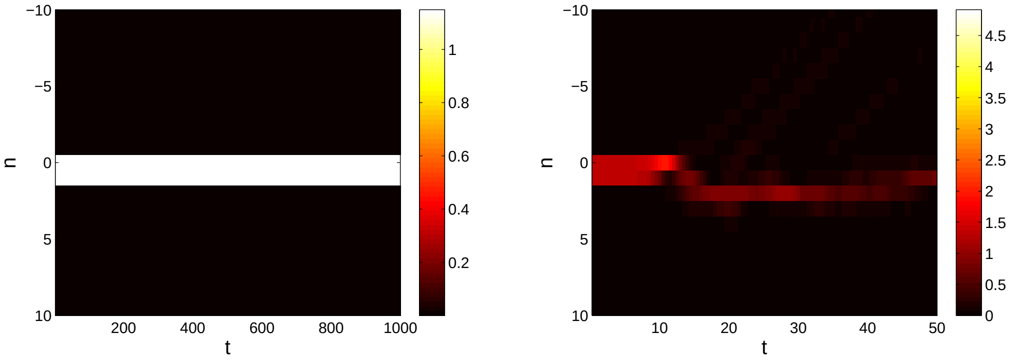

(a) $\gamma = 0.1$, $\varepsilon = 0.05$ (b) $\gamma = 0.1$, $\varepsilon = 0.3$

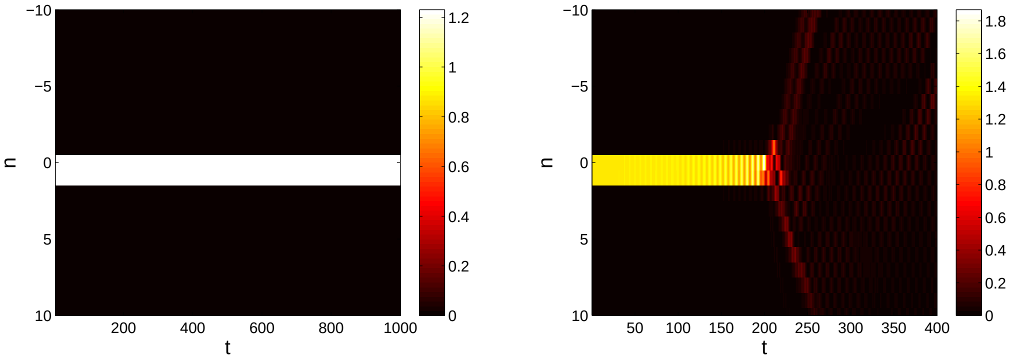

(c) $\gamma = 0.18$, $\varepsilon = 0.05$ (d) $\gamma = 0.18$, $\varepsilon = 0.18$

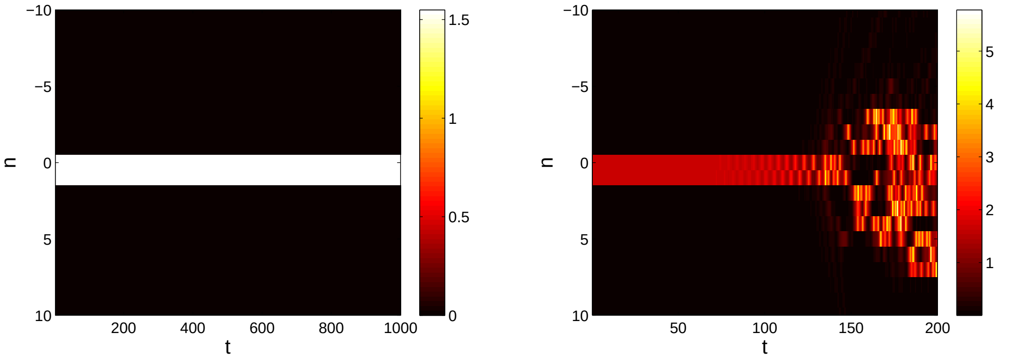

(e) $\gamma = 0.5$, $\varepsilon = 0.05$ (f) $\gamma = 0.5$, $\varepsilon = 0.2$

Figure 2.7: The numerical evolution of the time-dependent Eq. (2.1.1) for an intersite bright soliton (the contour plot shows the square modulus $|\phi_n|^2$). The parameter values are indicated in the caption of each panel which are the same as those in Fig. 2.5. The left and the right panels exhibit the dynamics of stable and unstable solitons, respectively.

and

$$u_n^{(0)} = \begin{cases} -\sqrt{\Lambda+\gamma}, & n = 0, -1, \ldots, \\ \sqrt{\Lambda+\gamma}, & n = 1, 2, \ldots. \end{cases} \tag{2.3.8}$$

Next, to study the eigenvalue(s) of the dark soliton analytically, we again expand η_n and Ω in powers of ε as in (2.2.15), and hence obtain from Eq. (2.3.3), at $\mathcal{O}(1)$ and $\mathcal{O}(\varepsilon)$, respectively, the equations

$$\left[\mathcal{L}_+(0)\mathcal{L}_-(0) - \Omega^{(0)}\right] \eta_n^{(0)} = 0, \tag{2.3.9}$$

and

$$\left[\mathcal{L}_+(0)\mathcal{L}_-(0) - \Omega^{(0)}\right] \eta_n^{(1)} = f_n, \tag{2.3.10}$$

where

$$f_n = [(\Delta_2 - 2u_n^{(0)}u_n^{(1)})\mathcal{L}_-(0) + \mathcal{L}_+(0)(\Delta_2 - 6u_n^{(0)}u_n^{(1)}) + \Omega^{(1)}]\eta_n^{(0)}. \tag{2.3.11}$$

As in bright solitons, the operator $[\mathcal{L}_+(0)\mathcal{L}_-(0) - \Omega^{(0)}]$ is self-adjoint.

Performing a stability analysis as before, we firstly investigate the significance of continuous spectrum for a dark soliton by substituting a plane-wave expansion (2.2.21) into Eq. (2.3.3). From this, we find the dispersion relation for a dark soliton to be

$$\Omega = [2\varepsilon(\cos\kappa - 1) - (\Lambda + 2\gamma)]^2 - \Lambda^2, \tag{2.3.12}$$

and so the continuous band lies between

$$\Omega_L = 4(\Lambda+\gamma)\gamma, \text{ when } \kappa = 0, \tag{2.3.13}$$

and

$$\Omega_U = 4(\Lambda+\gamma)\gamma + 8\varepsilon(\Lambda + 2\gamma + 2\varepsilon), \text{ when } \kappa = \pi. \tag{2.3.14}$$

Our analysis shows that there are only three possibilities for parameter values Λ and γ in the continuous spectrum above, i.e., either $\Lambda \geq \gamma > 0$, $\gamma > \Lambda > 0$ or $\gamma > -\Lambda \geq 0$ (note that the latter is for $\Lambda \leq 0$). For all cases, we can check that all the eigenvalues in $[\Omega_L, \Omega_U]$ are real positive for any value of ε which means that the continuous spectrum does not create any instability. In this section, however, we restrict ourselves to the first case only to make the same treatment with the focusing PDNLS.

2.3.1.1 Onsite dark solitons

The configuration of an onsite dark soliton at $\varepsilon = 0$ is given by (2.3.7). Upon substituting this into Eq. (2.3.6), we obtain the leading order correction, $u_n^{(1)}$, as

$$u_n^{(1)} = \begin{cases} 0, & n = -2, -3, \ldots, \\ 1/(2\sqrt{\Lambda+\gamma}), & n = -1, \\ 0, & n = 0, \\ -1/(2\sqrt{\Lambda+\gamma}), & n = 1, \\ 0, & n = 2, 3, \ldots. \end{cases} \tag{2.3.15}$$

Therefore, with errors of order ε^2, an onsite dark soliton is given by

$$u_n = \begin{cases} -\sqrt{\Lambda+\gamma}, & n = -2, -3, \ldots, \\ -\sqrt{\Lambda+\gamma} + \frac{1}{2}\varepsilon/\sqrt{\Lambda+\gamma}, & n = -1, \\ 0, & n = 0, \\ \sqrt{\Lambda+\gamma} - \frac{1}{2}\varepsilon/\sqrt{\Lambda+\gamma}, & n = 1, \\ \sqrt{\Lambda+\gamma}, & n = 2, 3, \ldots. \end{cases} \tag{2.3.16}$$

For this configuration, we have

$$\mathcal{L}_+(0)\mathcal{L}_-(0) = \begin{cases} \Lambda^2 - \gamma^2, & n = 0, \\ 4(\Lambda+\gamma)\gamma, & n \neq 0. \end{cases} \tag{2.3.17}$$

From Eq. (2.3.9), we then deduce that at $\varepsilon = 0$ the eigenvalues of onsite discrete dark solitons are given by $\Omega_C^{(0)} = 4(\Lambda+\gamma)\gamma$ and $\Omega_E^{(0)} = \Lambda^2 - \gamma^2$ which, respectively, become the continuous and discrete spectrum for nonzero ε. The eigenvalue $\Omega_E^{(0)}$ has the normalised eigenvector whose components are $\eta_n^{(0)} = 0$ for $n \neq 0$ and $\eta_0^{(0)} = 1$.

Because the continuous spectrum does not contribute to the instability of the soliton, the eigenvalue $\Omega_E^{(0)}$ must be taken into account to examine the stability. To do so, we need to find the continuation of the eigenvalue $\Omega_E^{(0)}$ for nonzero ε which can be calculated from Eq. (2.3.10). But, the coefficient of $\eta_n^{(1)}$ which is given by

$$\mathcal{L}_+(0)\mathcal{L}_-(0) - \Omega^{(0)} = \begin{cases} 0, & n = 0, \\ 4\Lambda\gamma - \Lambda^2 + 5\gamma^2, & n \neq 0, \end{cases} \tag{2.3.18}$$

leads to the rank deficiency in operator $L \equiv [\mathcal{L}_+(0)\mathcal{L}_-(0) - \Omega^{(0)}]$. Therefore we need a solvability condition, i.e., the nullspace of the adjoint of L, which is the eigenvector corresponding to the eigenvalue $\Omega_E^{(0)}$ due to the self-adjointness of L, is orthogonal to $\mathbf{f} = \mathrm{col}(\ldots, f_{-1}, f_0, f_1, \ldots)$. Because the components of the eigenvector are zero except at site $n = 0$, we only require $f_0 = 4\Lambda + \Omega^{(1)} = 0$ which then gives $\Omega^{(1)} \equiv \Omega_E^{(1)} = -4\Lambda$. Hence the discrete eigenvalue of an onsite dark soliton for small ε is

$$\Omega_E = \Lambda^2 - \gamma^2 - 4\Lambda\varepsilon + \mathcal{O}(\varepsilon^2). \tag{2.3.19}$$

Initially, i.e., for $\varepsilon = 0$, the relative positions of the eigenvalue and the continuous spectrum can be divided into two cases, according to whether $\gamma \gtrless \gamma_{\text{th}} = \Lambda/5$ (recall that the threshold value γ_{th} is obtained by taking $\Omega_E^{(0)} = \Omega_C^{(0)}$). When $\varepsilon = 0$ and $\gamma < \gamma_{\text{th}}$ ($\gamma > \gamma_{\text{th}}$) the eigenvalue (2.3.19) will be above (below) the continuous spectrum, as sketched in Fig. 2.8. These relative positions determine the instability mechanism for an onsite dark soliton, as we now describe.

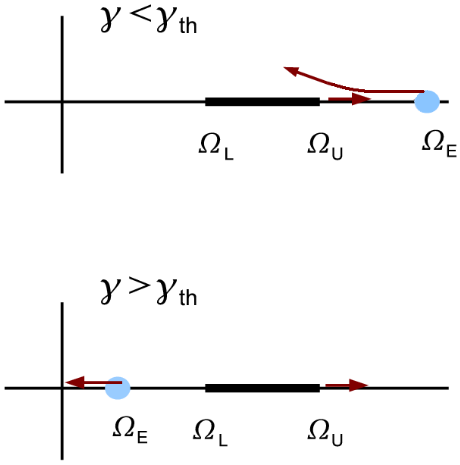

Figure 2.8: As Fig. 2.1, but for a stable onsite dark soliton.

For $\gamma < \gamma_{\text{th}}$, after numerical observations, the instability is due to a collision between the eigenvalue (2.3.19) and Ω_U, which approximately occurs when $\gamma = \gamma_{\text{cr},1}$, where

$$\gamma_{\text{cr},1} = -\frac{2}{5}\Lambda - \frac{8}{5}\varepsilon + \frac{1}{5}\sqrt{9\Lambda^2 - 28\Lambda\varepsilon - 16\varepsilon^2}. \tag{2.3.20}$$

Note that for small ε, this critical value is meaningful only when $\varepsilon \le 9\Lambda/(14 + 2\sqrt{85})$. For $\gamma > \gamma_{\text{th}}$, the instability is caused by the eigenvalue (2.3.19) becoming negative, which occurs when $\gamma = \gamma_{\text{cr},2}$, where

$$\gamma_{\text{cr},2} = \sqrt{\Lambda^2 - 4\Lambda\varepsilon}. \tag{2.3.21}$$

This value is meaningful only when $\varepsilon \le \Lambda/4$.

Furthermore, if we include terms up to $\mathcal{O}(\varepsilon^2)$, we obtain

$$\Omega_E = \Lambda^2 - \gamma^2 - 4\Lambda\varepsilon + 6\varepsilon^2 + \mathcal{O}(\varepsilon^3) \tag{2.3.22}$$

as the eigenvalue of an onsite discrete dark soliton. Using this expression, we find the critical value of γ indicating the onset of instability as

$$\gamma'_{\text{cr},1} = -\frac{2}{5}\Lambda - \frac{8}{5}\varepsilon + \frac{1}{5}\sqrt{9\Lambda^2 - 28\Lambda\varepsilon + 14\varepsilon^2}, \tag{2.3.23}$$

for $\gamma < \gamma_{\text{th}}$, and

$$\gamma'_{\text{cr},2} = \sqrt{\Lambda^2 - 4\Lambda\varepsilon + 6\varepsilon^2}, \tag{2.3.24}$$

for $\gamma > \gamma_{\text{th}}$. For small ε, $\gamma'_{\text{cr},1}$ above is defined on $\varepsilon \le (1 - \sqrt{70}/14)\Lambda$.

2.3.1.2 Intersite dark solitons

The leading-order solution of an intersite dark soliton is given by the configuration (2.3.8) and the next correction can be obtained from Eq. (2.3.6) resulting

$$u_n^{(1)} = \begin{cases} 0, & n = -2, -3, \ldots, \\ 1/\sqrt{\Lambda+\gamma}, & n = -1, \\ -1/\sqrt{\Lambda+\gamma}, & n = 0, \\ 0, & n = 1, 2, \ldots. \end{cases} \tag{2.3.25}$$

Hence, an intersite discrete dark soliton is given, with errors of $\mathcal{O}(\varepsilon^2)$, by

$$u_n = \begin{cases} -\sqrt{\Lambda+\gamma}, & n = -2, -3, \ldots, \\ -\sqrt{\Lambda+\gamma} + \varepsilon/\sqrt{\Lambda+\gamma}, & n = -1, \\ \sqrt{\Lambda+\gamma} - \varepsilon/\sqrt{\Lambda+\gamma}, & n = 0, \\ \sqrt{\Lambda+\gamma}, & n = 1, 2, \ldots. \end{cases} \tag{2.3.26}$$

Starting from Eq. (2.3.9), we then find

$$\mathcal{L}_+(0)\mathcal{L}_-(0) = 4(\Lambda+\gamma)\gamma \quad \text{for all } n, \tag{2.3.27}$$

from which we deduce that there is a single leading-order eigenvalue, given by $\Omega^{(0)} = 4(\Lambda+\gamma)\gamma$, with infinite multiplicity. This eigenvalue then expands to form the continuous spectrum for nonzero ε.

From the fact of a single eigenvalue above, we cannot say anything about the discrete eigenvalue(s) yet. However, we still can calculate its continuation as the coupling constant is turned on, which can be carried out from Eq. (2.3.10). Because

$$\mathcal{L}_+(0)\mathcal{L}_-(0) - \Omega^{(0)} = 0 \quad \text{for all } n, \tag{2.3.28}$$

the solvability condition for Eq. (2.3.10) requires $f_n = 0$ for all n. A simple calculation then yields

$$f_n = \begin{cases} \left[4\Lambda + 16\gamma + (2\Lambda+4\gamma)\Delta_2 + \Omega^{(1)}\right]\eta_n^{(0)}, & n = -1, 0, \\ \left[(2\Lambda+4\gamma)\Delta_2 + \Omega^{(1)}\right]\eta_n^{(0)}, & n \neq -1, 0. \end{cases} \tag{2.3.29}$$

Notice that the eigenvector for a localised mode in which there is only one eigenvalue with infinite multiplicity is also localised and decaying exponentially (see, e.g., Baesens *et al.* [103] for a justification). Thus, a suitable ansatz for $\eta_n^{(0)}$ can be chosen as

$$\eta_n^{(0)} = \begin{cases} A\mathrm{e}^{c(n+3/2)}, & n \leq -2, \\ A_0, & n = -1, \\ B_0, & n = 0, \\ B\mathrm{e}^{-c(n+3/2)}, & n \geq 1, \end{cases} \tag{2.3.30}$$

for $A, A_0, B_0, B \neq 0$ and $c > 0$. Substituting this ansatz into Eq. (2.3.29) and imposing the solvability condition $f_n = 0$ for all n, we arrive at the following equations

$$\begin{aligned}
A\mathrm{e}^{-c/2}[(2\Lambda+4\gamma)(\mathrm{e}^{-c}-2)+\Omega^{(1)}]+A_0(2\Lambda+4\gamma) &= 0, \quad n=-2,\\
A_0(8\gamma+\Omega^{(1)})+B_0(2\Lambda+4\gamma)+A(2\Lambda+4\gamma)\mathrm{e}^{-c/2} &= 0, \quad n=-1,\\
B_0(8\gamma+\Omega^{(1)})+A_0(2\Lambda+4\gamma)+B(2\Lambda+4\gamma)\mathrm{e}^{-5c/2} &= 0, \quad n=0,\\
B\mathrm{e}^{-5c/2}[(2\Lambda+4\gamma)(\mathrm{e}^{-c}-2)+\Omega^{(1)}]+B_0(2\Lambda+4\gamma) &= 0, \quad n=1,\\
(2\Lambda+4\gamma)(\mathrm{e}^{c}-2+\mathrm{e}^{-c})+\Omega^{(1)} &= 0, \quad n\neq -1,0.
\end{aligned} \tag{2.3.31}$$

Our analysis of the first four equations above shows that either $A_0 = B_0$ or $A_0 = -B_0$ from which we obtain, respectively, either

$$c = \ln\left(\frac{3\Lambda+10\gamma}{\Lambda+2\gamma}\right), \quad \Omega^{(1)} = \frac{-8(\Lambda+4\gamma)^2}{3\Lambda+10\gamma}, \tag{2.3.32}$$

or

$$c = \ln\left(\frac{\Lambda+6\gamma}{\Lambda+2\gamma}\right), \quad \Omega^{(1)} = \frac{-32\gamma^2}{\Lambda+6\gamma}. \tag{2.3.33}$$

Therefore, the bifurcating discrete eigenvalues of an intersite dark soliton for small ε are respectively given by

$$\Omega_{E,1} = 4(\Lambda+\gamma)\gamma - \frac{8(\Lambda+4\gamma)^2}{3\Lambda+10\gamma}\varepsilon + \mathcal{O}(\varepsilon^2), \tag{2.3.34}$$

$$\Omega_{E,2} = 4(\Lambda+\gamma)\gamma - \frac{32\gamma^2}{\Lambda+6\gamma}\varepsilon + \mathcal{O}(\varepsilon^2). \tag{2.3.35}$$

In the absence of parametric driving ($\gamma = 0$) and for $\Lambda = 1$, our results agree with that reported by Pelinovsky & Kevrekidis [90]. One should notice that in the AC limit $\varepsilon = 0$ the above eigenvalues correspond, respectively, to the following normalised eigenvectors

$$\eta_n^{(0)} = \begin{cases} \frac{2\sqrt{(\Lambda+3\gamma)(\Lambda+4\gamma)}}{\Lambda+2\gamma}\left(\frac{3\Lambda+10\gamma}{\Lambda+2\gamma}\right)^{n}, & n \leq -2,\\ \frac{2\sqrt{(\Lambda+3\gamma)(\Lambda+4\gamma)}}{3\Lambda+10\gamma}, & n=-1,\\ \frac{2\sqrt{(\Lambda+3\gamma)(\Lambda+4\gamma)}}{3\Lambda+10\gamma}, & n=0,\\ \frac{2\sqrt{(\Lambda+3\gamma)(\Lambda+4\gamma)}}{3\Lambda+10\gamma}\left(\frac{3\Lambda+10\gamma}{\Lambda+2\gamma}\right)^{-n}, & n \geq 1, \end{cases} \tag{2.3.36}$$

and

$$\eta_n^{(0)} = \begin{cases} \frac{2\sqrt{\gamma(\Lambda+4\gamma)}}{\Lambda+2\gamma}\left(\frac{\Lambda+6\gamma}{\Lambda+2\gamma}\right)^{n}, & n \leq -2,\\ \frac{2\sqrt{\gamma(\Lambda+4\gamma)}}{\Lambda+6\gamma}, & n=-1,\\ -\frac{2\sqrt{\gamma(\Lambda+4\gamma)}}{\Lambda+6\gamma}, & n=0,\\ -\frac{2\sqrt{\gamma(\Lambda+4\gamma)}}{\Lambda+6\gamma}\left(\frac{\Lambda+6\gamma}{\Lambda+2\gamma}\right)^{-n}, & n \geq 1. \end{cases} \tag{2.3.37}$$

Let us now analyse the above discrete eigenvalues. From Eq. (2.3.35) one can show that when $\varepsilon > 0$ the eigenvalue $\Omega_{E,2}$ is always less than Ω_L. As ε increases, both $\Omega_{E,1}$ and

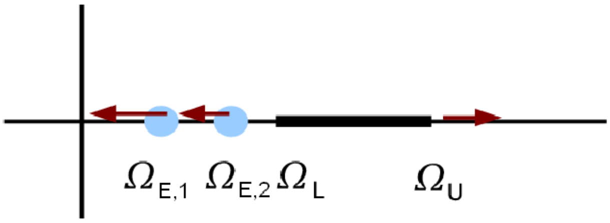

Figure 2.9: As Fig. 2.1, but for a stable intersite dark soliton.

$\Omega_{E,2}$ decrease to zero but $\Omega_{E,1} < \Omega_{E,2}$ (note that $\Omega_{E,2}$ decreases more slowly than $\Omega_{E,1}$). Therefore, we conclude that the instability may be due to $\Omega_{E,1}$ becoming negative as illustrated in Fig. 2.9. Equating $\Omega_{E,1} = 0$ yields the critical values

$$\varepsilon_{\mathrm{cr}} = \frac{\gamma(3\Lambda + 10\gamma)(\Lambda + \gamma)}{(\Lambda + 4\gamma)^2}, \tag{2.3.38}$$

which approximate the onset of instability.

2.3.2 Comparison with numerical computations

We now compare our analytical results with corresponding numerical calculations. As for bright solitons, for illustrative purposes we set $\Lambda = 1$. Again, such a setting is without loss of generality because $\Lambda > 0$ can be scaled to be 1 by transformation (2.2.40).

2.3.2.1 Onsite dark solitons

We start by checking the validity of our analytical approximation for the critical eigenvalue. As explained above, the change in the position of the eigenvalues relative to the continuous spectrum at $\varepsilon = 0$ occurs at $\gamma = 1/5$. Therefore we consider two values $\gamma = 0.1$ and $\gamma = 0.6$, representing both cases. Figure 2.10 depicts a comparison between our analytical result (2.3.19) and the numerical computations, from which we conclude that the prediction is quite accurate for small ε. The accuracy can be improved if one includes further orders in the perturbative expansion (2.3.22); this improvement is shown in the same figure by the dotted line.

The eigenvalue structure of onsite dark solitons for the two values of γ used above is depicted in Fig. 2.11; left and right panels refer respectively to conditions just before and just after a collision resulting in an instability. As sketched in Fig. 2.8, for $\gamma = 0.1$ the instability is caused by a collision between the critical eigenvalue and the upper edge of the continuous spectrum. On the other hand, when $\gamma = 0.6$ the instability is caused by a collision between the critical eigenvalue and its twin at the origin (see the bottom panels of Fig. 2.11). In the latter case we notice that there is an eigenvalue bifurcating from the lower edge of the continuous spectrum.

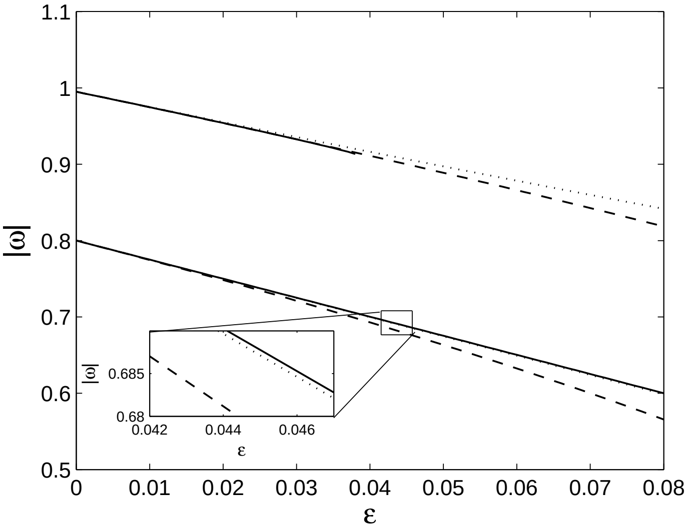

Figure 2.10: Comparisons between the critical eigenvalue for on-site dark solitons obtained numerically (solid lines) and analytically using Eq. (2.3.19) (dashed lines) for $\gamma = 0.1$ (upper curves) and $\gamma = 0.6$ (lower curves). An approximation that explicitly includes the next term in expansion Eq. (2.3.22) is also plotted (dotted lines).

We now proceed to evaluate the (in)stability region of this solution in (ε, γ)-space. We show in Fig. 2.12 the maximum of the imaginary part of the eigenvalue, together with our approximation to the (in)stability boundary. The white solid line represents Eq. (2.3.21), corresponding to the instability caused by the collision with the continuous spectrum. Equation (2.3.20) is represented by the white dash-dotted line, which corresponds to the other instability mechanism. In addition, white dashed and dotted lines show, respectively, Eqs. (2.3.24) and (2.3.23), where a better analytical approximation is obtained.

An important observation from Fig. 2.12 is that there is an interval of values of γ in which the onsite dark soliton is always stable, for any value of the coupling constant ε (numerically, it is $0.2 < \gamma < 0.335$). This indicates that a parametric driving can fully suppress the oscillatory instability reported for the first time by Johansson & Kivshar [87]. One can also check from Fig. 2.12 that for $\gamma < 0$ the onsite dark soliton is always unstable. In fact, contribution for such instability comes from the lower band of the continuous spectrum at $\omega = \pm\sqrt{\Omega_L}$ (see Eq. (2.3.13)) which becomes purely imaginary when $\gamma < 0$ (on condition $\Lambda > -\gamma$).

Next, to confirm our stability findings above, we present in Fig. 2.13 the numerical evolution of onsite dark solitons which correspond to the stability and instability modes in the respective left and right panels of Fig. 2.11. The typical dynamical behaviour of the

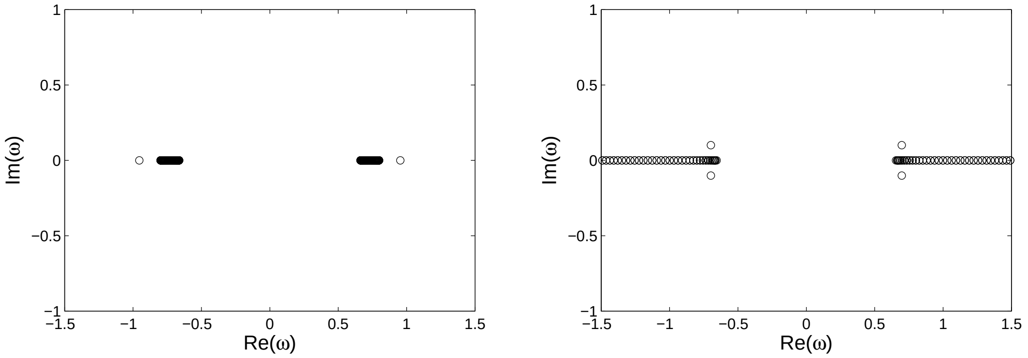

(a) $\gamma = 0.1$, $\varepsilon = 0.02$

(b) $\gamma = 0.1$, $\varepsilon = 0.2$

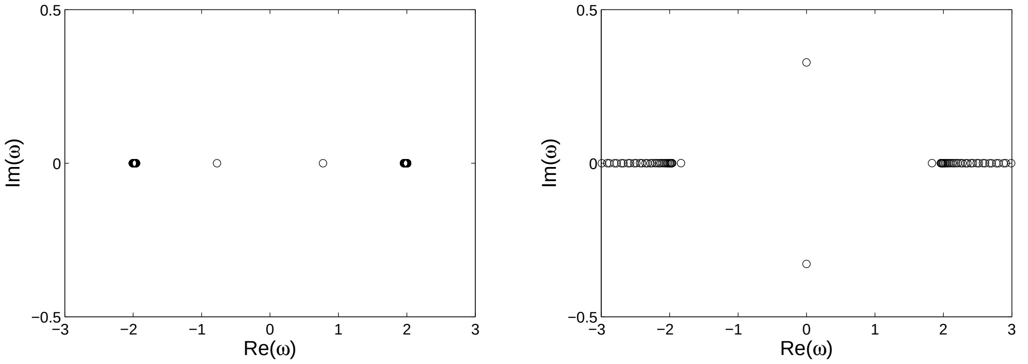

(c) $\gamma = 0.6$, $\varepsilon = 0.01$

(d) $\gamma = 0.6$, $\varepsilon = 1$

Figure 2.11: The eigenvalue structure of on-site dark solitons for several values of γ and ε, as indicated in the caption of each panel.

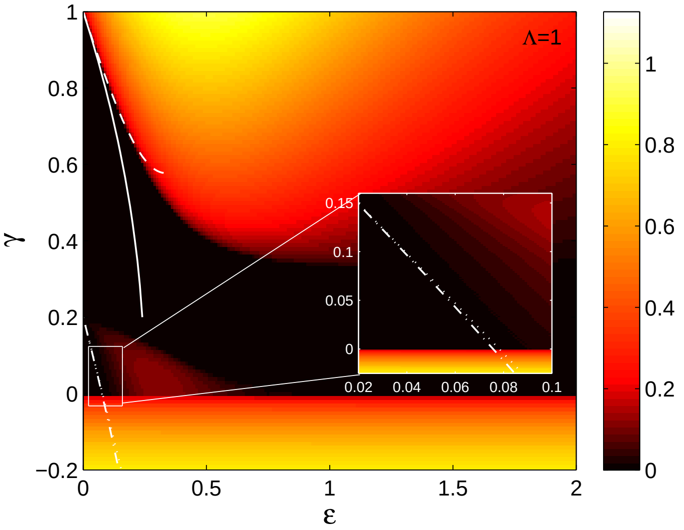

Figure 2.12: The (in)stability region of onsite dark solitons in the two-parameter (ε, γ)-space. The white solid and dashed lines respectively give the analytical approximations Eq. (2.3.21) and (2.3.24). White dash-dotted and dotted lines show Eqs. (2.3.20) and (2.3.23); note that these curves are indistinguishable in this plot.

unstable soliton in the top right panel of Fig. 2.13 is in the form of soliton destruction of which the centre then eventually shifts to the other site, while, interestingly, in the bottom right panel the unstable soliton becomes a discrete breather where the amplitude is alternately changed between the two neighbouring sites.

2.3.2.2 Intersite dark solitons

Now we examine intersite dark solitons. First, Fig. 2.14 shows the analytical prediction for the critical eigenvalues, given by Eqs. (2.3.34)-(2.3.35), compared to the corresponding numerical results. One should not be surprised by the appearance of the branching curves in the figure as they reveal the bifurcation of the critical eigenvalues from the inner edge of the continuous spectrum as soon as ε is turned on from which they then split into two distinct eigenvalues. We see that the approximations given by Eqs. (2.3.34)-(2.3.35) are in good agreement with the numerics. The range of validity of these approximations is wider for the upper branches in each branching curve.

The analytical calculation of the eigenvalues (2.3.34) and (2.3.35) is based on the formulation of the leading-order eigenvectors (2.3.36) and (2.3.37), respectively. The comparisons between the approximate eigenvectors and the numerical results, as presented in Fig. 2.15, show that our theoretical prediction is excellent.

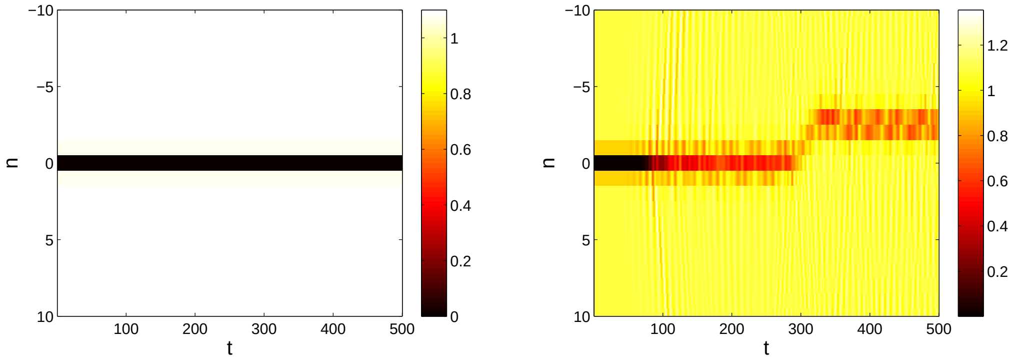

(a) $\gamma = 0.1$, $\varepsilon = 0.02$ (b) $\gamma = 0.1$, $\varepsilon = 0.2$

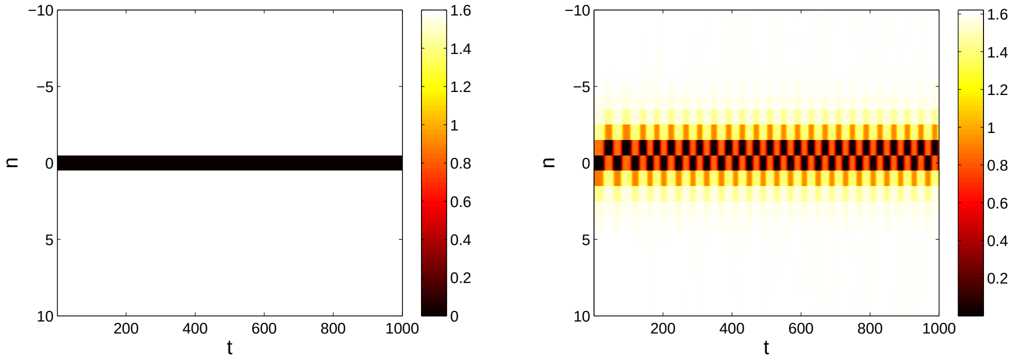

(c) $\gamma = 0.6$, $\varepsilon = 0.01$ (d) $\gamma = 0.6$, $\varepsilon = 1$

Figure 2.13: The numerical integration of Eq. (2.1.1) for the onsite dark solitons corresponding to the mode (in)stability in Fig. 2.11.

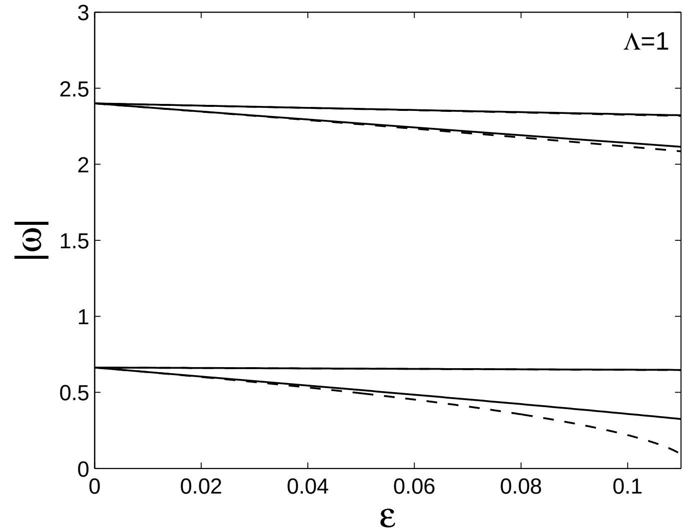

Figure 2.14: Comparisons between the critical eigenvalue of intersite dark solitons obtained numerically (solid lines) and analytically (dashed lines) for two values of γ. The upper branching curves correspond to $\gamma = 0.8$ while the lower ones to $\gamma = 0.1$. The analytical approximations for the lower-upper branches in each branching curve are given by Eqs. (2.3.34)-(2.3.35).

Next, we plot in Fig. 2.16 the eigenvalue structure of this configuration for the two values $\gamma = 0.1, 0.8$. The mechanism of instability explained in the section above can be seen clearly in the top panels of Fig. 2.16, i.e., the instability is caused by a collision between one of the critical eigenvalues and its twin at the origin (in Fig. 2.14, this eigenvalue corresponds to the lower branch of the lower branching curves). It is interesting to note that a parametric driving can also fully suppress the oscillatory instability of an intersite dark soliton. As shown in the bottom panels of Fig. 2.16, there are values of the parameter γ for which no instability-inducing collision ever occurs.

The (in)stability region of this configuration as well as the analytical prediction for the onset of instability are summarised in Fig. 2.17. We see from the figure that for any ε and $\gamma > 0.305$ an intersite dark soliton is always stable. By contrast, we also see that the intersite dark soliton is always unstable for $\gamma < 0$. The instability in this case is caused by the fact, as in onsite dark solitons, that the lower band of the continuous spectrum ($\omega = \pm\sqrt{\Omega_L}$) lies on the imaginary axis.

As a confirmation for the (in)stability scenarios discussed above, we depict in Fig. 2.18 the numerical dynamics of stable and unstable intersite dark solitons which correspond to stable and unstable modes of the eigenvalues in the top panels of Fig. (2.16). Interestingly, the unstable soliton eventually travels with the negative velocity which seemingly remains constant. This leading-to-travelling instability is similar to that reported

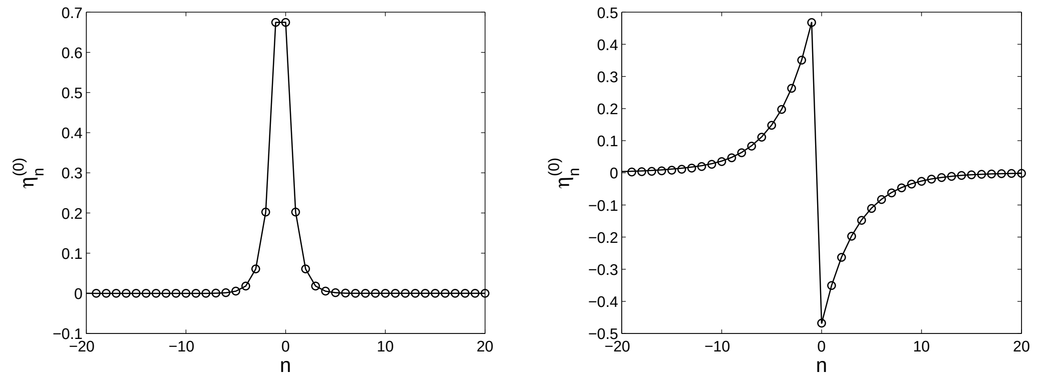

(a) $\gamma = 0.1$, $A = B$

(b) $\gamma = 0.1$, $A = -B$

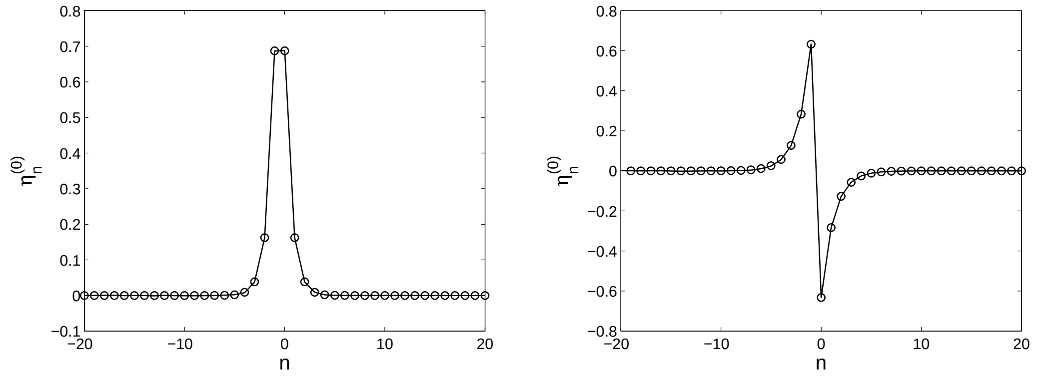

(c) $\gamma = 0.8$, $A = B$

(d) $\gamma = 0.8$, $A = -B$

Figure 2.15: Comparisons between the eigenvectors corresponding to the discrete eigenvalues of an intersite dark soliton in the uncoupled limit $\varepsilon = 0$ obtained numerically (solid lines) and analytically (circles) for two values of γ as indicated in the caption for each panel. The analytical approximations are obtained from Eqs. (2.3.36) (left panels) and (2.3.37) (right panels).

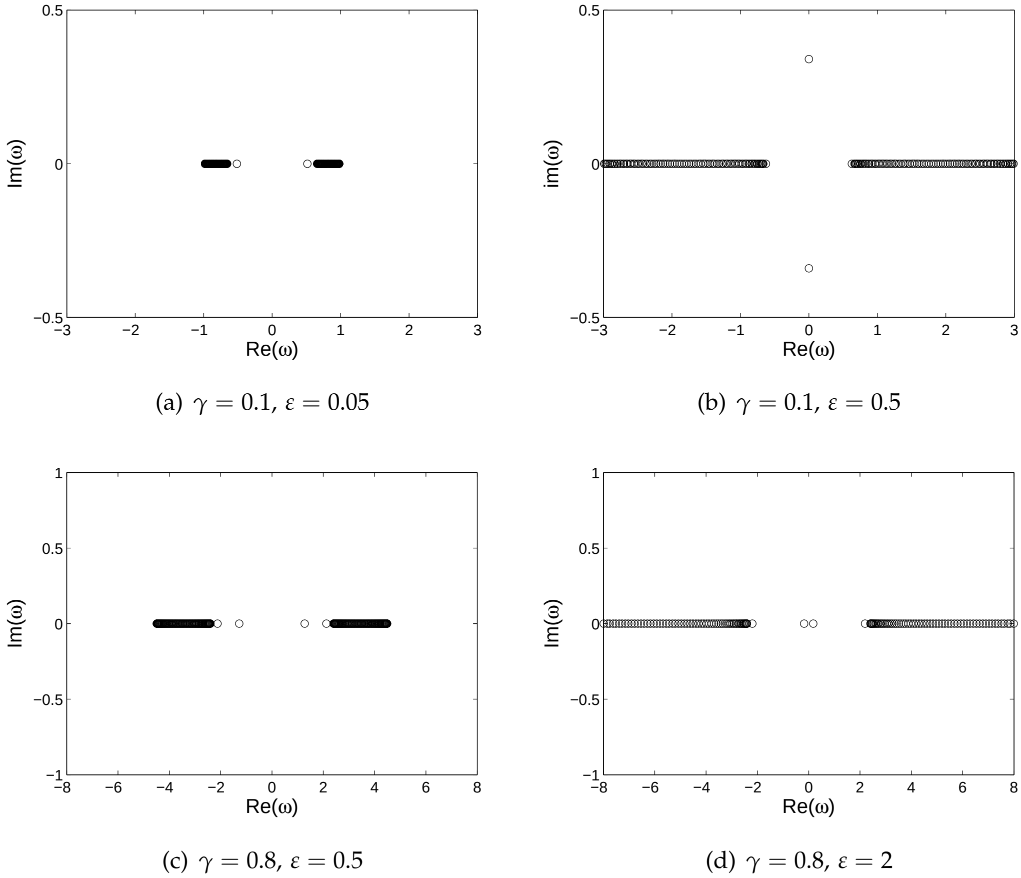

(a) $\gamma = 0.1$, $\varepsilon = 0.05$ (b) $\gamma = 0.1$, $\varepsilon = 0.5$

(c) $\gamma = 0.8$, $\varepsilon = 0.5$ (d) $\gamma = 0.8$, $\varepsilon = 2$

Figure 2.16: The eigenvalue structure of intersite dark solitons with parameter values as indicated in the caption for each panel.

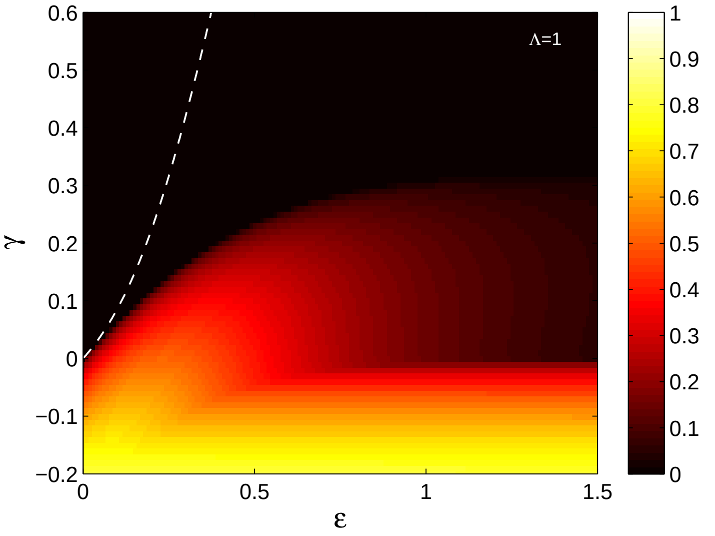

Figure 2.17: As Fig. 2.12, but for an intersite dark soliton. The white dashed line is our analytical approximation (2.3.38).

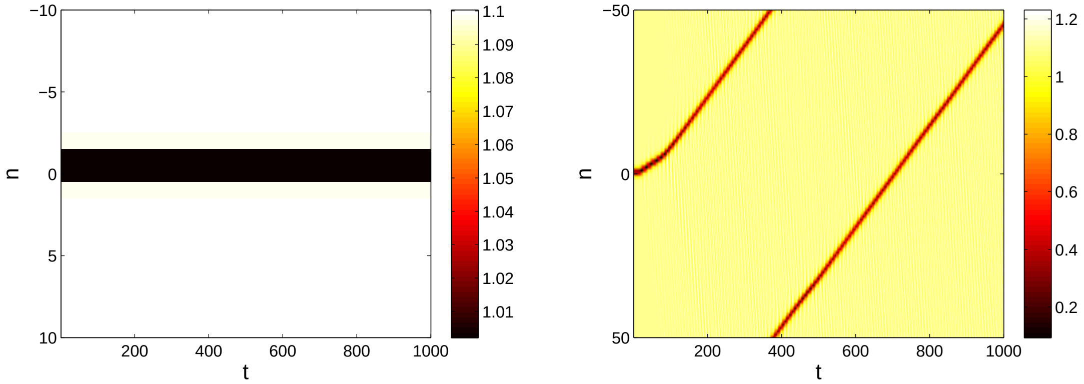

Figure 2.18: As Fig. 2.13, but for an intersite dark soliton with $\gamma = 0.1$. The left and right panels depict the evolution of a stable dark soliton with $\varepsilon = 0.05$ and an unstable one with $\varepsilon = 0.5$, respectively.

by Fitrakis *et al.* [86] for the case of undriven cubic and saturable DNLS equations.

2.4 PDNLS in electromechanical resonators

In this section, we discuss the use of parametrically driven DNLS equation in describing the dynamics of MEMS and NEMS resonators. We have provided a brief review of MEMS and NEMS resonators in Section 1.3.2.2.

2.4.1 The model and the reduction

Motivated by a recent experiment of Buks and Roukes [51] that succeeded in fabricating and exciting an array of MEMS and measuring oscillations of the resonators, here we consider the equation (Kenig *et al.* [58])

$$\ddot{\varphi}_n = D\Delta_2\varphi_n - [1 - H\cos(2\omega_p t)]\varphi_n \pm \varphi_n^3, \tag{2.4.1}$$

which governs the oscillation amplitude of such an array. Equation (2.4.1) is a simplified model of that discussed by Lifshitz & Cross [57], subject to an assumption that the piezoelectric parametric drive is applied directly to each oscillator as recently demonstrated by Masmanidis *et al.* [104]. The variable φ_n represents the oscillation amplitude of the nth oscillator from its equilibrium position, D is a dc electrostatic nearest-neighbour coupling term, H is a small ac component with frequency $2\omega_p$ responsible for the parametric driving, $\Delta_2\varphi_n = \varphi_{n+1} - 2\varphi_n + \varphi_{n-1}$ is the discrete Laplacian, the dot denotes the derivative with respect to time t (notice that time t here is not the same as time t in Eq. (2.1.1)), and the 'plus' and 'minus' signs of the cubic term correspond to 'softening' and 'stiffening' nonlinearities, respectively. Here, we assume ideal oscillators, so there is no damping present. The creation, stability and interactions of ILMs in Eq. (2.4.1) with low damping and in the strong-coupling limit or slowly varying solutions, have been investigated by Kenig *et al.* [58]. Here, we extend that study to the case of small coupling parameter D or strongly localised solutions.

In performing our analysis to the governing equation (2.4.1), we introduce a small parameter $\delta \ll 1$ and assume that the following scalings hold:

$$D = \delta^2 \tilde{D}, \quad H = \delta^2 \tilde{H}, \quad \omega_p = 1 + \delta^2 \tilde{\omega}_p. \tag{2.4.2}$$

Note that the leading order term for ω_p in the above equation is 1 due to it being the natural frequency of the unforced system linearised about $\phi_n = 0$, namely $\ddot{\phi}_n = -\phi_n$. We then expand each φ_n in powers of δ, with the leading-order term being of the form

$$\varphi_n \sim \delta \left(\psi_n(T_1, T_2, T_3, \dots) \mathrm{e}^{-\mathrm{i}T_0} + \overline{\psi}_n(T_1, T_2, T_3, \dots) \mathrm{e}^{\mathrm{i}T_0} \right), \tag{2.4.3}$$

with slow temporal variables $T_n = \delta^n t$. Substituting Eq. (2.4.3) into Eq. (2.4.1) and equating coefficients of powers of δ then yield

$$\mathcal{O}(\delta^2): \quad 2\mathrm{i}\frac{\partial \psi_n}{\partial T_1} \mathrm{e}^{-\mathrm{i}T_0} + \text{c.c.} = 0, \tag{2.4.4}$$

$$\begin{aligned} \mathcal{O}(\delta^3): \quad & \left(2\mathrm{i}\frac{\partial \psi_n}{\partial T_2} - \frac{\partial^2 \psi_n}{\partial T_1^2} + \tilde{D}\Delta_2 \psi_n + \frac{1}{2}\tilde{H}\overline{\psi}_n \mathrm{e}^{-2\mathrm{i}\tilde{\omega}_p T_2} \pm 3|\psi_n|^2 \psi_n \right) \mathrm{e}^{-\mathrm{i}T_0} \\ & + \left(\frac{1}{2}\tilde{H}\overline{\psi}_n \mathrm{e}^{-2\mathrm{i}\tilde{\omega}_p T_2} \pm \psi_n^3 \right) \mathrm{e}^{-3\mathrm{i}T_0} + \text{c.c.} = 0, \end{aligned} \tag{2.4.5}$$

where c.c. stands for the complex conjugate of the preceding expression.

Because $\partial^2 \psi_n / \partial T_1^2 = 0$, i.e., from Eq. (2.4.4), the terms at $\mathcal{O}(\mathrm{e}^{-\mathrm{i}T_0})$ in Eq. (2.4.5) then give the following equation for ψ_n (see Kivshar [105] and Remoissenet [106] for a related reduction method)

$$-2\mathrm{i}\dot{\psi}_n = \tilde{D}\Delta_2 \psi_n + \frac{1}{2}\tilde{H}\overline{\psi}_n \mathrm{e}^{-2\mathrm{i}\tilde{\omega}_p T_2} \pm 3|\psi_n|^2 \psi_n, \tag{2.4.6}$$

where the overdot now denotes the derivative with respect to T_2. Correction terms in Eq. (2.4.3) are $\mathcal{O}(\delta \mathrm{e}^{\pm \mathrm{i}(k+1)T_0}, \delta^3 \mathrm{e}^{\pm \mathrm{i}(k-1)T_0})$, with $k \in \mathbb{Z}^+$. A justification of this rotating-wave-type approximation can be obtained in, e.g., Kosevich & Corso [108].

Using the following scalings[2]

$$\tilde{D} = 3\varepsilon, \quad \tilde{H} = \mp 6\gamma, \quad \tilde{\omega}_p = \mp 3\Lambda/2, \tag{2.4.7}$$

and then writing $\psi_n(T_2) = \phi_n(T_2)\mathrm{e}^{\pm 3\mathrm{i}\Lambda T_2/2}$, Eq. (2.4.6) can be rewritten as

$$-\frac{2}{3}\mathrm{i}\dot{\phi}_n = \varepsilon\Delta_2 \phi_n \mp \Lambda\phi_n \mp \gamma\overline{\phi}_n \pm |\phi_n|^2 \phi_n. \tag{2.4.8}$$

---

[2] There is a typo in the scaling of $\tilde{H}$ in Syafwan *et al.* [107].

Finally by taking $T_2 = \frac{2}{3}\hat{t}$, we find that the equation above becomes the parametrically driven discrete nonlinear Schrödinger (PDNLS) equation as written in Eq. (2.1.1), where the overdot denotes the derivative with respect to $\hat{t}$. The softening and stiffening nonlinearities of Eq. (2.4.1) correspond, respectively, to the focusing and defocusing cases in the PDNLS (2.1.1). The continuum limit of Eq. (2.1.1), i.e., $\phi_n \approx \phi$, $\varepsilon\Delta_2\phi_n \approx \partial_x^2\phi$, was considered by Kenig *et al.* [58] from Eq. (2.4.1) and by Barashenkov *et al.* [109] from a parametrically driven sine-Gordon equation by considering slowly varying solitons.

2.4.2 Numerical integrations

In Sections 2.2 and 2.3, we discussed the existence and the stability of localised modes of the PDNLS equation (2.1.1). In this section, we confirm the relevance of our findings through solving numerically the time-dependent equation (2.4.1). We use a Runge–Kutta integration method, with the initial condition $\varphi_n = 2\delta u_n$ and $\dot{\varphi}_n = 0$, where u_n is the static solution of the PDNLS (2.1.1) and δ is the small parameter of Section 2.4.1. Throughout this section, we use the illustrative value $\delta = 0.2$. Recall that we have made scalings to the parameters as

$$D = 3\delta^2\varepsilon, \quad H = \mp 6\delta^2\gamma, \quad \omega_p = 1 \mp 3\delta^2\Lambda/2. \tag{2.4.9}$$

In the left and right panels of Fig. 2.19, we plot the numerical evolution of a stable and unstable onsite bright soliton, respectively. From the top right panel of the figure, we note that a parametric driving seems to destroy an unstable soliton. This observation is similar to the corresponding observation for the dynamics of an unstable soliton in the DNLS equation (2.1.1) reported by Susanto *et al.* [91]. In the bottom right panel, we present another case of unstable dynamics for a relatively large parametric driving amplitude γ, where the bright soliton is seemingly still preserved up to some time and then suddenly decays.

In Fig. 2.20 we present the numerical evolution of intersite bright solitons for the same parameter values as those in Fig. 2.5, corresponding to each of the instability scenarios. From the panels in this figure, we see that the typical outcome of the instability is that the profile of the soliton changes to a different form. In the top and middle right panels, the soliton becomes an onsite breather with the latter changing its centre position alternately. In the bottom right panel, the unstable soliton becomes two-separated-excited sites with radiation forming a breather.

We have also examined the dynamics of onsite dark solitons in the Klein–Gordon system (2.4.1). We show in Fig. 2.21 the numerical evolution of a solution with the eigenvalue structure illustrated in Fig. 2.11. The instability of an unstable onsite dark soliton

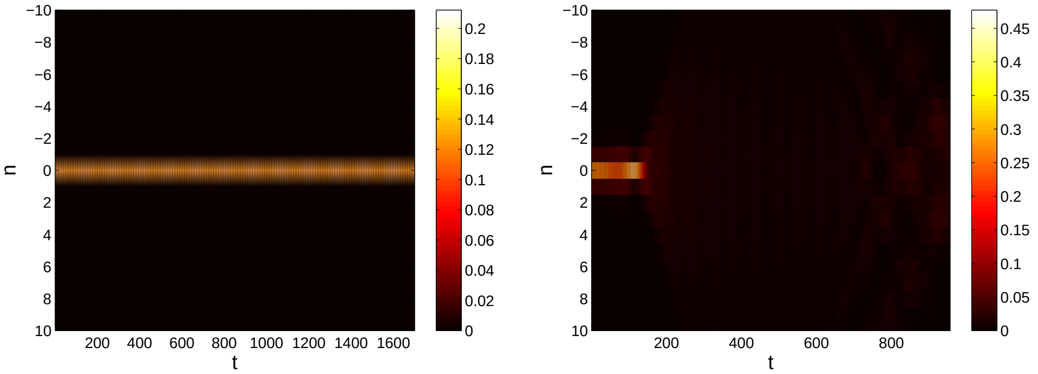

(a) $\gamma = 0.1$, $\varepsilon = 0.1$ (b) $\gamma = 0.1$, $\varepsilon = 1$

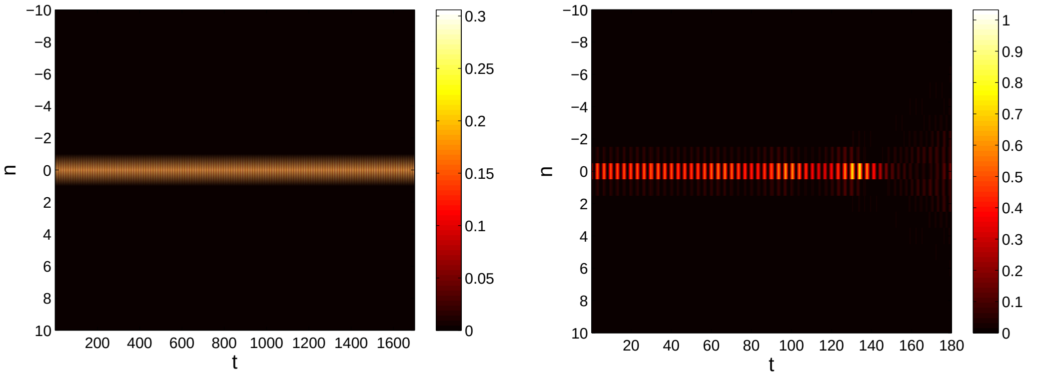

(c) $\gamma = 0.8$, $\varepsilon = 0.05$ (d) $\gamma = 0.8$, $\varepsilon = 1$

Figure 2.19: The spatio-temporal evolution of an onsite bright soliton governed by the time-dependent parametrically driven Klein–Gordon system (2.4.1), with $\delta = 0.2$ (the contour plot of the square modulus $|\varphi_n|^2$ is shown). The parameter values are indicated in the caption for each panel. The left and right panels show stable and unstable solitons, respectively.

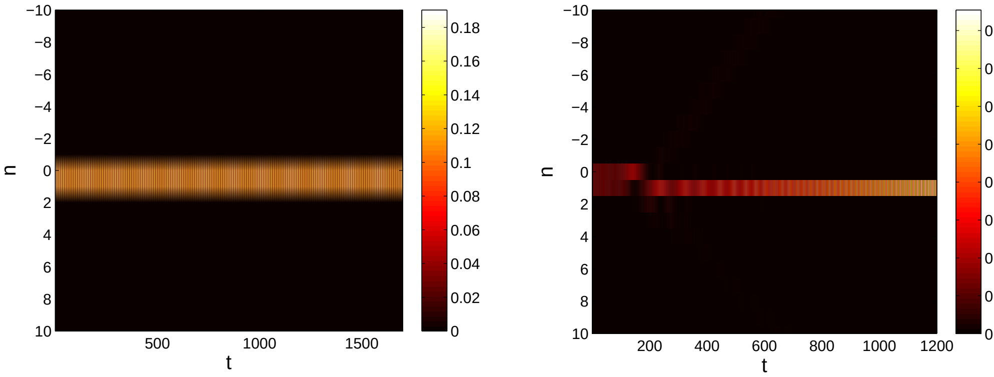

(a) $\gamma = 0.1$, $\varepsilon = 0.05$ (b) $\gamma = 0.1$, $\varepsilon = 0.3$

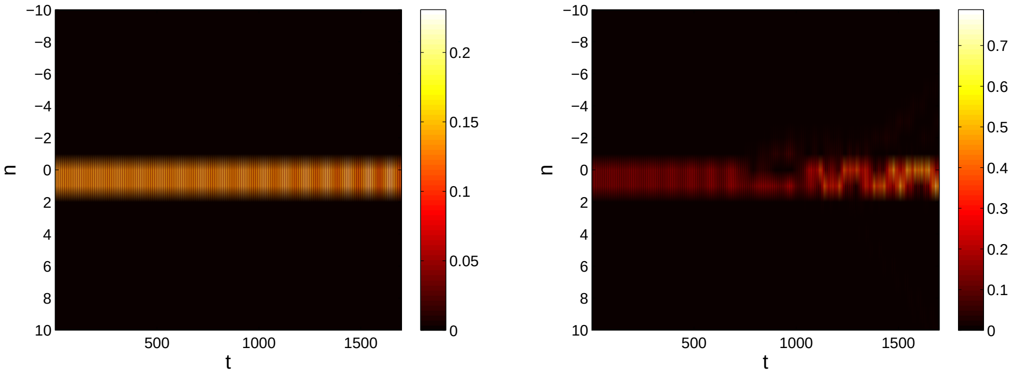

(c) $\gamma = 0.18$, $\varepsilon = 0.05$ (d) $\gamma = 0.18$, $\varepsilon = 0.18$

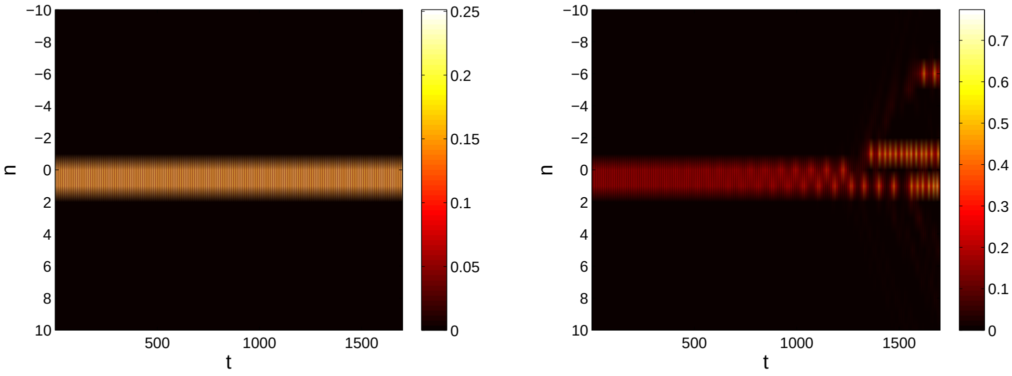

(e) $\gamma = 0.5$, $\varepsilon = 0.05$ (f) $\gamma = 0.5$, $\varepsilon = 0.2$

Figure 2.20: As Fig. 2.19, but for an intersite bright soliton, with parameter values as indicated in the caption for each panel. The initial profile in each panel corresponds to the same parameters as in Fig. 2.5.

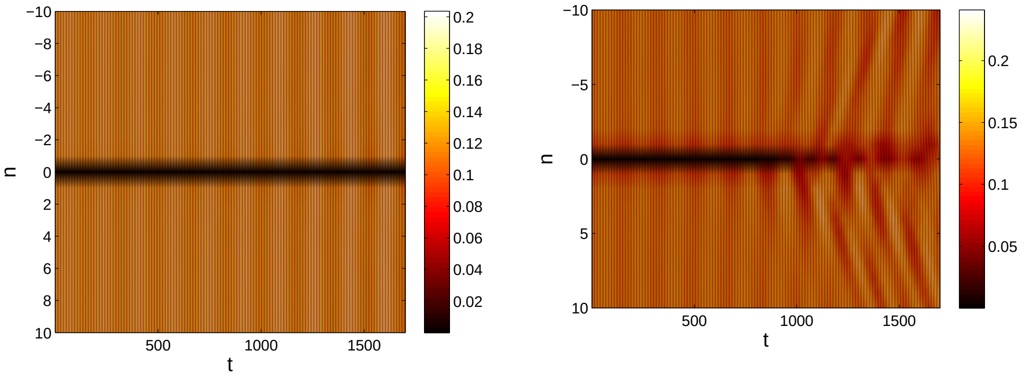

(a) $\gamma = 0.1$, $\varepsilon = 0.02$

(b) $\gamma = 0.1$, $\varepsilon = 0.2$

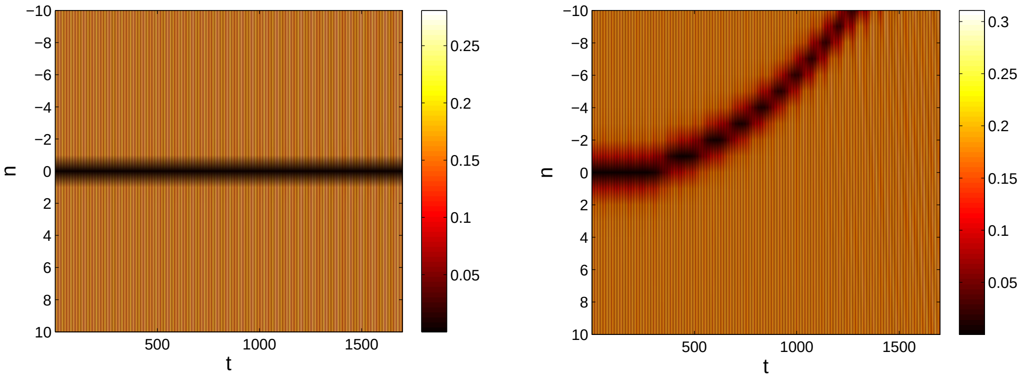

(c) $\gamma = 0.6$, $\varepsilon = 0.01$

(d) $\gamma = 0.6$, $\varepsilon = 1$

Figure 2.21: As Fig. 2.19, but for onsite dark solitons. The parameter values are as in Fig. 2.11.

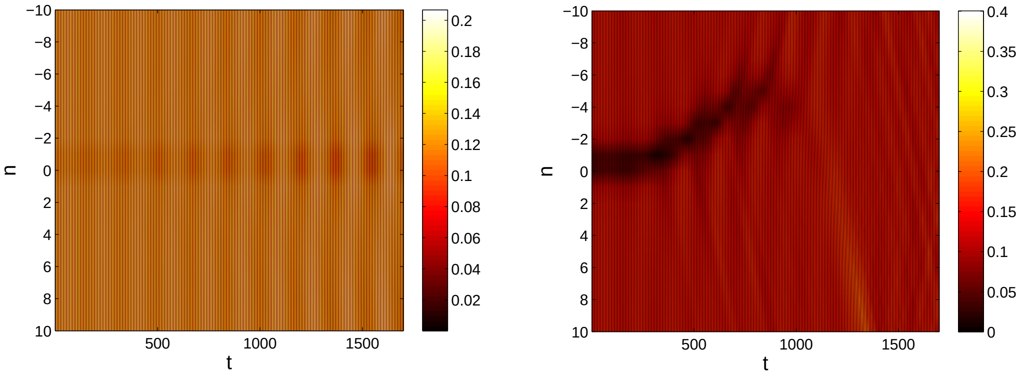

Figure 2.22: As Fig. 2.19, but for an intersite dark soliton with $\gamma = 0.1$. The left panel shows the evolution of a stable dark soliton with $\varepsilon = 0.05$, while the right panel shows the evolution of an unstable dark soliton with $\varepsilon = 0.5$.

typically manifests itself in the form of soliton destruction (top right panel) or travelling soliton (bottom right panel).

Finally, we illustrate the dynamical behaviour of an unstable intersite dark soliton in Fig. 2.22, from which we see that the instability makes the soliton travel but eventually is destroyed. This dynamics is similar to that presented in Fig. 2.18 for the time-dependent PDNLS equation (2.1.1).

2.5 Conclusion

In this chapter, we have performed analytical and numerical calculations to determine the existence and stability of fundamental bright and dark discrete solitons in the parametrically driven discrete nonlinear Schrödinger equation. We have shown that the presence of a parametric driving can destabilise an onsite bright soliton. On the other hand, a parametric driving has also been shown to stabilise intersite bright and dark discrete solitons. We even found an interval in γ for which a discrete dark soliton is stable for any value of the coupling constant, i.e., a parametric driving can suppress oscillatory instabilities. Stability windows for all the fundamental solitons have been presented and approximations using perturbation theory have been derived to accompany the numerical results.

In addition, by using a multiscale expansion method, we also show that our discrete nonlinear Schrödinger equation can be derived from a parametrically driven Klein–Gordon system describing the dynamics of nonlinear resonators in micro- and nanoelectromechanical systems (MEMS and NEMS). Numerical integrations of the Klein–Gordon system have demonstrated that our analytical and numerical investigations of the discrete nonlinear Schrödinger equation provide a useful guide to the behaviour in the MEMS and NEMS resonators.

CHAPTER 3

Lattice solitons in a parametrically driven damped discrete nonlinear Schrödinger equation

Here we extend the previous chapter by considering the presence of a damping term. The existence and stability analyses of the model are performed for fundamental bright discrete solitons.

3.1 Introduction

3.1.1 The model and review of earlier studies

The model studied in this chapter is governed by a parametrically driven damped discrete nonlinear Schrödinger (PDDNLS) equation in the focusing nonlinearity, given by

$$\mathrm{i}\dot{\phi}_n = -\varepsilon\Delta_2\phi_n + \Lambda\phi_n + \gamma\overline{\phi}_n - \mathrm{i}\alpha\phi_n - |\phi_n|^2\phi_n. \tag{3.1.1}$$

The notations used in the above equation are the same as those in Eq. (2.1.1), except the additional damping term with strength α. Note that for $\alpha \neq 0$ the PDDNLS (3.1.1) does not admit a Hamiltonian structure. Similarly to the driven case considered in Chapter 2, the present model also does not have a conserved norm. The change of the norm is given by

$$\frac{\mathrm{d}P}{\mathrm{d}t} = -\mathrm{i}\sum_{n=-\infty}^{\infty} \gamma(\overline{\phi}_n^2 - \phi_n^2) - 2\mathrm{i}\alpha|\phi_n|^2, \tag{3.1.2}$$

where $P = |\phi_n|^2$.

In the absence of parametric driving and damping, i.e., when $\gamma = 0$ and $\alpha = 0$, Eq. (3.1.1) reduces to the cubic discrete nonlinear Schrödinger (DNLS) equation (this model has been reviewed in Chapter 1). The undamped parametrically driven discrete nonlinear Schrödinger (PDNLS) equation, i.e., when $\gamma \neq 0$ and $\alpha = 0$, has been studied in Chapter 2. In particular, we showed that the PDNLS model can be derived, using a multiscale expansion reduction, from a parametrically driven Klein-Gordon system describing coupled arrays of nonlinear resonators in micro- and nano-electromechanical systems (MEMS and NEMS).

The discrete nonlinear Schrödinger equation with the inclusion of parametric driving and damping terms as written in Eq. (3.1.1) was studied for the first time, to the best of our knowledge, by Hennig [85] focusing on the existence and stability of localised solutions using a nonlinear map approach. He demonstrated that, depending upon the strength of the parametric driving, various types of localised lattice states emerge from the model, namely periodic, quasiperiodic and chaotic breathers. The impact of a damping parameter and external driving in the integrable version of the DNLS system, i.e., the discrete Ablowitz-Ladik equation, has also been studied by Kollmann *et al.* [110] who confirmed the existence of breathers and multibreathers. In deriving Eq. (3.1.1), one can follow, e.g., the method of reduction performed in Section 2.4.1 by including a damping term in the MEMS and NEMS resonators model.

On the other hand, the continuous version of the PDDNLS (3.1.1), i.e., when $\phi_n(t) \approx \phi(x,t)$ and $\varepsilon\Delta_2\phi_n(t) \approx \partial_x^2\phi(x,t)$ [$x \equiv n\Delta x$ and $\varepsilon \equiv 1/\Delta x$, with a spatial grid size Δx], was numerically discussed earlier by Bondila *et al.* [111] resulting in a single-soliton attractor chart on the (γ, α)-plane from which one may determine the regions of existence of stable stationary solitons as well as stable time-periodic solitons (with period-1 and higher). Instead of using direct numerical integration as performed by Bondila *et al.* [111], Barashenkov and co-workers recently proposed obtaining the time-periodic one-soliton [112] and two-soliton [113] solutions as solutions of a two-dimensional boundary-value problem.

3.1.2 Overview

Our objective in the present chapter is to examine the existence and stability of the fundamental onsite and intersite bright discrete solitons in the focusing PDDNLS (3.1.1). As in the previous chapter, the analysis of this model is performed through a perturbation theory for small ε which is then corroborated by numerical calculations. Moreover, our study here is also devoted to exploring the relevant bifurcations which occur in both stationary onsite and intersite discrete solitons, including time-periodic solitons emerging from Hopf bifurcations. For the latter scheme, we employ the numerical continuation software Matcont to path-follow limit cycles bifurcating from the Hopf points.

The presentation of this chapter is organised as follows. In Section 3.2, we firstly present our analytical formulation for the considered model. In Section 3.3, we perform the existence and stability analysis of the discrete solitons through a perturbation method. Next, in Section 3.4, we compare our analytical results with the corresponding numerical calculations and discuss bifurcations experienced by the fundamental solitons. The time-periodic solitons appearing from the Hopf bifurcation points of the corresponding stationary solitons are furthermore investigated in Section 3.5. Confirmation of the stability findings through numerical integration of Eq. (3.1.1) for both stationary and periodic solitons is given in Section 3.6. Finally, we conclude our results in Section 3.7.

3.2 Analytical formulation

Steady-state localised solutions of the focusing system (3.1.1) in the form of $\phi_n(t) = u_n$, where u_n is complex valued and time-independent, satisfy the stationary equation

$$-\varepsilon\Delta_2 u_n + \Lambda u_n + \gamma\overline{u}_n - \mathrm{i}\alpha u_n - |u_n|^2 u_n = 0, \tag{3.2.1}$$

with spatial localisation condition $u_n \to 0$ as $n \to \pm\infty$. We should notice that Eq. (3.2.1) (and accordingly Eq. (3.1.1)) admits the reflection symmetry under the transformation

$$u_n \to -u_n. \tag{3.2.2}$$

Following Bondila *et al.* [111] and Barashenkov *et al.* [112, 113], we assume that both the damping coefficient α and the driving strength γ are positive. We also set the coupling constant ε to be positive (the case $\varepsilon < 0$, as in Chapter 2, can be obtained accordingly by the staggering transformation (2.1.9)). The range of the parameter Λ is left to be determined later in the following discussion.

In the undriven and undamped cases, the localised solutions of Eq. (3.2.1) can be chosen, without lack of generality, to be real-valued (see Kevrekidis [24] and Hennig & Tsironis [59]); this has been discussed in Section 1.4.1. This is no longer the case for non-zero γ and α in the stationary PDDNLS (3.2.1), therefore we should always take into account complex-valued u_n. By writing $u_n = a_n + \mathrm{i}b_n$, where $a_n, b_n \in \mathbb{R}$, and decomposing the equation into real and imaginary parts, we obtain from Eq. (3.2.1) the following system of equations:

$$-\varepsilon\Delta_2 a_n + (\Lambda + \gamma)a_n + \alpha b_n - (a_n^2 + b_n^2)a_n = 0, \tag{3.2.3a}$$

$$-\varepsilon\Delta_2 b_n + (\Lambda - \gamma)b_n - \alpha a_n - (a_n^2 + b_n^2)b_n = 0. \tag{3.2.3b}$$

Thus, the solutions of Eq. (3.2.1) can be sought through solving the above system for a_n and b_n.

Next, to examine the stability of the obtained solutions, let us introduce the linearisation ansatz $\phi_n = u_n + \delta\epsilon_n$, where $\delta \ll 1$. Substituting this ansatz into Eq. (3.1.1) yields the following linearised equation at $\mathcal{O}(\delta)$:

$$\mathrm{i}\dot{\epsilon}_n = -\varepsilon\Delta_2\epsilon_n + \Lambda\epsilon_n + \gamma\overline{\epsilon}_n - \mathrm{i}\alpha\epsilon_n - 2|u_n|^2\epsilon_n - u_n^2\overline{\epsilon}_n. \tag{3.2.4}$$

By writing $\epsilon_n = \eta_n e^{\mathrm{i}\omega t} + \overline{\xi}_n e^{-\mathrm{i}\overline{\omega} t}$, Eq. (3.2.4) can be transformed into the eigenvalue problem (EVP)

$$\begin{bmatrix} \varepsilon\Delta_2 - \Lambda + \mathrm{i}\alpha + 2|u_n|^2 & u_n^2 - \gamma \\ \gamma - \overline{u}_n^2 & -\varepsilon\Delta_2 + \Lambda + \mathrm{i}\alpha - 2|u_n|^2 \end{bmatrix} \begin{bmatrix} \eta_n \\ \xi_n \end{bmatrix} = \omega \begin{bmatrix} \eta_n \\ \xi_n \end{bmatrix}. \tag{3.2.5}$$

The stability of the solution u_n is then determined by the eigenvalues ω, i.e., u_n is stable only when $\mathrm{Im}(\omega) \geq 0$ for all eigenvalues ω.

As the EVP (3.2.5) is linear, we can eliminate one of the eigenvectors, for instance ξ_n, so that we obtain the simplified form

$$\left[\mathcal{L}_+(\varepsilon)\mathcal{L}_-(\varepsilon) - 4(a_n b_n)^2\right]\eta_n = (\omega - \mathrm{i}\alpha)^2\eta_n, \tag{3.2.6}$$

where the operators $\mathcal{L}_+(\varepsilon)$ and $\mathcal{L}_-(\varepsilon)$ are given by

$$\begin{aligned} \mathcal{L}_+(\varepsilon) &\equiv -\varepsilon\Delta_2 - (a_n^2 + 3b_n^2 - \Lambda + \gamma), \\ \mathcal{L}_-(\varepsilon) &\equiv -\varepsilon\Delta_2 - (3a_n^2 + b_n^2 - \Lambda - \gamma). \end{aligned}$$

3.3 Perturbation analysis

Solutions of Eq. (3.2.1) for small coupling constant ε can be calculated analytically through a perturbative analysis, i.e., by expanding u_n in powers of ε as

$$u_n = u_n^{(0)} + \varepsilon u_n^{(1)} + \varepsilon^2 u_n^{(2)} + \cdots . \tag{3.3.1}$$

Solutions $u_n = u_n^{(0)}$ correspond to the case of the uncoupled limit $\varepsilon = 0$. For this case, Eq. (3.2.1) permits the exact solutions $u_n^{(0)} = a_n^{(0)} + \mathrm{i}b_n^{(0)}$ in which $\left(a_n^{(0)}, b_n^{(0)}\right)$ can take one of the following values

$$(0,0), \quad (sA_+, -sB_-), \quad (sA_-, -sB_+), \tag{3.3.2}$$

where

$$\begin{aligned} A_{\pm} &= \sqrt{\frac{(\gamma \pm \sqrt{\gamma^2-\alpha^2})(\Lambda \pm \sqrt{\gamma^2-\alpha^2})}{2\gamma}}, \\ B_{\pm} &= \sqrt{\frac{(\gamma \pm \sqrt{\gamma^2-\alpha^2})(\Lambda \mp \sqrt{\gamma^2-\alpha^2})}{2\gamma}}, \end{aligned}$$

and $s = \pm 1$. Due to the reflection symmetry (3.2.2), we are allowed to restrict consideration to the case $s = +1$.

Following the assumption $\gamma, \alpha > 0$, we can easily confirm that nonzero $(A_+, -B_-)$ and $(A_-, -B_+)$ are together defined in the following range of parameters

$$\Lambda > \gamma \geq \alpha > 0. \tag{3.3.3}$$

In particular, when $\gamma = \alpha$, the values of $(A_+, -B_-)$ are exactly the same as $(A_-, -B_+)$. Moreover, one can notice that when $\alpha = 0$, i.e., for the case of a parametrically driven DNLS model, the resulting nonzero solution in the AC limit $\varepsilon = 0$ is either real or purely imaginary. By using perturbation expansions, we can conclude that the undamped solutions remain real or purely imaginary for all ε.

Once a configuration for $u_n^{(0)}$ is determined, its continuation for small ε can be sought by substituting expansion (3.3.1) into Eq. (3.2.1). Here we only focus on two fundamental localised solutions, i.e., onsite and (in-phase) intersite bright solitons.

Next, to study the stability of the solitons, we also expand the eigenvector having component η_n and the eigenvalue ω in powers of ε as

$$\eta_n = \eta_n^{(0)} + \varepsilon\eta_n^{(1)} + \mathcal{O}(\varepsilon^2), \quad \omega = \omega^{(0)} + \varepsilon\omega^{(1)} + \mathcal{O}(\varepsilon^2). \tag{3.3.4}$$

Substituting these expansions into Eq. (3.2.6) and collecting coefficients at successive powers of ε yield the $\mathcal{O}(1)$ and $\mathcal{O}(\varepsilon)$ equations which are respectively given by

$$\begin{aligned} L\eta_n^{(0)} &= 0, \qquad (3.3.5) \\ L\eta_n^{(1)} &= f_n, \qquad (3.3.6) \end{aligned}$$

where

$$\begin{aligned} L &= \mathcal{L}_+(0)\mathcal{L}_-(0) - 4(a_n^{(0)}b_n^{(0)})^2 - (\omega^{(0)} - \mathrm{i}\alpha)^2, \qquad (3.3.7) \\ f_n &= \Big[\mathcal{L}_-(0)(\Delta_2 + 2a_n^{(0)}a_n^{(1)} + 6b_n^{(0)}b_n^{(1)}) + \mathcal{L}_+(0)(\Delta_2 + 2b_n^{(0)}b_n^{(1)} + 6a_n^{(0)}a_n^{(1)}) \\ &\quad +8a_n^{(0)}b_n^{(0)}(a_n^{(0)}b_n^{(1)} + a_n^{(1)}b_n^{(0)}) + 2\omega^{(0)}\omega^{(1)} - 2\mathrm{i}\alpha\omega^{(1)}\Big]\eta_n^{(0)}. \qquad (3.3.8) \end{aligned}$$

One can check that the operator L is self-adjoint and thus the eigenvector $\mathbf{h} = \mathrm{col}(..., \eta_{-1}^{(0)}, \eta_0^{(0)}, \eta_1^{(0)}, ...)$ is in the null-space of the adjoint of L.

From Eq. (3.3.5), we obtain that the eigenvalues in the uncoupled limit $\varepsilon = 0$ are

$$\omega_C^{(0)} = \pm\sqrt{\Lambda^2 - \gamma^2} + \mathrm{i}\alpha, \tag{3.3.9}$$

and

$$\omega_E^{(0)} = \pm\sqrt{\mathcal{L}_+(0)\mathcal{L}_-(0) - 4(a_n^{(0)} b_n^{(0)})^2} + \mathrm{i}\alpha, \tag{3.3.10}$$

which correspond, respectively, to the solutions $u_n^{(0)} = 0$ (for all n) and $u_n^{(0)} = a_n^{(0)} + \mathrm{i}b_n^{(0)} \neq 0$ (for all n). For bright soliton solutions having boundary condition $u_n \to 0$ as $n \to \pm\infty$, the eigenvalues $\omega_E^{(0)}$ and $\omega_C^{(0)}$ have, respectively, finite and infinite multiplicities which then generate a corresponding discrete and continuous spectrum as ε is turned on.

Let us first investigate the significance of the continuous spectrum. By introducing a plane-wave expansion $\eta_n = \mu e^{\mathrm{i}\kappa n} + \nu e^{-\mathrm{i}\kappa n}$, one can obtain the dispersion relation

$$\omega = \pm\sqrt{(2\varepsilon(\cos\kappa - 1) - \Lambda)^2 - \gamma^2} + \mathrm{i}\alpha, \tag{3.3.11}$$

from which we conclude that the continuous band lies between

$$\omega_L = \pm\sqrt{\Lambda^2 - \gamma^2} + \mathrm{i}\alpha, \text{ when } \kappa = 0, \tag{3.3.12}$$

and

$$\omega_U = \pm\sqrt{\Lambda^2 - \gamma^2 + 8\varepsilon(\Lambda + 2\varepsilon)} + \mathrm{i}\alpha, \text{ when } \kappa = \pi. \tag{3.3.13}$$

From the condition (3.3.3), one can check that all the eigenvalues $\omega \in \pm[\omega_L, \omega_U]$ always lie on the axis $\mathrm{Im}(\omega) = \alpha > 0$ for all ε, which means that the continuous spectrum does not contribute to the instability of the soliton. Therefore, the analysis of stability is only devoted to the discrete eigenvalues. As in Chapter 2, discrete eigenvalues that potentially lead to instability are also sometimes referred here to as critical eigenvalues.

3.3.1 Onsite bright solitons

In this section we perform perturbation analysis for the existence and stability of onsite bright soliton in Eq. (3.2.1). In the context of this theory, the exact solutions of Eq. (3.2.1) are available when $\varepsilon = 0$ which has been given in (3.3.2). For an onsite bright soliton, its configuration in the uncoupled limit is of the form

$$u_n^{(0)} = 0 \quad \text{for} \quad n \neq 0, \quad u_0^{(0)} = A + \mathrm{i}B, \tag{3.3.14}$$

where $(A, B) \neq (0, 0)$. From the combination of nonzero solutions (3.3.2), we can classify the onsite bright solitons, indicated by the different values of (A, B), as follows:

(i) Type I, which has $(A, B) = (A_+, -B_-)$,

(ii) Type II, which has $(A, B) = (A_-, -B_+)$,

which we denote hereinafter by $u_{n\{\pm\}}$ and $u_{n\{\mp\}}$, respectively.

The continuation of the above solutions for small ε can be calculated from the expansion (3.3.1), from which one can show that an onsite soliton type I and type II, up to $\mathcal{O}(\varepsilon^2)$, are respectively given by

$$u_{n\{\pm\}} = \begin{cases} (A_+ - \mathrm{i}B_-) + \frac{(A_+ - \mathrm{i}B_-)\varepsilon}{\Lambda + \sqrt{\gamma^2 - \alpha^2}}, & n = 0, \\ \frac{(A_+ - \mathrm{i}B_-)\varepsilon}{\Lambda + \sqrt{\gamma^2 - \alpha^2}}, & n = -1, 1, \\ 0, & \text{otherwise}, \end{cases} \tag{3.3.15}$$

and

$$u_{n\{\mp\}} = \begin{cases} (A_- - \mathrm{i}B_+) + \frac{(A_- - \mathrm{i}B_+)\varepsilon}{\Lambda - \sqrt{\gamma^2 - \alpha^2}}, & n = 0, \\ \frac{(A_- - \mathrm{i}B_+)\varepsilon}{\Lambda - \sqrt{\gamma^2 - \alpha^2}}, & n = -1, 1, \\ 0, & \text{otherwise}. \end{cases} \tag{3.3.16}$$

In particular, when $\alpha = \gamma$, the onsite type I and type II become exactly the same.

To examine the stability of the solitons, we need to calculate the corresponding discrete eigenvalues for each of type I and type II, which we elaborate successively.

3.3.1.1 Onsite type I

One can show from Eq. (3.3.5) that at $\varepsilon = 0$, an onsite bright soliton type I has a leading-order discrete eigenvalue which comes as the pair

$$\omega^{(0)}_{\{\pm\}} = \pm\sqrt{\mathcal{P}} + \mathrm{i}\alpha, \tag{3.3.17}$$

where

$$\mathcal{P} = 4\Lambda\sqrt{\gamma^2 - \alpha^2} + 4\gamma^2 - 5\alpha^2. \tag{3.3.18}$$

The eigenvector corresponding to the above eigenvalue has components $\eta_n^{(0)} = 0$ for $n \neq 0$ and $\eta_0^{(0)} \neq 0$.

We notice that $\mathcal{P}$ can be either positive or negative depending on whether $\alpha \lessgtr \alpha_{\text{th}}$, where

$$\alpha_{\text{th}} = \frac{2}{5}\sqrt{5\gamma^2 - 2\Lambda^2 + \Lambda\sqrt{4\Lambda^2 + 5\gamma^2}}. \tag{3.3.19}$$

Therefore, the eigenvalue $\omega^{(0)}_{\{\pm\}}$ can be either

$$\omega_1{}^{(0)}_{\{\pm\}} = \pm\sqrt{4\Lambda\sqrt{\gamma^2 - \alpha^2} + 4\gamma^2 - 5\alpha^2} + \mathrm{i}\alpha, \tag{3.3.20}$$

for the case $\alpha < \alpha_{\text{th}}$, or

$$\omega 2^{(0)}_{\{\pm\}} = \mathrm{i}\left(\alpha \pm \sqrt{5\alpha^2 - 4\Lambda\sqrt{\gamma^2-\alpha^2} - 4\gamma^2}\right), \tag{3.3.21}$$

for the case $\alpha_{\text{th}} < \alpha \leq \gamma$.

The continuation of the eigenvalues (3.3.20) and (3.3.21) for nonzero ε can be evaluated from Eq. (3.3.6) by applying a Fredholm solvability condition. As the corresponding eigenvector has zero components except at site $n = 0$, we only need to require $f_0 = 0$, from which we obtain the discrete eigenvalue of $u_{n\{\pm\}}$ for small ε, up to $\mathcal{O}(\varepsilon^2)$, as follows.

(i) For the case $\alpha < \alpha_{\text{th}}$:

$$\omega_{1\{\pm\}} = \pm\sqrt{4\Lambda\sqrt{\gamma^2-\alpha^2} + 4\gamma^2 - 5\alpha^2} \pm \frac{(4\sqrt{\gamma^2-\alpha^2})\varepsilon}{\sqrt{4\Lambda\sqrt{\gamma^2-\alpha^2} + 4\gamma^2 - 5\alpha^2}} + \mathrm{i}\alpha. \tag{3.3.22}$$

(ii) For the case $\alpha_{\text{th}} < \alpha \leq \gamma$:

$$\omega_{2\{\pm\}} = \mathrm{i}\left(\alpha \pm \sqrt{5\alpha^2 - 4\Lambda\sqrt{\gamma^2-\alpha^2} - 4\gamma^2} \mp \frac{(4\sqrt{\gamma^2-\alpha^2})\varepsilon}{\sqrt{5\alpha^2 - 4\Lambda\sqrt{\gamma^2-\alpha^2} - 4\gamma^2}}\right). \tag{3.3.23}$$

We should note here that the above expansions remain valid if $\pm\mathcal{P}$ are $\mathcal{O}(1)$.

Let us now investigate the behaviour of the above eigenvalue in each case. In case (i), the imaginary part of $\omega 1^{(0)}_{\{\pm\}}$ (i.e., when $\varepsilon = 0$) is α, which is positive. We also note that $|\omega 1^{(0)}_{\{\pm\}}| \gtrless |\omega^{(0)}_C|$ when $\alpha \lessgtr \alpha_{\text{cp}}$, where

$$\alpha_{\text{cp}} = \frac{1}{5}\sqrt{25\gamma^2 - \Lambda^2}. \tag{3.3.24}$$

As ε increases, the value of $|\omega_{1\{\pm\}}|$ also increases. As a result, the eigenvalues $\omega_{1\{\pm\}}$ will collide either with the upper band (ω_U) of the continuous spectrum for $\alpha < \alpha_{\text{cp}}$, or with the lower band (ω_L) for $\alpha_{\text{cp}} < \alpha < \alpha_{\text{th}}$. These collisions then create a corresponding pair of eigenvalues bifurcating from the axis $\mathrm{Im}\left(\omega_{1\{\pm\}}\right) = \alpha$. This collision, however, does not immediately lead to the instability of the soliton as it does for $\alpha = 0$ (shown in the previous chapter). In addition, the distance between $\omega 1^{(0)}_{\{\pm\}}$ and $\omega^{(0)}_C$ increases as α tends to 0, which means that the corresponding collisions for smaller α happen at larger ε. From the above analysis we hence argue that for $\alpha < \alpha_{\text{th}}$ and for relatively small ε, the onsite soliton type I is stable.

In case (ii), due to the condition (3.3.3) and after some algebraic manipulations, we have $\sqrt{5\alpha^2 - 4\Lambda\sqrt{\gamma^2-\alpha^2} - 4\gamma^2} \leq \alpha$. The latter implies $0 \leq \min(\mathrm{Im}(\omega 2^{(0)}_{\{\pm\}})) < \alpha$ which indicates that the soliton is stable when $\varepsilon = 0$. As ε increases, both $\max(\mathrm{Im}(\omega 2_{\{\pm\}}))$ and $\min(\mathrm{Im}(\omega 2_{\{\pm\}}))$ tend to α at which they finally collide. From this fact, we conclude that for small ε and for $\alpha_{\text{th}} < \alpha \leq \gamma$, the soliton remains stable. In particular, when $\alpha = \gamma$, we have $\min(\mathrm{Im}(\omega 2_{\{\pm\}})) = 0$ for all ε, which then implies that the soliton is always stable.

3.3.1.2 Onsite type II

Performing the calculations as before, we obtain that the discrete eigenvalue (in pairs) of an onsite bright soliton type II is given, up to $\mathcal{O}(\varepsilon^2)$, by

$$\omega_{\{\mp\}} = \mathrm{i}\left(\alpha \pm \sqrt{4\Lambda\sqrt{\gamma^2-\alpha^2} - 4\gamma^2 + 5\alpha^2} \pm \frac{(4\sqrt{\gamma^2-\alpha^2})\varepsilon}{\sqrt{4\Lambda\sqrt{\gamma^2-\alpha^2} - 4\gamma^2 + 5\alpha^2}}\right). \quad (3.3.25)$$

Again, we should assume that the term $(4\Lambda\sqrt{\gamma^2-\alpha^2} - 4\gamma^2 + 5\alpha^2)$ in the above expansion is $\mathcal{O}(1)$.

When $\alpha < \gamma$, we simply have $\sqrt{4\Lambda\sqrt{\gamma^2-\alpha^2} - 4\gamma^2 + 5\alpha^2} > \alpha$, from which we deduce $\min(\mathrm{Im}(\omega^{(0)}_{\{\mp\}})) < 0$, meaning that at $\varepsilon = 0$ the soliton is unstable. In fact, as ε increases, the value of $\min(\mathrm{Im}(\omega_{\{\mp\}}))$ decreases. Therefore, in this case we infer that the soliton is unstable for all ε (notice that the same type of instability also occurs for the case of the undamped onsite bright soliton type II which is purely imaginary).

When $\alpha = \gamma$, by contrast, the value of $\min(\mathrm{Im}(\omega_{\{\mp\}}))$ is zero for all ε, which indicates that the soliton is always stable. In fact, the stability of an onsite type II in this case is exactly the same as in type I. This is understandable as the onsite type I and type II possess the same profile when $\alpha = \gamma$.

3.3.2 Intersite bright solitons

Another natural fundamental solution to be studied is an intersite bright soliton whose mode structure in the uncoupled limit is of the form

$$u_n^{(0)} = \begin{cases} A_0 + \mathrm{i}B_0, & n = 0, \\ A_1 + \mathrm{i}B_1, & n = 1, \\ 0, & \text{otherwise}, \end{cases} \quad (3.3.26)$$

where $(A_0, B_0) \neq (0,0)$ and $(A_1, B_1) \neq (0,0)$. The combination of the nonzero solutions (3.3.2) gives the classification for the intersite bright solitons, indicated by different values of (A_0, B_0) and (A_1, B_1), as follows:

(i) Type I, which has $(A_0, B_0) = (A_1, B_1) = (A_+, -B_-)$,

(ii) Type II, which has $(A_0, B_0) = (A_1, B_1) = (A_-, -B_+)$,

(iii) Type III, which has $(A_0, B_0) = (A_+, -B_-)$ and $(A_1, B_1) = (A_-, -B_+)$,

(iv) Type IV, which has $(A_0, B_0) = (A_-, -B_+)$ and $(A_1, B_1) = (A_+, -B_-)$.

Let us henceforth denote the respective types by $u_{n\{\pm\pm\}}$, $u_{n\{\mp\mp\}}$, $u_{n\{\pm\mp\}}$ and $u_{n\{\mp\pm\}}$.

From the expansion (3.3.1), we obtain the continuation of each type of solution for small ε, which are given, up to order ε^2, by

$$u_{n\{\pm\pm\}} = \begin{cases} (A_+ - \mathrm{i}B_-) + \frac{1}{2}\frac{(A_+ - \mathrm{i}B_-)\varepsilon}{\Lambda + \sqrt{\gamma^2-\alpha^2}}, & n = 0, \\ (A_+ - \mathrm{i}B_-) + \frac{1}{2}\frac{(A_+ - \mathrm{i}B_-)\varepsilon}{\Lambda + \sqrt{\gamma^2-\alpha^2}}, & n = 1, \\ \frac{(A_+ - \mathrm{i}B_-)\varepsilon}{\Lambda + \sqrt{\gamma^2-\alpha^2}}, & n = -1, 2, \\ 0, & \text{otherwise}, \end{cases} \tag{3.3.27}$$

$$u_{n\{\mp\mp\}} = \begin{cases} (A_- - \mathrm{i}B_+) + \frac{1}{2}\frac{(A_- - \mathrm{i}B_+)\varepsilon}{\Lambda - \sqrt{\gamma^2-\alpha^2}}, & n = 0, \\ (A_- - \mathrm{i}B_+) + \frac{1}{2}\frac{(A_- - \mathrm{i}B_+)\varepsilon}{\Lambda - \sqrt{\gamma^2-\alpha^2}}, & n = 1, \\ \frac{(A_- - \mathrm{i}B_+)\varepsilon}{\Lambda - \sqrt{\gamma^2-\alpha^2}}, & n = -1, 2, \\ 0, & \text{otherwise}, \end{cases} \tag{3.3.28}$$

$$u_{n\{\pm\mp\}} = \begin{cases} \frac{(A_+ - \mathrm{i}B_-)\varepsilon}{\Lambda + \sqrt{\gamma^2-\alpha^2}}, & n = -1, \\ (A_+ - \mathrm{i}B_-) + \frac{1}{2}\frac{(\mathcal{A}_+ - \mathrm{i}\mathcal{B}_-)\varepsilon}{\gamma(\Lambda + \sqrt{\gamma^2-\alpha^2})}, & n = 0, \\ (A_- - \mathrm{i}B_+) + \frac{1}{2}\frac{(\mathcal{A}_- - \mathrm{i}\mathcal{B}_+)\varepsilon}{\gamma(\Lambda - \sqrt{\gamma^2-\alpha^2})}, & n = 1, \\ \frac{(A_- - \mathrm{i}B_+)\varepsilon}{\Lambda - \sqrt{\gamma^2-\alpha^2}}, & n = 2, \\ 0, & \text{otherwise}, \end{cases} \tag{3.3.29}$$

$$u_{n\{\mp\pm\}} = \begin{cases} \frac{(A_- - \mathrm{i}B_+)\varepsilon}{\Lambda - \sqrt{\gamma^2-\alpha^2}}, & n = -1, \\ (A_- - \mathrm{i}B_+) + \frac{1}{2}\frac{(\mathcal{A}_- - \mathrm{i}\mathcal{B}_+)\varepsilon}{\gamma(\Lambda - \sqrt{\gamma^2-\alpha^2})}, & n = 0, \\ (A_+ - \mathrm{i}B_-) + \frac{1}{2}\frac{(\mathcal{A}_+ - \mathrm{i}\mathcal{B}_-)\varepsilon}{\gamma(\Lambda + \sqrt{\gamma^2-\alpha^2})}, & n = 1, \\ \frac{(A_+ - \mathrm{i}B_-)\varepsilon}{\Lambda + \sqrt{\gamma^2-\alpha^2}}, & n = 2, \\ 0, & \text{otherwise}, \end{cases} \tag{3.3.30}$$

where

$$\mathcal{A}_\pm = 2\gamma A_\pm + (\Lambda \pm \sqrt{\gamma^2 - \alpha^2})A_\mp, \tag{3.3.31}$$

$$\mathcal{B}_\pm = 2\gamma B_\pm - (\Lambda \mp \sqrt{\gamma^2 - \alpha^2})B_\mp. \tag{3.3.32}$$

All solutions above are defined on the region (3.3.3) and exhibit the same profiles when $\alpha = \gamma$. One can check that intersite type III and IV are symmetric, thus they should really be considered as one solution. However, we write them here as two 'different' solutions because, as shown later in the next section, they form two different branches in a pitchfork bifurcation (together with intersite type I).

Let us now examine the stability of each solution by investigating their corresponding discrete eigenvalues.

3.3.2.1 Intersite type I

By considering Eq. (3.3.5) and carrying out the same analysis as in onsite type I, we obtain that the intersite type I has the double leading-order discrete eigenvalue

$$\omega 1^{(0)}_{\{\pm\pm\}} = \pm\sqrt{4\Lambda\sqrt{\gamma^2-\alpha^2}+4\gamma^2-5\alpha^2}+\mathrm{i}\alpha, \tag{3.3.33}$$

for $\alpha < \alpha_{\text{th}}$, and

$$\omega 2^{(0)}_{\{\pm\pm\}} = \mathrm{i}\left(\alpha \pm \sqrt{5\alpha^2-4\Lambda\sqrt{\gamma^2-\alpha^2}-4\gamma^2}\right), \tag{3.3.34}$$

for $\alpha_{\text{th}} < \alpha \leq \gamma$. The corresponding eigenvector for the above eigenvalues has components $\eta_n^{(0)} = 0$ for $n \neq 0, 1$, $\eta_0^{(0)} \neq 0$, and $\eta_1^{(0)} \neq 0$.

One can check, as in onsite type I, that the position of $\omega 1^{(0)}_{\{\pm\pm\}}$ relative to $\omega_C^{(0)}$ depends on whether $\alpha \lessgtr \alpha_{\text{cp}} = \frac{1}{5}\sqrt{25\gamma^2-\Lambda^2}$, i.e., the value of $|\omega 1^{(0)}_{\{\pm\pm\}}|$ is greater (less) than $|\omega_C^{(0)}|$ when α is less (greater) than α_{cp}.

The next correction for the discrete eigenvalues of an intersite type II can be calculated from Eq. (3.3.6), for which we need a solvability condition. Due to the presence of two non-zero components of the corresponding eigenvector at $n = 0, 1$, we only require $f_0 = 0$ and $f_1 = 0$. Our simple analysis then shows $\eta_0^{(0)} = \pm\eta_1^{(0)}$ from which we obtain that each of double eigenvalues (3.3.33) and (3.3.34) bifurcates into two distinct eigenvalues, which are given, up to order ε^2, as follows.

(i) For the case $\alpha < \alpha_{\text{th}}$:

$$\omega_{11\{\pm\pm\}} = \pm\sqrt{4\Lambda\sqrt{\gamma^2-\alpha^2}+4\gamma^2-5\alpha^2} \pm \frac{(2\sqrt{\gamma^2-\alpha^2})\varepsilon}{\sqrt{4\Lambda\sqrt{\gamma^2-\alpha^2}+4\gamma^2-5\alpha^2}}+\mathrm{i}\alpha, \tag{3.3.35}$$

$$\omega_{12\{\pm\pm\}} = \pm\sqrt{4\Lambda\sqrt{\gamma^2-\alpha^2}+4\gamma^2-5\alpha^2} \mp \frac{2(\Lambda+\sqrt{\gamma^2-\alpha^2})\varepsilon}{\sqrt{4\Lambda\sqrt{\gamma^2-\alpha^2}+4\gamma^2-5\alpha^2}}+\mathrm{i}\alpha. \tag{3.3.36}$$

(ii) For the case $\alpha_{\text{th}} < \alpha \leq \gamma$:

$$\omega_{21\{\pm\pm\}} = \mathrm{i}\left(\alpha \pm \sqrt{5\alpha^2 - 4\Lambda\sqrt{\gamma^2-\alpha^2} - 4\gamma^2} \mp \frac{(2\sqrt{\gamma^2-\alpha^2})\varepsilon}{\sqrt{5\alpha^2 - 4\Lambda\sqrt{\gamma^2-\alpha^2} - 4\gamma^2}}\right), \tag{3.3.37}$$

$$\omega_{22\{\pm\pm\}} = \mathrm{i}\left(\alpha \pm \sqrt{5\alpha^2 - 4\Lambda\sqrt{\gamma^2-\alpha^2} - 4\gamma^2} \pm \frac{2(\Lambda + \sqrt{\gamma^2-\alpha^2})\varepsilon}{\sqrt{5\alpha^2 - 4\Lambda\sqrt{\gamma^2-\alpha^2} - 4\gamma^2}}\right). \tag{3.3.38}$$

te

As before, we assume here that the terms $\pm(4\Lambda\sqrt{\gamma^2-\alpha^2}+4\gamma^2-5\alpha^2)$ are $\mathcal{O}(1)$ so that the above expansions remain valid.

Let us first observe the behaviour of the eigenvalues in case (i). In the uncoupled limit $\varepsilon = 0$, the imaginary part of $\omega_{11\{\pm\pm\}}^{(0)} = \omega_{12\{\pm\pm\}}^{(0)}$ is $\alpha > 0$ which indicates that the soliton is initially stable. When ε is turned on, the value of $|\omega_{11\{\pm\pm\}}|$ increases but $|\omega_{12\{\pm\pm\}}|$ decreases. Therefore, we can determine the mechanism of collision of these two eigenvalues with the inner or outer boundary of continuous spectrum (ω_L or ω_U) as follows.

- For $\alpha < \alpha_{\text{cp}}$, the first collision is between $\omega_{12\{\pm\pm\}}$ and ω_U. Because ω_U moves faster (as ε is varied) than $\omega_{11\{\pm\pm\}}$, the next collision is between these two aforementioned eigenvalues.
- For $\alpha > \alpha_{\text{cp}}$, the mechanism of collision can be either between $\omega_{11\{\pm\pm\}}$ and ω_L, or between $\omega_{12\{\pm\pm\}}$ and itself.

All of the mechanisms of collision above generate new corresponding pairs of eigenvalues bifurcating from their original imaginary parts, which is α. Yet these collisions do not immediately cause an instability, because $\alpha > 0$. Therefore, we may conclude that for sufficiently small ε and for $\alpha < \alpha_{\text{th}}$, an intersite bright soliton type I is stable.

Next, we describe the analysis for the eigenvalues in case (ii). When $\varepsilon = 0$, we have $0 \leq \min(\mathrm{Im}(\omega_{21\{\pm\pm\}}^{(0)})) = \min(\mathrm{Im}(\omega_{22\{\pm\pm\}}^{(0)})) < \alpha$. As ε is increased, $\min(\mathrm{Im}(\omega_{21\{\pm\pm\}}))$ increases but $\min(\mathrm{Im}(\omega_{22\{\pm\pm\}}))$ decreases. The latter then becomes negative, leading to the instability of soliton. By taking $\min(\mathrm{Im}(\omega_{22\{\pm\pm\}})) = 0$, one obtains

$$\varepsilon_{\text{cr}} = \frac{\alpha\sqrt{5\alpha^2 - 4\Lambda\sqrt{\gamma^2-\alpha^2} - 4\gamma^2}}{2(\Lambda + \sqrt{\gamma^2-\alpha^2})} - \frac{5\alpha^2 - 4\Lambda\sqrt{\gamma^2-\alpha^2} - 4\gamma^2}{2(\Lambda + \sqrt{\gamma^2-\alpha^2})}, \tag{3.3.39}$$

which yields an approximate boundary for the onset of instability, e.g., in the (ε, α)-plane for fixed Λ and γ.

3.3.2.2 Intersite type II

From our analysis of Eqs. (3.3.5) and (3.3.6), we obtain the discrete eigenvalues for an intersite bright soliton type II, which are given, with errors of order ε^2, by

$$\omega_{1\{\mp\mp\}} = \mathrm{i}\left(\alpha \pm \sqrt{4\Lambda\sqrt{\gamma^2-\alpha^2} - 4\gamma^2 + 5\alpha^2} \pm \frac{(2\sqrt{\gamma^2-\alpha^2})\varepsilon}{\sqrt{4\Lambda\sqrt{\gamma^2-\alpha^2} - 4\gamma^2 + 5\alpha^2}}\right), \tag{3.3.40}$$

$$\omega_{2\{\mp\mp\}} = \mathrm{i}\left(\alpha \pm \sqrt{4\Lambda\sqrt{\gamma^2-\alpha^2} - 4\gamma^2 + 5\alpha^2} \pm \frac{2(\Lambda-\sqrt{\gamma^2-\alpha^2})\varepsilon}{\sqrt{4\Lambda\sqrt{\gamma^2-\alpha^2} - 4\gamma^2 + 5\alpha^2}}\right), \tag{3.3.41}$$

assuming the term $(4\Lambda\sqrt{\gamma^2-\alpha^2} - 4\gamma^2 + 5\alpha^2)$ is $\mathcal{O}(1)$. Notice that $\omega_{1\{\mp\mp\}}$ and $\omega_{2\{\mp\mp\}}$ are equal when $\alpha = \sqrt{4\gamma^2 - \Lambda^2}/2$.

When $\alpha < \gamma$, both $\min(\mathrm{Im}(\omega_{1\{\mp\mp\}}))$ and $\min(\mathrm{Im}(\omega_{2\{\mp\mp\}}))$ are negative at $\varepsilon = 0$ and always decrease as ε is increased; the decrement of $\min(\mathrm{Im}(\omega_{2\{\mp\mp\}}))$ is greater than $\min(\mathrm{Im}(\omega_{1\{\mp\mp\}}))$ for $\alpha > \sqrt{4\gamma^2 - \Lambda^2}/2$. When $\alpha = \gamma$, $\min(\mathrm{Im}(\omega_{1\{\mp\mp\}}))$ and $\min(\mathrm{Im}(\omega_{2\{\mp\mp\}}))$ are zero at $\varepsilon = 0$. At nonzero ε, the former remains zero, but the latter becomes negative and decreases as ε increases. These facts allow us to conclude that an intersite bright soliton type II is always unstable, except at $\alpha = \gamma$ and $\varepsilon = 0$ (this is also the case for the undamped intersite type II, which is, in fact, a purely imaginary valued solution). One can check that when $\alpha = \gamma$, the eigenvalues of intersite type II are the same as in intersite type I.

3.3.2.3 Intersite type III and IV

As intersite type III and IV are symmetric, their eigenvalues are exactly the same. Our calculation shows the following.

(i) For the case $\alpha < \alpha_{\text{th}}$, the eigenvalues of the intersite type III and IV, up to $\mathcal{O}(\varepsilon^2)$, are

$$\begin{aligned}\omega_{11\{\pm\mp\}} &= \omega_{11\{\mp\pm\}} = \mathrm{i}\alpha \pm \sqrt{4\Lambda\sqrt{\gamma^2-\alpha^2} + 4\gamma^2 - 5\alpha^2} \\ &\quad \pm \frac{(2\gamma\sqrt{\gamma^2-\alpha^2} - \Lambda\gamma + \alpha\sqrt{\Lambda^2-\gamma^2+\alpha^2})\varepsilon}{\gamma\sqrt{4\Lambda\sqrt{\gamma^2-\alpha^2} + 4\gamma^2 - 5\alpha^2}},\end{aligned} \tag{3.3.42}$$

$$\begin{aligned}\omega_{12\{\pm\mp\}} &= \omega_{12\{\mp\pm\}} = \mathrm{i}\left(\alpha \pm \sqrt{4\Lambda\sqrt{\gamma^2-\alpha^2} - 4\gamma^2 + 5\alpha^2}\right. \\ &\quad \left.\pm \frac{(2\gamma\sqrt{\gamma^2-\alpha^2} + \Lambda\gamma - \alpha\sqrt{\Lambda^2-\gamma^2+\alpha^2})\varepsilon}{\gamma\sqrt{4\Lambda\sqrt{\gamma^2-\alpha^2} - 4\gamma^2 + 5\alpha^2}}\right).\end{aligned} \tag{3.3.43}$$

(ii) For the case $\alpha_{\text{th}} < \alpha \leq \gamma$, the eigenvalues, up to order ε^2, are

$$
\begin{aligned}
\omega_{21\{\pm\mp\}} &= \omega_{21\{\mp\pm\}} = \mathrm{i}\left(\alpha \pm \sqrt{5\alpha^2 - 4\Lambda\sqrt{\gamma^2-\alpha^2} - 4\gamma^2}\right. \\
&\qquad \left. \mp \frac{(2\gamma\sqrt{\gamma^2-\alpha^2} - \Lambda\gamma + \alpha\sqrt{\Lambda^2-\gamma^2+\alpha^2})\varepsilon}{\gamma\sqrt{5\alpha^2 - 4\Lambda\sqrt{\gamma^2-\alpha^2} - 4\gamma^2}}\right), \qquad (3.3.44) \\
\omega_{22\{\pm\mp\}} &= \omega_{22\{\mp\pm\}} = \mathrm{i}\left(\alpha \pm \sqrt{4\Lambda\sqrt{\gamma^2-\alpha^2} - 4\gamma^2 + 5\alpha^2}\right. \\
&\qquad \left. \pm \frac{(2\gamma\sqrt{\gamma^2-\alpha^2} + \Lambda\gamma - \alpha\sqrt{\Lambda^2-\gamma^2+\alpha^2})\varepsilon}{\gamma\sqrt{4\Lambda\sqrt{\gamma^2-\alpha^2} - 4\gamma^2 + 5\alpha^2}}\right). \qquad (3.3.45)
\end{aligned}
$$

We should assume again that the terms $\pm(4\Lambda\sqrt{\gamma^2-\alpha^2} + 4\gamma^2 - 5\alpha^2)$ and $(4\Lambda\sqrt{\gamma^2-\alpha^2} - 4\gamma^2 + 5\alpha^2)$ in the above expansions are of $\mathcal{O}(1)$.

In the first case, the eigenvalues (3.3.43) are apparently pure imaginary, with an imaginary part whose minimum value is negative for all ε. In the second case, it is clear that for $\alpha < \gamma$ the minimum value of the imaginary part of the eigenvalues (3.3.44) is positive (less than α) initially at $\varepsilon = 0$ and then increases as ε increases. However, for this case ($\alpha < \gamma$), the minimum value of the imaginary part of the eigenvalues (3.3.45), which are exactly the same as the eigenvalues (3.3.43), is negative at $\varepsilon = 0$ and then decreases as ε is turned on. In contrast, for $\alpha = \gamma$ the minimum value of the imaginary part of the eigenvalues (3.3.44) and (3.3.45) remains zero for all ε. The above fact shows that both intersite soliton type III and IV are always unstable, except at $\alpha = \gamma$. In fact, as shown in the numerical calculation later, the intersite type III and IV are no longer defined along this line, due to a pitchfork bifurcation with intersite type I.

3.4 Comparisons with numerical results, and bifurcations

In order to find the numerical solutions for each soliton discussed in the previous section, we solve the stationary equation (3.2.1) [cf. Eq. (3.2.3)] using a Newton-Raphson (NR) method. The evaluation is performed in domain $n \in [-N, N]$, i.e., for a lattice of $2N+1$ sites, with periodic boundary conditions $u_{\pm(N+1)} = u_{\mp N}$. As an initial guess, we use the corresponding exact soliton solutions in the uncoupled limit $\varepsilon = 0$ from which we then numerically continue for nonzero ε. As an illustrative example, the numerical solutions for each type of onsite and intersite bright soliton with parameter values $(\varepsilon, \Lambda, \gamma, \alpha) = (0.1, 1, 0.5, 0.1)$ are depicted in Fig. 3.1. The corresponding analytical approximations are also plotted therein showing good agreement with the numerical results.

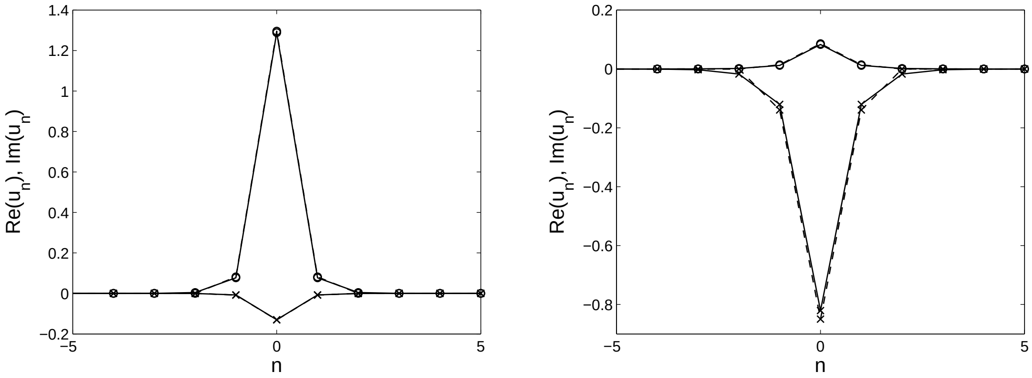

(a) Onsite type I (b) Onsite type II

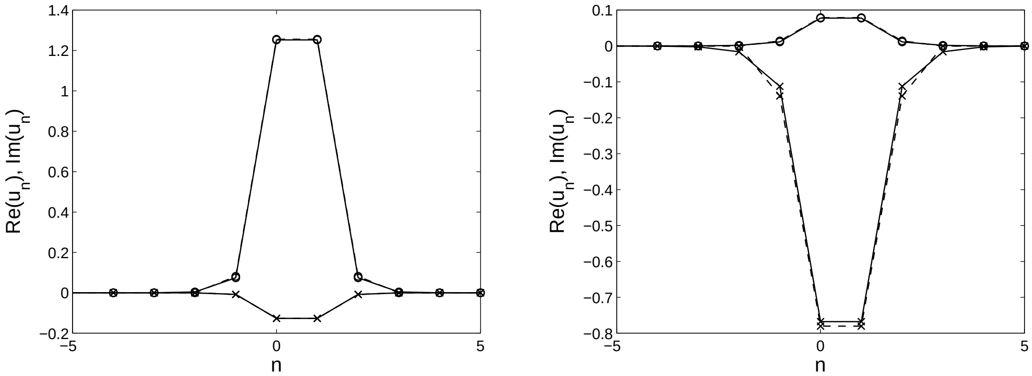

(c) Intersite type I (d) Intersite type II

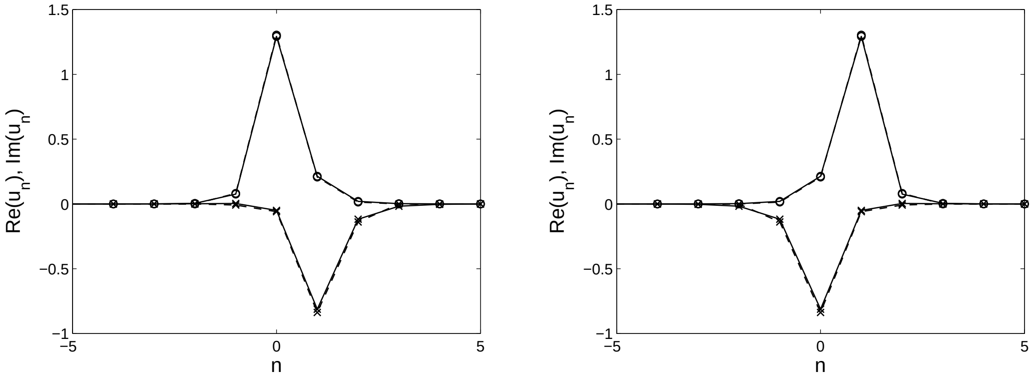

(e) Intersite type III (f) Intersite type IV

Figure 3.1: Profiles of onsite and intersite bright solitons of different types, as indicated in the caption of each panel, for parameter values $(\varepsilon, \Lambda, \gamma, \alpha) = (0.1, 1, 0.5, 0.1)$. Solid lines show the numerical results while dashed lines indicate the analytical approximations given by Eqs. (3.3.15) and (3.3.16) for the onsite type I and II, respectively, and by Eqs. (3.3.27), (3.3.28), (3.3.29) and (3.3.30) for the intersite type I, II, III and IV, respectively. The circle and cross markers correspond to the real and imaginary part of the solutions, respectively.

To examine the stability of each soliton, we solve the eigenvalue problem (3.2.5) numerically and then compare the results with the analytical calculations. Moreover, we show later that the relevant solitons experience saddle-node and/or pitchfork bifurcations. To depict the diagram of these bifurcations, we use a pseudo-arclength method which allows us to continue the solution past turning points (by varying one parameter). In addition, our analysis of the eigenvalues for some particular solutions leads to the fact of the presence of Hopf bifurcations. We will determine the nature of Hopf bifurcation points and perform continuation of the bifurcating limit cycles in the next section by employing the numerical continuation package Matcont.

In all illustrative examples below, we use $N = 50$ (we also used larger values of N but there was almost no change in the quantitative behaviour). In addition, for the sake of simplicity, we set $\Lambda = 1$ and $\gamma = 0.5$.

3.4.1 Onsite bright solitons

3.4.1.1 Onsite type I

We start by testing the validity of our analytical approximation for the critical eigenvalues given by Eqs. (3.3.22) and (3.3.23). We present in Fig. 3.2 comparisons between the analytical and numerical results for the critical eigenvalues as functions of ε. We plot comparisons for three values $\alpha = 0.1, 0.485, 0.497$ to represent the cases $\alpha < \alpha_{\text{cp}}$, $\alpha_{\text{cp}} < \alpha < \alpha_{\text{th}}$ and $\alpha_{\text{th}} < \alpha < \gamma$, respectively (see again the relevant discussion in the previous section). From the figure, we conclude that our prediction for small ε is relatively close to the numerics.

For the three values of α given above, we now present in Fig. 3.3 the eigenvalue structure of the soliton and the corresponding diagram for the imaginary part of the critical eigenvalues as functions of ε. Let us now describe the results in more detail.

First, we notice that at $\varepsilon = 0$ the critical eigenvalues for $\alpha = 0.1$ lie beyond the outer band of the continuous spectrum, while for $\alpha = 0.485$ they are trapped between the two inner bands of the continuous spectrum. As ε is turned on, the corresponding critical eigenvalues for $\alpha = 0.1$ and $\alpha = 0.485$ collide with, respectively, the outer and the inner bands, leading to the bifurcation of the corresponding eigenvalues. The minimum imaginary part of these bifurcating eigenvalues, however, does not immediately become negative. Hence, for relatively small ε we conclude that the soliton is always stable; this in accordance with our analytical prediction of the previous section. The critical values of ε at which $\min(\text{Im}(\omega)) = 0$ indicating the onset of the instability are depicted by the star markers in panels (c) and (f) in Fig. 3.3. Interestingly, for $\alpha = 0.485$

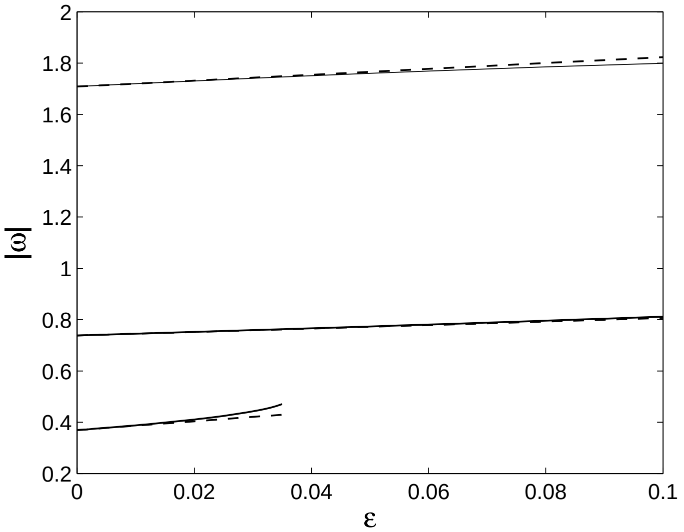

Figure 3.2: Comparisons between the critical eigenvalues of an onsite bright soliton type I obtained numerically (solid lines) and analytically (dashed lines). The upper and middle curves correspond, respectively, to $\alpha = 0.1$ and $\alpha = 0.485$, which are approximated by Eq. (3.3.22), whereas the lower corresponds to $\alpha = 0.497$, which is approximated by Eq. (3.3.23).

there is a re-stabilisation of the soliton as shown by the larger ε star marker in panel (f).

Next, for $\alpha = 0.497$ the discrete eigenvalues initially (at $\varepsilon = 0$) lie on the imaginary axis; they come in pairs and are symmetric about the line $\mathrm{Im}(\omega) = \alpha = 0.497$, and the minimum one is above the real axis. When ε increases, both eigenvalues approach one another and finally collide at the point $(\varepsilon, \alpha) = (0, 0.497)$ creating a new pair of discrete eigenvalues along the line $\mathrm{Im}(\omega) = \alpha = 0.497$. Each pair of the eigenvalues then again bifurcates after hitting the inner edge of the continuous spectrum. However, the minimum imaginary part of these bifurcating eigenvalues is always greater than zero even for larger ε [see panel (i)]. From this fact, we therefore conclude that the soliton in this case is always stable. This conclusion agrees with our analytical investigation.

The minimum value of $\mathrm{Im}(\omega)$ (in color representation) of the onsite bright soliton type I for a relatively large range of ε and α gives the (in)stability region in the (ε, α)-plane as presented in Fig. 3.4. The stable region is indeed determined whenever $\min(\mathrm{Im}(\omega)) \geq 0$ for each ε and α. The lower and upper dotted horizontal lines in this figure, i.e., respectively, $\alpha = \alpha_{\mathrm{cp}} \approx 0.4583$ and $\alpha = \alpha_{\mathrm{th}} \approx 0.49659$, represent the boundaries of the regions which distinguish the description of the eigenvalue structure of the soliton. The solid line in this figure indicates the (in)stability boundary, i.e., when $\min(\mathrm{Im}(\omega)) = 0$. Three representative points (star markers) lying on this line reconfirm the corresponding points in panels (c) and (f) in Fig. 3.3. As shown in the figure, there is an interval of

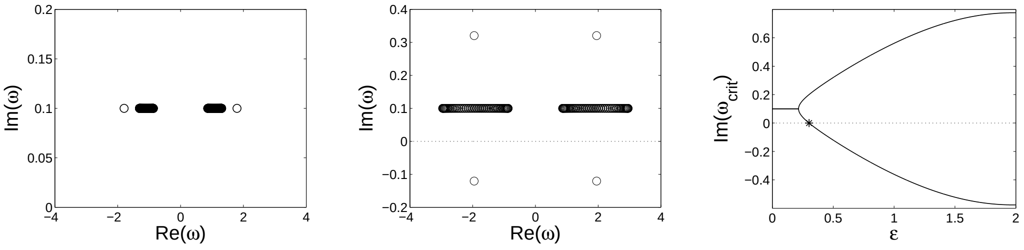

(a) $\alpha = 0.1, \varepsilon = 0.1$ (b) $\alpha = 0.1, \varepsilon = 0.5$ (c) $\alpha = 0.1$

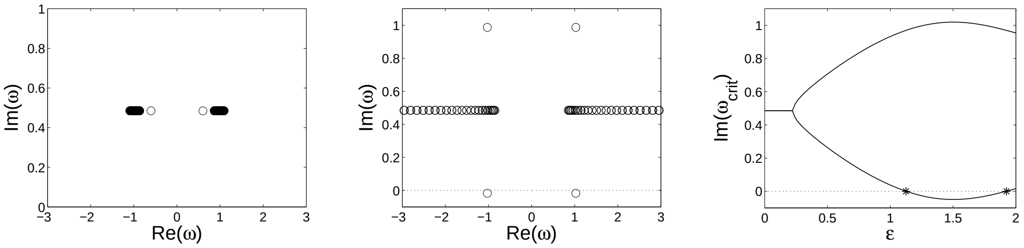

(d) $\alpha = 0.485, \varepsilon = 0.05$ (e) $\alpha = 0.485, \varepsilon = 1.2$ (f) $\alpha = 0.485$

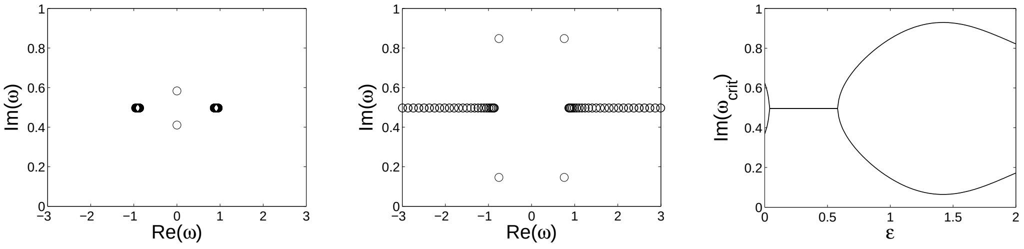

(g) $\alpha = 0.497, \varepsilon = 0.02$ (h) $\alpha = 0.497, \varepsilon = 1$ (i) $\alpha = 0.497$

Figure 3.3: The first and second columns of panels show the $(\mathrm{Re}(\omega), \mathrm{Im}(\omega))$-plane of the eigenvalues of onsite bright solitons type I for several values of α and ε, as indicated in the caption of each panel (each row of panels depicts three different values of α). For $\alpha = 0.1$ and $\alpha = 0.485$, the corresponding left and middle panels illustrate the eigenvalues of stable and unstable solitons. The third column shows the path of the imaginary part of the critical eigenvalues ω_{crit} as functions of ε for the corresponding α. The locations of ε at which $\mathrm{Im}(\omega_{\mathrm{crit}}) = 0$ are indicated by the star markers.

α in which the soliton is stable for all ε. This is interesting as the onsite soliton, which was shown in Chapter 2 to be destabilised by a parametric driving in the case of no dissipation, now can be re-stabilised by a damping constant.

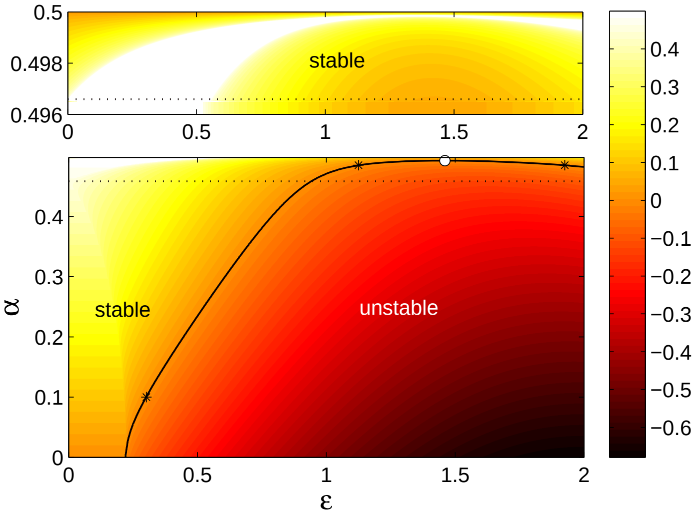

Figure 3.4: The (in)stability region of onsite bright solitons type I in the (ε, α)-plane. The corresponding color represents the minimum value of $\mathrm{Im}(\omega)$ (for all eigenvalues ω) for each ε and α. Thus, the region in which min $(\mathrm{Im}(\omega)) \geq 0$ indicates the region of stable soliton, otherwise unstable. The boundary of stable-unstable regions, i.e., when min $(\mathrm{Im}(\omega)) = 0$, is given by the solid line (three representative points (star markers) on this line correspond to those points in panels (c) and (f) in Fig. 3.3). The boundary curve also indicates the occurrence of Hopf bifurcations with one degenerate point, i.e., a double-Hopf bifurcation, at $\varepsilon \approx 1.46$ as indicated by the white-filled circle. The lower and upper horizontal dotted lines correspond to Eqs. (3.3.24) and (3.3.19), respectively (see text).

Let us revisit Fig. 3.3 for $\alpha = 0.1$ and $\alpha = 0.485$. We notice that at zero-crossing points ε_c (shown by the star markers in panels (c) and (f)), the following conditions hold:

(i) There is a pair (equal and opposite) of non-zero real eigenvalues, and

(ii) The ε-derivative of the imaginary part of the pair of eigenvalues mentioned in (i) is non-zero at ε_c.

The second condition is also called the transversality condition. We assume that the so-called *first Lyapunov coefficient* of the zero-crossing points is nonzero, i.e. the genericity condition. According to the Hopf bifurcation theorem (see, e.g., Kuznetsov [115], keeping in mind that our eigenvalue is denoted by $\mathrm{i}\omega$), the above conditions imply that at $\varepsilon = \varepsilon_c$ Eq. (3.1.1) has time-periodic (limit cycle) solutions bifurcating from a (steady-state) onsite bright soliton type I. We then call such a critical point ε_c a Hopf point.

Because the occurrence of Hopf bifurcation in the onsite type I also indicates the onset of (in)stability, the collection of Hopf bifurcation points in the (ε, α)-plane therefore lies precisely on the (in)stability boundary line (see again Fig. 3.4). However, at the stationary point $\varepsilon \approx 1.46$ the condition (ii) for the occurrence of a (non-degenerate) Hopf bifurcation does not hold. At this special point, we have a saddle-node bifurcation of Hopf points, i.e., a double-Hopf (Hopf-Hopf) bifurcation. Due to the violation of the transversality condition, there may be no periodic solution or even multiple periodic solutions at the denegerate point. We will examine this point later in Section 3.5, where it will be shown through numerical continuations of limit cycles near the degenerate point that the former possibility occurs.

3.4.1.2 Onsite type II

For this type of solution, a comparison between the critical eigenvalues obtained by analytical calculation, which is given by Eq. (3.3.25), and by numerics, is presented in Fig. 3.5. We conclude that our analytical prediction for small ε is quite accurate.

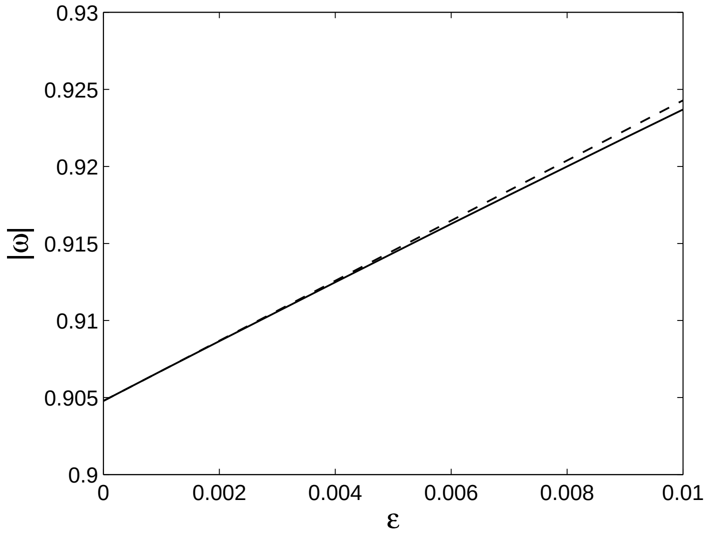

Figure 3.5: Comparison between the critical eigenvalues of onsite bright solitons type II for $\alpha = 0.1$ produced by numerics (solid line) and by analytical approximation (3.3.25) (dashed line).

The eigenvalue structure of onsite solitons type II for $\alpha = 0.1$ and the two values $\varepsilon = 0.1, 1$ and the corresponding curve of imaginary part of the critical eigenvalues are given in Fig. 3.6. This figure shows that the soliton is always unstable even for a large ε.

This fact is consistent with the analytical prediction. We notice in the figure that there is a new pair of discrete eigenvalues bifurcating from the inner edge of continuous spectrum at relatively large ε [see panel (b)].

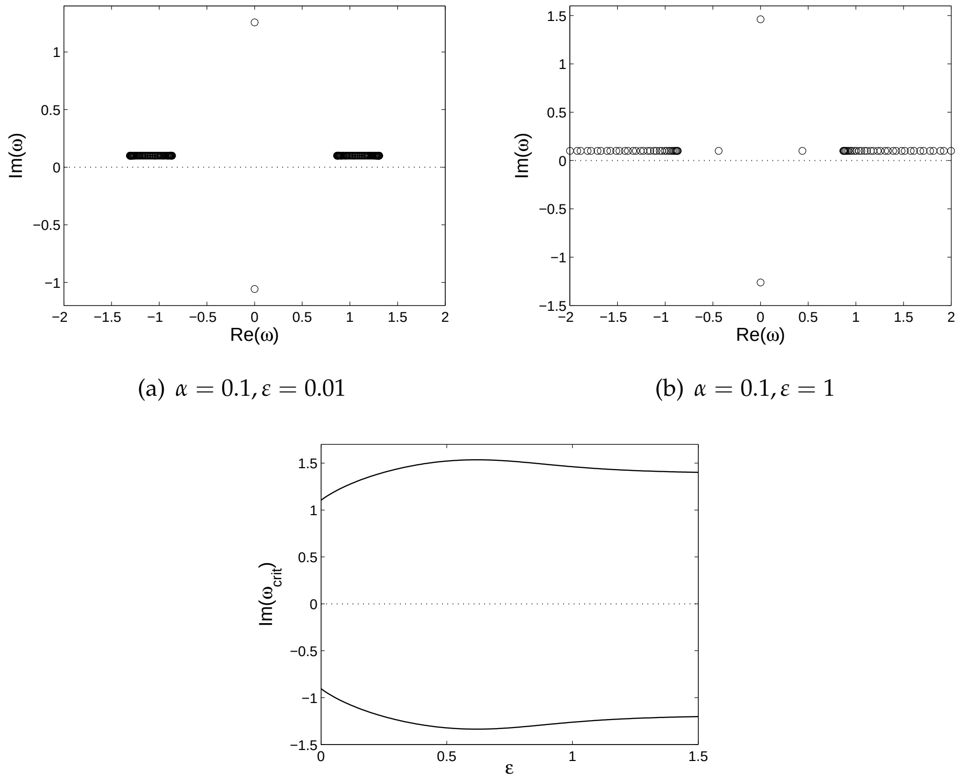

(a) $\alpha = 0.1, \varepsilon = 0.01$

(b) $\alpha = 0.1, \varepsilon = 1$

(c) $\alpha = 0.1$

Figure 3.6: The top panels show the eigenvalue structure of onsite bright solitons type II for $\alpha = 0.1$ and two values of ε as indicated in the caption. The bottom panel depicts the imaginary part of the critical eigenvalues as a function of ε.

By evaluating the minimum value of $\mathrm{Im}(\omega)$ for a relatively large ε and α, we obtain that the soliton is always unstable for $\alpha < \gamma = 0.5$ and, contrastingly, stable for $\alpha = \gamma$. In the latter case, the eigenvalues of the onsite type II are exactly the same as in the onsite type I; the minimum value of the imaginary part remains zero for all ε.

3.4.1.3 Saddle-node bifurcation of onsite bright solitons

We observed from numerics and analytics that when approaching $\alpha = \gamma$, the onsite bright soliton type I and type II possess the same profile as well as the same stability, consistent with the saddle-node bifurcation experienced by the two solitons. A diagram of this bifurcation can be produced, e.g., by plotting the norm of the numerical solution of these two solitons as a function of α for fixed $\varepsilon = 0.1$. To do so, we apply a pseudo-arc-length method to perform the numerical continuation, starting from the onsite type I at $\alpha = 0$. The obtained diagram is presented in Fig. 3.7 and the corresponding analytical approximation is also depicted therein. As shown in the figure, the onsite type I, which is stable, turns into the onsite type II, which is unstable. Both numerics and analytics give the same turning point [or so-called limit point (LP)] at $\alpha = \gamma = 0.5$. We also conclude that the analytical approximation for the norm is quite close to the numerics, with the accuracy for the onsite type I better than type II. Indeed, their accuracy could be improved if one uses smaller ε.

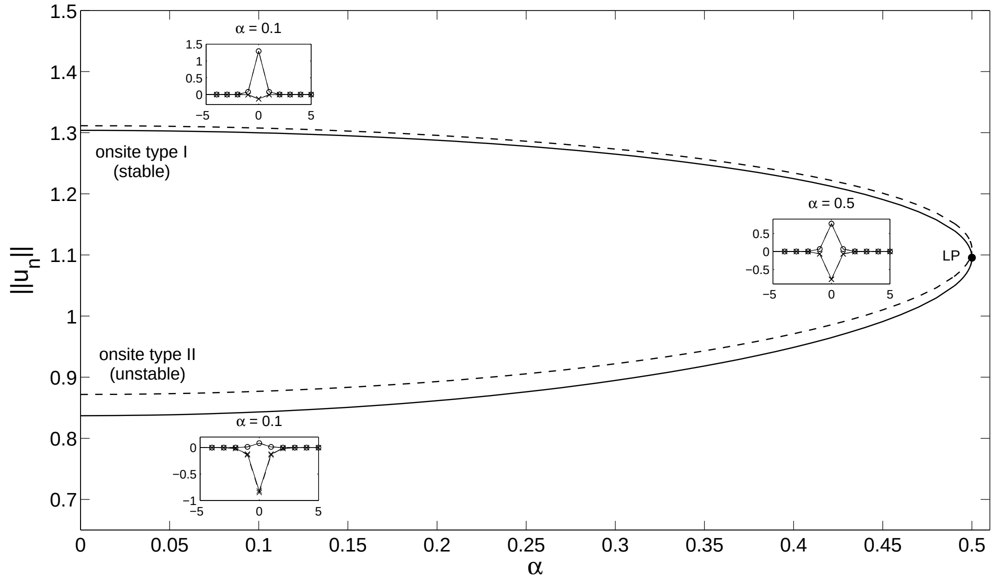

Figure 3.7: A saddle-node bifurcation of onsite bright solitons for $\varepsilon = 0.1$. The onsite type I (stable) merges with the onsite type II (unstable) at a limit point (LP) $\alpha = \gamma = 0.5$. The solid and dashed lines represent the norm of the solutions obtained by numerical calculation and analytical approximation, respectively. The insets depict the profile of the corresponding solutions at the two values $\alpha = 0.1, 0.5$. As in Fig. 3.1, solid (dashed) line in the insets corresponds to numerical (analytical) solution whose the real and imaginary parts are indicated by circle and cross markers, respectively.

3.4.2 Intersite bright solitons

3.4.2.1 Intersite type I

Let us first compare our analytical prediction for the critical eigenvalues, given by Eqs. (3.3.35)-(3.3.36) or (3.3.37)-(3.3.38), with the corresponding numerical results. We present the comparisons in Fig. 3.8 by considering three values of $\alpha = 0.1, 0.465, 0.497$ as representative points for the three cases discussed in the previous section. From the figure we see that the double eigenvalues which coincide originally at $\varepsilon = 0$ then split into two distinct eigenvalues as ε increases. One can notice a 'kink' in the upper solid line in Fig. 3.8(b). This occurs due to the collision of the corresponding eigenvalue with the lower boundary of the continuous spectrum (this will be discussed further in the next paragraph). We conclude that our approximation for small ε is generally quite accurate.

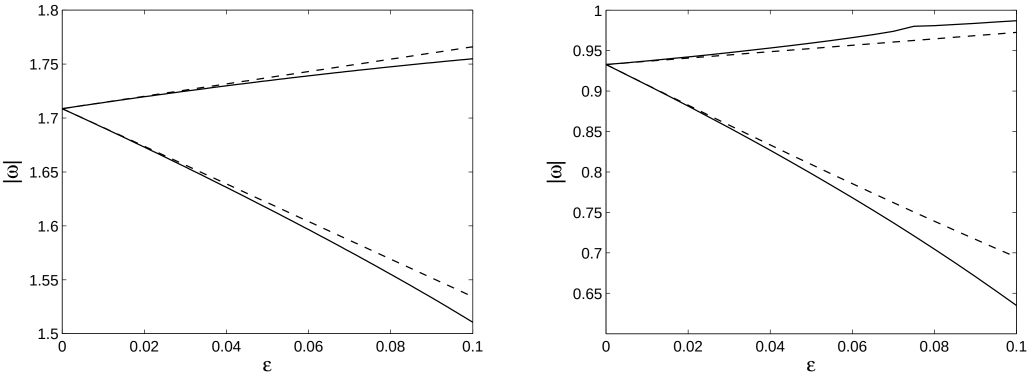

(a) $\alpha = 0.1$ (b) $\alpha = 0.465$

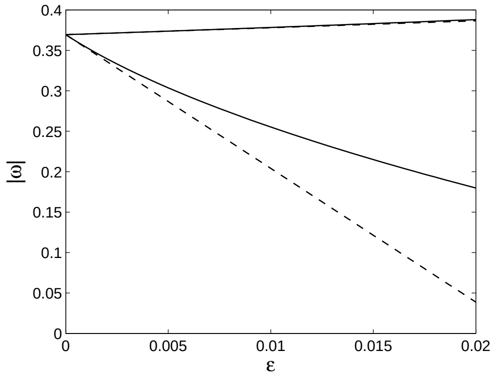

(c) $\alpha = 0.497$

Figure 3.8: Comparisons of the two distinct critical eigenvalues of intersite bright solitons type I obtained numerically (solid lines) and analytically (dashed lines) for three values of α as indicated in the caption of each panel. The upper and lower curves in panels (a) and (b) are plotted from, respectively, Eqs. (3.3.35) and (3.3.36), while in panel (c) from Eqs. (3.3.38) and (3.3.37).

Next, we move on to the description of the eigenvalue structure of the intersite bright solitons type I and the corresponding imaginary part of the two critical eigenvalues as functions of ε; these are depicted in Fig. 3.9 for the three values of α used before. The first and second columns in the figure represent conditions of stability and instability, respectively. For $\alpha = 0.1$, the two critical eigenvalues successively collide with the outer band of the continuous spectrum and the corresponding bifurcating eigenvalues coming from the first collision contribute to the instability. For $\alpha = 0.465$, the first collision is between one of the critical eigenvalues with the inner edge of the continuous spectrum. The second collision is between the other critical eigenvalue with its pair. In contrast to the previous case, the instability in this case is caused by the bifurcating eigenvalues coming from the second collision. Moreover, for $\alpha = 0.497$, contribution to the instability is given by one of the critical eigenvalues moving down along the imaginary axis. All the numerical results described above are in accordance with our analytical observations in Section 3.3.

Let us now focus our attention on the right panels of Fig. 3.9 by particularly discussing the properties of the critical points of ε at which the curve of the minimum imaginary part of the critical eigenvalues crosses the real axis (these are shown by the star markers). The first and third points (from left to right) in panel (c) as well as the points in panels (f) and (i) indicate the onset of stable-to-unstable transition. Contrastingly, the second point in panel (c) illustrates the beginning of the re-stabilisation of solitons. In fact, the first three points in panel (c) mentioned above admit all conditions for the occurrence of a Hopf bifurcation (see again the relevant explanation about these conditions in our discussion of onsite type I); therefore, they also correspond to Hopf points. In addition, the fourth point of zero crossing in panel (c), which comes from one of the purely imaginary eigenvalues, indicates the branch point of a pitchfork bifurcation experienced by the solutions of intersite type I, III and IV. We will discuss this type of bifurcation in more detail in the next section.

The (in)stability region of intersite bright solitons type I in the (ε, α)-plane is given in Fig. 3.10. In the figure, we also depict the two distinguishable (solid and dashed) lines representing the two distinct critical eigenvalues whose imaginary parts become zero. The star points on the lines correspond to those points in the right panels of Fig. 3.9. The boundary line which separates the stable and unstable regions in the figure is shown by the bold (solid and dashed) lines. The lower and upper dotted horizontal lines in the figure represent, respectively, $\alpha = \alpha_{\text{cp}} \approx 0.4583$ and $\alpha = \alpha_{\text{th}} \approx 0.49659$ which divide the region into three different descriptions of the eigenvalue structure. Interestingly, for $\alpha_{\text{th}} < \alpha$, we can make an approximation for the numerically obtained stability boundary (see the inset). This approximation is given by Eq. (3.3.39) which is quite close to the numerics for small ε.

We notice in Fig. 3.10 that the solid line (not the rightmost) and dashed line also represent Hopf bifurcations, with one special point (the white-filled circle) which does not

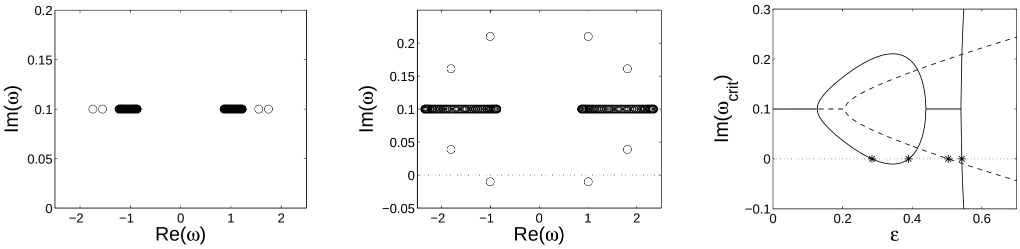

(a) $\alpha = 0.1, \varepsilon = 0.08$ (b) $\alpha = 0.1, \varepsilon = 0.35$ (c) $\alpha = 0.1$

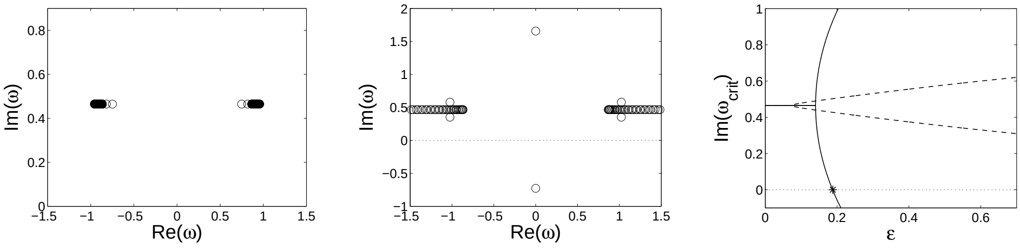

(d) $\alpha = 0.465, \varepsilon = 0.02$ (e) $\alpha = 0.465, \varepsilon = 0.5$ (f) $\alpha = 0.465$

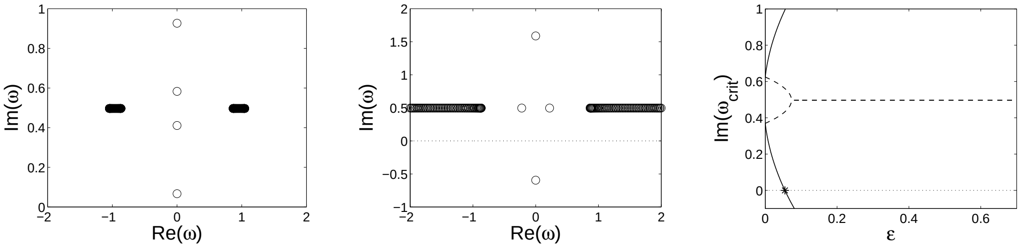

(g) $\alpha = 0.497, \varepsilon = 0.04$ (h) $\alpha = 0.497, \varepsilon = 0.3$ (i) $\alpha = 0.497$

Figure 3.9: The first and second columns of panels show the structure of eigenvalues of intersite bright solitons type I in the complex plane, for three values of α, each of which uses two different values of ε, to depict the condition of stability (left panel) and instability (middle panel). The third column shows the imaginary part of the two distinct critical eigenvalues (presented by solid and dashed lines) as functions of ε for the corresponding α. The locations of zero-crossings in these panels are indicated by the star markers.

meet the second condition for the occurrence of a (non-degenerate) Hopf bifurcation mentioned above (we will analyse the special point in the next section). We see from the figure that the bold parts of the Hopf lines coincide with the (in)stability boundary, while the nonbold ones exist in the unstable region. In addition, we also observe that the rightmost solid line in Fig. 3.10 indicates the collection of branch points of pitchfork bifurcation experienced by the intersite type I, III and IV; the bold part of this line also indicates the (in)stability boundary.

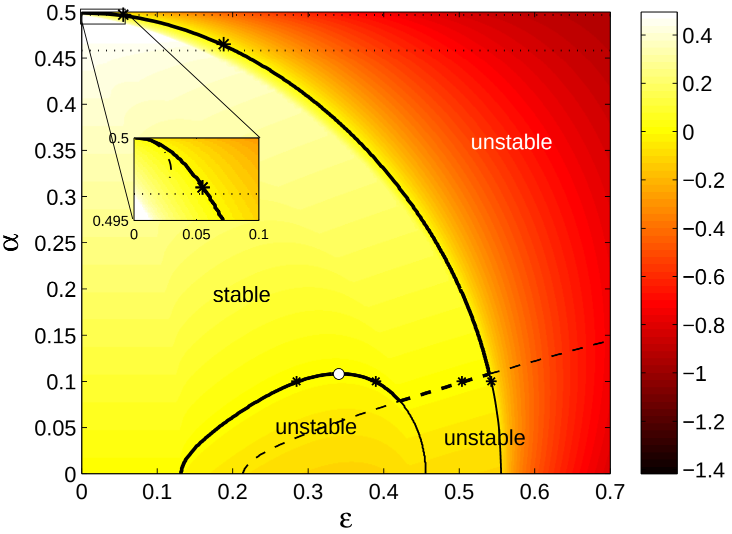

Figure 3.10: As Fig. 3.4 but for intersite bright solitons type I. The boundary between stable and unstable regions is given by the bold (solid and dashed) lines. The dashed-dotted line in the inset is our analytical approximation given by Eq. (3.3.39). The Hopf bifurcation lines are depicted by the solid (not the rightmost) and dashed lines. The white-filled circle indicates a degenerate Hopf point. The branch points of pitchfork bifurcation are shown by the rightmost solid lines.

3.4.2.2 Intersite type II

For intersite bright solitons type II, we present in Fig. 3.11 a comparison of two critical eigenvalues between the numerics and the analytical calculation given by Eqs. (3.3.40) and (3.3.41). We see from the figure that our approximation for relatively small ε is quite close to the numerics. The snapshot of the eigenvalue structure of this type of solution for two points (α, ε) and the path of the imaginary part of corresponding two discrete eigenvalues are depicted in Fig. 3.12. We conclude that the intersite soliton type II is unstable even for large ε.

Moreover, the evaluation of the minimum value of $\mathrm{Im}(\omega)$ of the intersite bright solitons

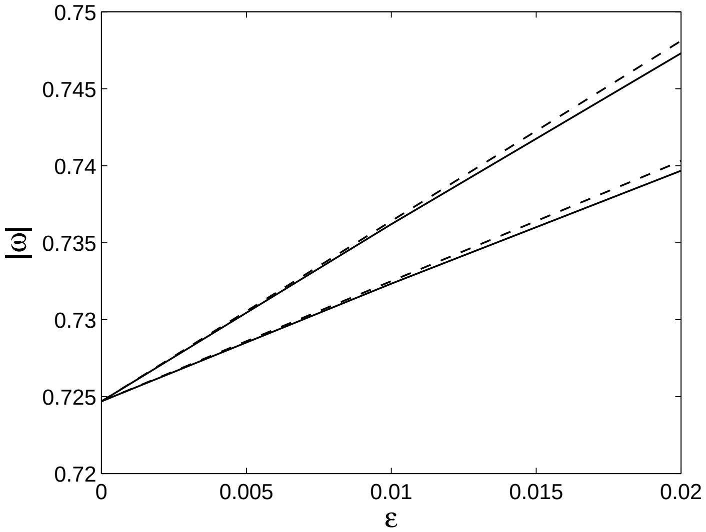

Figure 3.11: Comparison of two critical eigenvalues of intersite bright solitons type II for $\alpha = 0.3$ between numerics (solid lines) and analytics (dashed lines). The analytical approximation is given by Eq. (3.3.40) (lower curve) and Eq. (3.3.41) (upper curve).

type II in the (ε, α)-plane shows that the soliton, except at the point $\alpha = \gamma = 0.5$ and $\varepsilon = 0$, is always unstable. This result agrees with our analytical prediction.

3.4.2.3 Intersite type III and IV

Now we examine the intersite bright soliton type III which, due to symmetry, has exactly the same eigenvalues as type IV. In Fig. 3.13, we plot the analytical approximation for two critical eigenvalues given by Eqs. (3.3.42)-(3.3.43) or (3.3.44)-(3.3.45), which are compared with the corresponding numerical results. We conclude that the approximation is quite accurate for small ε and that the range of accuracy is wider for smaller value of α.

The structure of the eigenvalues of this type of solution and the curves of the imaginary part of the corresponding two critical eigenvalues are given in Fig. 3.14 for the three values of α used in Fig. 3.13. The figure reveals the condition of instability of solitons up to the limit points of ε at which the minimum imaginary part of the eigenvalues becomes zero; these conditions are indicated by the corresponding vertical lines in the third column. In fact, these limit points indicate the branch points of pitchfork bifurcation experienced by the intersite solitons type I, III and IV (we will discuss this bifurcation in more detail in the next section).

The first and second columns of Fig. 3.14 respectively present the condition just be-

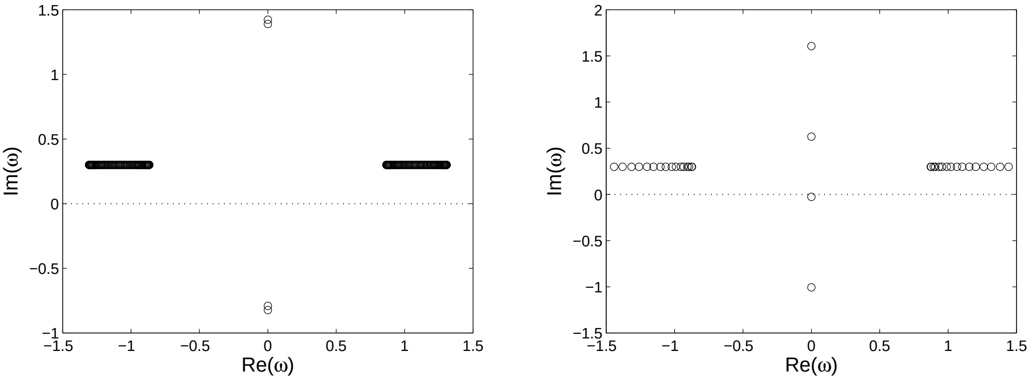

(a) $\alpha = 0.3, \varepsilon = 0.1$ (b) $\alpha = 0.3, \varepsilon = 2$

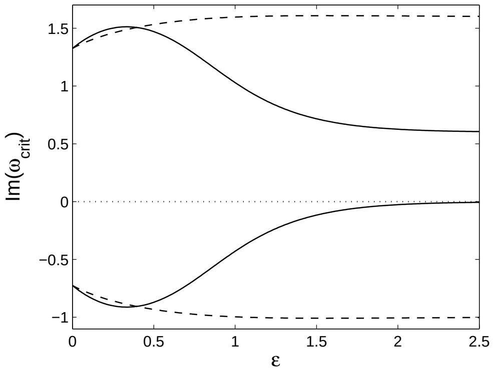

(c) $\alpha = 0.3$

Figure 3.12: (a)-(b) The eigenvalue structure of intersite bright solitons type II for two values (α, ε) as indicated in the caption. (c) The imaginary part of two discrete eigenvalues in varied ε (indicated by solid and dashed lines).

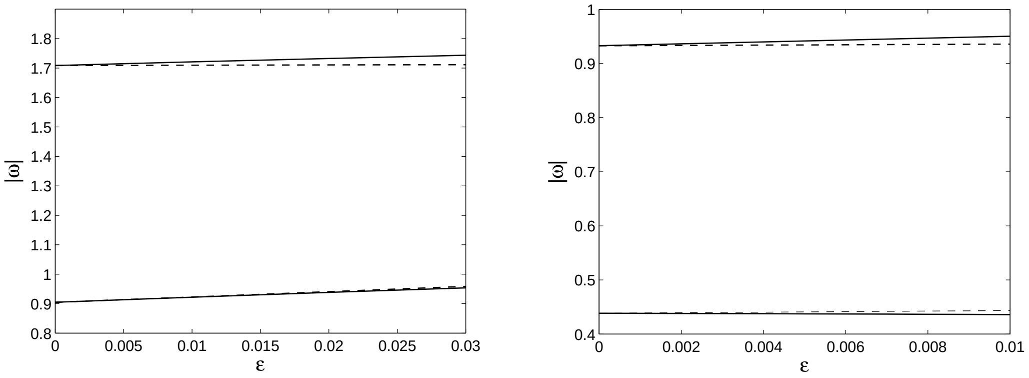

(a) $\alpha = 0.1$

(b) $\alpha = 0.465$

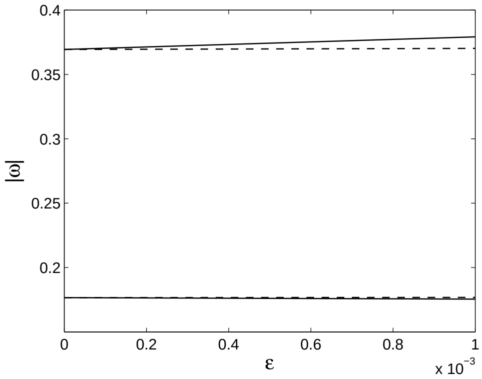

(c) $\alpha = 0.497$

Figure 3.13: Comparisons between two critical eigenvalues of intersite bright solitons III and IV obtained numerically (solid lines) and analytically (dashed lines) for values of α as shown in the caption. In panels (a) and (b), the upper and lower dashed curves correspond, respectively, to Eqs. (3.3.42) and (3.3.43), whereas in panel (c) they correspond to Eqs. (3.3.44) and (3.3.45).

fore and after a collision of one of the discrete eigenvalues which does not contribute to the instability of solitons. Interestingly, as shown in panel (c), such an eigenvalue also crosses the real axis at some critical ε as indicated by the empty circle. The latter condition, in fact, indicates a Hopf bifurcation, which occurs when the soliton is already in unstable mode. This is different from the previous discussions where the Hopf bifurcations also indicate the change of stability of solitons.

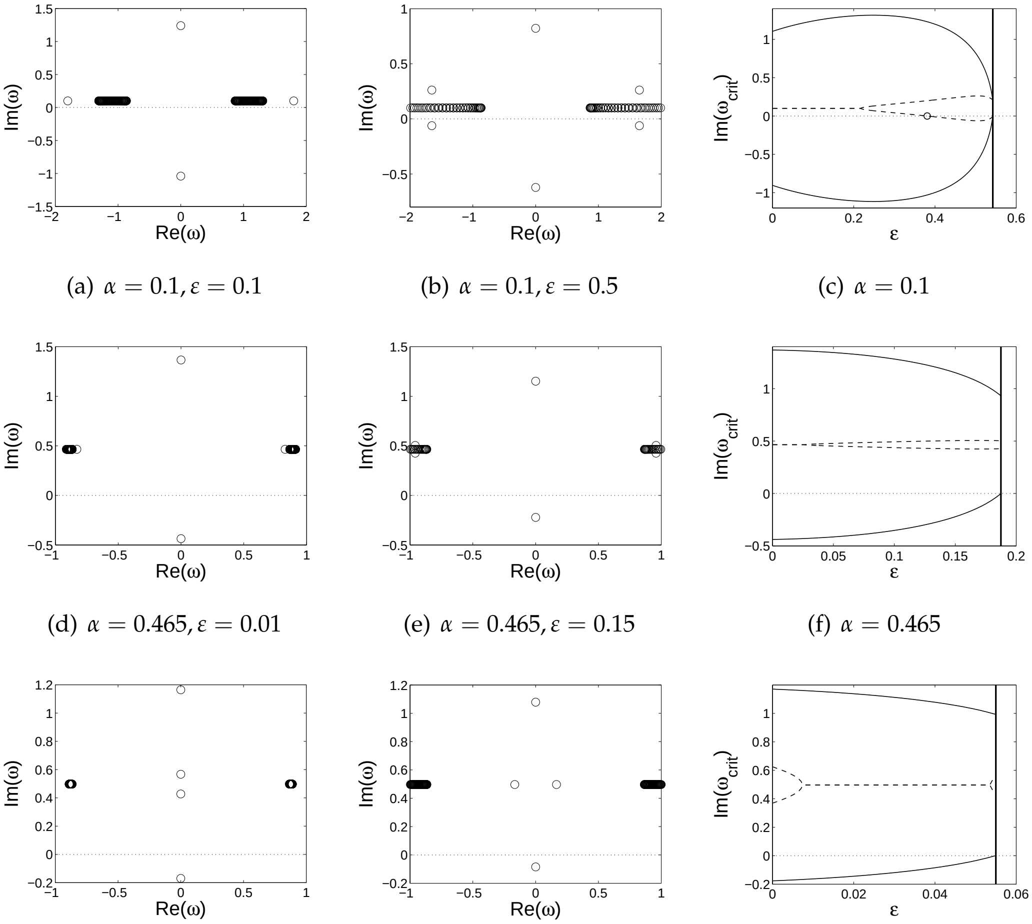

(a) $\alpha = 0.1, \varepsilon = 0.1$ (b) $\alpha = 0.1, \varepsilon = 0.5$ (c) $\alpha = 0.1$

(d) $\alpha = 0.465, \varepsilon = 0.01$ (e) $\alpha = 0.465, \varepsilon = 0.15$ (f) $\alpha = 0.465$

(g) $\alpha = 0.497, \varepsilon = 0.005$ (h) $\alpha = 0.497, \varepsilon = 0.04$ (i) $\alpha = 0.497$

Figure 3.14: (First and second columns) The structure of eigenvalues of intersite bright solitons type III and IV for parameter values (α, ε) as indicated in the caption. (Third column) The imaginary part of two critical eigenvalues (shown by solid and dashed lines) obtained by varying ε. The vertical lines indicate the limit points of ε up to which the soliton exists, i.e., when the minimum imaginary part of the eigenvalues becomes zero.

In Fig. 3.15 we present the (in)stability window for intersite bright solitons type III and IV which is defined as the area to the left of the solid line; this line represents the set of the branch points of pitchfork bifurcation in the (ε, α)-plane. From the figure, we conclude that the intersite type III and IV are always unstable. The area to the right of the solid line belongs to the unstable region of intersite type I. One can check that this line is exactly the same as the rightmost solid line in Fig. 3.10. In addition, the dashed line appearing in Fig. 3.15 depicts the occurrence of Hopf bifurcations. However, there is one special point indicated by the white-filled circle, at which the ε-derivative of the imaginary part of the corresponding critical eigenvalue is zero; this degenerate point will be discussed further in Section 3.5. The empty circle lying on the Hopf line reconfirms the corresponding point in panel (c) of Fig. 3.14.

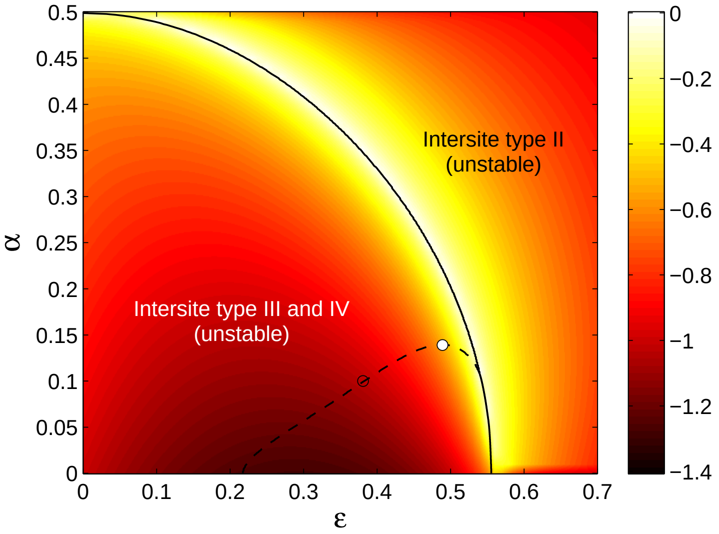

Figure 3.15: The (in)stability region of intersite bright solitons type III and IV in (ε, α)-space. The solid line indicates the branch-point line of pitchfork bifurcation. The dashed line represents the occurrence of Hopf bifurcations (with one degenerate point at the white-filled circle), which arises from one of the critical eigenvalues which does not contribute to the instability of solitons. The empty circle lying on the dashed line corresponds to that point depicted in panel (c) of Fig. 3.14.

3.4.2.4 Saddle-node and pitchfork bifurcation of intersite bright solitons

From both numerical and analytical results discussed above, we observed that the intersite type I and II have the same profile and stability when approaching $\alpha = \gamma$. This fact indicates the appearance of a saddle-node bifurcation undergone by the two solitons. Moreover, there also exists a pitchfork bifurcation experienced by the intersite type I, III and IV.

One can check that the norm of the intersite type III and IV is exactly the same for all parameter values so that this quantity can no longer be used for depicting a clear bifurcation diagram. Therefore, we now simply plot the value of $|u_0|^2$ for each solution, e.g., as a function of α and fixed $\varepsilon = 0.1$; this is shown in Fig. 3.16 where the numerics (solid lines) is obtained by a pseudo-arc-length method. As seen in the figure, the intersite type I, III and IV meet at a (pitchfork) branch point (BP) $\alpha \approx 0.49$. At this point, the stability of the intersite type I is switched. Furthermore, the intersite type I and II also experience a saddle-node bifurcation where they merge at a limit point (LP) $\alpha = \gamma = 0.5$. Just before this point, the intersite type I possesses one unstable eigenvalue, while the type II has two unstable eigenvalues. The two critical eigenvalues for the intersite type I and II then coincide at LP. We confirm that our analytical approximation for the value of $|u_0|^2$ is relatively close to the corresponding numerical counterpart.

Next, let us plot the value of $|u_0|^2$ for each soliton by fixing $\alpha = 0.1$ and varying ε (presented in Fig. 3.17). The pitchfork bifurcation experienced by the intersite type I (solid line), type III (upper dashed line) and type IV (lower dashed line) is clearly shown in the figure. The three solitons meet together at a branch point BP. We also depict in the figure the points at which Hopf bifurcations emerge (labelled by indexed H). For the shake of completeness, we also plot the relevant curve for the intersite type II (dotted line).

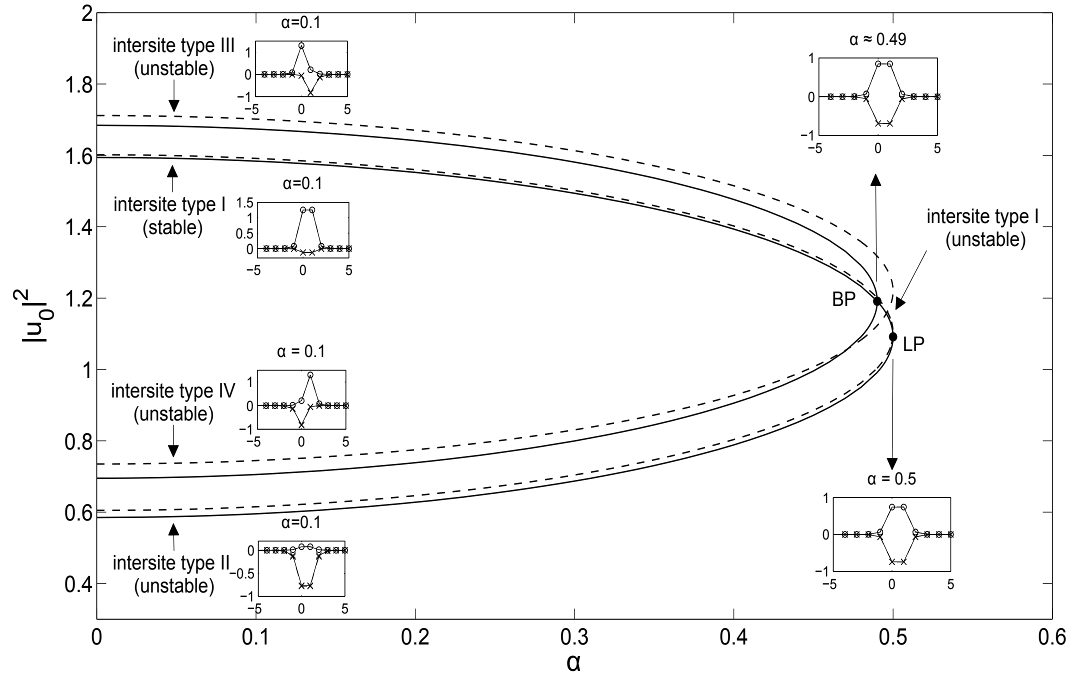

Figure 3.16: Saddle-node and pitchfork bifurcations of intersite bright solitons by varying α and fixing $\varepsilon = 0.1$. The curves depict the value of $|u_0|^2$ of each solutions obtained numerically (solid lines) and analytically (dashed lines). The profiles of the corresponding solutions at some values of α are shown in the relevant insets. The intersite type I, III and IV merge at a branch point (BP) $\alpha \approx 0.49$ and the intersite type I and II meet at a limit point (LP) $\alpha = \gamma = 0.5$.

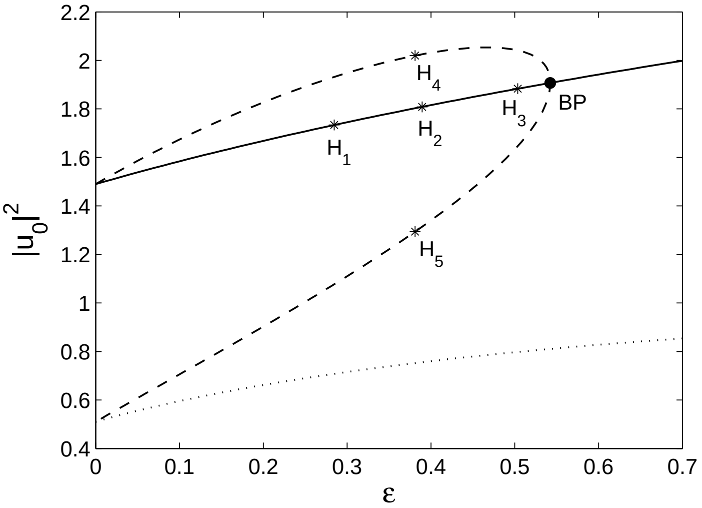

Figure 3.17: A pitchfork bifurcation of intersite bright solitons for fixed $\alpha = 0.1$ and varied ε. The curves represent the numerical value of $|u_0|^2$ for the corresponding solutions as a function of ε. The intersite type I (solid line), type III (upper dashed line) and type IV (lower dashed line) merge at a branch point (BP). The occurrence of Hopf bifurcation (H_i) is detected in intersite type I, III and IV. The dotted line corresponds to the intersite type II.

3.5 Nature of Hopf bifurcations and continuation of limit cycles

If there is only one pair of non-zero real eigenvalues and the other eigenvalues have strictly positive imaginary parts, a Hopf bifurcation also indicates the change of stability of the steady state solution. In this case, the periodic solutions bifurcating from the Hopf point coexist with either the stable or unstable mode of the steady state solution. If the periodic solutions coexist with the unstable steady state solution, they are stable and the Hopf bifurcation is called *supercritical*. On the other hand, if the periodic solutions coexist with the stable steady state solution, they are unstable and the Hopf bifurcation is called *subcritical*.

By applying, for example, the centre manifold theorem, we can generally determine the nature of a Hopf point ε_c through its first Lyapunov coefficient $l_1(\varepsilon_c)$ (see, e.g., Kuznetsov [115]); the Hopf bifurcation is subcritical iff $l_1(\varepsilon_c) > 0$ and supercritical iff $l_1(\varepsilon_c) < 0$.

To numerically calculate the first Lyapunov coefficient for a Hopf point and perform a continuation of the bifurcating limit cycle, we use the numerical continuation package Matcont. Due to the limitations of Matcont, we evaluate the soliton using 21 sites. In fact, this setting does not affect significantly the soliton behaviour compared to that used in the previous section.

In this section, we examine the nature of Hopf points and the stability of cycle continuations in onsite type I, intersite type I and intersite type III-IV.

3.5.1 Onsite type I

For this type of solution, in particular at $\alpha = 0.1$, we have one Hopf point, which occurs at $\varepsilon_c \approx 0.3077$ (see again panel (c) in Fig. 3.3). From Matcont, we obtain $l_1(\varepsilon_c \approx 0.3077) > 0$ which indicates that the Hopf point ε_c is subcritical and hence the limit cycle bifurcating from this point is unstable. A continuation of the corresponding limit cycle is given in Fig. 3.18(a). As the Hopf point in this case also indicates the change of stability of the stationary soliton, one can confirm that the bifurcating periodic solitons are unstable because they coexist with the stable onsite type I; this agrees with the computed first Lyapunov coefficient above (the instability will be clearly shown in the next section when we numerically evaluate its dynamics). Interestingly, the continuation of the limit cycle also experiences saddle-node and torus bifurcations, as indicated by the points labelled LPC (limit point cycle) and NS (Neimark-Sacker), respectively. The profile of a representative periodic soliton over one period is shown in Fig. 3.18(b), from which we clearly see the typical oscillation in the soliton amplitude.

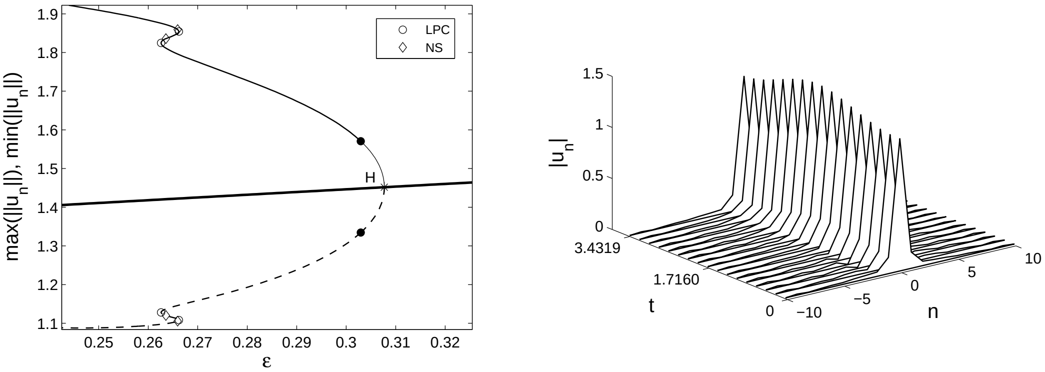

(a) (b)

Figure 3.18: (a) The continuation of the limit cycle from a Hopf point H for an onsite soliton type I with $\alpha = 0.1$. The first Lyapunov coefficient for H calculated by Matcont is positive, i.e., H is subcritical. The bold solid line represents the norm of the stationary soliton while the solid and dashed lines indicate, respectively, the maximum and minimum of the norm of the bifurcating periodic solitons. (b) The profile of a periodic soliton over one period ($T \approx 3.4319$) corresponding to the black-filled circle in panel (a).

From the previous discussion we have mentioned that there is one degenerate point for Hopf bifurcations in onsite type I, which is indicated by the white-filled circle in Fig. 3.4. In Fig. 3.19, we depict numerical continuations of periodic orbits of two Hopf bifurcations near the degenerate point. We obtained that the limit cycle branches bifurcating from the Hopf points are connected and form a closed loop. This informs us that as α approaches the critical value for a degenerate Hopf point, the "radius" of the loop tends to zero. Hence, one may conclude that at the double-Hopf point, there is no bifurcation of periodic orbits.

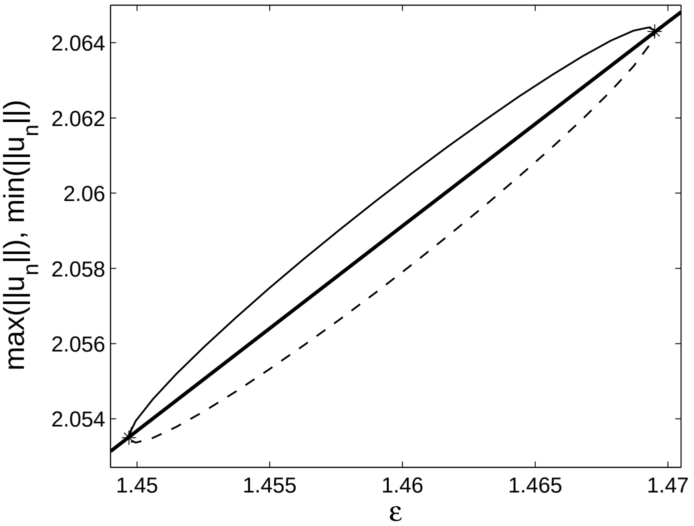

Figure 3.19: As Fig. 3.18(a) but for $\alpha = 0.492642$. Two Hopf points (stars) in the neighbourhood of the degenerate point (the while-filled circle in Fig. 3.4) are shown to be connected by a branch of limit cycles.

3.5.2 Intersite type I

In particular for $\alpha = 0.1$, there are three Hopf points detected for the intersite type I (see again Fig. 3.17). For point H_1 ($\varepsilon_c \approx 0.2782$), Matcont gives a negative value for the first Lyapunov coefficient, which means that the bifurcating periodic soliton is stable or H_1 is supercritical (we confirm the stability in the next section by examining its numerical evolution). The corresponding cycle continuation is presented in Fig. 3.20(a). As shown in the figure, the limit cycle bifurcating from H_1 coexist with the unstable mode of the (steady-state) intersite type I which confirms the supercritical H_1 (recall that the Hopf bifurcation in this case also indicates the change of stability of the soliton, i.e., it is stable (unstable) just below (above) $\varepsilon_c \approx 0.2782$ [see again Fig. 3.9(c)]). We also see from the figure that the cycle continuation contains NS, LPC and BPC (branch point cycle) points which indicate the occurrence of, respectively, torus, saddle-node and pitchfork bifurcations for limit cycle. The branches of the cycle continuation from the BPC point are shown in the figure. A representative periodic soliton (in one period) which occurs at one representative point along the cycle continuation is depicted in Fig. 3.20(b), which shows the oscillation between the two excited sites.

Next, for H_2 ($\varepsilon_c \approx 0.3871$) and H_3 ($\varepsilon_c \approx 0.4934$), the first Lyapunov coefficients given by Matcont are negative and positive valued, respectively. Thus, H_2 is supercritical while H_3 is subcritical, which implies that the limit cycles bifurcating from H_2 and H_3 are stable and unstable, respectively (confirmation of these stability findings through their numerical dynamics will be shown in the next section). The continuations of the corresponding limit cycles are shown in Fig. 3.21(a). From the figure, we see that the limit cycles bifurcating from H_2 and H_3 respectively coexist with the unstable and stable stationary intersite soliton type I. This fact is consistent with the nature of H_2 and H_3 as given by Matcont. In addition, as shown in the figure, a period-doubling (PD) bifurcation also occurs in the cycle continuation coming from H_3. This bifurcation seems to coincide with the turning point of cycle (LPC) which appears in the cycle continuation starting from H_2. The profile of one-period periodic solitons at the two representative points near H_2 and H_3 are presented in Figs. 3.21(b) and 3.21(c), respectively. We cannot see clearly the typical oscillation of the periodic soliton shown in the upper panel of Fig. 3.21(b) as it occurs very near to H_2. However by plotting the absolute value of the solution at site $n = 0$ and $n = 1$ over one period (see the lower panel of Fig. 3.21(b)), one can confirm the oscillation between the two excited sites. By contrast, the oscillation in the soliton amplitude is clearly visible in Fig. 3.21(c).

Similarly to the onsite type I, we also noticed the presence of a double-Hopf bifurcation in the intersite type I, i.e., the white-filled circle in Fig. 3.10. To investigate the point, we evaluate several Hopf points nearby the bifurcation point and perform numerical continuations for limit cycles, which are presented in Fig. 3.22. Unlike the case in the onsite type I, here the (non-degenerate) Hopf points are not connected to each other by a closed loop of a branch of limit cycles. As we observe this scenario at any Hopf point that is arbitrarily close (up to a numerical accuracy) to the degenerate (codimension 2) bifurcation, it indicates that at the double-Hopf point, there is a bifurcation of at least two branches of periodic solutions.

3.5.3 Intersite type III and IV

As intersite bright soliton type III and IV possess the same eigenvalue structures, the nature of the corresponding Hopf bifurcation and the stability of the continuation of each limit cycle will be the same as well. Therefore it is sufficient to devote our discus-

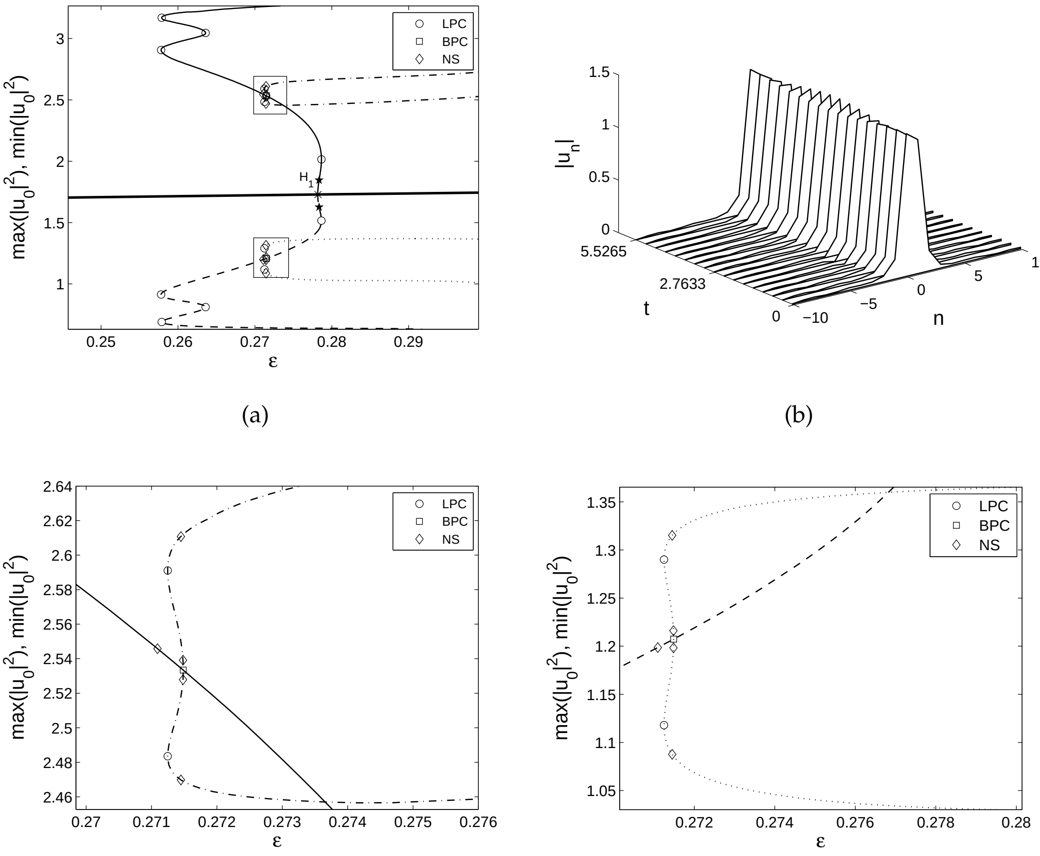

(a)

(b)

(c)

(d)

Figure 3.20: (a) The cycle continuation from Hopf point H_1 for intersite bright soliton type I with $\alpha = 0.1$. In this case, H_1 is supercritical. The bold solid line indicates the value of $|u_0|^2$ for the stationary soliton, which is the same as that shown in Fig. 3.17. The solid and dashed lines represent, respectively, the maximum and minimum value of $|u_0|^2$ for the bifurcating periodic solitons, which also experience a pitchfork cycle bifurcation. The branches of the cycle are depicted by the dash-dotted (maximum $|u_0|^2$) and dotted (minimum $|u_0|^2$) lines. (b) The profile of a periodic soliton over one period ($T \approx 5.5265$) corresponding to the star point in panel (a). (c,d) Enlargements of, respectively, the upper and the lower rectangles in panel (a).

.

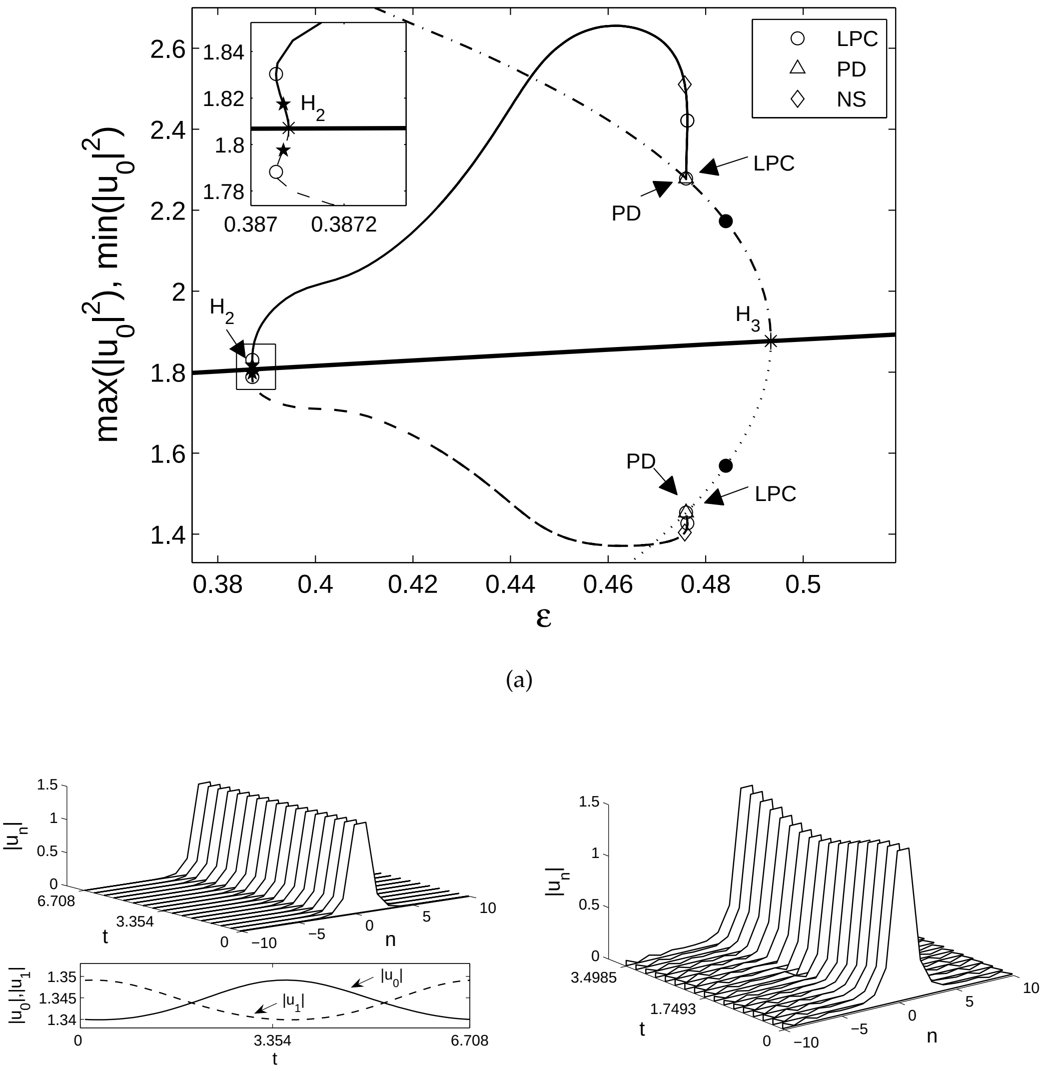

(a)

(b)

(c)

Figure 3.21: (a) As Fig. 3.20(a) but for H_2 and H_3, where the inset gives the zoom-in for the corresponding region showing that H_2 and H_3 are supercritical and subcritical, respectively. The bold solid line is the same as that shown in Fig. 3.17, i.e., representing the value of $|u_0|^2$ for the stationary intersite soliton. The solid (dashed) and dash-dotted (dotted) lines shows the maximum (minimum) value of $|u_0|^2$ for the periodic soliton which bifurcates from, respectively, H_2 and H_3. (b,c) The profile of periodic solitons over one period $T \approx 6.708$ and $T \approx 3.4985$ which corresponds, respectively, to the star and the black-filled circle in panel (a).

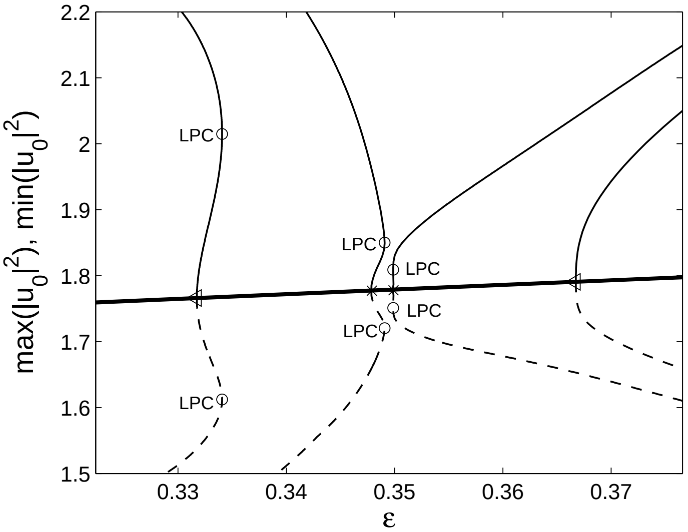

Figure 3.22: As Fig. 3.21(a) but for $\alpha = 0.108$ (triangles) and $\alpha = 0.11082$ (stars) in the proximity of the while-filled circle in Fig. 3.10.

sion to intersite type III only.

As shown in Fig. 3.17, there is one Hopf point, namely H_4, for the intersite type III at $\alpha = 0.1$. In this type of solution, the Hopf bifurcation occurs while other eigenvalues already give rise to instability; this is different from the type of Hopf bifurcation discussed previously. Therefore we cannot perform the analysis as before in determining the stability of the bifurcating periodic soliton. In fact, according to calculation given by Matcont, the first Lyapunov coefficient for H_4 is positive (subcritical), which means that the bifurcating periodic soliton is unstable. As shown in the next section, this instability will be confirmed through its time evolution.

Fig. 3.23(a) shows the continuation of the corresponding limit cycle from H_4. A representative one-period periodic soliton at ε near H_4 (indicated by the black-filled circle) is shown in Fig. 3.23(b), from which we can see clearly the oscillation in the amplitude of soliton.

Next, we study the double-Hopf bifurcation for the intersite type III-IV shown by the white-filled circle in Fig. 3.15. We present in Fig. 3.24 the continuation of the limit cycles from two Hopf points about the degenerate point, from which we see that they are connected to each other. Therefore, as for the case of the onsite type I, we argue that there is no bifurcation of periodic solutions at the degenerate point.

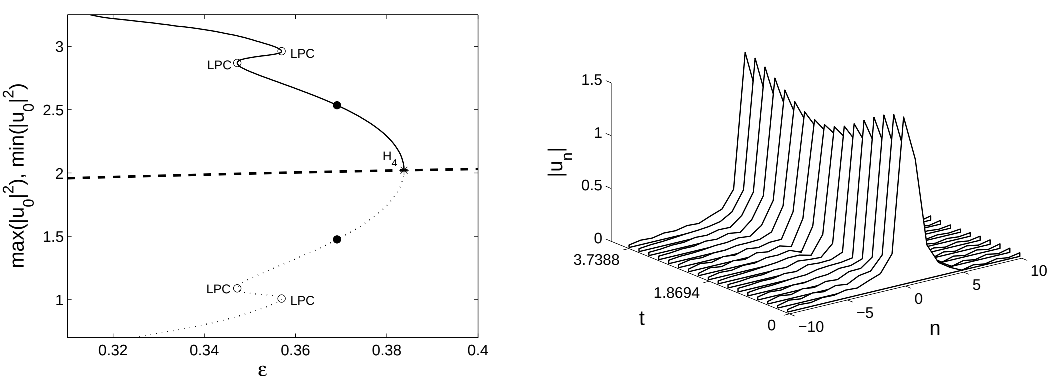

(a) (b)

Figure 3.23: (a) The cycle continuation from Hopf point H_4 for intersite bright soliton type III with $\alpha = 0.1$ showing that H_4 is subcritical. The dashed line shows the value of $|u_0|^2$ for the stationary soliton (the same as that shown in Fig. 3.17) while the solid and dotted lines represent, respectively, the maximum and minimum $|u_0|^2$ of the bifurcating periodic solitons. (b) The profile of a periodic soliton over one period $T \approx 3.7388$ corresponding to the black-filled circle in panel (a).

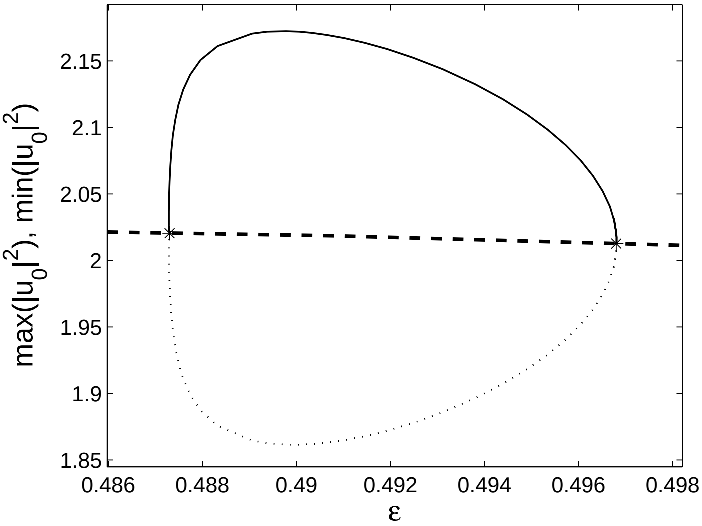

Figure 3.24: As Fig. 3.23(a) but for $\alpha = 0.1411$. The degenerate (Hopf-Hopf) point indicated as the while-filled circle in Fig. 3.15 is at $\varepsilon \approx 0.49$.

3.6 Numerical integrations

In this section, we confirm our stability findings through integrating numerically the time-dependent equation (3.1.1). To do so, we use a fourth-order Runge-Kutta method with the initial condition being the corresponding stationary soliton solution of equation (3.2.1). The numerical integration of Eq. (3.1.1) is also examined to confirm the stability findings for the bifurcating periodic solutions as discussed above.

3.6.1 Stationary solitons

Here we particularly examine the dynamics of the stationary solitons of which the initial profiles correspond to the eigenvalue structures depicted in the figures of Section 3.4. We show that the dynamics of the stable and unstable solitons are consistent with, respectively, the stability and instability mode of the corresponding eigenvalue structures.

We begin by evaluating the onsite soliton type I. The numerical evolution of this type of soliton is shown in Fig. 3.25. In the top right panel, the typical dynamics of the unstable soliton is in the form of oscillatory instability which decays and then vanishes completely. In contrast, the unstable soliton in the middle right panel evolves to a seemingly stable oscillatory solution.

In Fig. 3.26 we present the dynamics of the onsite soliton type II which was observed previously as being always unstable, except at $\alpha = \gamma$ (note that the linearised Eq. (3.1.1) has solutions of the form $\mathrm{e}^{(\gamma-\alpha)t}$, thus the stability of soliton when $\alpha = \gamma$ is basically due to a balance between damping and driving parameters). As shown in the left panel, the unstable soliton manifests itself in the form of oscillation in the centre of the soliton with different frequency and amplitude, which then becomes constant. Contrastingly, the typical instability of the unstable soliton in the right panel is in the form of soliton decay, which leads to the zero solution just after a short period of time.

Next, we examine the dynamics of the intersite bright soliton type I, which is illustrated in Fig. 3.27. In the middle and bottom right panels, we see that the unstable intersite soliton changes into an onsite soliton. By contrast, the unstable intersite soliton in the top right panel still preserves its two-excited-state nature but suddenly shifts to the next sites with different amplitude.

For intersite bright soliton type II, which was shown to be always unstable except at the point $\alpha = \gamma = 0.5$ and $\varepsilon = 0$, we present its time dynamics in Fig. 3.28 for two representative unstable solitons. As we see from the figure, the instability makes the

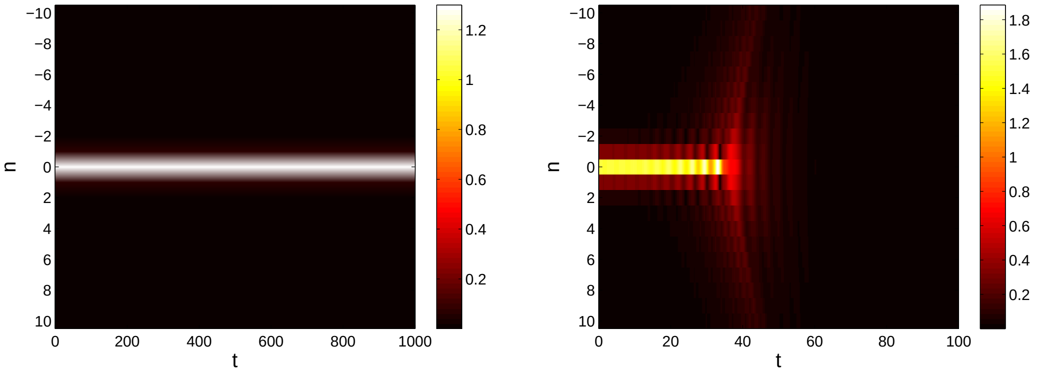

(a) $\alpha = 0.1, \varepsilon = 0.1$ (b) $\alpha = 0.1, \varepsilon = 0.5$

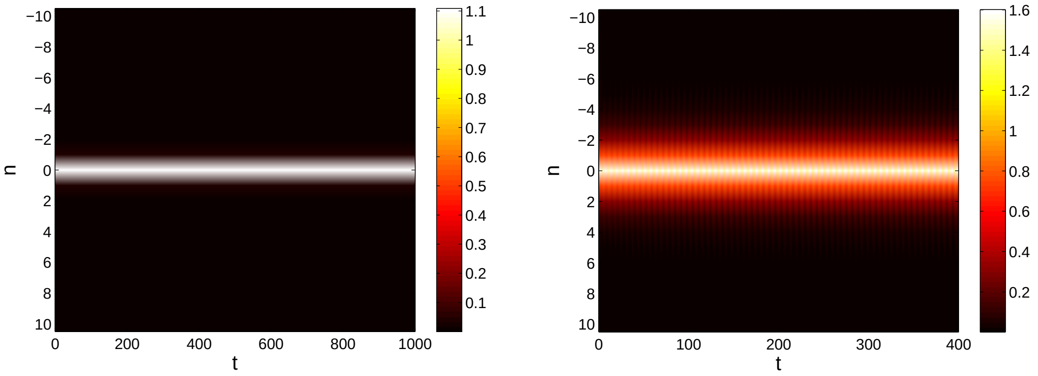

(c) $\alpha = 0.485, \varepsilon = 0.05$ (d) $\alpha = 0.485, \varepsilon = 1.2$

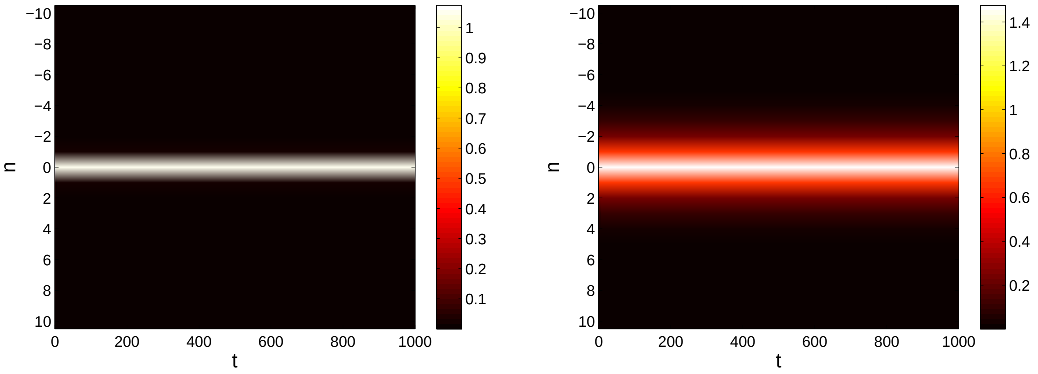

(e) $\alpha = 0.497, \varepsilon = 0.02$ (f) $\alpha = 0.497, \varepsilon = 1$

Figure 3.25: The time evolution of onsite bright soliton type I governed by the time-dependent equation (3.1.1). The parameter values are indicated in the caption of each panel, i.e., they correspond to the same parameters as those in the left and middle panels of Fig 3.3. The contour plot indicates the value of $|\phi_n|$.

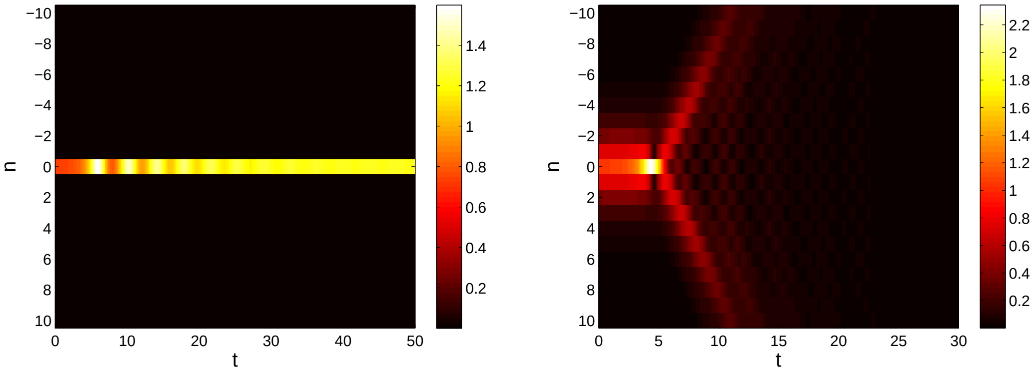

(a) $\alpha = 0.1, \varepsilon = 0.01$ (b) $\alpha = 0.1, \varepsilon = 1$

Figure 3.26: As Fig. 3.25, but for onsite type II. The eigenvalue structure of the initial profile in each panel is shown in Fig. 3.6.

soliton change its profile into an onsite mode (left panel) or decay (right panel).

Finally, we present the numerical evolution of intersite soliton type III-IV in Fig. 3.29. We have confirmed the instability of this soliton in the previous discussion. All the typical dynamics of the unstable soliton presented in Fig. 3.29 are in the form of loss of its asymmetry, i.e., each soliton turns into a symmetric intersite soliton just after a short time.

3.6.2 Periodic solitons

In this section, we examine the dynamics of the time-dependent Eq. (3.1.1) for the periodic solitons which arise at the corresponding Hopf bifurcations experienced by the onsite type I, intersite type I and intersite type III-IV. The time evolution of the periodic solitons whose profiles were depicted in the corresponding figures in Section 3.5 is presented in Fig. 3.30. From the figure, we can confirm the relevance of the stability of the periodic solitons investigated in Section 3.5. The typical dynamics of the unstable periodic solitons is in the form of breather destruction which eventually leads to zero solution. For periodic intersite soliton type III and IV [panel (e)], this destruction happens after just a short time.

3.7 Conclusion

In this chapter, we have considered a parametrically driven damped discrete nonlinear Schrödinger (PDDNLS) equation. The existence and stability of fundamental discrete bright solitons have been examined analytically through a perturbation theory for

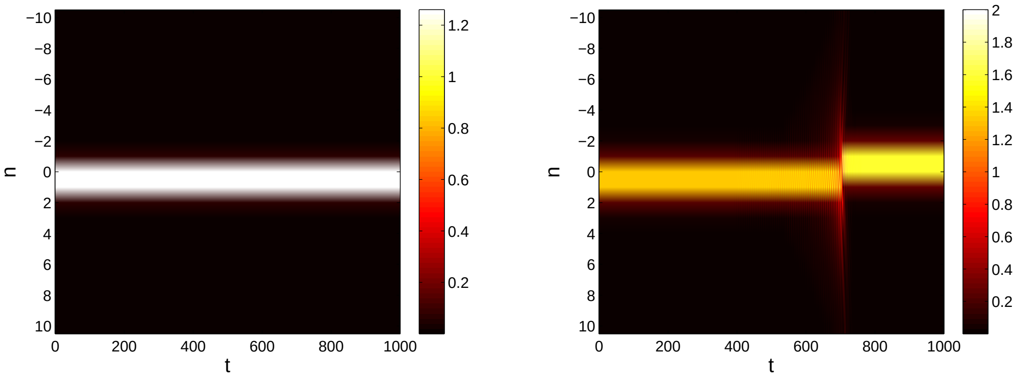

(a) $\alpha = 0.1, \varepsilon = 0.08$ (b) $\alpha = 0.1, \varepsilon = 0.35$

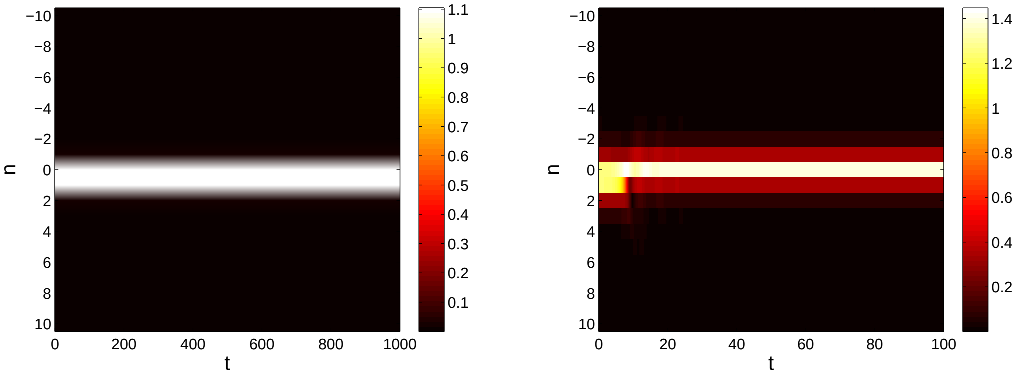

(c) $\alpha = 0.465, \varepsilon = 0.02$ (d) $\alpha = 0.465, \varepsilon = 0.5$

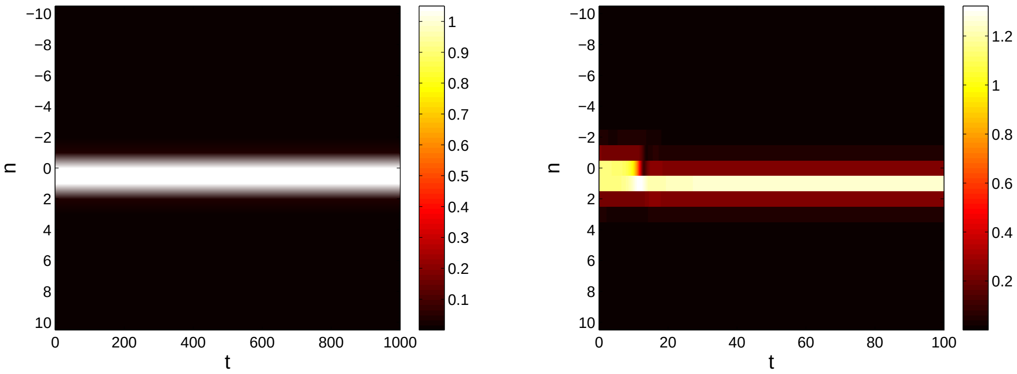

(e) $\alpha = 0.497, \varepsilon = 0.04$ (f) $\alpha = 0.497, \varepsilon = 0.3$

Figure 3.27: As Fig. 3.25, but for intersite type I with the same parameter values as those in the left and middle panels of Fig. 3.9.

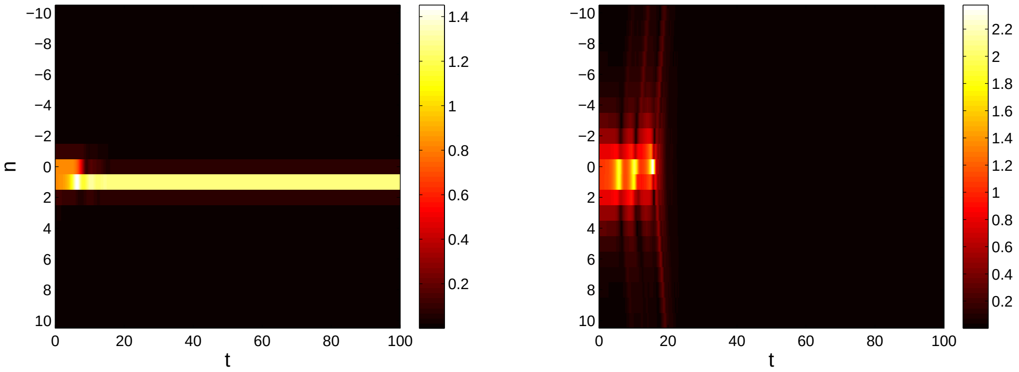

(a) $\alpha = 0.3, \varepsilon = 0.1$

(b) $\alpha = 0.3, \varepsilon = 2$

Figure 3.28: As Fig. 3.25, but for intersite bright soliton type II. The initial profile in each panel has the corresponding eigenvalue structure depicted in Fig. 3.12.

small ε and then corroborated by numerical calculations. We showed that there are two types of onsite discrete soliton, namely onsite type I and II. For onsite type I, we found an interval in α for which the soliton is stable for any coupling constant, i.e., a damping can re-stabilise a driven onsite soliton. Contrastingly, the onsite type II was found to be always unstable for all ε. These two solitons experience a saddle-node bifurcation with the limit point $\alpha = \gamma$ for any ε.

We also showed that there are four types of intersite discrete soliton, called intersite type I, II, III and IV. In fact, intersite type III and IV are essentially considered as one solution due to its symmetry. We obtained that intersite type I in the region of instability in the non-dissipative case can be stabilised by damping while intersite type II and III-IV are always unstable. A saddle-node bifurcation, as for the onsite soliton, was found to be undergone by intersite type I and II. Moreover, we also obtained that intersite type I, III and IV experience a pitchfork bifurcation. The branch points of such a bifurcation in the (ε, α)-plane have been calculated numerically.

More interestingly, we observed that Hopf bifurcation also occurs in onsite type I, intersite type I and intersite type III-IV, which confirms the existence of the corresponding periodic solitons (limit cycles) in the PDDNLS equation. The continuation of the limit cycles as well as the stability of the periodic solitons have been demonstrated numerically using the numerical continuation software Matcont. In particular, subcritical Hopf bifurcations for onsite type I and intersite type III-IV were observed. Moreover, we obtained three Hopf bifurcations for intersite type I. It was shown that two of these points generate stable periodic solitons, i.e., the bifurcations are supercritical. The relevance of the stability findings has been confirmed through numerical integrations of

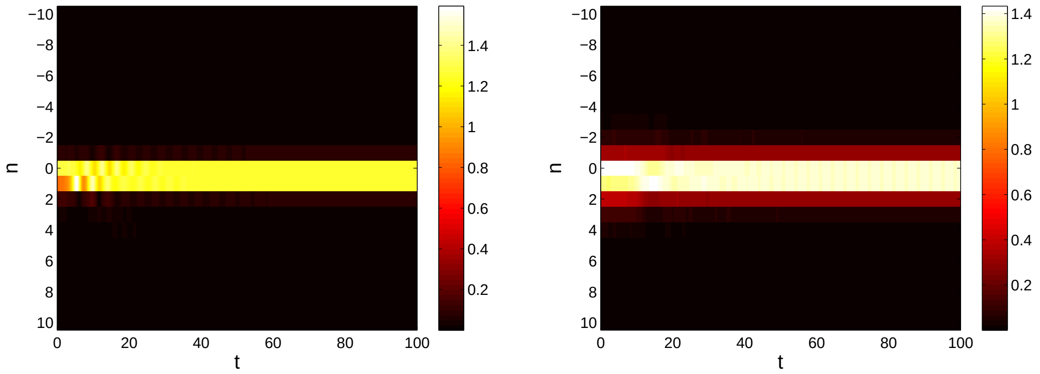

(a) $\alpha = 0.1, \varepsilon = 0.1$ (b) $\alpha = 0.1, \varepsilon = 0.5$

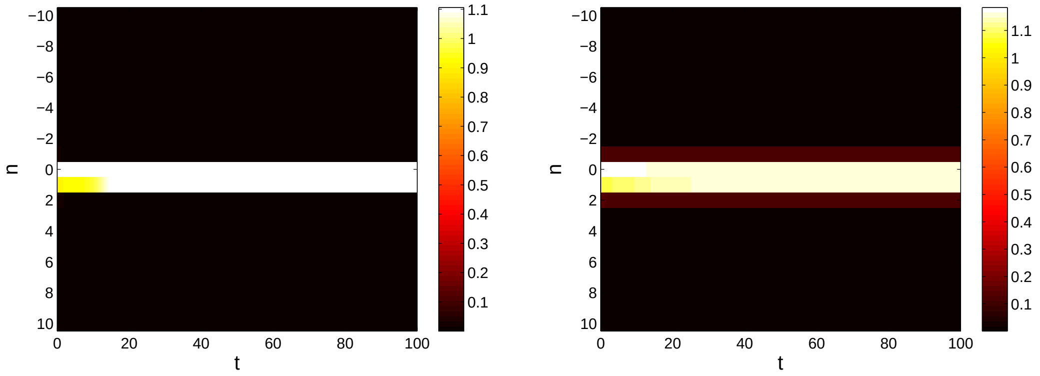

(c) $\alpha = 0.465, \varepsilon = 0.01$ (d) $\alpha = 0.465, \varepsilon = 0.15$

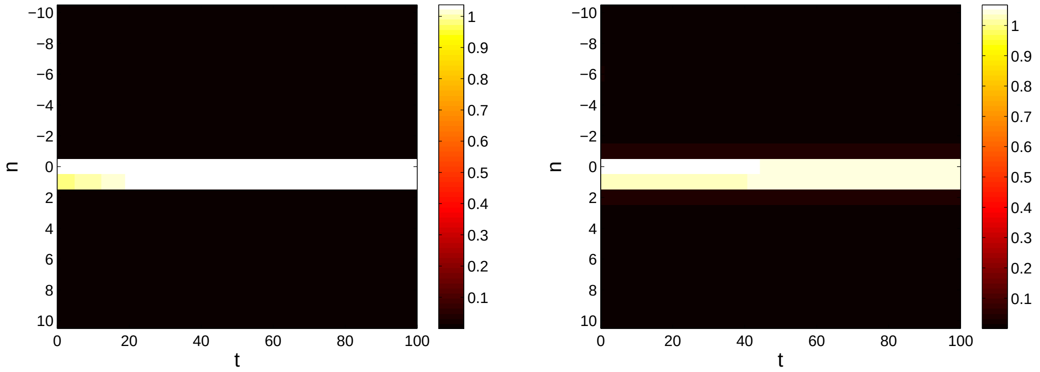

(e) $\alpha = 0.497, \varepsilon = 0.005$ (f) $\alpha = 0.497, \varepsilon = 0.04$

Figure 3.29: As Fig. 3.25, but for intersite type III and IV. The dynamics of all unstable solitons presented here corresponds to the unstable mode of the eigenvalue structures in Fig. 3.14.

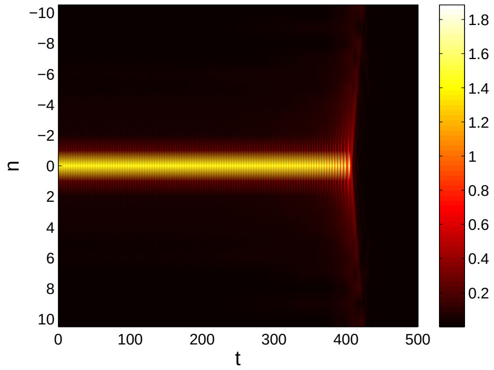

(a) Onsite type I

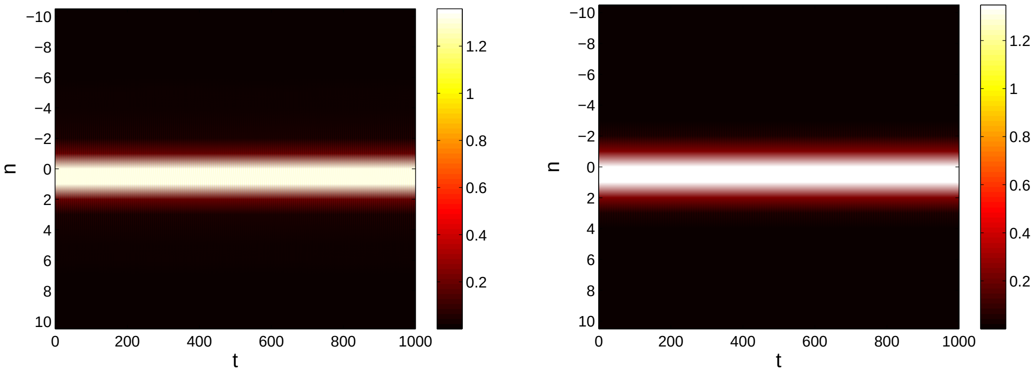

(b) Intersite type I, H_1

(c) Intersite type I, H_2

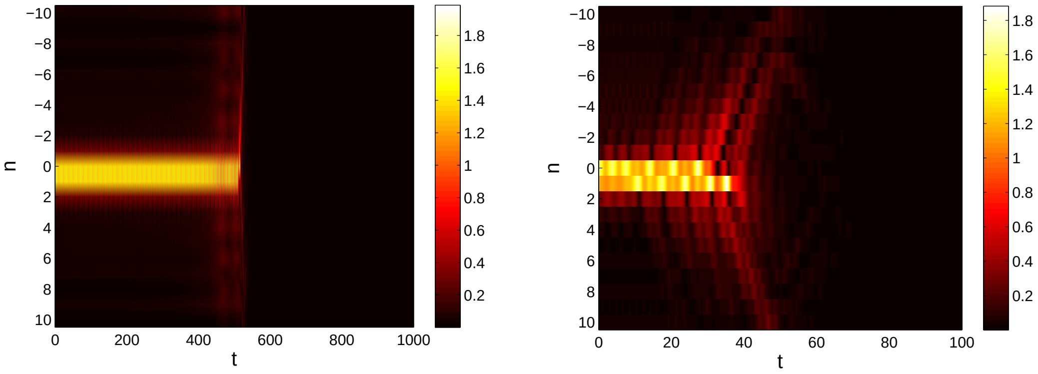

(d) Intersite type I, H_3

(e) Intersite type III-IV

Figure 3.30: The time dynamics of Eq. (3.1.1) for periodic solitons bifurcating from the Hopf bifurcation of onsite type I, intersite type I and intersite type III-IV. The initial profile in panels (a)-(f) corresponds to the profile of the periodic soliton depicted in Figs. 3.18(b), 3.20(b), 3.21(b), 3.21(c) and 3.23(b), respectively. The contour plots show the value of $|\phi_n|$.

the time-dependent PDDNLS equation for both stationary and periodic solitons.

CHAPTER 4

Travelling solitons in a discrete nonlinear Schrödinger equation with saturable nonlinearity

In the last two chapters, we have dealt with the discrete nonlinear Schrödinger (DNLS) equation with cubic nonlinearity by introducing the effect of parametric driving and/or damping. In this chapter, our study is devoted to another type of DNLS systems characterised by the so-called saturable nonlinearity. While the study in Chapters 2 and 3 is particularly concerned with standing wave solutions, here we focus our attention on travelling waves of the lattice system.

4.1 Introduction

One of the major issues in studies of spatially discrete systems is whether such systems can support solitary waves that travel without losing energy to radiation, which results in deceleration and eventually pinning of the solitons. The celebrated Peierls-Nabarro (PN) barrier [63, 64] is the reason that discrete systems do not generically support exponentially localised travelling solitary waves. The barrier corresponds to the energy difference between the onsite- and the intersite-centred lattice solitons, with the latter usually having a higher energy.

The first attempt at finding travelling solitons in lattice system modelled by a discrete nonlinear Schrödinger (DNLS) equation was undertaken by Eilbeck [116], followed by a more systematic study by Feddersen [117] and Duncan *et al.* [118]. The latter works indicate that travelling lattice solitons in the DNLS system are accompanied by nonzero-radiation tails, which was confirmed by more recent studies (see, e.g., Gómez-

Gardeñes *et al.* [68, 119], Melvin *et al.* [69] and Pelinovsky *et al.* [120]).

While the most typical onsite nonlinearity in DNLS models is cubic, waveguiding arrays made of photorefractive materials feature the saturable nonlinearity. Under appropriate conditions, the saturable nonlinearity may be approximated by a truncated polynomial nonlinearity, e.g., a cubic–quintic truncation. One- and two-dimensional (1D and 2D) solitons in the DNLS with the cubic–quintic onsite nonlinearity have also been studied in some detail (see, e.g., Carretero-González *et al.* [81] and Chong *et al.* [121]).

It was found that the saturable nonlinearity readily supports travelling solitons in discrete media (Hadžievski *et al.* [65] and Vicencio & Johansson [122]). A reason for this property is the fact that the PN barrier can change its sign in the case of the saturable nonlinearity [65], hence the barrier may vanish at isolated points (see the relevant discussion about this in Section 1.4.3). This property may be essential in finding lattice solitary waves that can travel permanently without emitting radiation (lattice phonons).

4.1.1 The considered model and preliminary analyses

The saturable DNLS equation modelling the propagation of optical waves in a photorefractive medium is

$$\mathrm{i}\frac{\mathrm{d}\phi_n}{\mathrm{d}t} = -\varepsilon\Delta_2\phi_n(t) - \Lambda\phi_n(t) + \frac{\sigma\phi_n(t)}{1+|\phi_n(t)|^2}, \tag{4.1.1}$$

where, as in the previous governing equations in Chapters 2 and 3, ϕ_n is a complex-valued wave function at site n, ε is the strength of the coupling between adjacent sites, $\Delta_2\phi_n(t) = \phi_{n+1}(t) - 2\phi_n(t) + \phi_{n-1}(t)$ is the 1D discrete Laplacian, Λ is a background frequency and σ is the nonlinearity coefficient. We note that the transformation

$$t \to t/\sigma, \quad \varepsilon \to \sigma\varepsilon, \quad \Lambda \to \sigma\Lambda \tag{4.1.2}$$

allows us to replace σ in Eq. (4.1.1), without loss of generality, by 1, implying that the onsite nonlinearity is self-focusing provided that $\varepsilon > 0$.

To study travelling-wave solutions of Eq. (4.1.1), an ansatz of the form

$$\phi_n(t) = \psi(z,\tau), \tag{4.1.3}$$

with $z = n - ct$ and $\tau = t$, is substituted into the equation to yield the time-dependent advance–delay-differential equation

$$\begin{aligned} -\mathrm{i}c\psi_z(z,\tau) + \mathrm{i}\psi_\tau(z,\tau) &= (2\varepsilon-\Lambda)\psi(z,\tau) - \varepsilon\left[\psi(z+1,\tau)+\psi(z-1,\tau)\right] \\ &\quad + \frac{\psi(z,\tau)}{1+|\psi(z,\tau)|^2}, \end{aligned} \tag{4.1.4}$$

where c is the velocity. Travelling-wave solutions of Eq. (4.1.1) can be sought using the time-independent version of Eq. (4.1.4),

$$-\mathrm{i}c\psi' = (2\varepsilon - \Lambda)\psi(z) - \varepsilon\left[\psi(z+1) + \psi(z-1)\right] + \frac{\psi(z)}{1 + |\psi(z)|^2}, \tag{4.1.5}$$

with $\psi' \equiv \frac{\mathrm{d}\psi}{\mathrm{d}z}$.

Eq. (4.1.5) admits the existence of rotational and translational invariance under transformations

$$\psi \to \psi e^{\mathrm{i}\theta}, \quad \theta \in \mathbb{R}, \tag{4.1.6}$$

and

$$\psi(z) \to \psi(z + \tilde{z}), \quad \tilde{z} \in \mathbb{R}, \tag{4.1.7}$$

respectively. However, our attention is focused on the fundamental single hump soliton solutions of Eq. (4.1.5). Therefore we will look for solutions that are invariant under the reversing symmetry

$$z \to -z, \quad \psi \to \psi^*, \tag{4.1.8}$$

where the asterisk denotes complex conjugation. From this reversibility property, we may construct a soliton solution whose real part is an even function whereas the imaginary part is odd, and thus $\psi(0)$ is real.

4.1.2 Previous works on the saturable DNLS model

In the particular case of $\sigma = \Lambda$, exact stationary solutions of Eq. (4.1.1) including the soliton solutions have been derived by Khare *et al.* [123, 124]. The stability of the obtained solutions was also discussed therein, and the solutions were shown numerically to be linearly stable in most cases. Moreover, the stationary onsite and intersite dark solitons in the defocusing case of Eq. (4.1.1), i.e., when $\Lambda < 0$ and $\sigma < 0$, have also been considered by Fitrakis *et al.* [86] by using an anticontinuum (AC) limit approach. In the latter reference, it was shown that the onsite solutions are stable for small values of ε, while the intersite solutions are always unstable.

The existence of travelling solitons for the saturable DNLS was investigated numerically by Melvin *et al.* [66, 67] by solving Eq. (4.1.5) using a pseudo-spectral method, which yielded weakly delocalised solitary waves, i.e., the solutions are accompanied by nonzero oscillating tails. Genuinely localised pulse-like solutions were then generated by finding zeros of an appropriately defined measure of the tail amplitude. The idea of identifying truly localised solutions from the "tail condition" is similar to that used by Yang *et al.* [125]. In the later reference, the term *embedded solitons* (ESs) was introduced for the first time for such solutions, which we will explain later. In Melvin *et* *al.* [66], the stability of the obtained solutions was analysed numerically by calculating the Floquet multipliers of the solutions, using methods similar to that developed by Gómez-Gardeñes *et al.* [119].

The presence of genuinely travelling lattice solitons in the saturable DNLS in the strong-coupling case has been shown analytically by Oxtoby and Barashenkov, using exponential asymptotic methods [126] (see also Melvin *et al.* [69]). The use of this sophisticated technique is necessary, as the radiation emitted by moving solitary waves is exponentially small in the wave's amplitude. This is a reason why broad, small-amplitude pulses in weakly coupled systems or lattice solitons in strongly coupled systems are highly mobile, seeming like freely travelling solitons.

4.1.3 Overview

In this chapter, we revisit the study of the existence and stability of travelling solitary waves in the saturable DNLS (4.1.1), which, as pointed out in the previous section, has been discussed and solved numerically by Melvin *et al.* [66, 67]. Here we use a different approach in both our numerical and analytical methods.

To examine the existence of the travelling solitary waves, following Melvin *et al.* [66, 67], first we need to solve the linear spectrum of Eq. (4.1.5); we perform this both numerically and analytically using a perturbation expansion. The analysis leads us to produce the diagram of the spectral bands from which we can identify the parameter regions where a single resonance of the travelling solutions with plane waves occurs, and thus finding isolated solutions with vanishing tails by varying one parameter only within this regions becomes possible.

Next, to solve numerically Eq. (4.1.5) within the single-resonance parameter regions, instead of using a pseudo spectral method as implemented by Melvin *et al.* [66, 67], we propose an alternative scheme based on the discretization of Eq. (4.1.5). This discretization results in a system of difference equations which is then solved using a Newton–Raphson method.

The numerically obtained soliton solutions in our scheme, as in Melvin *et al.* [66, 67], are generally accompanied by oscillatory tails with a non-vanishing amplitude. Therefore, to find solutions with non-oscillatory tails, as suggested in the latter references, we need to add an extra tail condition. For this condition we consider either the measure modified from that proposed by Melvin *et al.* [66, 67] or our alternative measure. All of our numerical findings are then benchmarked against those in [66], confirming the robustness of the results. However, we find that our numerical method is not accurate to examine the stability of solitons as the calculation of the corresponding eigenvalue problem by means of our alternative scheme gives spurious unstable eigenvalues. This is in contrast to the numerical results of [66], where the solitons were reported to be linearly stable.

Moreover, we apply the variational approximation (VA) to study travelling solitary waves and their stability analytically. The VA is also derived to predict the location of ESs, i.e., the genuinely localised travelling solitary waves. The VA was applied to construct fundamental discrete soliton solutions in the DNLS equation with cubic nonlinearity as well as in other variants of DNLS models (see Section 1.4.4.3 for a review of the previous works which implemented the VA).

The chapter is organised as follows. In Section 4.2, we discuss the linear spectrum of the advance–delay equation (4.1.5), and a perturbation expansion is performed to obtain analytical approximations for the spectral bands. In Section 4.3, we introduce our numerical scheme for solving Eq. (4.1.5) and then benchmark our results against those obtained by Melvin *et al.* [66]. Next, in Section 4.4, we develop the VA for the solitary-wave solutions of the advance-delay equation. In the same section, we derive an analytical function whose zeros correspond to the location of ESs. The use of the VA in analysing the stability of the travelling solitary waves is also discussed in the section. In addition to saturable model, for comparison purposes, we also derived in Section 4.4 the similar variational formulations for a polynomial DNLS equation. Comparisons of our findings obtained from the VA with the corresponding numerical results are then presented in Section 4.5. Moreover, we address in Section 4.6 the failure of our numerical scheme in examining the stability of the solitons. Finally, we summarise our results in Section 4.7.

4.2 Dispersion relations

As discussed by Melvin *et al.* [66, 67], travelling solitary waves of the saturable DNLS are in general accompanied by nonzero oscillating tails, i.e., Λ will always resonate with the system's linear spectral (phonon) band. Because of this, a genuinely travelling solitary wave is *embedded* into the continuous spectrum, which appears as an exceptional solution. For that reason, such a solution is called an "embedded soliton" (ES). Therefore, in order to find localised solutions, it is necessary to minimise such resonances.

The frequency of the oscillating tail can be obtained by substituting

$$\psi(z) = \mathrm{e}^{\mathrm{i}\lambda z} \tag{4.2.1}$$

into the linear part of Eq. (4.1.5), i.e.,

$$\mathrm{i}c\psi' + (2\varepsilon - \Lambda + 1)\,\psi(z) - \varepsilon\,[\psi(z+1) + \psi(z-1)] = 0, \tag{4.2.2}$$

which then yields

$$F \equiv c\lambda + (\Lambda - 1) - 2\varepsilon\,(1 - \cos(\lambda)) = 0. \tag{4.2.3}$$

There is always at least one real value of λ satisfying this equation. To minimise the resonances, one needs to find a region in parameter space in which Eq. (4.2.3) has only one root with $\lambda > 0$. To find such a region efficiently, we need to solve Eq. (4.2.3) simultaneously with the condition for the (dis)appearance of a double root ($\mathrm{d}F/\mathrm{d}\lambda = c - 2\varepsilon\sin(\lambda) = 0$), i.e.,

$$\lambda = \lambda_+ \equiv 2m\pi + \arcsin\left(\frac{c}{2\varepsilon}\right),\ \lambda = \lambda_- \equiv (2m+1)\pi - \arcsin\left(\frac{c}{2\varepsilon}\right), \tag{4.2.4}$$

with integer m. These roots produce curves separating regions with different numbers of roots. Equations (4.2.3) and (4.2.4) have been solved numerically and analysed by Melvin *et al.* [66, 67]. In the following, we will solve Eqs. (4.2.3) and (4.2.4) analytically, using perturbation expansions.

When $|c| \ll 1$, $\varepsilon = \mathcal{O}(1)$, and $\lambda = \lambda_+$, Eq. (4.2.3) yields

$$\Lambda = 1 - 2m\pi c - (4\varepsilon)^{-1}\,c^2 + \mathcal{O}(c^3). \tag{4.2.5}$$

Omitting the terms of $\mathcal{O}(c^3)$, we may solve Eq. (4.2.5) for c, to give

$$c_{s,1} = -4m\pi\varepsilon \pm 2\sqrt{(2m\pi\varepsilon)^2 - (\Lambda - 1)\varepsilon}, \tag{4.2.6}$$

which is meaningful only when $\Lambda \leq (2m\pi)^2\varepsilon + 1$. In particular, one needs $\Lambda \leq 1$ to ensure that Eq. (4.2.6) is valid for all n and ε. For $\Lambda < 1$, taking the plus and minus signs in Eq. (4.2.6) will, respectively, make $c_{s,1}$ positive and negative, while taking the plus sign in Eq. (4.2.6) will make $c_{s,1} = 0$ for $\Lambda = 1$.

With the same small parameter (c), but now $\lambda = \lambda_-$, the solution of Eq. (4.2.3) is given by

$$\Lambda = 1 + 4\varepsilon - (2m+1)\pi c + (4\varepsilon)^{-1}\,c^2 + \mathcal{O}(c^3). \tag{4.2.7}$$

Eq. (4.2.7), after omission of the terms of $\mathcal{O}(c^3)$, may also be solved for c, to yield

$$c_{s,2} = 2(2m+1)\pi\varepsilon \pm 2\sqrt{((2m+1)\pi\varepsilon)^2 - 4\varepsilon^2 + (\Lambda - 1)\varepsilon}, \tag{4.2.8}$$

provided that $\Lambda \geq (4-(2m+1)^2\pi^2)\varepsilon + 1$. Note that setting $\Lambda \leq 1$ in the above equation will result in $c_{s,2}$ being non-negative for all m and ε.

Together, $c_{s,1}$ and $c_{s,2}$ are defined for all m and $\Lambda \leq 1$ if

$$\varepsilon \geq \varepsilon_1 \equiv \frac{1-\Lambda}{(2m+1)^2\pi^2-4}. \tag{4.2.9}$$

Furthermore, our analysis shows that $c_{s,1} = c_{s,2}$ when either $\varepsilon = \varepsilon_2$ or $\varepsilon = \varepsilon_3$, where

$$\varepsilon_2 = \frac{\left(-4+\pi^2+4\pi^2 m - \sqrt{\pi^2(\pi^2-8)(4m+1)^2}\right)(1-\Lambda)}{8(1+8m^2\pi^2+2\pi^2 m)}, \tag{4.2.10}$$

$$\varepsilon_3 = \frac{\left(-4+\pi^2+4\pi^2 m + \sqrt{\pi^2(\pi^2-8)(4m+1)^2}\right)(1-\Lambda)}{8(1+8m^2\pi^2+2\pi^2 m)}, \tag{4.2.11}$$

which then gives the following two possible relations,

1. $c_{s,1} \leq c_{s,2}$ if either $\varepsilon \in [\varepsilon_1, \varepsilon_2]$ or $\varepsilon \in [\varepsilon_3, \infty)$,
2. $c_{s,1} > c_{s,2}$ if $\varepsilon \in (\varepsilon_2, \varepsilon_3)$.

In practice, since ε is assumed to be of $\mathcal{O}(1)$, we should choose $c_{s,1}$ and $c_{s,2}$ defined for $\varepsilon \in [\varepsilon_3, \infty)$.

Another case in which useful asymptotic progress may be made is where $|c| \ll 1$ and $0 < \varepsilon \ll 1$. Substituting $\lambda = \lambda_+$ into Eq. (4.2.3) and expanding quantities in terms of ε yields, for $m \neq 0$,

$$\Lambda = 1 - \Lambda_1\varepsilon^2, \quad c = \frac{\Lambda_1\varepsilon^2}{2m\pi} - \frac{\Lambda_1^2\varepsilon^3}{4(2m\pi)^3} + \mathcal{O}(\varepsilon^4). \tag{4.2.12}$$

Eliminating Λ_1 from Eq. (4.2.12) for c then yields the approximate relation

$$c_{l,1} = \frac{1-\Lambda}{2m\pi} - \frac{(1-\Lambda)^2}{4\varepsilon(2m\pi)^3}. \tag{4.2.13}$$

For $m = 0$, substituting $\lambda = \lambda_+$ into Eq. (4.2.3) gives instead the expansions

$$\Lambda = 1 - \Lambda_1\varepsilon^3, \quad c = \pm\left(2\sqrt{\Lambda_1}\varepsilon^2 - \frac{\Lambda_1^{3/2}\varepsilon^4}{12} + \mathcal{O}(\varepsilon^6)\right). \tag{4.2.14}$$

This time, eliminating Λ_1 from Eq. (4.2.14) for c yields the approximate relations

$$c_{l,2} = \pm\left(2\sqrt{1-\Lambda}\sqrt{\varepsilon} - \frac{1}{12\sqrt{\varepsilon}}(1-\Lambda)^{3/2}\right), \tag{4.2.15}$$

which is defined only for $\Lambda \leq 1$. One may readily check that, for $\Lambda < 1$, the plus and minus sign in the above equation correspond, respectively, to positive and negative $c_{l,2}$, whereas for $\Lambda = 1$ it follows that $c_{l,2} = 0$.

Next, for the same small parameter (c), but with $\lambda = \lambda_-$, we obtain from Eq. (4.2.3)

$$\Lambda = 1 + \Lambda_1 \varepsilon, \quad c = c_1 \varepsilon + \mathcal{O}(\varepsilon^2), \tag{4.2.16}$$

for $m \neq 0$ and for c_1 satisfying

$$-c_1 \arcsin\left(\frac{c_1}{2}\right) + (2m+1)\pi c_1 + \Lambda_1 - 2 - \sqrt{4 - c_1^2} = 0. \tag{4.2.17}$$

Then, by eliminating Λ_1 and c_1 from this equation, we obtain $c_{l,3}$ as a function of ε, defined implicitly by

$$-c_{l,3} \arcsin\left(\frac{c_{l,3}}{2\varepsilon}\right) + (2m+1)\pi c_{l,3} + \Lambda - 1 - 2\varepsilon - \sqrt{4\varepsilon^2 - c_{l,3}^2} = 0; \tag{4.2.18}$$

in practice this equation must be solved numerically. For $m = 0$, after substituting $\lambda = \lambda_-$ into Eq. (4.2.3), we obtain instead

$$\Lambda = 1 + 4\varepsilon + \Lambda_1 \varepsilon^2, \quad c = -\frac{\Lambda_1}{\pi}\varepsilon^2 + \frac{\Lambda_1^2}{4\pi^3}\varepsilon^3 + \mathcal{O}(\varepsilon^4), \tag{4.2.19}$$

which, after elimination of Λ_1, gives

$$c_{l,4} = -\frac{\Lambda - 1 - 4\varepsilon}{\pi} + \frac{(\Lambda - 1 - 4\varepsilon)^2}{4\pi^3 \varepsilon}. \tag{4.2.20}$$

It turns out that for some values of ε ($\varepsilon = \varepsilon_L$, say, which must obtained numerically) we have $c_{l,1} = c_{l,3}$. In the case of $|c| \ll 1$, $c_{l,1}$ and $c_{l,3}$ are defined for $\varepsilon \in [\varepsilon_L, \infty)$. Similar remarks apply to $c_{l,2}$ and $c_{l,4}$.

The results of numerically solving Eqs. (4.2.3) and (4.2.4) for non-negative c and $\Lambda = 0.5$, i.e., the same parameter values as used by Melvin *et al.* [66, 67], are shown as solid lines in Fig. 4.1. The figure shows the first few spectral bands with more than one pair of roots to Eq. (4.2.3). The fact that the spectral bands accumulate at one point as $c \to 0$ in Fig. 4.1 indicates that the number of resonances increases as c approaches 0. On the other hand, there are no resonances in the decoupling limit, $\varepsilon = 0$: as ε increases, the number of resonances increases.

We also show in Fig. 4.1 the analytical approximations of the spectral bands that were obtained above. For small c and $\varepsilon = \mathcal{O}(1)$, the approximations using Eqs. (4.2.6) and (4.2.8) for $m = 0, 1, 2, \ldots$ are given as the lower and upper dashed lines, respectively, for each m. For small c and small ε, the approximations using Eqs. (4.2.15) and (4.2.20) are shown as the lower and upper dotted lines, respectively, for $m = 0$. Moreover, the lower and upper dash-dotted lines in Fig. 4.1 show, respectively, the approximations using Eqs. (4.2.13) and (4.2.18), for each $m \neq 0$. We can see that the approximations are in excellent agreement with the numerical results. Interestingly, as shown in the figure, our approximations which are calculated for small parameters, in fact, are still relatively good in the $\mathcal{O}(1)$-parameter regions.

The value of frequency Λ (see Eq. (4.1.3)) influences the shape of the spectral bands, as shown in Fig. 4.2. Taking a smaller value of Λ results in a wider gap between the fundamental and the second lower band, as illustrated in Fig. 4.2(a) for $\Lambda = 0$. On the other hand, a larger value of Λ yields a smaller gap, as illustrated in Fig. 4.2(b) with $\Lambda = 0.7$. Furthermore, the gap disappears for $\Lambda = 1$, as seen in Fig. 4.2(c).

4.3 Numerical scheme: a finite-difference method

To solve Eq. (4.1.5) numerically, we use a scheme based on the discretization of the equation, resulting in a system of difference equations. For approximating the spatial derivative terms, we employ the central finite difference, so that the corresponding Jacobian matrix is sparse. The difference equations are then solved using a Newton–Raphson method. This is different from the previously used pseudo-spectral collocation method (Melvin *et al.* [66, 67]), in which the dependent variable ψ was represented as a Fourier series, whose coefficients were then determined by solving a system of algebraic equations obtained by requiring the series approximation to satisfy the governing equation at collocation points.

4.3.1 Numerical setup

In the framework of the finite-difference method, with grid size Δz, we approximate $\psi(z)$ on a finite interval $[-L, L]$, where $L \in \mathbb{Z}^+$, as follows:

$$\psi(z) \approx \psi(-L + (k-1)\Delta z) \equiv \psi_k, \tag{4.3.1}$$

$$\psi(z \pm 1) \approx \psi(-L + [(k-1) \pm (1/\Delta z)]\Delta z) \equiv \psi_{k\pm(1/\Delta z)}, \tag{4.3.2}$$

for $k = 1, 2, ..., N = 2L/\Delta z + 1$. N is the number of grid points which is odd (positive) integer provided $1/\Delta z \in \mathbb{Z}^+$. For $\psi'(z) \equiv \frac{\mathrm{d}\psi}{\mathrm{d}z}$, we use the central two-point stencil,

$$\psi'(z) \approx \frac{\psi_{k+1} - \psi_{k-1}}{2\Delta z}. \tag{4.3.3}$$

Substituting the discretizations (4.3.1)–(4.3.3) into Eq. (4.1.5) yields

$$\frac{\mathrm{i}c}{2\Delta z}(\psi_{k+1} - \psi_{k-1}) + (2\varepsilon - \Lambda)\psi_k - \varepsilon(\psi_{k+(1/\Delta z)} + \psi_{k-(1/\Delta z)}) + \frac{\psi_k}{1 + |\psi_k|^2} = 0. \tag{4.3.4}$$

Here, we use periodic boundary condition

$$\psi_{N-1+j} = \psi_j \text{ and } \psi_{1-j} = \psi_{N-j}, \tag{4.3.5}$$

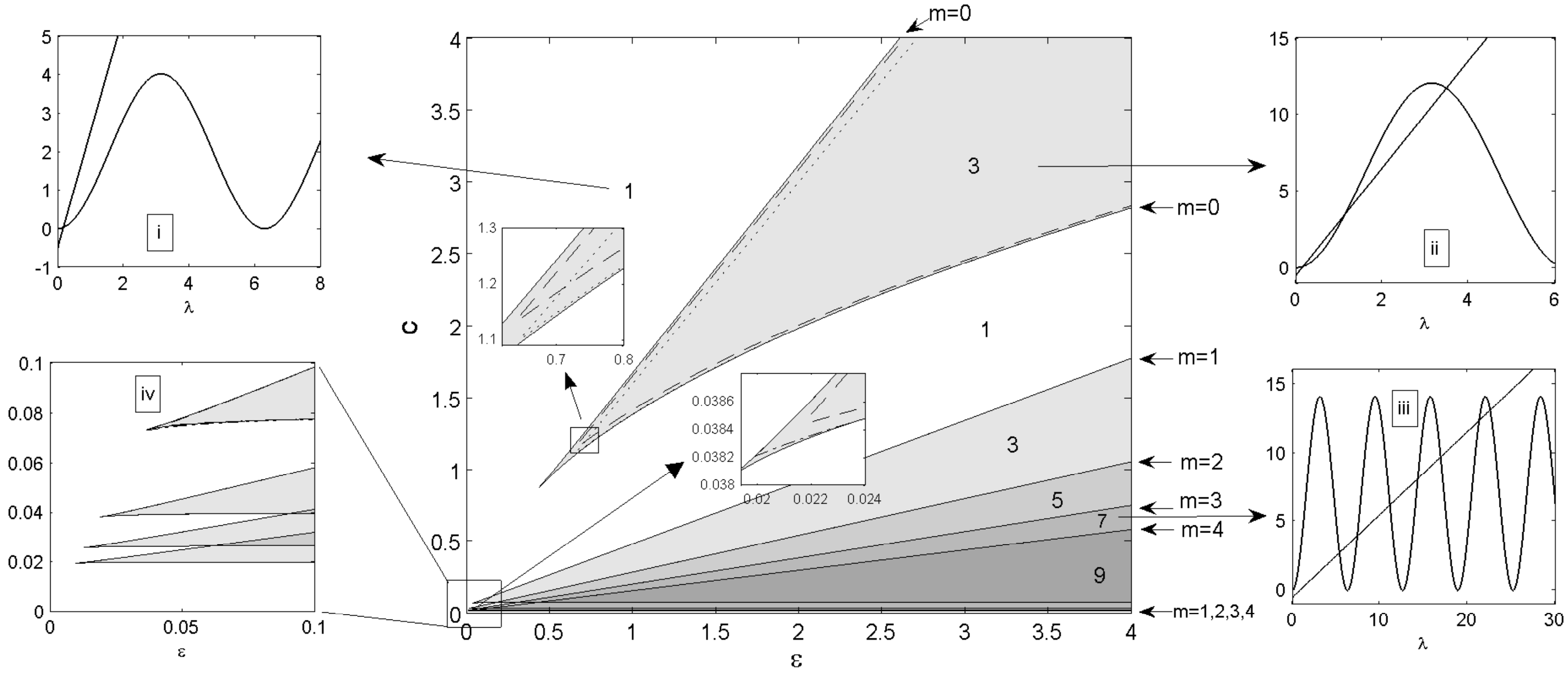

Figure 4.1: Spectral bands in the (ε, c) plane obtained by solving Eqs. (4.2.3) and (4.2.4) for $\Lambda = 0.5$. The shaded areas and the values therein show different regions with different numbers of roots to Eq. (4.2.3). The subplots show F, as defined in (4.2.3), indicating (i) one root at parameter values $\varepsilon = 1$, $c = 3$, (ii) three roots at $\varepsilon = 3$, $c = 3.5$, and (iii) seven roots at $\varepsilon = 3.5$, $c = 0.6$. Panel (iv) zooms in on the region of small ε and c, and only the first five bands are shown. The approximations for the spectral bands at small c, obtained from Eqs. (4.2.6) and (4.2.8), are shown by the lower and upper dashed lines, respectively, for each m, while for small ε and c, approximations using Eqs. (4.2.15)–(4.2.20) and Eqs. (4.2.13)–(4.2.18) are, respectively, shown by the lower-upper dotted lines for $m = 0$ and lower-upper dash-dotted lines for each $m \neq 0$.

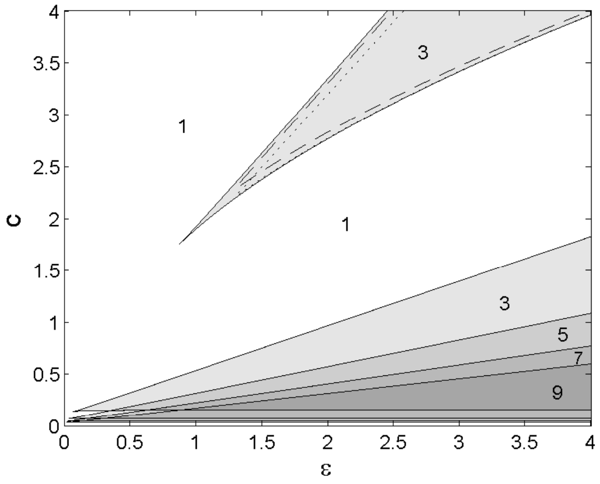

(a) $\Lambda = 0$

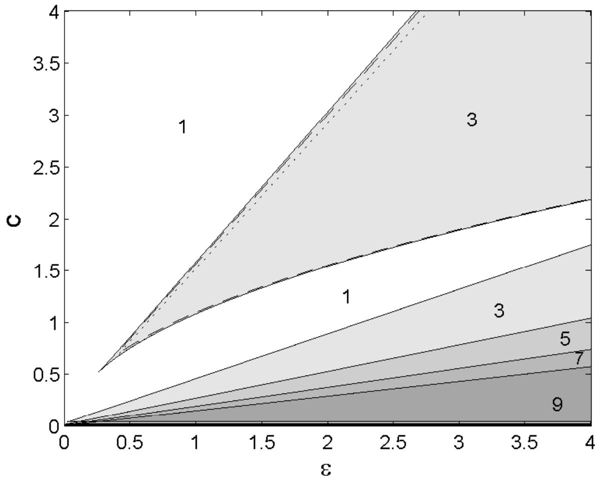

(b) $\Lambda = 0.7$

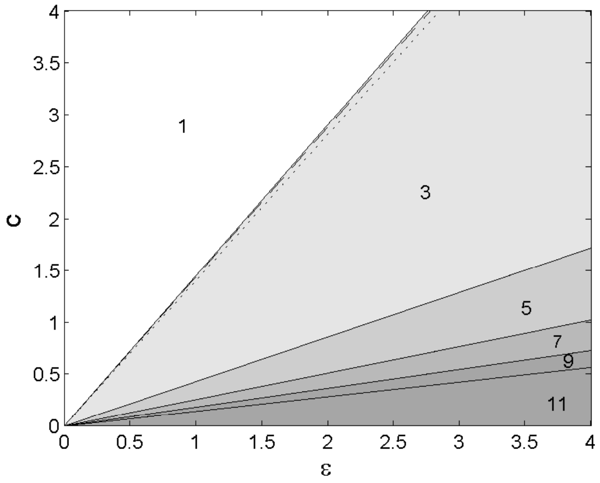

(c) $\Lambda = 1$

Figure 4.2: As in Fig. 4.1, but using Λ as indicated in the caption of each panel.

for $j = 1, 2, \ldots, 1/\Delta z$.

Next, we solve the resulting system of nonlinear equations (4.3.4) numerically for a fixed set of parameters $(c, \varepsilon, \Lambda)$, using the Newton–Raphson method with an error tolerance of order 10^{-15}. To do so, we define the left-hand side of Eq. (4.3.4) as f_k and then seek a solution with $f_k = 0$ for $k = 1, 2, ..., N-1$. Because ψ is complex, we seek solutions in the form of $\psi = \mathrm{Re}(\psi) + \mathrm{i}\mathrm{Im}(\psi)$ (note that one may apply Newton's method to the complex equations (4.3.4), but the convergence can be complicated as was demonstrated by Cayley [127]). Accordingly, we define a (real) functional vector,

$$\mathbf{F} = [\mathrm{Re}(f_1), \ldots, \mathrm{Re}(f_{N-1}), \mathrm{Im}(f_1), \ldots, \mathrm{Im}(f_{N-1})]^T, \tag{4.3.6}$$

and a (real) solution vector,

$$\boldsymbol{\Psi} = [\mathrm{Re}(\psi_1), \ldots, \mathrm{Re}(\psi_{N-1}), \mathrm{Im}(\psi_1), \ldots, \mathrm{Im}(\psi_{N-1})]^T. \tag{4.3.7}$$

Note that Eq. (4.1.5) has rotational and translational invariance. Therefore, to ensure the uniqueness of solutions, we impose two constraints,

$$\begin{aligned} \mathrm{Re}\left(\psi_{\frac{N+1}{2}-1}\right) - \mathrm{Re}\left(\psi_{\frac{N+1}{2}+1}\right) &= 0, \\ \mathrm{Im}\left(\psi_{\frac{N+1}{2}}\right) &= 0, \end{aligned} \tag{4.3.8}$$

upon $\mathbf{F}$ at $((N+1)/2+1)$th and $((N+1)/2+N)$th elements, respectively (the position of these imposed constraints in $\mathbf{F}$ is chosen solely based on trial-and-error). These constraints significantly improve the convergence of the Newton–Raphson scheme.

4.3.2 The measure for seeking the embedded solitons

As shown by Melvin *et al.* [66, 67], in the general case the numerically obtained solitary waves are weakly delocalised, i.e., oscillatory tails with a nonvanishing amplitude are attached to them. Nevertheless, as suggested in [66, 67], it is possible to find solutions with vanishing tails (i.e., genuine solitons) by considering a quantity

$$\Delta_i = \mathrm{Im}(\psi_N), \tag{4.3.9}$$

which is a signed measure, whose zeros correspond to solutions with vanishing tails.

Note that the periodic boundary condition (4.3.5) leads to $\mathrm{Im}(\psi(N)) = 0$, since the imaginary part of ψ is odd. Therefore, we modify the signed measure (4.3.9) and define it as

$$\Delta_r = \mathrm{Re}(\psi_N). \tag{4.3.10}$$

In addition, we also define and use an alternative measure, given by

$$\rho = \max\left\{|\psi_i/\psi_N| : i = N - \zeta/\Delta z, \ldots, N\right\}, \tag{4.3.11}$$

whose usefulness in detecting genuine solitons will be compared with that of the function Δ_r. In all the illustrative figures presented in the next discussion, we take $\zeta = L - 20$ (provided $L > 20$), which means that the observed tail is in interval $[L/2 + 10, L]$. Thus the longer L we use, the longer interval of tail we observe.

It is clear that $\rho \to \infty$ whenever $\psi_N \to 0$. Hence, if ρ is plotted as a parameter is varied, then any vertical asymptote(s) will correspond to solutions with decaying oscillatory tails. We note that, in general, both Δ_r and ρ depend on the finite value chosen for L. However, if L is large enough, then the positions of the zeros of Δ_r and the asymptotes of ρ may be considered to have converged, and should change little with any further increase in L (corresponding to the limit of $L \to \infty$).

4.3.3 Numerical results for the existence of travelling lattice solitons

In this work, we do not provide any rigorous proof of the convergence of the numerical scheme outlined above. Therefore, to check the validity of our numerical scheme, we benchmarked our results against those reported by Melvin *et al.* [66] for the same parameter values. We show in Fig. 4.3 an example of a soliton with $\varepsilon = 1, c = 0.7, \Lambda = 0.5, L = 60, \Delta z = 0.2$, which is virtually the same as that obtained using the pseudo-spectral collocation method in [66].

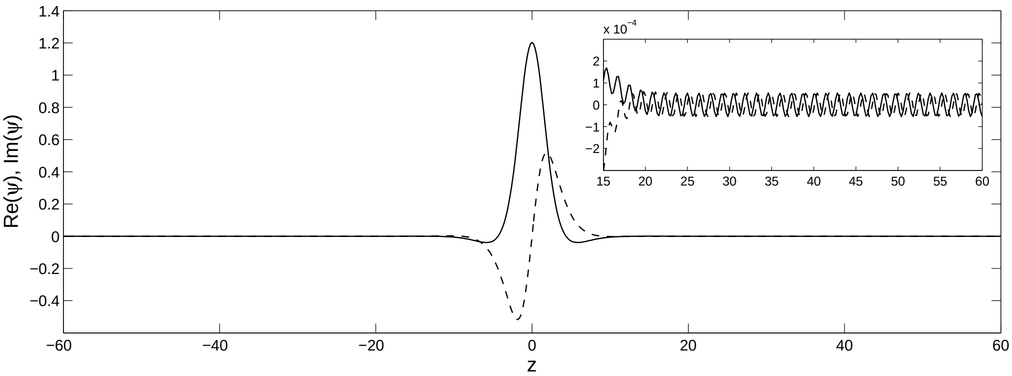

Figure 4.3: A soliton obtained by means of the alternative scheme presented herein for $\varepsilon = 1$, $c = 0.7$, $\Lambda = 0.5$, $L = 60$, with the grid spacing $\Delta z = 0.2$. This solution is to be compared with the profile that was found by Melvin *et al.* [66]. The solid and dashed lines are, respectively, $\mathrm{Re}(\psi)$ and $\mathrm{Im}(\psi)$. The inset shows a magnification of the oscillating tail.

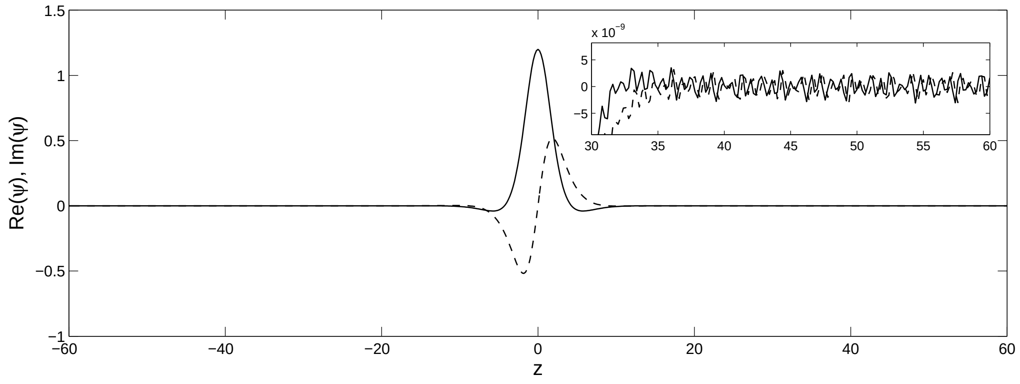

(a) $\Delta z = 0.2, \varepsilon \approx 0.988$

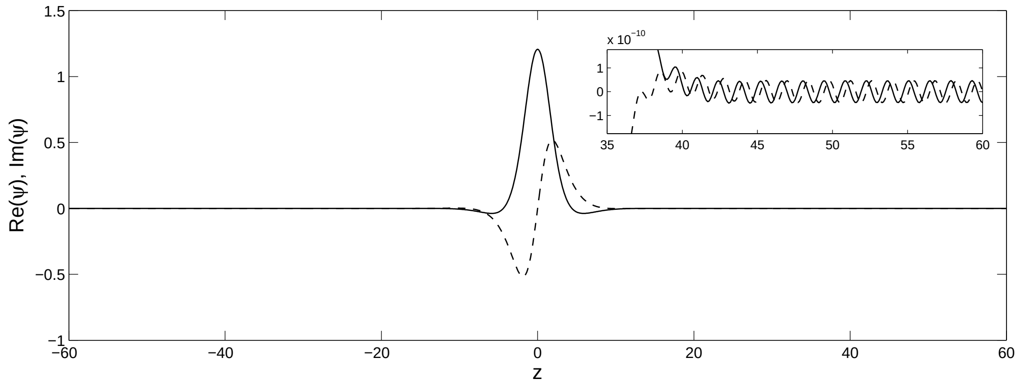

(b) $\Delta z = 0.1, \varepsilon \approx 1.012$

Figure 4.4: A soliton with a vanishing tail, corresponding to a zero of Δ_r found by varying ε. Both panels use $c = 0.7$, $\Lambda = 0.5$, $L = 60$, but use different values for Δz; correspondingly, slightly different values for ε are necessary to achieve a zero of Δ_r, as indicated in the caption to each panel.

Once a solution is obtained, we perform numerical continuation by varying a parameter, calculating and recording the signed measure Δ_r for each solution, as given by Eq. (4.3.10). We seek the zeros of Δ_r, which indicate solutions with vanishing oscillatory tails. Using the parameter values in Fig. 4.3, we exhibit in Fig. 4.4 an example of a soliton with a vanishing tail amplitude, which corresponds to a zero of Δ_r, found by varying ε. In this example, the soliton is found at $\varepsilon \approx 0.988$. If we decrease the grid size to $\Delta z = 0.1$, the parameter value for an ES changes slightly to $\varepsilon \approx 1.012$; thus the location of the zero of Δ_r depends slightly on the spatial discretization parameter Δz. However, we argue that the locations of the zeros converge as Δz decreases, a conjecture supported by numerical observations shown in Fig. 4.5. We plot in the figure the measure Δ_r as a function of ε for several values of Δz, at parameter values $c = 0.7$, $\Lambda = 0.5$ and $L = 30$. It was reported by Melvin *et al.* [66] that, for the same parameters, $\Delta_r = 0$ occurred for $\varepsilon \approx 0.76, 1.02, 1.36$ (or, equivalently, for $1/\varepsilon \approx 1.316, 0.98, 0.74$). From our figures, we see that our numerical scheme yields nearly the same values.

Note that, as discussed by Melvin *et al.* [66], in the regions where the dispersion relation has more than one root, travelling lattice solitons would become objects of codimension two and might cease to exist. Interestingly, from our numerical scheme, as shown in Fig. 4.5, we found zero crossings in regions where three roots of linear wave frequency λ occurs by varying one parameter only (see the shaded areas, cf. Fig. 4.1). This result, however, needs a further justification which is beyond the scope of this thesis.

Just as Δ_r was shown to be a function of the discretization parameter Δz, it is to be expected that Δ_r should also be a function of L. In Fig. 4.6 we plot the signed measure Δ_r (top panels) and function ρ (bottom panels), obtained from Eq. (4.3.11), for $c = 0.7$, $\Lambda = 0.7$, $\Delta z = 0.2$ and several values of L.

First we consider the value $L = 30$. In Fig. 4.6(a) we show Δ_r and ρ as functions of $1/\varepsilon$. We observe that Δ_r has several zeros at which coincide with the asymptotes of ρ. When L is taken slightly larger, i.e., $L = 50$, we see, in Fig. 4.6(b), that the number of zeros of Δ_r decreases and ρ has asymptotes that coincide with zeros of Δ_r at $\varepsilon \approx 0.828, 1.158, 1.544, 1.560, 1.623$. For the sake of completeness, in Fig. 4.7 we depict the deformation of the tail of the soliton as we vary the coupling constant ε around one of the zeros of Δ_r. Increasing the value of L further, to $L = 100$, we observe in Fig. 4.6(c) that the zeros of Δ_r are nearly the same as at $L = 50$, i.e., at $\varepsilon \approx 0.828, 1.158, 1.584$, with the local maxima of ρ also occurring at the same values. Note that the leftmost zero-crossing point in both Figs. 4.6(b) and 4.6(c) is also found in the regions where the number of resonances of the travelling solution with plane waves is three (see the shaded areas, cf. Fig. 4.2(b)).

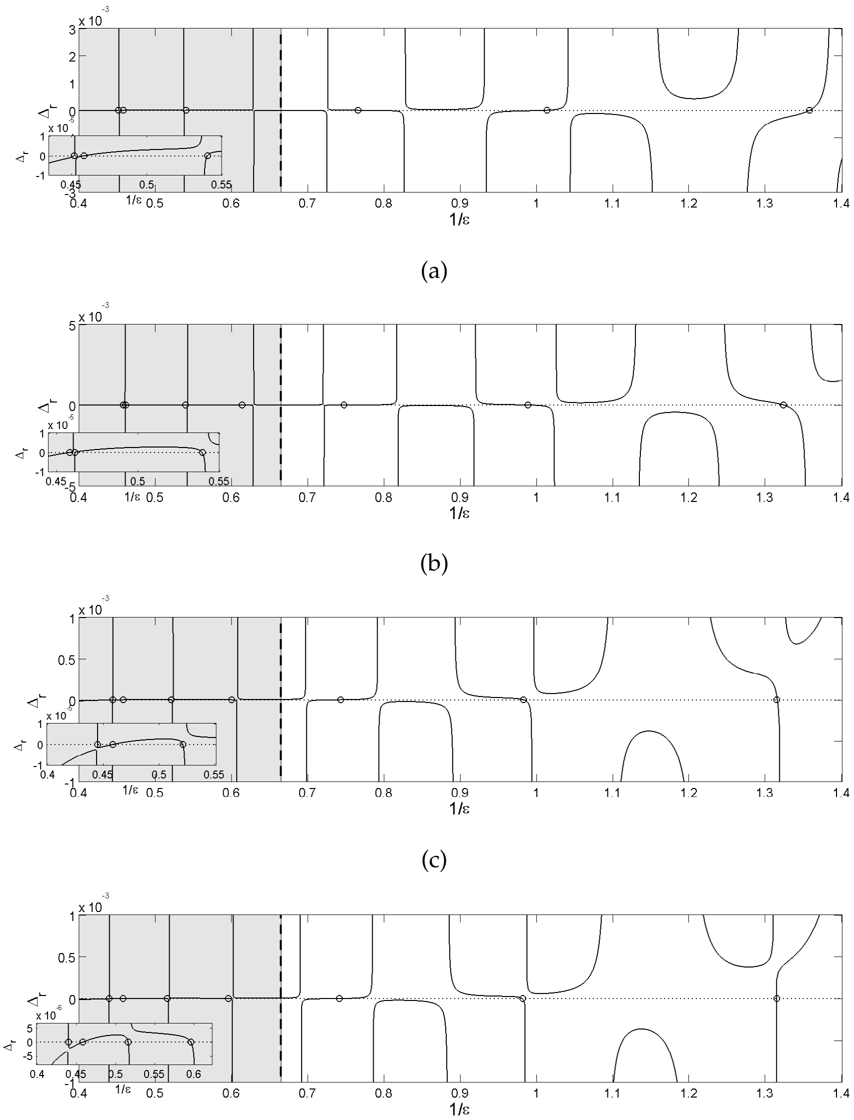

(a)

(b)

(c)

(d)

Figure 4.5: Numerical continuations of weakly nonlocal solitons obtained by varying $1/\varepsilon$ for $c = 0.7$, $\Lambda = 0.5$ $L = 30$, and the grid spacing: (a) $\Delta z = 0.2$, where zeros of Δ_r are found at $\varepsilon \approx 0.737, 0.987, 1.306, 1.850, 2.181, 2.212$ (or at $1/\varepsilon \approx 1.357, 1.013, 0.766, 0.541, 0.459, 0.452$); (b) $\Delta z = 0.1$, with the zeros of Δ_r occurring at $\varepsilon \approx 0.756, 1.012, 1.338, 1.629, 1.853, 2.167, 2.182$ (or at $1/\varepsilon \approx 1.323, 0.988, 0.747, 0.614, 0.540, 0.461, 0.458$); (c) $\Delta z = 0.05$, where the zeros of Δ_r occur at $\varepsilon \approx 0.761, 1.018, 1.346, 1.666, 1.919, 2.182, 2.249$ (or at $1/\varepsilon \approx$ 1.314,0.982,0.743,0.600,0.521,0.458,0.445); and (d) $\Delta z = 0.01$, with the zeros of Δ_r found at $\varepsilon \approx 0.761, 1.019, 1.349, 1.678, 1.938, 2.183, 2.273$ (or at $1/\varepsilon \approx$ 1.314,0.981,0.741,0.596,0.516,0.458,0.440). Empty circles show the positions of the zeros. The shaded regions indicate the regions in which there are three roots of the linear wave frequency λ (see cf. Fig. 4.1).

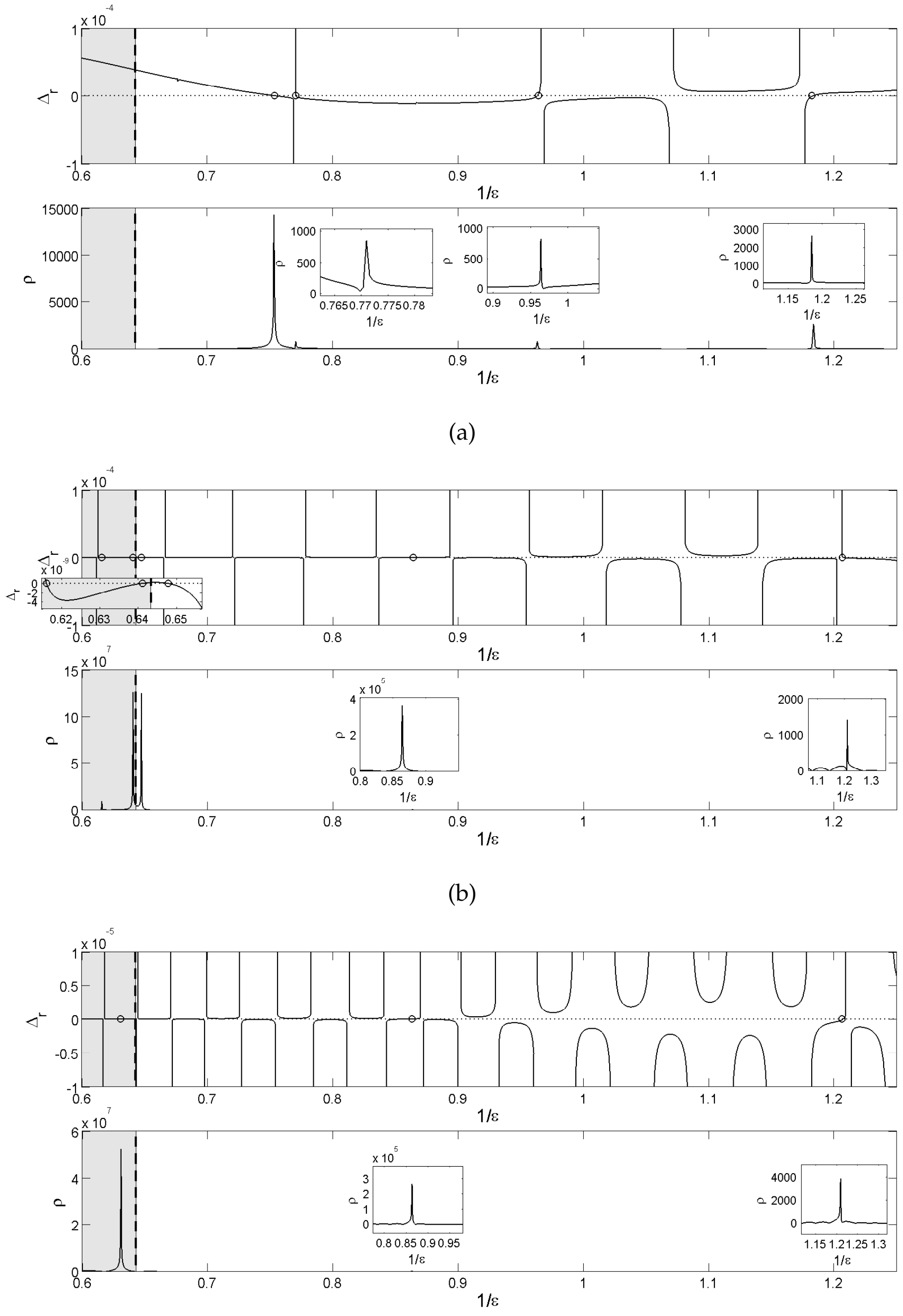

(a)

(b)

(c)

Figure 4.6: The signed measure Δ_r (top panel, cf. Eq. (4.3.10)) and ρ (bottom panel, cf. Eq. (4.3.11)) as a function of $1/\varepsilon$ for $c = 0.7$, $\Lambda = 0.7$, $\Delta z = 0.2$, and (a) $L = 30$, with the zeros of Δ_r occurring at $\varepsilon \approx 0.846, 1.037, 1.297, 1.326$ at which coincide with the asymptotes of ρ; (b) $L = 50$, with Δ_r vanishing at $\varepsilon \approx 0.828, 1.158, 1.544, 1.560, 1.623$ and ρ exhibiting asymptotes at the same values; (c) $L = 100$, with zeros of Δ_r and asymptotes of ρ at $\varepsilon \approx 0.828, 1.158, 1.584$. The shaded regions correspond to the regions where the number of resonance with linear waves is three (see cf. Fig. 4.2).

From the computational results discussed above, we conclude that for parameter values $c = 0.7$ and $\Lambda = 0.7$, $L = 30$ is too small to be used to capture the behaviour of travelling solitons in an infinite domain. In addition, as clearly seen in Figs. 4.6(b) and 4.6(c), we notice the increasing of the magnitude of the asymptotes of ρ for larger ε (smaller $1/\varepsilon$) which happens because the solitons are getting broader when ε increases ($1/\varepsilon$ decreases). Therefore, we argue that the measure ρ can also be used to detect whether or not the value taken for L is sufficiently large.

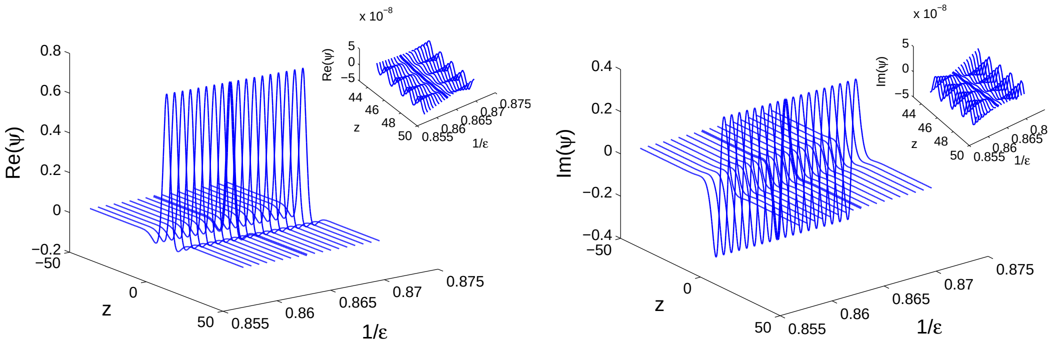

(a) (b)

Figure 4.7: The change in the soliton profile around one of the zeros of Δ_r shown in Fig. 4.6(b), as one varies ε. The bold curves show the profile with zero amplitude tail at $\varepsilon \approx 1.158$ (or at $1/\varepsilon \approx 0.864$). (a) $\mathrm{Re}(\psi)$, (b) $\mathrm{Im}(\psi)$.

Using the conclusions for the measure ρ formulated above, we have tested the results shown in Fig. 4.5 by using this measure; this is presented in Fig. 4.8. From the two aforementioned figures, we conclude that the local maxima of ρ coincide with zeros of Δ_r. However, the results in the shaded region are rather inconclusive. It is because the solitons, as also the case for $\Lambda = 0.7$ (Fig. 4.6), become wider as ε increases ($1/\varepsilon$ decreases) while the value of L taken is not long enough to permit meaningful investigation of the behaviour of the soliton's tail. Therefore, to obtain convincing results concerning the presence of the additional zeros, we now use $L = 60$ and $\Delta z = 0.1$; we present Δ_r and ρ for this setting in Fig. 4.9, which is focused on the additional zeros. We observe in the figure that the positions of the asymptotes of ρ coincide with those of the zeros of Δ_r. Another interesting output we notice in that figure is that we still can find a zero crossing in the region where the number of roots λ is five (see the darker shaded areas, cf. Fig. 4.1). Again, the result for this additional zero does not necessarily mean that it is a genuine one as a further justification is required.

It is also interesting to note that $L = 30$, which is not long enough for the case $\Lambda = 0.7$, may be sufficient for the case $\Lambda = 0.5$ for some values of ε. This happens because

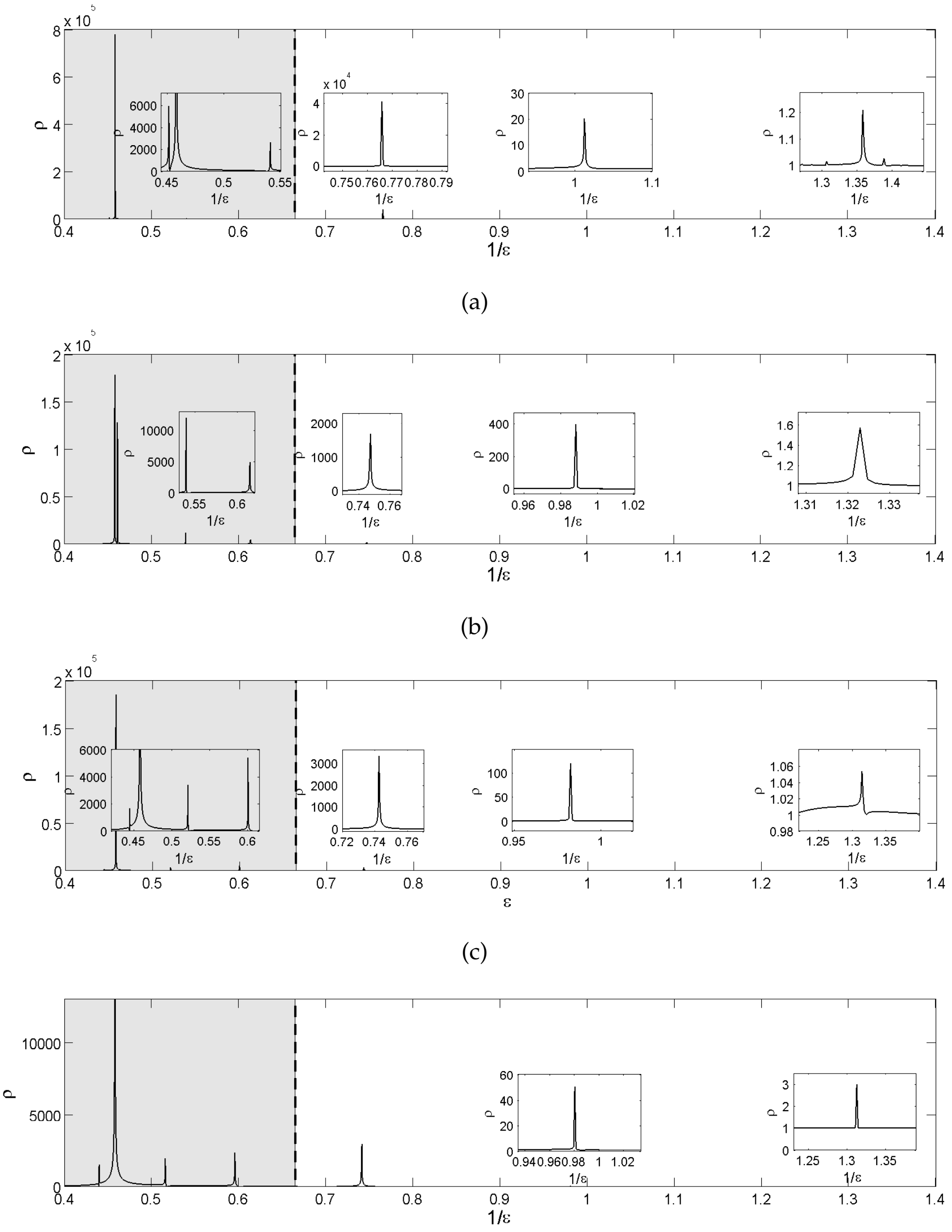

(a)

(b)

(c)

(d)

Figure 4.8: The measure ρ corresponding to Fig. 4.5. The asymptotes of ρ coincide with the zeros of Δ_r in Fig. 4.5.

larger values of Λ correspond to wider profiles for the soliton, which then require a longer computational domain (see, e.g., Fig. 4.10).

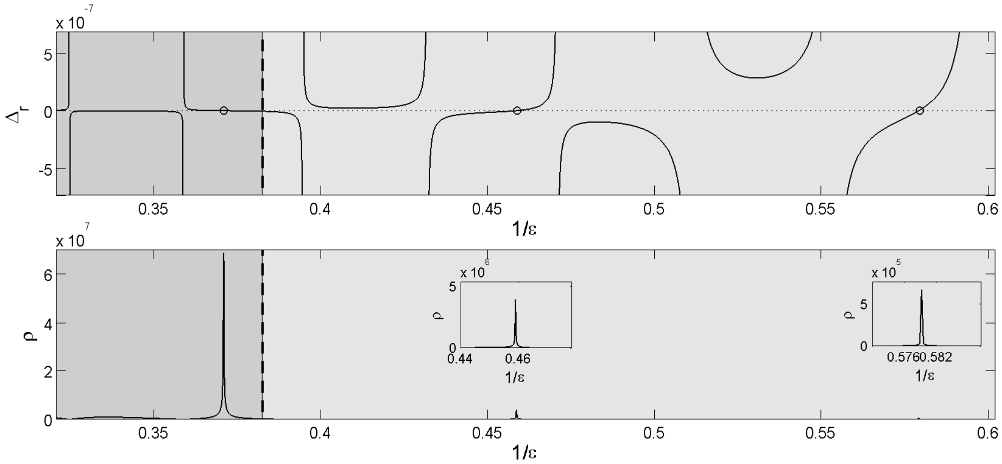

Figure 4.9: Measures Δ_r (top panel) and ρ (bottom panel) as a function of $1/\varepsilon$ focusing on the additional zeros of Δ_r in Fig. 4.5, i.e., obtained by using $\Delta z = 0.1$ and a longer computational domain with $L = 60$. The zeros of Δ_r and the asymptotes of ρ occur at $\varepsilon \approx 1.726, 2.179, 2.695$ (or at $1/\varepsilon \approx 0.579, 0.459, 0.371$) with the latter lying in the region where the number of roots of frequency λ is five (darker shaded regions).

4.4 The variational approximation

The objective of this section is to derive a variational approximation (VA) for the solitons obtained numerically above.

4.4.1 Core soliton solutions

As suggested in previous work (Gómez-Gardeñes *et al.* [119]), a travelling lattice wave may be considered as superpositions of an exponentially localised core, ψ_{core}, and a non-vanishing oscillatory background, ψ_{bckg}, which is a delocalised solution of the linearised version of Eq. (4.1.5). Hence, we may write

$$\psi(z) = \psi_{\text{core}}(z) + b\psi_{\text{bckg}}(z), \tag{4.4.1}$$

where b is an arbitrary real small amplitude.

In this section, we first derive the VA for the core. To this end, we recall that Eq. (4.1.5) can be represented in the variational form,

$$\frac{\delta L}{\delta \psi^*(z)} = 0, \tag{4.4.2}$$

where $\delta/\delta\psi^*$ stands for the variational derivative of a functional and the Lagrangian is

$$\begin{aligned} L \;=\; & \int_{-\infty}^{\infty} \Big[(2\varepsilon - \Lambda)|\psi|^2 + \ln\left(1 + |\psi|^2\right) + \frac{\mathrm{i}c}{2}\left[\psi^*\psi' - \psi(\psi^*)'\right] \\ & -\frac{\varepsilon}{2}\left\{\psi^*[\psi(z+1) + \psi(z-1)] + \psi[\psi^*(z+1) + \psi^*(z-1)]\right\}\Big]\, \mathrm{d}z. \end{aligned} \tag{4.4.3}$$

A suitable trial function, or *ansatz*, for the core may be chosen as

$$\psi_{\text{core}}(z) = F(z)\,\mathrm{e}^{\mathrm{i}pz}, \tag{4.4.4}$$

where

$$F(z) = A\,\text{sech}(az), \tag{4.4.5}$$

with A, a and p non-zero real variational parameters. The ansatz is chosen because it is an exact solution of the continuous nonlinear Schrödinger equation with cubic nonlinearity. While this ansatz postulates exponential tails of the soliton, the prediction of solitons within the framework of the VA does not necessarily mean that the corresponding solitons exist in a rigorous sense, as the actual tail may be non-vanishing at $|z| \to \infty$. In fact, the prediction of solitons by the VA may imply a situation in which the amplitude of the nonvanishing tail is not zero, but attains its minimum (Kaup & Malomed [128]).

The next step is to substitute ansatz (4.4.4) into Lagrangian (4.4.3), perform the integration, and derive the (stationary) Euler-Lagrange equations

$$\frac{\partial L}{\partial A} = \frac{\partial L}{\partial a} = \frac{\partial L}{\partial p} = 0. \tag{4.4.6}$$

By substituting ansatz (4.4.4) into the Lagrangian and performing the integration, we obtain the effective Lagrangian, as a function of parameters A, a and p,

$$L_{\text{eff}} = \frac{2A^2(2\varepsilon - \Lambda - cp) + \mathcal{A}_+^2 + \mathcal{A}_-^2}{a} - \frac{4A^2\varepsilon\cos(p)}{\sinh(a)}, \tag{4.4.7}$$

where $\mathcal{A}_\pm = \ln\left(\sqrt{1 + A^2} \pm A\right)$.

Then, substituting Lagrangian (4.4.7) into Eqs. (4.4.6) yields

$$\begin{aligned} \frac{A(2\varepsilon - \Lambda - cp)}{a} + \frac{\mathcal{A}_+}{a\sqrt{1 + A^2}} - \frac{2A\varepsilon\cos(p)}{\sinh(a)} &= 0, && (4.4.8) \\ -\frac{2A^2(2\varepsilon - \Lambda - cp) + \mathcal{A}_+^2 + \mathcal{A}_-^2}{a^2} + \frac{4A^2\varepsilon\cos(p)\cosh(a)}{\sinh^2(a)} &= 0, && (4.4.9) \\ -\frac{c}{a} + \frac{2\varepsilon\sin(p)}{\sinh(a)} &= 0. && (4.4.10) \end{aligned}$$

This system of algebraic equations for A, a and p will be solved numerically.

Before proceeding to the next section, it is noteworthy to mention that if one replaces the term $\ln\left(1+|\psi|^2\right)$ in the Lagrangian (4.4.3) by its truncated expansions (up to some order), then the new expression of the integral becomes a Lagrangian of a DNLS equation with polynomial nonlinearity. Therefore, using the ansatz (4.4.4), the effective Lagrangian (4.4.7) can be used to determine an effective Lagrangian of a polynomial DNLS equation whose the nonlinearity is a Taylor expansion of the transcendental function. This is carried out by simply expanding the term $(\mathcal{A}_+^2+\mathcal{A}_-^2)/a$ in Eq. (4.4.7), which is the exact result of the integration of the transcendental function in Eq. (4.4.3), with respect to A up to some order, depending on a polynomial DNLS system one is interested in. For example, if one uses $\mathcal{O}(A^4)$ and $\mathcal{O}(A^6)$ expansions, the resulting effective Lagrangian corresponds to the cubic and cubic-quintic DNLS equations, respectively.

Here, for the sake of comparison, we analyse the polynomial DNLS model

$$\mathrm{i}c\psi' + (2\varepsilon-\Lambda)\,\psi - \varepsilon\left[\psi(z+1)+\psi\,(z-1)\right] + \left(1-|\psi|^2+|\psi|^4-|\psi|^6\right)\psi = 0. \quad (4.4.11)$$

The effective Lagrangian and the system of variational equations, by expanding $(\mathcal{A}_+^2+\mathcal{A}_-^2)/a$ up to $\mathcal{O}(A^8)$, are given, respectively, by

$$L'_{\text{eff}} = \frac{2A^2(2\varepsilon-\Lambda+1-cp)}{a} - \frac{2A^4}{3a} + \frac{16A^6}{45a} - \frac{8A^8}{35a} - \frac{4A^2\varepsilon\cos(p)}{\sinh(a)}, \quad (4.4.12)$$

and

$$\begin{aligned} \frac{2\varepsilon-\Lambda+1-cp}{a} - \frac{2A^2}{3a} + \frac{8A^4}{15a} - \frac{16A^6}{35a} - \frac{2\varepsilon\cos(p)}{\sinh(a)} &= 0, && (4.4.13)\\ -\frac{2\varepsilon-\Lambda+1-cp}{a^2} + \frac{A^2}{3a^2} - \frac{8A^4}{45a^2} + \frac{4A^6}{35a^2} + \frac{2\varepsilon\cos(p)\cosh(a)}{\sinh^2(a)} &= 0, && (4.4.14)\\ -\frac{c}{a} + \frac{2\varepsilon\sin(p)}{\sinh(a)} &= 0. && (4.4.15) \end{aligned}$$

We also have computed the effective Lagrangian (4.4.12) directly by integrating a corresponding Lagrangian of the polynomial DNLS equation and obtained the same result.

4.4.2 Prediction of the VA for embedded solitons

We now seek a condition for the possible existence of ESs. Following Kaup & Malomed [128], we consider b in the general form of tailed solution (4.4.1) as an additional variational parameter. Thus, a new variational equation,

$$\frac{\partial L}{\partial b} = 0, \quad (4.4.16)$$

must be added to the system of equations (4.4.10). By writing the integrand in the Lagrangian (4.4.3) as $\mathcal{L}(\psi, \psi^*, \psi', (\psi^*)')$, which is the Lagrangian density, differentiation in Eq. (4.4.16) yields

$$\int_{-\infty}^{+\infty} \left[\frac{\partial \mathcal{L}}{\partial \psi}\psi_{\mathrm{bckg}} + \frac{\partial \mathcal{L}}{\partial \psi^*}\psi^*_{\mathrm{bckg}} + \frac{\partial \mathcal{L}}{\partial \psi'}\psi'_{\mathrm{bckg}} + \frac{\partial \mathcal{L}}{\partial (\psi^*)'}(\psi^*_{\mathrm{bckg}})'\right] \mathrm{d}z = 0. \tag{4.4.17}$$

By integrating the third and the fourth terms by parts to obtain common factors ψ_{bckg} and ψ^*_{bckg}, respectively, and from the fact that

$$\frac{\partial \mathcal{L}}{\partial (\psi^*)'} = -\frac{\mathrm{i}c}{2}\psi, \tag{4.4.18}$$

$$\frac{\partial \mathcal{L}}{\partial \psi'} = \frac{\mathrm{i}c}{2}\psi^*, \tag{4.4.19}$$

Eq. (4.4.17) becomes

$$\int_{-\infty}^{+\infty} \left[\left(\frac{\partial \mathcal{L}}{\partial \psi^*} - \frac{\mathrm{d}}{\mathrm{d}z}\frac{\partial \mathcal{L}}{\partial (\psi^*)'}\right)\psi^*_{\mathrm{bckg}} + \mathrm{c.c.}\right] \mathrm{d}z + \left[-\frac{\mathrm{i}c}{2}\psi\psi^*_{\mathrm{bckg}} + \mathrm{c.c.}\right]_{-\infty}^{\infty} = 0, \tag{4.4.20}$$

where c.c. stands for the complex conjugate of the preceding expression.

As we are interested in solutions with the absence of nonzero backgrounds, one should substitute $\psi(z)$ in Eq. (4.4.20) with the solution form (4.4.1) by setting $b = 0$ (no tail). This setting leads to the vanishing of the second term in the left-hand side of Eq. (4.4.20). Therefore, the condition for the possible existence of ESs is given by a natural orthogonality relation,

$$\int_{-\infty}^{+\infty} \left\{ \delta L/\delta\psi^*|_{\psi(z)=\psi_{\mathrm{core}}(z)}\, \psi^*_{\mathrm{bckg}}(z) + \mathrm{c.c.}\right\} \mathrm{d}z = 0, \tag{4.4.21}$$

where the variational derivative $\delta L/\delta\psi^*|_{\psi(z)=\psi_{\mathrm{core}}(z)}$ is the left-hand side of Eq. (4.1.5) with $\psi(z)$ replaced by $\psi_{\mathrm{core}}(z)$.

In the context of the VA, $\psi_{\mathrm{core}}(z)$ in Eq. (4.4.21) should be substituted by the (approximate) form (4.4.4) corresponding to the soliton. Here, the background function is taken as

$$\psi_{\mathrm{bckg}}(z) = \mathrm{e}^{\mathrm{i}\lambda z}, \tag{4.4.22}$$

which is nothing other than the linear solution (4.2.1). Note that this background function is a crude approximation because to the leading order ψ_{bckg} should satisfy the linearised equation of (4.1.5) about ψ_{core} with the limiting properties $\psi_{\mathrm{bckg}} \to \mathrm{e}^{\mathrm{i}\lambda z}$ as $z \to \pm\infty$.

The substitution of Eqs. (4.4.4) and (4.4.22) into Eq. (4.4.21) yields

$$\int_{-\infty}^{\infty} \mathcal{M}(z)\mathrm{d}z = 0, \tag{4.4.23}$$

where

$$
\begin{aligned}
\mathcal{M}(z) \quad = \quad & -\varepsilon\left[F(z+1)\cos((\lambda-p)z-p)+F(z-1)\cos((\lambda-p)z+p)\right] \\
& +\left\{(2\varepsilon-c\lambda-\Lambda)\,F(z)+\frac{F(z)}{1+F(z)^2}\right\}\cos((\lambda-p)z). \qquad (4.4.24)
\end{aligned}
$$

It is readily checked that $\mathcal{M}(z)$ is an even function. Therefore, after some manipulations, integral relation (4.4.23) may be cast into the form

$$
\begin{aligned}
\int_0^\infty & \left[\frac{(2\varepsilon-c\lambda-\Lambda)\cos((\lambda-p)z)}{\cosh(az)}-\frac{2\cosh(az)\cos((\lambda-p)z)}{\cosh(2az)+1+2A^2}\right. \\
& \left.-\frac{\mathcal{B}\varepsilon\cos((\lambda-p)z)\cosh(az)}{\cosh(2az)+\cosh(2a)}+\frac{\mathcal{C}\varepsilon\sin((\lambda-p)z)\sinh(az)}{\cosh(2az)+\cosh(2a)}\right]\mathrm{d}z \quad = \quad 0, \qquad (4.4.25)
\end{aligned}
$$

where $\mathcal{B}=4\cos(p)\cosh(a)$ and $\mathcal{C}=4\sin(p)\sinh(a)$. The integrals in each term can be evaluated using the formulas (Gradshteyn & Ryzhik [129])

(i) $$\int_0^\infty \frac{\cos(\mathfrak{a}x)}{\cosh\left(\frac{\mathfrak{b}}{2}x\right)}\mathrm{d}x=\frac{\pi}{\mathfrak{b}\cosh\left(\frac{\mathfrak{a}\pi}{\mathfrak{b}}\right)}, \qquad (4.4.26)$$

provided $\mathrm{Re}(\mathfrak{b})>0$ and $\mathfrak{a}\in\mathbb{R}$;

(ii) $$\int_0^\infty \frac{\cos(\mathfrak{a}x)\cosh\left(\frac{\mathfrak{b}}{2}x\right)}{\cosh(\mathfrak{b}x)+\cosh(\mathfrak{c})}\mathrm{d}x=\frac{\pi\cos\left(\frac{\mathfrak{a}\mathfrak{c}}{\mathfrak{b}}\right)}{2\mathfrak{b}\cosh\left(\frac{\mathfrak{c}}{2}\right)\cosh\left(\frac{\mathfrak{a}\pi}{\mathfrak{b}}\right)}, \qquad (4.4.27)$$

provided $\pi\mathrm{Re}(\mathfrak{b})>|\mathrm{Im}(\mathfrak{b}^*\mathfrak{c})|$;

(iii) $$\int_0^\infty \frac{\cos(\mathfrak{a}x)\cosh\left(\frac{\mathfrak{b}}{2}x\right)}{\cosh(\mathfrak{b}x)+\mathfrak{d}}\mathrm{d}x=\frac{\pi\cos\left(\frac{\mathfrak{a}}{\mathfrak{b}}\cosh^{-1}(\mathfrak{d})\right)}{2\mathfrak{b}\cosh\left(\frac{1}{2}\cosh^{-1}(\mathfrak{d})\right)\cosh\left(\frac{\mathfrak{a}\pi}{\mathfrak{b}}\right)}, \qquad (4.4.28)$$

provided $\pi\mathrm{Re}(\mathfrak{b})>|\mathrm{Im}(\mathfrak{b}^*\cosh^{-1}(\mathfrak{d}))|$;

(iv) $$\int_0^\infty \frac{\sin(\mathfrak{a}x)\sinh\left(\frac{\mathfrak{b}}{2}x\right)}{\cosh(\mathfrak{b}x)+\cos(\mathfrak{e})}\,\mathrm{d}x=\frac{\pi\left[\chi_+-\chi_-\right]}{\mathfrak{b}\sin(\mathfrak{e})\left[\cosh\left(\frac{2\mathfrak{a}\pi}{\mathfrak{b}}\right)-\cos\left(\pi\right)\right]}, \qquad (4.4.29)$$

where $\chi_\pm=\sin\left(\frac{1}{2}(\pi\mp\mathfrak{e})\right)\sinh\left(\frac{\mathfrak{a}}{\mathfrak{b}}(\pi\pm\mathfrak{e})\right)$, provided $\pi\mathrm{Re}(\mathfrak{b})>|\mathrm{Re}(\mathfrak{b}^*\mathfrak{e})|$, $\mathrm{Re}(\mathfrak{b})>0$ and $\mathfrak{a}>0$.

Substituting $\mathfrak{a}=\lambda-p$, $\mathfrak{b}=\mathfrak{c}=2a$, $\mathfrak{d}=1+2A^2$ and $\mathfrak{e}=2a\mathrm{i}$ into Eqs. (4.4.26)–(4.4.29), the calculation for the integration (4.4.25) yields

$$E\equiv(2\varepsilon-c\lambda-\Lambda)-2\varepsilon\cos(\lambda)+\frac{\cos\left(\dfrac{1}{2a}\left[(\lambda-p)\cosh^{-1}(1+2A^2)\right]\right)}{\cosh\left(\dfrac{1}{2}\left[\cosh^{-1}(1+2A^2)\right]\right)}=0, \qquad (4.4.30)$$

provided $a>0$ and $\lambda>p$. Thus, in the framework of the VA, along with the results of the VA for the soliton's core given by Eqs. (4.4.8)–(4.4.10) and with the root(s) λ of Eq. (4.2.3), we may predict a curve E as a function of $(\varepsilon, c, \Lambda)$ along which the existence of the ESs may be expected, i.e., when $E=0$.

If we expand E with respect to A up to $\mathcal{O}(A^8)$, we arrive at the following form:

$$E' \equiv (2\varepsilon - c\lambda - \Lambda + 1) - 2\varepsilon\cos(\lambda) + \sum_{k=1}^{3}\left[\frac{(-1)^k}{(2k)!}\left(\frac{A}{a}\right)^{2k}\prod_{j=1}^{k}\left((\lambda-p)^2+(a(2j-1))^2\right)\right] = 0, \tag{4.4.31}$$

which is the corresponding result of the integral relation (4.4.21) for the polynomial DNLS (4.4.11). The same result for E' is also obtained through the integration of polynomial terms which confirms the validity of the result in Eq. (4.4.30). As we discuss later in Section 4.5.2, Eq. (4.4.31) is useful to support our conjecture regarding the use of VA in searching for ESs in the saturable DNLS model.

4.4.3 The VA-based stability analysis

Here, we propose to use the VA to study the stability of the core of the travelling lattice solitary wave by calculating eigenvalues for modes of small perturbations in the moving coordinate frame, following Flytzanis *et al.* [130]. The stability of the background, i.e., the modulational (in)stability of the plane lattice waves, was studied by Gómez-Gardeñes *et al.* [119].

The Lagrangian of the time-dependent equation (4.1.4) is

$$\begin{aligned} L \;=\; \int_{-\infty}^{\infty}\Big[& (2\varepsilon-\Lambda)|\psi|^2 + \ln\left(1+|\psi|^2\right) + \frac{\mathrm{i}c}{2}\left[\psi^*\psi_z - \psi\psi_z^*\right] \\ & -\frac{\varepsilon}{2}\left\{\psi^*[\psi(z+1,\tau)+\psi(z-1,\tau)] + \psi[\psi^*(z+1,\tau)+\psi^*(z-1,\tau)]\right\} \\ & -\frac{\mathrm{i}}{2}\left(\psi^*\psi_\tau - \psi\psi_\tau^*\right)\Big]\,\mathrm{d}z. \end{aligned} \tag{4.4.32}$$

Note that Eq. (4.1.4) is produced by the variation with respect to ψ^* from the action functional $S = \int L\mathrm{d}\tau$, not from the Lagrangian (4.4.32). However, for practical purposes (the derivation of VA equations), it is enough to calculate Lagrangian (4.4.32) (it is not necessary to calculate the action functional explicitly).

A time-dependent ansatz, generalising the static one (4.4.4), is

$$\psi_{\text{core}}(z,\tau) \;=\; A(\tau)\operatorname{sech}\left[a(\tau)(z-\xi(\tau))\right]\mathrm{e}^{\left(\mathrm{i}\phi(\tau)+\mathrm{i}p(\tau)z+\frac{\mathrm{i}}{2}C(\tau)[z-\xi(\tau)]^2\right)}, \tag{4.4.33}$$

where all parameters are real functions of time. Additional variational parameters which appear here are the coordinate of soliton's centre, $\xi(\tau)$, the overall phase, $\phi(\tau)$, and the intrinsic chirp, $C(\tau)$. In particular, the inclusion of the chirp in the above ansatz was due to Anderson [131]. Substituting ansatz (4.4.33) into Lagrangian (4.4.32) and performing the integration yields the corresponding effective Lagrangian,

$$\begin{aligned} L_{\text{eff}} &= A(\tau)^2 \left\{ \frac{-2\Lambda + \varepsilon Q(\tau) + 2\left[\xi(\tau)p'(\tau) + \phi'(\tau) - cp(\tau)\right]}{a(\tau)} + \frac{\pi^2 C'(\tau)}{12a(\tau)^3} \right\} \\ &\quad + \frac{\ln^2\left(\sqrt{1+A(\tau)^2} + A(\tau)\right) + \ln^2\left(\sqrt{1+A(\tau)^2} - A(\tau)\right)}{a(\tau)}, \end{aligned} \tag{4.4.34}$$

with primes standing for the derivatives, and

$$\begin{aligned} Q(\tau) &= 4 - \frac{4\pi \sin\left(\frac{C(\tau)}{2}\right)\cos\left(p(\tau)\right)}{\sinh\left(a(\tau)\right)\sinh\left(\frac{C(\tau)\pi}{2a(\tau)}\right)} \\ &= 4 - \frac{4a(\tau)\cos(p(\tau))}{\sinh(a(\tau))} + \frac{(a(\tau)^2+\pi)\cos(p(\tau))C(\tau)^2}{6a(\tau)\sinh(a(\tau))} + \mathcal{O}(C^4). \end{aligned} \tag{4.4.35}$$

The (dynamical) Euler–Lagrange equations for the variational parameters take the form of a nonlinear ODE system, which can be symbolically written in the vectorial form,

$$\dot{\mathbf{x}} = \mathbf{g}(\mathbf{x}), \tag{4.4.36}$$

where $\mathbf{x} = [A(\tau), a(\tau), p(\tau), C(\tau), \phi(\tau), \xi(\tau)]^T$. The VA-predicted linear stability analysis is based on the linearisation ansatz,

$$\mathbf{x} = \mathbf{x}_0 + \delta \mathbf{y} e^{\Omega\tau}, \quad \delta \ll 1;\ \Omega \in \mathbb{C}, \tag{4.4.37}$$

where $\mathbf{x}_0 = [A_0, a_0, p_0, 0, 0, 0]^T$ represents the steady state solution of the core soliton with (A_0, a_0, p_0) satisfying the system of variational equations (4.4.8)–(4.4.10). The substitution of Eq. (4.4.37) into Eq. (4.4.36) and the linearisation in δ lead to the eigenvalue problem,

$$\mathbf{H}\mathbf{y} = \Omega\mathbf{y}, \tag{4.4.38}$$

with the corresponding stability matrix $\mathbf{H}$. The stability of the stationary solution $\mathbf{x}_0$ is then determined by the eigenvalues Ω, which must be found in a numerical form; the solution $\mathbf{x}_0$ is stable if $\text{Re}(\Omega) \le 0$ for all eigenvalues.

4.5 Comparisons: numerics vs analytics

4.5.1 The soliton's core

For given parameters ε, c and Λ, we solved the variational equations (4.4.8)–(4.4.10) to produce suitable real solutions A, a and p, which then give a quasi-analytical approximation for the soliton's core described by function $\psi_{\text{core}}(z)$ (see Eq. (4.4.4)). As generic examples, in Fig. 4.10 we present, at $\varepsilon = 1$ and $c = 0.7$, the comparison of two soliton profiles obtained from the numerical results and VA for two different values of Λ. We have found $A \approx 1.228$, $a \approx 0.554$, $p \approx 0.377$ for $\Lambda = 0.5$ (Fig. 4.10(a)), and $A \approx 0.685$, $a \approx 0.414$, $p \approx 0.368$ for $\Lambda = 0.7$ (Fig. 4.10(b)). Particularly good agreement is observed in both cases.

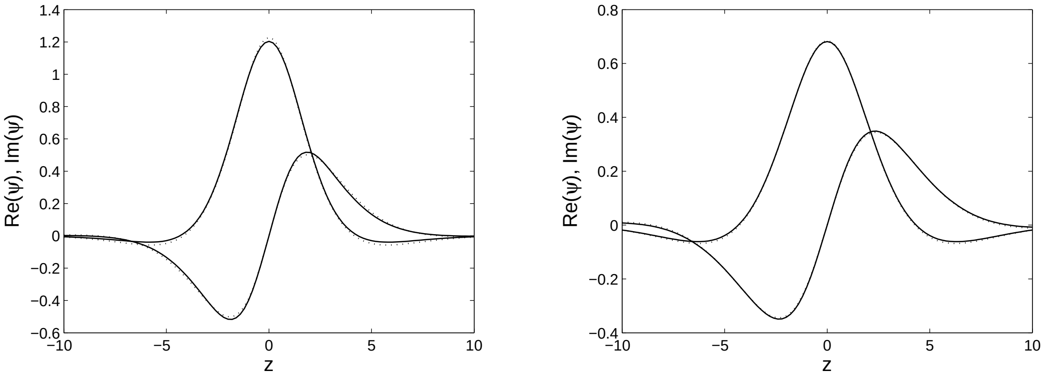

(a) $\varepsilon = 1, c = 0.7$, and $\Lambda = 0.5$

(b) $\varepsilon = 1, c = 0.7$, and $\Lambda = 0.7$

Figure 4.10: The comparison of two soliton profiles for two different values of Λ, as indicated in the caption to each panel. The solid lines correspond to numerical results, i.e., solutions of Eq. (4.3.4) imposed by constraints (4.3.8), with $\Delta z = 0.2$ and $L = 50$ (the z-axis is truncated to focus the picture on the soliton's core), both the real and imaginary parts being shown. The dotted lines are predictions of the variational approximation through solving system of Eqs. (4.4.8)–(4.4.10).

As we have considered the polynomial DNLS (4.4.11) in our VA calculations, here we also present the comparison of two profiles of the soliton's core, which are calculated from numerics and VA formulations for two different sets of parameter values; this is shown in Fig. 4.11. The obtained variational parameters in Figs. 4.11(a) and 4.11(b) are $(A, a, p) \approx (1.034, 0.338, 0.071)$ and $(A, a, p) \approx (0.668, 0.426, 0.369)$, respectively. As in the case of the saturable DNLS system, we observe from the figures that the VA-based analytical calculations for the polynomial DNLS equation are also in a good agreement with the corresponding numerical results.

To further confirm the agreement for different values of Λ, ε and c, in the following we compare parameters A, a and p produced by the VA with their numerical counterparts (we only do this for the saturable case). To calculate the latter, we make use of the following relations, which are generated by ansatz (4.4.4) at $z = 0$:

$$\psi(0) = A,\ \psi'(0) = \mathrm{i}pA,\ \psi''(0) = -A(a^2 + p^2). \tag{4.5.1}$$

Thus, using the central finite differences, we obtain the numerical counterparts of A, p

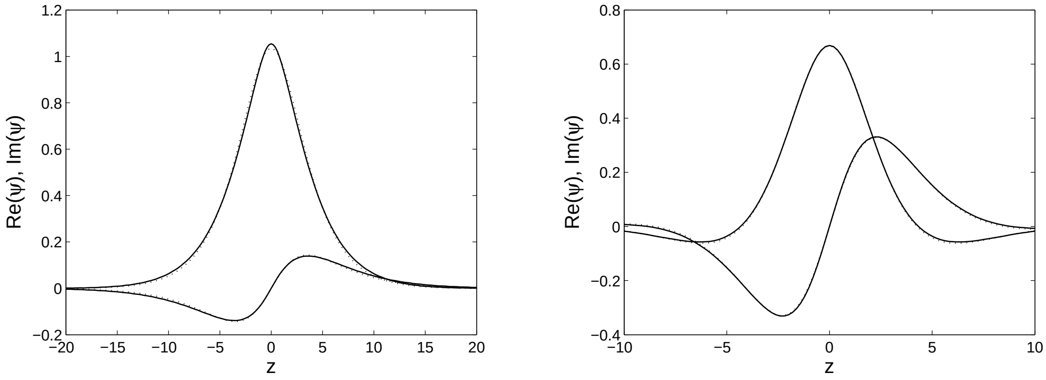

(a) $\varepsilon = 5, c = 0.7$, and $\Lambda = 0.5$ (b) $\varepsilon = 1, c = 0.7$, and $\Lambda = 0.7$

Figure 4.11: As Fig. 4.10 but for the polynomial DNLS equation (4.4.11) where the VA solutions for the soliton's core are obtained through solving Eqs. (4.4.13)–(4.4.15).

and a as

$$A_{\text{num}} = \psi_{\frac{N+1}{2}}, \tag{4.5.2}$$

$$p_{\text{num}} = \frac{\text{Im}\left(\psi_{\frac{N+1}{2}+1}\right) - \text{Im}\left(\psi_{\frac{N+1}{2}-1}\right)}{2A_{\text{num}}\Delta z}, \tag{4.5.3}$$

$$a_{\text{num}} = \pm\sqrt{-\frac{\text{Re}\left(\psi_{\frac{N+1}{2}-1}\right) - 2\text{Re}\left(\psi_{\frac{N+1}{2}}\right) + \text{Re}\left(\psi_{\frac{N+1}{2}+1}\right)}{A_{\text{num}}(\Delta z)^2} - p_{\text{num}}^2}. \tag{4.5.4}$$

The comparison of parameters (A, a, p) obtained numerically (solid lines) and from the VA (dashed lines) is shown in Fig. 4.12(a) for varying $1/\varepsilon$ and fixed $(c, \Lambda) = (0.7, 0.5)$. In that figure we only take the positive value of a in Eq. (4.5.4) to make it in accordance with the VA. We observe that the solid and dashed lines are generally close for all the three parameters. Nevertheless, we also obtain isolated values of $1/\varepsilon$, which behave as singular points. Near the singularities the numerical results deviate very rapidly from the predictions of the VA. In fact, at these singular points the numerically obtained solutions are strongly delocalised due to the resonance of the oscillating tails with the finite size of the computational domains (compare these points with those in Fig. 4.14(a)). Hence, the positions of such singularities depend on L and they may be considered as artifacts of approximating the infinite region by the finite domain.

Next, as in Fig. 4.10, where a better approximation is obtained for larger Λ, we also observe in Fig. 4.12(b) that the variational and numerical curves for A, a, p are closer for $\Lambda = 0.7$ than those in 4.12(a). In the latter case, the singularities are present too, even though they are less pronounced here.

To obtain a full description of the effect of Λ on the validity of the VA, let us now

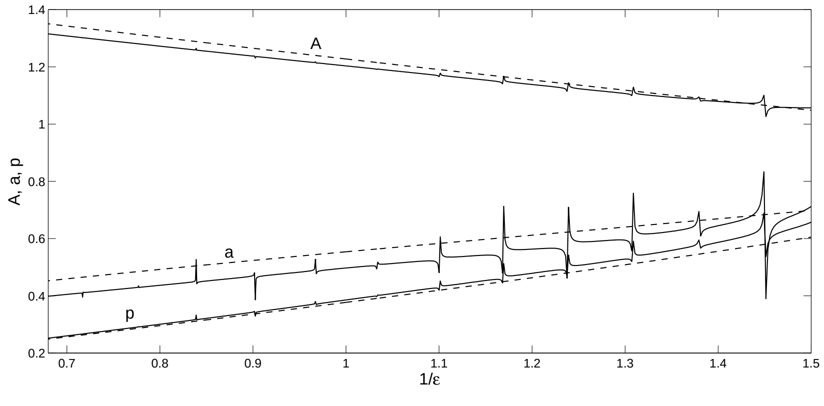

(a) $(c, \Lambda) = (0.7, 0.5)$

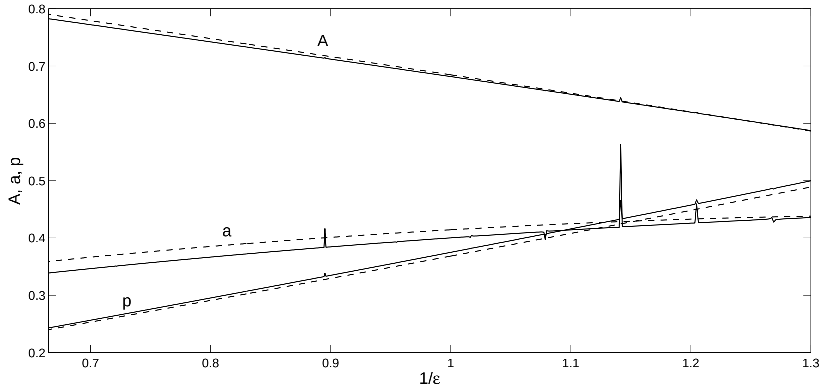

(b) $(c, \Lambda) = (0.7, 0.7)$

Figure 4.12: The comparison of parameters (A, a, p) calculated from the numerical data (solid lines) through Eqs. (4.5.2)–(4.5.4), and from the VA (dashed lines) through Eqs. (4.5.1), for varying $1/\varepsilon$ and fixed (c, Λ), as shown in the caption of each panel.

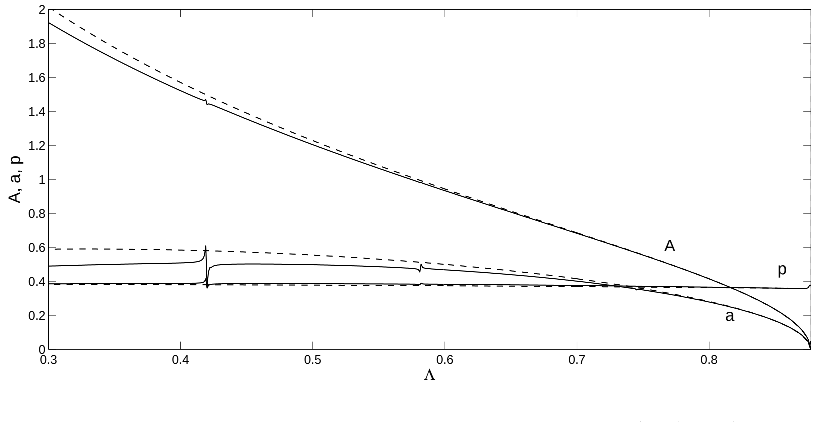

Figure 4.13: As Fig. 4.12 but for varying Λ and fixed $(\varepsilon, c) = (1, 0.7)$.

examine (A, a, p) as functions of Λ for fixed $(\varepsilon, c) = (1, 0.7)$, which is presented in Fig. 4.13. From the figure, we can confirm that the VA is more accurate for larger Λ. This agreement still holds even when the solutions become wide and vanish indicated by $a \to 0$ and $A \to 0$, respectively.

From the comparisons presented in Figs. 4.12 and 4.13 above, we can conclude that the VA provides a reliable approximation for the soliton's core. Nevertheless, the VA as well as our numerics are not capable of exploring the regime close to the anti-continuum limit. We observed that the amplitude of the oscillating tails of the numerical solutions increases as ε decreases, which creates a problem in the convergence of our numerical continuation. We also noted that the amplitude A in the ansatz (4.4.4) decreases as ε decreases and vanishes at a threshold point of ε. It is not yet clear whether or not there is embedded soliton close to the anti-continuum limit.

4.5.2 Embedded solitons

For the sake of comparisons, let us first plot the measure Δ_r as a function of $1/\varepsilon$ for the parameter values $(\Lambda, c, \Delta z, L)$ used in Figs. 4.10(a) and 4.10(b), which are shown, respectively, in Figs. 4.14(a) and 4.15(a). One should notice that the former figure is basically similar to Fig. 4.5(a) but with a longer computational domain and a shorter interval of $1/\varepsilon$, whereas the latter is replotted from the top panel of Fig. 4.6(b) by cutting the domain of $1/\varepsilon$.

Next, to predict the location of ESs in the framework of the VA, as explained in the previous section, we substitute the solution of Eqs. (4.4.8)–(4.4.10) and the root(s) λ of Eq. (4.2.3) into Eqs. (4.4.30) to find E as a function of ε, c and Λ. Therefore, the existence of ESs can be predicted by seeking for the values of parameters at which $E = 0$. For the parameter values used in Figs. 4.14(a) and 4.15(a), curves for E are displayed, respectively, in Figs. 4.14(b) and 4.15(b). It is seen that $E \neq 0$ in both figures, i.e., genuinely localised solitons cannot be directly predicted by the VA.

However, we can propose a conjecture, based on a "phenomenological" consideration of the figures, that there are two zeros of Δ_r on the left and right of a maximum of E. For example, in Fig. 4.14 we have the maximum of E at $\varepsilon \approx 0.853$ (i.e., at $1/\varepsilon \approx 1.172$), which is located between two adjacent numerically found zeros of Δ_r. The same phenomenon also takes place in Fig. 4.15, where two zero-crossing points lie between a maximum of E, i.e., at $\varepsilon \approx 1.020$ (i.e., at $1/\varepsilon \approx 0.980$). We have also computed the signed measure Δ_r and E for other combinations of parameter values, where we observed the same pattern (see, e.g., Fig. 4.16). Thus, we conclude that, with the addition of a

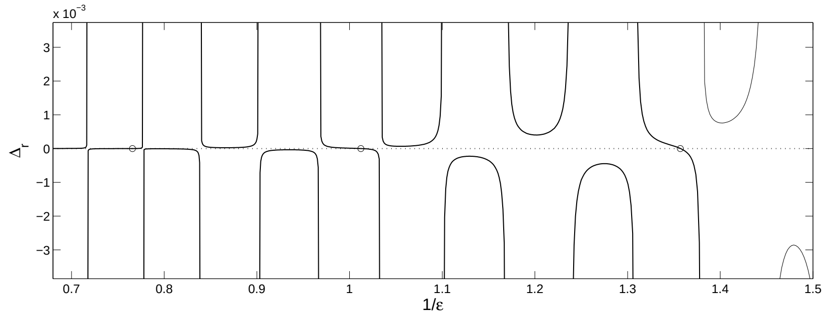

(a)

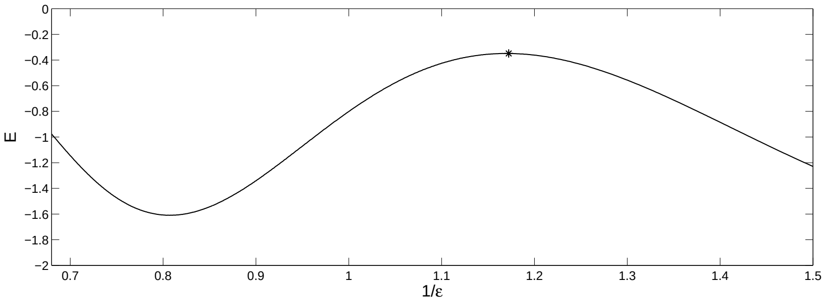

(b)

Figure 4.14: (a) The signed measure Δ_r (cf. Eq. (4.3.10)) as a function of $1/\varepsilon$ for $c = 0.7$, $\Lambda = 0.5$, $\Delta z = 0.2$ and $L = 50$, where Δ_r is zero at $\varepsilon \approx 0.737, 0.988, 1.306$ (or at $1/\varepsilon \approx 1.357, 1.012, 0.766$), as shown by empty circles. (b) E versus $1/\varepsilon$ (cf. Eq. (4.4.30)), for the same parameter values (Λ, c) as in panel (a) and for the corresponding (A, a, p) and root(s) λ obtained from Eqs. (4.4.8)-(4.4.10) and Eq. (4.2.3), respectively. It is clearly seen that $E \neq 0$ in the observed domain of $1/\varepsilon$. However, we can conjecture that ESs are located near the maximum of E, i.e., at $\varepsilon \approx 0.853$ (or at $1/\varepsilon \approx 1.172$), as indicated by the star.

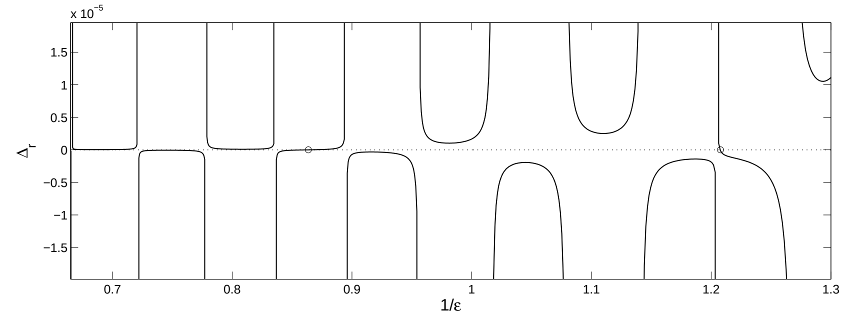

(a)

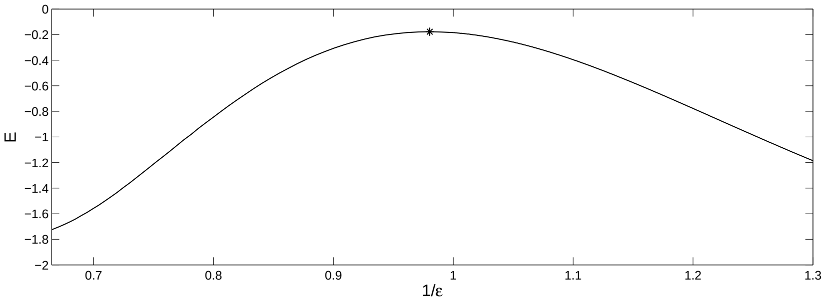

(b)

Figure 4.15: The same as Fig. 4.14, but for $\Lambda = 0.7$. Zeros of Δ_r are found at $\varepsilon \approx 0.828, 1.158$ (or at $1/\varepsilon \approx 1.208, 0.864$), which are the same as those in Fig. 4.6(b), and the maximum of E occurs at $\varepsilon \approx 1.020$ (or at $1/\varepsilon \approx 0.980$).

constant, function E may be able to predict the location of ESs. We suspect that the missing constant, which amounts to the shift of the plot for E vertically, is related to the choice of the ansatz (see, e.g., Boyd [132] for different ansatz accounting for the oscillating tails).

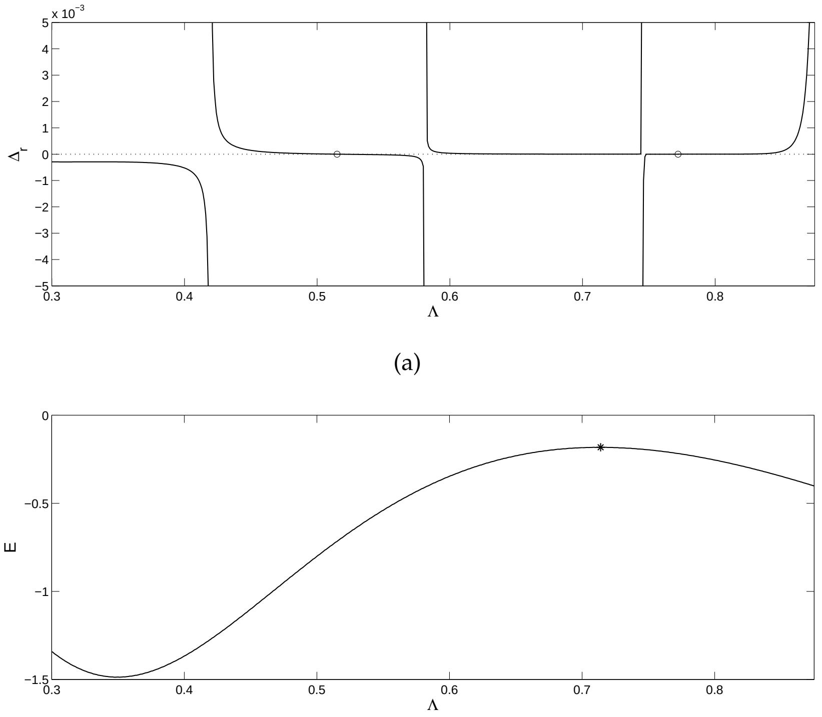

(a)

(b)

Figure 4.16: As Fig. 4.14, but with the signed measure Δ_r being a function of Λ (for fixed $c = 0.7$, $\varepsilon = 1$, $\Delta z = 0.2$ and $L = 50$). Zeros of Δ_r are found at $\Lambda \approx 0.515, 0.772$ and curve E is maximum at $\Lambda \approx 0.714$.

To support further our conjecture, we also plot the same quantities as those presented in the previous figures, but now for the polynomial DNLS (4.4.11). These plots are shown in Fig. 4.17 by using parameter values as in Fig. 4.11(b). From the top panel of the figure, we can see clearly that $\Delta_r \neq 0$ along the observed domain of $1/\varepsilon$, which indicates that the polynomial DNLS (4.4.11) does not support the travelling lattice solitons with vanishing tails. Most interestingly, as shown in the bottom panel, the curve E' does not have any local maximum, which is in accordance with the contraposition statement of our conjecture for the saturable DNLS.

4.5.3 Stability

To determine the stability of the soliton based on the VA, we have solved the eigenvalue problem (4.4.38). For the soliton shown in Fig. 4.10(a), i.e., with $\mathbf{x}_0 \approx [1.228, 0.554, 0.377,$

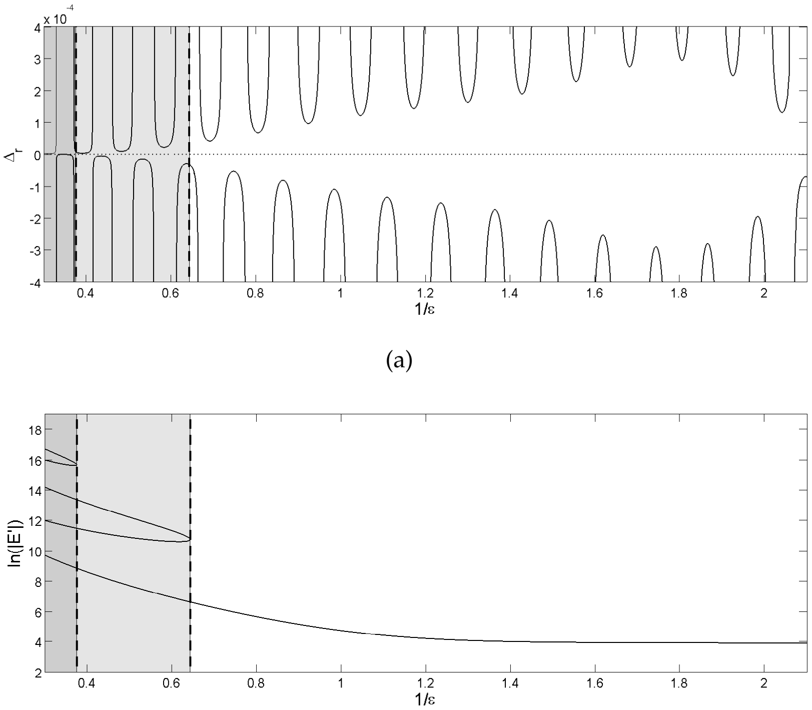

(a)

(b)

Figure 4.17: As Fig. 4.14 but for the polynomial DNLS (4.4.11) where ln $(|E'|)$ (see expression (4.4.31)) is plotted. The parameter values used are the same as in Fig. 4.11(b). The number of roots λ, which is indicated by the white (one root), light shaded (three roots) and dark shaded (five roots) regions (see cf. Fig. 4.2(b)), are the same as the number of curves E' in the corresponding regions.

$0, 0, 0]^T$, we obtain the corresponding eigenvalues $\Omega \approx 0, 0, 0, 0, 0.436\mathrm{i}, -0.436\mathrm{i}$. For the soliton in Fig. 4.10(b), i.e., $\mathbf{x}_0 \approx [0.685, 0.414, 0.368, 0, 0, 0]^T$, the corresponding eigenvalues are $\Omega \approx 0, 0, 0, 0, 0.225\mathrm{i}, -0.225\mathrm{i}$. As the real part of all the eigenvalues is zero, we conclude that both solitons are *stable*. These results are in agreement with the numerical findings of Melvin *et al.* [66].

4.6 A failure of the finite-difference method: numerical stability

To examine the stability of the numerically obtained solutions to Eq. (4.1.1), recall the time-dependent model (4.1.4). Introducing the linearisation ansatz $\psi(z, \tau) = \acute{\psi}(z) + \delta(r(z)\mathrm{e}^{\mathrm{i}\mu\tau} + s^*(z)\mathrm{e}^{-\mathrm{i}\mu^*\tau})$, with $|\delta| \ll 1$ being a small perturbation amplitude and with the asterisk indicating complex conjugation, into Eq. (4.1.4), we thereby obtain the linear eigenvalue problem (EVP) for the stability of $\acute{\psi}(z)$, given by

$$-\mu \begin{pmatrix} r \\ s \end{pmatrix} = \begin{pmatrix} \mathcal{L}_+ & -\dfrac{\acute{\psi}^2}{(1+|\acute{\psi}|^2)^2} \\ \dfrac{\acute{\psi}^{*2}}{(1+|\acute{\psi}|^2)^2} & \mathcal{L}_- \end{pmatrix} \begin{pmatrix} r \\ s \end{pmatrix} = \mathcal{H} \begin{pmatrix} r \\ s \end{pmatrix}, \tag{4.6.1}$$

where we have introduced the operators

$$\mathcal{L}_\pm \equiv \mathrm{i}c\frac{\mathrm{d}}{\mathrm{d}z} \pm \left[(2\varepsilon - \Lambda) - \varepsilon\Delta_1 + \frac{1}{(1+|\acute{\psi}|^2)^2}\right], \tag{4.6.2}$$

with $\Delta_1 x(z) = x(z+1) + x(z-1)$. The stability of the solution $\acute{\psi}(z)$ is then determined by the eigenvalues of Eq. (4.6.1). It is clear that the solution is unstable if and only if there is at least one eigenvalue μ with a negative imaginary part. Here, we then solve Eq. (4.6.1) numerically by means of the finite-difference method, as previously discussed in Section 4.3.

For a soliton that corresponds to one of the zero crossings in Fig. 4.15(a), i.e., $\varepsilon = 1.158$, we present in Fig. 4.18(a) the EVP spectra in the complex plane. As there are eigenvalues with negative imaginary parts, the soliton is *unstable*. We show in Fig. 4.18(b) combination of the eigenfunction $(r + s^*)$ corresponding to the most unstable eigenvalue, which demonstrate that the eigenfunction is indeed localised. These results are in contrast to our VA stability and the numerical results of Melvin *et al.* [66] obtained by calculating the corresponding Floquet multipliers, where the solitons were shown to be linearly stable.

To understand the discrepancy, we investigate the effect of the grid spacing Δz on the EVP (4.6.1). By using the same parameter values, we show in Fig. 4.18(a) the distribu-

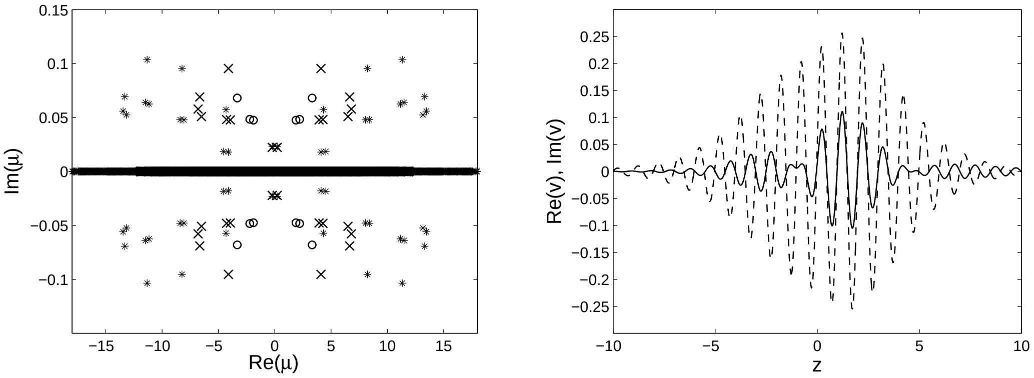

(a) $\varepsilon = 1.158$

(b) $\mu = 3.3295 + 0.0681\mathrm{i}$

Figure 4.18: (a) The eigenvalues structure in the complex plane of an embedded soliton in Fig. 4.15(a). The effect of different grid spacings on the distribution of the eigenvalues are also shown, i.e., $\Delta z = 0.2$ (circle), $\Delta z = 0.1$ (cross) and $\Delta z = 0.05$ (star). (b) Eigenfunction $v = r + s^*$ obtained from the numerical solution of the linear eigenvalue problem (4.6.1), corresponding to the most unstable eigenvalue shown in panel (a) with $\Delta z = 0.2$.

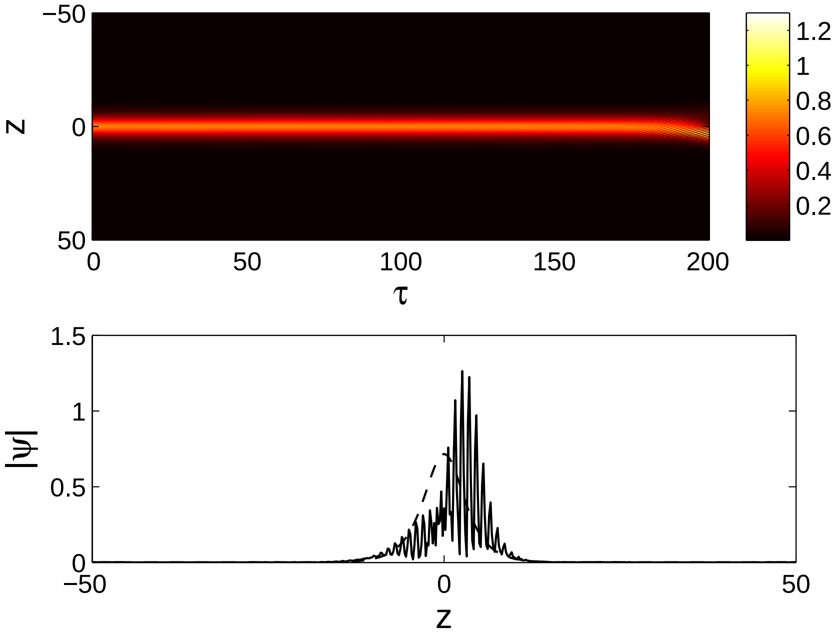

Figure 4.19: Numerical evolution of the soliton confirming the 'instability' shown in Fig. 4.18(a) with $\Delta z = 0.2$. The dashed line is the initial condition and the solid line is the solution at $\tau = 200$.

tion of the eigenstructures for $\Delta z = 0.2, \Delta z = 0.1$ and $\Delta z = 0.05$, where we obtain that the smaller the Δz, the more unstable eigenvalues one will gain. This contradicts the common intuition that a discrete approximation will converge to the continuous limit for a small enough Δz. We believe that the spurious instability is caused by the numerical approximation of the advance–delay terms. The instability can indeed be observed in the time-dynamics of the advance–delay-differential equation (4.1.4) as shown in Fig. 4.19, where we have used the same spatial discretization and a Runge-Kutta method for the time integration. One can see that the soliton suffers from high-frequency unstable modes, as predicted by the unstable eigenfunctions in Fig. 4.18(b).

One possible solution to resolve the discrepancy is to use the pseudo-spectral method as suggested and successfully applied in a Fermi-Pasta-Ulam equation by Flytzanis *et al.* [130]. This issue will be studied further.

4.7 Conclusion

The aim of this work was to revisit the general problem of the existence and stability of travelling localised pulses in discrete models based on the one-dimensional discrete nonlinear Schrödinger (DNLS) equation with saturable nonlinearity. After analysing the linear spectrum of the model, carried out through numerical calculations and perturbation analyses, we obtained the bifurcation diagram of the spectral bands. According to Melvin *et al.* [66, 67], finding genuinely localised solutions by varying one parameter only becomes possible within parameter regions of the spectral bands in which there is a single resonance with linear waves.

In the aforementioned references, it was demonstrated that the DNLS equation with saturable onsite nonlinearity admits isolated genuine travelling-soliton states. In this work, we have used a numerical scheme to solve the saturable DNLS equation in a moving coordinate frame, which is an advance–delay-differential equation. By using a Newton–Raphson method, together with a measure for the tails (either the one modified from that proposed by Melvin *et al.* [66, 67] or our alternative measure), we confirmed the existence of genuinely travelling discrete solitons, which are embedded solitons (ESs). We showed that the outputs from our numerical scheme, for a grid spacing small enough and a computational domain large enough, are identical with those reported in [66].

In addition to the numerical work, we have developed a semi-analytical approach for seeking travelling solitons, based on the application of the variational approximation (VA) to the advance–delay-differential form of the saturable DNLS equation in the moving coordinate frame. The approximated (core) solitons are in good agreement with the corresponding numerical findings. The VA was also derived to examine the stability of the travelling solitons which shows that they are stable, i.e., in agreement with [66]. Moreover, the VA was also developed to predict the locations of travelling lattice solitons with strictly vanishing tails and the relevance of the results was discussed.

Although we obtained the solutions reported in [66] through our numerical scheme, we showed that the corresponding scheme for the eigenvalue problem did not produce the correct results. This discrepancy is left for future investigation.

CHAPTER 5

Conclusion

In this thesis, we have examined the existence and stability of discrete solitons in two main lattice models, i.e., cubic and saturable discrete nonlinear Schrödinger (DNLS) equations. In the cubic-type model, we considered stationary discrete solitons under the effect of parametric driving and/or damping. In the saturable-type model, we studied travelling lattice solitons. Let us now summarise the work and the main results obtained in the abovementioned studies as well as point out several problems that would be interesting to consider in the future.

5.1 Summary

We began our discussion in Chapter 1 by providing background information about solitons and the considered lattice equations. These include a definition and historical development of (discrete) solitons, and a general review of the DNLS equations. In particular, we outlined the development of theoretical and experimental studies of discrete solitons in the context of two applications, i.e., optical waveguide arrays and systems of micro- and nanoelectromechanical (MEMS and NEMS) resonators. Moreover, in the same chapter, we presented preliminary analyses of stationary and travelling discrete solitons in the cubic and saturable DNLS models. Some analytical methods used throughout this thesis were also reviewed briefly in this chapter.

In Chapter 2 we investigated a parametrically driven discrete nonlinear Schrödinger (PDNLS) equation, i.e., a cubic DNLS model with the inclusion of parametric driving with strength γ. The existence and stability of fundamental (onsite and intersite) bright and dark discrete solitons were discussed both analytically and numerically. Our analyses relied on the anticontinuum (AC) limit approach from which we can employ a perturbation expansion to approximate the fundamental soliton solutions for the case of small coupling constant ε. In carrying out the examination of the stability of solitons, we solved numerically a corresponding eigenvalue problem (EVP) from which we obtained the stability region in the (ε, γ)-plane. Analytical calculations of the EVP based on a perturbation method were also derived to predict the onset of instability for each soliton. Moreover, to confirm the typical dynamics of solitons in the stable and unstable parameter regions, we performed numerical integrations of the PDNLS equation. All of the aforementioned analyses were presented in Sections 2.2 and 2.3 for, respectively, bright and dark solitons.

From our studies above, we obtained that our analytical calculations, for small ε, are generally consistent with the numerics. Regarding the effect of parametric driving on the stability results, we found that undriven onsite bright solitons, which are stable for any coupling constant, and onsite dark solitons, which are stable for small coupling constant, can be destabilised by a parametric driving; for the onsite bright soliton, this result has been reported earlier by Susanto *et al.* [91]. By contrast, intersite bright and dark solitons, which were shown to be always unstable in the undriven case, can be stabilised by the driving. Interestingly, we also found a range of values of γ in which a discrete dark soliton is stable for all ε.

Additional work in Chapter 2, discussed in Section 2.4, was on the application of a PDNLS model in arrays of parametrically-driven MEMS and NEMS resonators. By using a multiscale expansion method, we showed that our DNLS equation can be derived from a governing equation of MEMS and NEMS resonators, i.e., a particular type of parametrically driven discrete Klein–Gordon equation. The numerical integrations of the Klein–Gordon system were then demonstrated to confirm the relevance of our stability findings in the PDNLS model. From the results of the latter work, we concluded that the parametrically driven DNLS equation can be used to describe, under certain conditions, the behaviour of MEMS and NEMS resonators.

Next, in Chapter 3, we extended the ideas of Chapter 2 by introducing a damping term with strength α in the PDNLS system. A study for such a model, called a parametrically driven damped discrete nonlinear Schrödinger (PDDNLS) equation, was performed for onsite and intersite bright solitons (in focusing PDDNLS). We identified that there exist two and four types of onsite and intersite discrete solitons, respectively. We called those solutions onsite type I and II, and intersite type I, II, III and IV, where the last two types are essentially the same, due to symmetry. We observed that the type I solution for onsite and intersite solitons, which can be unstable in the case of no dissipation, can be stabilised by the damping, whereas the other types of solution are always unstable. We also found an interval of values of α in which the onsite type I is stable for all ε. Our further analysis demonstrated that the onsite type I and II experience a saddle-node bifurcation where the limit point is achieved when the damping and driving strengths are equal (for any coupling constant). The same bifurcation was also shown to be undergone by the intersite type I and II. Furthermore, we observed a pitchfork bifurcation occurring in intersite type I, III and IV. The corresponding branch points for such a bifurcation in the (ε, α)-plane have been calculated analytically, for small ε, and numerically.

The most interesting result in the study of PDDNLS equation is the existence of periodic solitons (limit cycles) which emerge from Hopf bifurcations experienced by onsite type I, intersite type I and intersite type III-IV. By using the numerical continuation software Matcont, we performed continuations of the corresponding limit cycles as well as the stability of the periodic solitons; this was discussed in Section 3.5. We found subcritical Hopf bifurcations along the existence curve of the onsite type I and intersite type III-IV. In addition, we observed three Hopf bifurcations for intersite type I, of which two were shown to be supercritical.

Next, in Chapter 4 we discussed the existence and stability of travelling solitary waves in the DNLS model with saturable nonlinearity. This study basically followed the idea of Melvin *et al.* [66, 67] who initially investigated the problem using a pseudo-spectral numerical scheme.

As noted in the abovementioned references, a travelling solitary wave of the saturable DNLS equation would be easy to seek by varying one parameter only. This becomes possible if one can identify the parameter regions of the spectral bands where a single resonance of the travelling solitons with plane waves occurs. To do this, we examined the linear spectrum of the model in the travelling wave frame, i.e., an advance–delay-differential equation, carried out numerically, as done by Melvin *et al.* [66, 67], and analytically through a perturbation expansion. This analysis was presented in Section 4.2.

To solve numerically the travelling solutions in the saturable model, i.e., via the advance-delay-differential equation, we applied a finite difference discretization. From this scheme, we had a system of difference equations which was then solved using a Newton-Raphson method. Since the obtained solutions were generally accompanied by nonzero oscillatory tails, as suggested in the latter references, we need to add an extra tail condition to find solutions with vanishing tails, i.e., embedded solitons (ESs). For this condition, we used the measure which was modified from that proposed by Melvin *et al.* [66, 67], corroborated by our alternative measure. For a grid spacing small enough and a computational domain large enough, we showed that the results produced from our numerical scheme are consistent with those in [66, 67]. The numerical works above were given in Section 4.3.

For the analytical part of our study in Chapter 4, presented in Section 4.4, we employed a variational approximation (VA). We observed that the approximated (core) solitons are in good agreement with the corresponding numerical results. The VA-based stability analysis was also performed, showing that the solutions are stable, i.e., in accordance with that reported by Melvin *et al*. [66]. In addition, we also derived the VA to predict the locations of the ESs. In the latter work, our analytical prediction could not be verified numerically and we argued that this is related to the choice of the ansatz for the tails as discussed in the chapter. The condition when there are two waves in the linear spectrum is indeed another case that our tail will fail, even though it is still a big question whether embedded solitons exist at all in such a case, as explained in the chapter.

5.2 Future work

In this section, we note several problems that could be interestingly proposed as future work. Some of them arise from the extension of the ideas in the present work, while the others emerge from the questions raised in the course of our study which need further investigations.

One possible problem is to expand the work of Chapter 2 to, e.g., a twisted localised mode. In the absence of parametric driving, such a solution has been considered, e.g., by Kevrekidis *et al*. [114] where it was shown that it is stable for small coupling constant. Unlike the case of an undriven intersite soliton with in-phase oscillation where the bifurcating unstable eigenvalues lie along the imaginary axis of the spectral plane, the instability of the out-of-phase intersite mode occurs because of the presence of a quartet of complex eigenvalues. Thus, its typical dynamics is in the form of an unstable breather. Moreover, it was also shown that an undriven twisted soliton experiences a saddle-node bifurcation, and this must be also the case in the driven mode.

Another interesting problem that could be pursued in the future is the study of dark solitons in the defocusing PDDNLS equation. For the case of bright solitons in the focusing PDDNLS model, it was already shown in this thesis that these solutions have rich dynamical localisation effects, including the existence of periodic solitons. Thus, one could immediately predict that dark solitons in the driven and damped DNLS equation will also permit such interesting properties. In addition, the existence and stability of a twisted discrete soliton in the PDDNLS system would be also interesting to investigate.

The interaction of stable standing waves and perturbations in the PDDNLS system is also interesting. From equation (3.1.1), we note the balance equation

$$\mathrm{i}\frac{\mathrm{d}}{\mathrm{d}t}|\phi_n|^2 = \varepsilon(J_n - J_{n-1}) - 2\mathrm{i}\alpha|\phi_n|^2 + \gamma(\overline{\phi}_n^2 - \phi_n^2), \tag{5.2.1}$$

where $J_n = \overline{\phi}_{n+1}\phi_n - \phi_{n+1}\overline{\phi}_n$. For simplicity, consider the case $\varepsilon = 0$. Perturbing the solitary waves will cause the right hand side of (5.2.1) to be nonzero, which may lead to instability. Hence, the instability of solitary waves in this case is rather not surprising. Nevertheless, we reported that stable solitary waves exist, which indicate that there should be a delicate balance on the right-hand side of (5.2.1). It is interesting to study whether perturbations applied initially to a stable standing wave will persist or radiate and later vanish due to the damping. Note that such a study has been presented by Johansson and Aubry [133] for the conservative limit when $\gamma = \alpha = 0$.

Next, as it has been pointed out in Chapter 4, our study of travelling solitons of the saturable DNLS model left an unanswered question regarding the discrepancies of the numerical stability results due to the presence of spurious unstable eigenvalues. The failure of a finite difference numerical scheme in calculating the eigenvalue problems has been also noted, e.g., by Yang [134] and Boyd [135]. These references recommend a pseudo-spectral method which is arguably more accurate and reliable to solve the stability problem numerically. This method has been successfully applied in a Fermi-Pasta-Ulam equation by Flytzanis *et al.* [130].

The most interesting problem that we also would like to address is the study of travelling lattice solitary waves in the PDDNLS equation. The existence and stability of travelling solitons in the continuous version of the PDDNLS equation has been considered by Barashenkov & Zemlyanaya [136] where it was shown that a single-hump travelling soliton does not exist, while a multi-hump travelling soliton exists but is unstable. Travelling solitons in an undamped parametrically driven nonlinear Schrödinger equation were also studied previously by Barashenkov *et al.* [95], showing that a stable travelling soliton solution exists for a small driving constant, whereas a strongly driven soliton can only be stable when it travels with high velocity.

As a preliminary analysis to the problem above, we force a discrete soliton to move across the lattice by introducing a phase variation, i.e., by setting the initial condition $\phi_n(0) = \mathrm{e}^{\mathrm{i}Kn}u_n$, where u_n is a localised standing wave of the PDDNLS equation and K is the phase 'kick' controlling the initial velocity of the soliton, and then follow the evolution of the soliton through numerically integrating the PDDNLS equation. A couple of simulations for different parameter values is presented in Fig. 5.1. Here we set

$\varepsilon = 5$, which corresponds to relatively strong coupled lattices so that the obtained results are comparable with the continuous counterparts, and frequency $\Lambda = 1$. In the case of no dissipation and for relatively small and large driving strengths, our simulation seemingly agrees with that reported by Barashenkov *et al*. [95]; see the top panels of the figure. For relatively small damping and driving strengths (see the middle panels of the figure), the soliton can move across the lattice but it loses energy to radiation or dissipation. The loss is more pronounced for larger phase 'kick'. Moreover, in the case of a relatively strong driving and damping, as shown in the bottom panels of the figure, the soliton propagates across a few lattice before it quickly vanishes. From the above observations, we may argue that travelling lattice solitons in the PDDNLS equation either exist but are unstable or do not exist. It is of particular interest to study the problem.

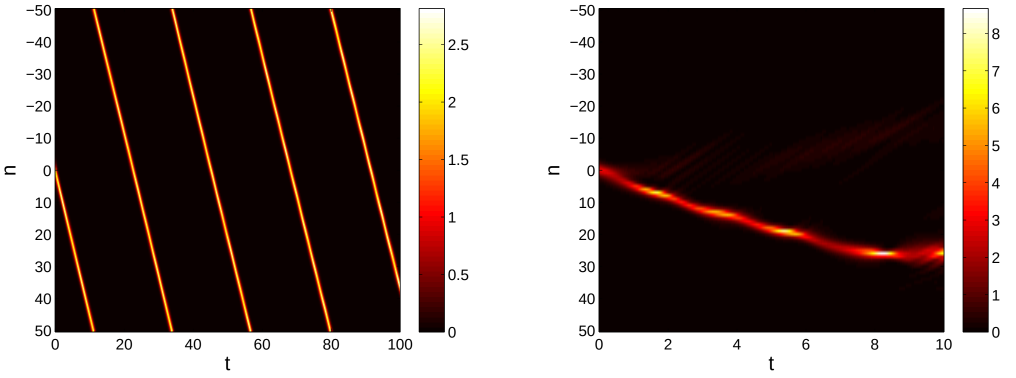

(a) $\alpha = 0, \gamma = 0.01, K = 0.5$ (b) $\alpha = 0, \gamma = 0.5, K = 0.5$

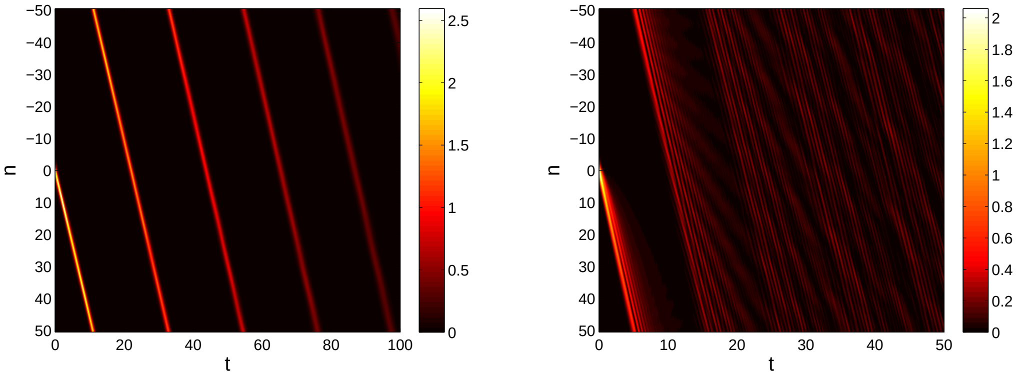

(c) $\alpha = 0.005, \gamma = 0.01, K = 0.5$ (d) $\alpha = 0.005, \gamma = 0.01, K = 2$

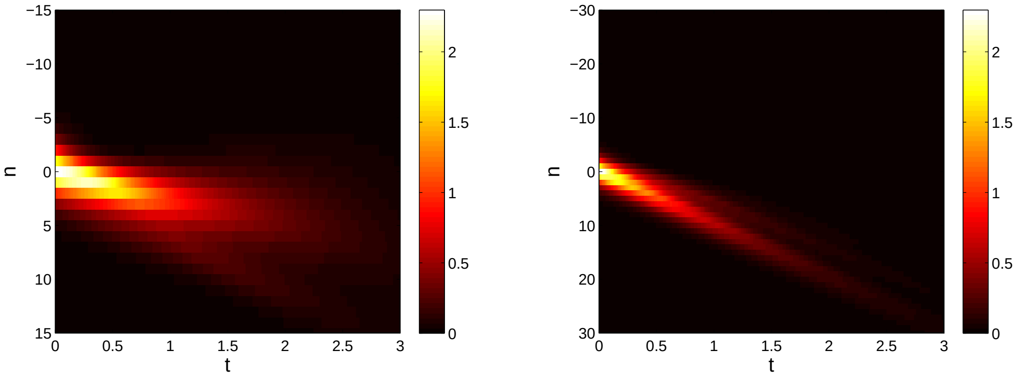

(e) $\alpha = 0.485, \gamma = 0.5, K = 0.5$ (f) $\alpha = 0.485, \gamma = 0.5, K = 2$

Figure 5.1: Numerical evolution of discrete solitons in the PDDNLS equation with the introduction of initial phase 'kick' K, for different values of damping and driving strengths, α and γ, as indicated in the caption in each panel. In all the figures, we take the coupling constant $\varepsilon = 5$ and frequency $\Lambda = 1$.

References

[1] A. Scott (Editor), *Encyclopedia of Nonlinear Science* (Routledge, New York and London, 2005).

[2] P. G. Drazin and R. S. Johnson, *Solitons: An Introduction* (Cambridge University Press, Cambridge, 1989).

[3] N. J. Zabusky and M. D. Kruskal, *Interaction of "solitons" in a collisionless plasma and the recurrence of initial states*, Phys. Rev. Lett. **15**, 240 (1965).

[4] J. E. Allen, *The early history of solitons (solitary waves)*, Phys. Scr. **57**, 436 (1998).

[5] M. Remoissenet, *Waves Called Solitons: Concepts and Experiments* (Springer, Berlin, 1999).

[6] N. J. Zabusky and M. A. Porter, *Soliton*, Scholarpedia 5(8):2068 (2010).

[7] A. Scott, *Nonlinear Science: Emergence and Dynamics of Coherent Structures* (Oxford University Press, Oxford, 2003).

[8] R. K. Dodd, J. C. Eilbeck, J. D. Gibbon and H. C. Morris, *Solitons and Nonlinear Wave Equations* (Academic Press, London, 1982).

[9] J. S. Russell, *Report on Waves*, Rep. Meet. British Assoc. Adv. Sci. **14**, 311 (1844).

[10] D. J. Korteweg and G. de Vries, *On the change of form of long waves advancing in a rectangular canal, and on a new type of long stationary waves*, Phil. Mag. (5) **39**, 422 (1895).

[11] J. V. Boussinesq, *Théorie de l'intumescence liquide appelée onde solitaire ou de translation se propageant dans un canal rectangulaire*, Comptes Rendus **72**, 755 (1871).

[12] L. Rayleigh, *On waves*, Phil. Mag. (5) **1**, 257 (1876).

[13] E. Fermi, J. R. Pasta and S. Ulam, *Studies of nonlinear problems. I.*, Report LA-1940 (1955).

[14] T. Dauxois, *Fermi, Pasta, Ulam and a mysterious lady*, Physics Today (1) **61**, 55 (2008).

[15] C. S. Gardner, J. M. Greene, M. D. Kruskal and R. M. Miura, *Method for solving the Korteweg-deVries equation*, Phys. Rev. Lett. **19**, 1095 (1967).

[16] B. Skuse, *The soliton: a wave less ordinary*, Isquared **12**, 9 (2010).

[17] V. E. Zakharov and A. B. Shabat, *Exact theory of two-dimensional self-focusing and one-dimensional selfmodulation of waves in nonlinear media*, Sov. Phys. JETP **34**, 62 (1972).

[18] M. J. Ablowitz, D. J. Kaup, A. C. Newell and H. Segur, *Method for solving the Sine-Gordon equation*, Phys. Rev. Lett. **30**, 1262 (1973).

[19] M. Toda, *Vibration of a chain with nonlinear interaction*, J. Phys. Soc. Japan **22(2)**, 431 (1967).

[20] M. Toda, *Wave propagation in anharmonic lattices*, J. Phys. Soc. Japan **23(3)**, 501 (1967).

[21] M. J. Ablowitz and J. F. Ladik, *Nonlinear differential-difference equations and Fourier analysis*, J. Math. Phys. **17**, 1011 (1976).

[22] H. Flaschka, *The Toda lattice. II. Existence of integrals*, Phys. Rev. B **9**, 1924 (1974).

[23] A. Scott, F. Y. F. Chu and D. W. McLaughlin, *The soliton: a new concept in applied science*, Proceedings of the IEEE. (10) **16**, 1443 (1973).

[24] P. G. Kevrekidis (Editor), *Discrete Nonlinear Schrödinger Equation: Mathematical Analysis, Numerical Computations and Physical Perspectives* (Springer, Berlin, 2009).

[25] F. Lederer, G. I. Stegeman, D. N. Christodoulides, G. Assanto, M. Segev and Y. Silberberg, *Discrete solitons in optics*, Phys. Rep. **463**, 1 (2008).

[26] M. Salerno, *Quantum deformations of the discrete nonlinear Schrödinger equation*, Phys. Rev. A **46**, 6856 (1992).

[27] V. O. Vinetskii and N. V. Kukhtarev, *Theory of the conductivity induced by recording holographic grating in nonmetallic crystals*, Sov. Phys. Solid State **16**, 2414 (1975).

[28] A. Piccardi, A. Alberucci, N. Tabiryan and G. Assanto, *Dark nematicons*, Opt. Lett. **36**, 1356 (2011).

[29] D. N. Christodoulides, F. Lederer and Y. Silberberg, *Discretizing light behaviour in linear and nonlinear waveguide lattices*, Nature (London) **424**, 817 (2003).

[30] A. L. Jones, *Coupling of optical fibers and scattering in fibers*, J. Opt. Soc. Am. **55**, 261 (1965).

[31] S. Somekh, E. Garmire, A. Yariv, H. L. Garvin and R. G. Hunsperger, *Channel optical waveguide directional couplers*, Appl. Phys. Lett. **22**, 46 (1973).

[32] D. N. Christodoulides and R. I. Joseph, *Discrete self-focusing in nonlinear arrays of coupled waveguides*, Opt. Lett. **13**, 794 (2003).

[33] H. S. Eisenberg, Y. Silberberg, R. Morandotti, A. R. Boyd and J. S. Aitchison, *Discrete spatial optical solitons in waveguide arrays*, Phys. Rev. Lett. **81**, 3383 (1998).

[34] R. Morandotti, U. Peschel, J. S. Aitchison, H. S. Eisenberg and Y. Silberberg, *Dynamics of discrete solitons in optical waveguide arrays*, Phys. Rev. Lett. **83**, 2726 (1999).

[35] H. S. Eisenberg, Y. Silberberg, R. Morandotti and J. S. Aitchison, *Diffraction management*, Phys. Rev. Lett. **85**, 1863 (2000).

[36] R. Morandotti, H. S. Eisenberg, D. Mandelik, Y. Silberberg, D. Modotto, M. Sorel, C. R. Stanley and J. S. Aitchison, *Interactions of discrete solitons with structural defects*, Opt. Lett. **28**, 834 (2003).

[37] M. Segev, B. Crosignani, A. Yariv and B. Fischer, *Spatial solitons in photorefractive media*, Phys. Rev. Lett. **68**, 923 (1992).

[38] N. K. Efremidis, S. Sears, D. N. Christodoulides, J. W. Fleischer and M. Segev, *Discrete solitons in photorefractive optically induced photonic lattices*, Phys. Rev. E **66**, 046602 (2002).

[39] J. W. Fleischer, T. Carmon, M. Segev, N. K. Efremidis and D. N. Christodoulides, *Observation of discrete solitons in optically induced real time waveguide arrays*, Phys. Rev. Lett. **90**, 023902 (2003).

[40] Yu. S Kivshar and G. P. Agrawal, *Optical Solitons: From Fibers to Photonic Crystals* (Academic Press, Amsterdam and London, 2003).

[41] D. N. Christodoulides and E. D. Eugenieva, *Blocking and routing discrete solitons in two-dimensional networks of nonlinear waveguide arrays*, Phys. Rev. Lett. **87**, 233901 (2001).

[42] D. N. Christodoulides and E. D. Eugenieva, *Minimizing bending losses in two-dimensional discrete soliton networks*, Opt. Lett. **26**, 1876 (2001).

[43] E. D. Eugenieva, N. K. Efremidis and D. N. Christodoulides, *Design of switching junctions for twodimensional discrete soliton networks*, Opt. Lett. **26**, 1978 (2001).

[44] R. Keil, M. Heinrich, F. Dreisow, T. Pertsch, A. Tünnermann, S. Nolte, D. N. Christodoulides and A. Szameit, *All-optical routing and switching for three-dimensional photonic circuitry*, Scientific Reports **94**, 1 (2011).

[45] M. D. Ventra, S. Evoy and J. R. Heflin, *Introduction to Nanoscale Science and Technology* (Springer, New York, 2004).

[46] A. N. Cleland, *Foundation of Nanomechanics: From Solid-State Theory to Device Applications* (Springer, New York, 2003).

[47] M. L. Roukes, *Nanoelectromechanical systems face the future*, Phys. World **14**, 25 (2001).

[48] A. N. Cleland and M. L. Roukes, *A nanometre-scale mechanical electrometer*, Nature (London) **392**, 160 (1998).

[49] I. Katz, R. Lifshitz, A. Retzker and R. Straub, *Classical to quantum transition of a driven nonlinear nanomechanical resonator*, New J. Phys. **10**, 125023 (2008).

[50] R. Lifshitz, E. Kenig and M. C. Cross, *Collective dynamics in arrays of coupled nonlinear resonators*, arXiv:1111.2967v1.

[51] E. Buks and M. L. Roukes, *Electrically tunable collective response in a coupled micromechanical array*, J. Microelectromech. Syst. **11**, 802 (2002).

[52] J. Wiersig, S. Flach and K.-H. Ahn, *Discrete breathers in ac-driven nanoelectromechanical shuttle arrays*, Appl. Phys. Lett. **93**, 222110 (2008).

[53] M. Sato, B. E. Hubbard and A. J. Sievers, *Nonlinear energy localization and its manipulation in micromechanical oscillator arrays*, Rev. Mod. Phys. **78**, 137 (2006).

[54] M. Sato and A. J. Sievers, *Driven localized excitations in the acoustic spectrum of small nonlinear macroscopic and microscopic lattices*, Phys. Rev. Lett. **98**, 214101 (2007).

[55] M. Sato, S. Yasui, M. Kimura and A. J. Sievers, *Management of localized energy in discrete nonlinear transmission lines*, EPL **80**, 30002 (2007).

[56] M. A. Porter, N. J. Zabusky, B. Hu and D. K. Campbell, *Fermi, Pasta, Ulam and the Birth of Experimental Mathematics*, American Scientist **97**, 214 (2009).

[57] R. Lifshitz and M. C. Cross, *Response of parametrically driven nonlinear coupled oscillators with application to micromechanical and nanomechanical resonator arrays*, Phys. Rev. B **67**, 134302 (2003).

[58] E. Kenig, B. A. Malomed, M. C. Cross and R. Lifshitz, *Intrinsic localized modes in parametrically driven arrays of nonlinear resonators*, Phys. Rev. E **80**, 046202 (2009).

[59] D. Hennig and G. Tsironis, *Wave transmission in nonlinear lattices*, Phys. Rep. **307**, 333 (1999).

[60] P. G. Kevrekidis, K. Ø. Rasmussen and A. R. Bishop, *The discrete nonlinear Schrödinger equation: a survey of recent results*, Internal. J. Modern Phys. B **15**, 2833 (2001).

[61] A. J. Sievers and S. Takeno, *Intrinsic localized modes in anharmonic crystals*, Phys. Rev. Lett. **61**, 970 (1988).

[62] J. B. Page, *Asymptotic solutions for localized vibrational modes in strongly anharmonic periodic systems*, Phys. Rev. B. **41**, 7835 (1990).

[63] R. Peierls, *The size of a dislocation*, Proc. Phys. Soc. London **52**, 34 (1940).

[64] F. R. N. Nabarro, *Dislocations in a simple cubic lattice*, Proc. Phys. Soc. London **59**, 256 (1947).

[65] L. Hadžievski, A. Maluckov, M. Stepić and D. Kip, *Power controlled soliton stability and steering in lattices with saturable nonlinearity*, Phys. Rev. Lett. **93**, 033901 (2004).

[66] T. R. O. Melvin, A. R. Champneys, P. G. Kevrekidis and J. Cuevas, *Travelling solitary waves in the discrete Schrödinger equation with saturable nonlinearity: existence, stability, and dynamics*, Physica D **237**, 551 (2008).

[67] T. R. O. Melvin, A. R. Champneys, P. G. Kevrekidis and J. Cuevas, *Radiationless travelling waves in saturable nonlinear Schrödinger lattices*, Phys. Rev. Lett. **97**, 124101 (2006).

[68] J. Gómez-Gardeñes, L. M. Floría, M. Peyrard and A. R. Bishop, *Nonintegrable Schrödinger discrete breathers*, Chaos **14**, 1130 (2004).

[69] T. R. O. Melvin, A. R. Champneys and D. E. Pelinovsky, *Discrete traveling solitons in the Salerno model*, SIAM J. Appl. Dyn. Syst. **8(2)**, 689 (2009).

[70] R. S. MacKay and S. Aubry, *Proof of existence of breathers for time-reversible or Hamiltonian networks of weakly coupled oscillators*, Nonlinearity **7**, 1623 (1994).

[71] G. L. Alfimov, V. A. Brazhnyi and V. V. Konotop, *On classification of intrinsic localized modes for the discrete nonlinear Schrödinger equation*, Physica D **194**, 127 (2004).

[72] D. E. Pelinovsky, P. G. Kevrekidis and D. J. Frantzeskakis, *Stability of discrete solitons in nonlinear Schröodinger lattices*, Physica D **212**, 1 (2005).

[73] D. J. Kaup and T. K. Vogel, *Quantitative measurement of variational approximations*, Phys. Lett. A **362**, 289 (2007).

[74] B. A. Malomed, *Variational methods in nonlinear fiber optics and related fields*, Prog. Opt. **43**, 69 (2002).

[75] A. B. Aceves, C. De Angelis, T. Peschel, R. Muschall, F. Lederer, S. Trillo and S. Wabnitz, *Discrete self-trapping, soliton interactions, and beam steering in nonlinear waveguide arrays*, Phys. Rev. E **53**, 1172 (1996).

[76] J. Cuevas, G. James, P. G. Kevrekidis, B.A. Malomed and B. Sánchez-Rey, *Approximation of solitons in the discrete NLS equation*, J. Nonlinear Math. Phys. **15** 124 (2008).

[77] D. J. Kaup, *Variational solutions for the discrete nonlinear Schrödinger equation*, Math. Comput. Simulat. **69**, 322 (2005).

[78] C. Chong, D. E. Pelinovsky and G. Schneider, *On the validity of the variational approximation in discrete nonlinear Schrödinger equations*, Physica D **241**, 115 (2011).

[79] B. A. Malomed and M. I. Weinstein, *Soliton dynamics in the discrete nonlinear Schrödinger equation*, Phys. Lett. A **220**, 91 (1996).

[80] J. Cuevas, P. G. Kevrekidis, D. J. Frantzeskakis and B. A. Malomed, *Discrete solitons in nonlinear Schrödinger lattices with a power-law nonlinearity*, Physica D **238** 67 (2009).

[81] R. Carretero-González, J. D. Talley, C. Chong and B. A. Malomed, *Multistable solitons in the cubic-quintic discrete nonlinear Schrödinger equation*, Physica D **216** 77 (2006).

[82] C. Chong and D. E. Pelinovsky, *Variational approximations of bifurcations of asymmetric solitons in cubic-quintic nonlinear Schrödinger lattices*, Disc. Cont. Dyn. Sys. S **4**, 1019 (2011).

[83] K. Ø. Rasmussen, P. L. Christiansen, Y. B. Johansson, M. Gaididei and S. F. Mingaleev, *Localized excitations in discrete nonlinear Schrödinger systems: effects of nonlocal dispersive interactions and noise*, Physica D **113**, 134 (1998).

[84] C. Chong, R. Carretero-González, B. A. Malomed and P. G. Kevrekidis, *Variational approximations in discrete nonlinear Schrödinger equations with next-nearest-neighbor couplings*, Physica D **240**, 1205 (2011).

[85] D. Hennig, *Periodic, quasiperiodic, and chaotic localized solutions of a driven, damped nonlinear lattice*, Phys. Rev. E **59**, 1637 (1999).

[86] E. P. Fitrakis, P. G. Kevrekidis, H. Susanto and D. J. Frantzeskakis, *Dark solitons in discrete lattices: Saturable versus cubic nonlinearities*, Phys. Rev. E **75**, 066608 (2007).

[87] M. Johansson and Yu. S. Kivshar, *Discreteness-induced oscillatory instabilities of dark solitons*, Phys. Rev. Lett. **82**, 85 (1999).

[88] Yu. S. Kivshar, W. Królikowski and O. A. Chubykalo, *Dark solitons in discrete lattices*, Phys. Rev. E **50**, 5020 (1994).

[89] H. Susanto and M. Johansson, *Discrete dark solitons with multiple holes*, Phys. Rev. E **72**, 016605 (2005).

[90] D. E. Pelinovsky and P. G. Kevrekidis, *Stability of discrete dark solitons in nonlinear Schrödinger lattices*, J. Phys. A. **41**, 185206 (2008).

[91] H. Susanto, Q. E. Hoq and P. G. Kevrekidis, *Stability of discrete solitons in the presence of parametric driving*, Phys. Rev. E **74**, 067601 (2006).

[92] N. V. Alexeeva, I. V. Barashenkov and G. P. Tsironis, *Impurity-induced stabilization of solitons in arrays of parametrically driven nonlinear oscillators*, Phys. Rev. Lett. **84**, 3053 (2000).

[93] I. V. Barashenkov, N. V. Alexeeva and E. V. Zemlyanaya, *Two- and three-dimensional oscillons in nonlinear faraday resonance*, Phys. Rev. Lett. **89**, 104101 (2002).

[94] N. V. Alexeeva, *Stabilization mechanism for two-dimensional solitons in nonlinear parametric resonance*, Theor. Math. Phys. **144**, 1075 (2005).

[95] I. V. Barashenkov, E. V. Zemlyanaya and M. Bär, *Traveling solitons in the parametrically driven nonlinear Schrödinger equation*, Phys. Rev. E **64**, 016603 (2001).

[96] I. V. Barashenkov, S. R. Woodford and E. V. Zemlyanaya, *Parametrically driven dark solitons*, Phys. Rev. Lett. **90**, 054103 (2003).

[97] I. V. Barashenkov, S. Cross and B. A. Malomed, *Multistable pulselike solutions in a parametrically driven Ginzburg-Landau equation*, Phys. Rev. E **68**, 056605 (2003).

[98] I. V. Barashenkov and S. R. Woodford, *Complexes of stationary domain walls in the resonantly forced Ginzburg-Landau equation*, Phys. Rev. E **71**, 026613 (2005).

[99] I. V. Barashenkov, S. R. Woodford and E. V. Zemlyanaya, *Interactions of parametrically driven dark solitons. I. Néel-Néel and Bloch-Bloch interactions*, Phys. Rev. E **75**, 026604 (2007).

[100] I. V. Barashenkov and S. R. Woodford, *Interactions of parametrically driven dark solitons. II. Néel-Bloch interactions*, Phys. Rev. E **75**, 026605 (2007).

[101] V. M. Kaurov and A. B. Kuklov, *Josephson vortex between two atomic Bose-Einstein condensates*, Phys. Rev. A **71**, 011601(R) (2005).

[102] V. M. Kaurov and A. B. Kuklov, *Atomic Josephson vortices*, Phys. Rev. A **73**, 013627 (2006).

[103] C. Baesens, S. Kim and R. S. MacKay, *Localised modes on localised equilibria*, Physica D **133**, 242 (1998).

[104] S. C. Masmanidis, R. B. Karabalin, I. De Vlaminck, G. Borghs, M. R. Freeman and M. L. Roukes, *Multifunctional nanomechanical systems via tunably coupled piezoelectric actuation*, Science **317**, 780 (2007).

[105] Yu. S. Kivshar, *Localized modes in a chain with nonlinear on-site potential*, Phys. Lett. A **173**, 172 (1993).

[106] M. Remoissenet, *Low-amplitude breather and envelope solitons in quasi-one-dimensional physical models*, Phys. Rev. B **33**, 2386 (1986).

[107] M. Syafwan, H. Susanto and S. M. Cox, *Discrete solitons in electromechanical resonators*, Phys. Rev. E **81**, 026207 (2010).

[108] Yu. A. Kosevich and G. Corso, *Temporal Fourier spectra of stationary and slowly moving breathers in Fermi–Pasta–Ulam anharmonic lattice*, Physica D **170**, 1 (2002).

[109] I. V. Barashenkov, M. M. Bogdan and V. I. Korobov, *Stability diagram of the phase-locked solitons in the parametrically driven, damped nonlinear Schrödinger equation*, EPL **15**, 113 (1991).

[110] M. Kollmann, H. W. Capel and T. Bountis, *Breathers and multibreathers in a periodically driven damped discrete nonlinear Schrödinger equation*, Phys. Rev. E **60**, 1195 (1999).

[111] M. Bondila, I. V. Barashenkov and M. M. Bogdan, *Topography of attractors of the parametrically driven nonlinear Schrödinger equation*, Physica D **87**, 314 (1995).

[112] I. V. Barashenkov, E. V. Zemlyanaya and T. C. van Heerden, *Time-periodic solitons in a damped-driven nonlinear Schrödinger equation*, Phys. Rev. E **83**, 056609 (2011).

[113] I. V. Barashenkov and E. V. Zemlyanaya, *Soliton complexity in the damped-driven nonlinear Schrödinger equation: Stationary to periodic to quasiperiodic complexes*, Phys. Rev. E **83**, 056610 (2011).

[114] P. G. Kevrekidis, A. R. Bishop and K. Ø. Rasmussen, *Twisted localized modes*, Phys. Rev. E **63**, 036603 (2001).

[115] Yu. A. Kuznetsov, *Elements of Applied Bifurcation Theory* (Applied Mathematical Sciences Vol. 112), 2nd edn, (Springer-Verlag, New York, 1998)

[116] J. C. Eilbeck, *Numerical simulations of the dynamics of polypeptide chains and proteins*. In C. Kawabata and A. R. Bishop (Editors), *Computer Analysis for Life Science: Progress and Challenges in Biological and Synthetic Polymer Research*, pages 12-21 (Ohmsha, Tokyo, 1986).

[117] H. Feddersen, *Solitary wave solutions to the discrete nonlinear Schrödinger equation*. In M. Remoissenet and M. Peyrard (Editors), *Nonlinear Coherent Structures in Physics and Biology*, vol. 393 of Lecture Notes in Physics, pages 159-167 (Springer, Berlin, 1991).

[118] D. B. Duncan, J. C. Eilbeck, H. Feddersen and J. A. D. Wattis, *Solitons on lattices*, Physica D **68**, 1 (1993).

[119] J. Gómez-Gardeñes, F. Falo and L. M. Floría, *Mobile localization in nonlinear Schrödinger lattices*, Phys. Lett. A **332**, 213 (2004).

[120] D. E. Pelinovsky, T. R. O. Melvin and A. R. Champneys, *One-parameter localized traveling waves in nonlinear Schrödinger lattices*, Physica D **236**, 22 (2007).

[121] C. Chong, R. Carretero-González, B. A. Malomed and P. G. Kevrekidis, *Multistable solitons in higher-dimensional cubic quintic nonlinear Schrödinger lattices*, Physica D **238**, 126 (2009).

[122] R. A. Vicencio and M. Johansson, *Discrete soliton mobility in two-dimensional waveguide arrays with saturable nonlinearity*, Phys. Rev. E **73**, 046602 (2006).

[123] A. Khare, K. Ø. Rasmussen, M. R. Samuelsen and A. Saxena, *Exact solutions of the saturable discrete nonlinear Schrödinger equation*, J. Phys. A: Math. Gen. **38**, 807 (2005).

[124] A. Khare, K. Ø. Rasmussen, M. R. Samuelsen and A. Saxena, *Staggered and short-period solutions of the saturable discrete nonlinear Schrödinger equation*, J. Phys. A: Math. Gen. **42**, 085002 (2009).

[125] J. Yang, B. A. Malomed and D. J. Kaup, *Embedded solitons in second-harmonic-generating systems*, Phys. Rev. Lett. **83**, 1958 (1999).

[126] O. F. Oxtoby and I. V. Barashenkov, *Moving solitons in the discrete nonlinear Schrödinger equation*, Phys. Rev. E **76**, 036603 (2007).

[127] A. Cayley, *The Newton-Fourier imaginary problem*, Am. J. Math. **2**, 97 (1879).

[128] D. J. Kaup and B. A. Malomed, *Embedded solitons in Lagrangian and Semi-Lagrangian Systems*, Physica D **184**, 153 (2003).

[129] I. S. Gradshteyn and I. M. Ryzhik, *Tables of Integrals, Series, and Products* (Academic Press: New York, 2000).

[130] N. Flytzanis, B.A. Malomed and J. A. D. Wattis, *Analysis of stability of solitons in one-dimensional lattices*, Phys. Lett. A **180**, 107 (1993).

[131] D. Anderson, *Variational approach to nonlinear pulse propagation in optical fibers*, Phys. Rev. A **27**, 3135 (1983).

[132] J. P. Boyd, *Weakly nonlocal solitary waves and beyond-all-orders asymptotics*, (Kluwer Academic Publishers: Dordrecht, 1998).

[133] M. Johansson and S. Aubry, G*rowth and decay of discrete nonlinear Schrödinger breathers interacting with internal modes or standing-wave phonons*, Phys. Rev. E **61**, 5864 (2000).

[134] J. Yang, *Nonlinear Waves in Integrable and Nonintegrable Systems* (SIAM, Philadelphia, 2010).

[135] J. P. Boyd, *Chebyshev and Fourier spectral methods* (Dover Publications, Mineola, N.Y., 2001).

[136] I. V. Barashenkov and E. V. Zemlyanaya, *Traveling solitons in the damped-driven nonlinear Schrödinger equation*, SIAM J. Appl. Math. **64**, 800 (2004).